Performance of Azimuth and Bow Thrusters during Ship Maneuvers

Vom Promotionsausschuss der
Technischen Universität Hamburg

zur Erlangung des akademischen Grades

Doktor-Ingenieur

genehmigte Dissertation (Monografie)

von
Keqi Wang

aus
Changchun, China

2025

Vorsitzender des Prüfungsausschusses
Prof. Dr.-Ing. Hermann Lödding

Gutachter
1. Gutachter: Prof. Dr.-Ing. Moustafa Abdel-Maksoud
2. Gutachter: Prof. Dr.-Ing. Carlos Jahn

Tag der mündlichen Prüfung
03.03.2025

Digital Object Identifier (DOI): https://doi.org/10.15480/882.15017
https://orcid.org/0000-0002-4166-5223

Acknowledgments

First of all, I would like to sincerely thank Prof. Moustafa Abdel-Maksoud, my supervisor, for his many weekend hours of help with revisions, as well as his patience, professional guidance, and valuable comments during the development of this thesis. He also provided me with the opportunity to participate in the InterThrust, HiOcav, NATO, and ASSESS projects, which allowed me to acquire a deeper understanding of the scientific issues involved. In addition, the financial support from the Federal Ministry for Economic Affairs and Energy is appreciated. I would like to offer my special thanks to Prof. Carlos Jahn for reviewing this thesis and Prof. Hermann Lödding for chairing the examination board.

I would also like to extend my thanks to my former colleague Patrick Schiller for his assistance in keeping my work on schedule; to Dr. Vladimir Krasilnikov from SINTEF, Norway, for providing me with detailed mathematical descriptions of the bow thruster; to Dr. Jörg Hinnenthal from Jastram, Hamburg, Germany, for sharing his practical experience in the industry; to Michael Palm from Voith, Heidenheim, Germany, for his advice on the numerical calculations; and finally to SINTEF, Norway, for sharing the experimental results.

Many thanks to Helen Ketelsen, our friendly team assistant, who helped me navigate through the plethora of English. I also wish to thank my wonderful colleague and officemate, Dr. Gerrit Olbert, for his contribution to the office atmosphere, which was always harmonious and friendly. His presence always kept the work interesting and lively. Thanks also to Dr. Markus Pergande and Dr. Jan Clemens Neitzel for their support in offering me the resources to run the long-period simulations and Prof. Youjiang Wang and Dr. Chen Zeng for many useful discussions.

I would like to extend my special thanks to Dr. Martin Greve and Dr. Markus Druckenbrod, my tutors during my student years. They helped me find subjects of interest and provided professional support for many years.

Special thanks to my wife, Yining Chen, for providing me with delicious dinners when I came home late from the university. While I was writing my dissertation, my daughter, Wenke Wang, joined our family and is giving me unlimited happiness and joy. So I also would like to take this opportunity to thank her as well. Finally, I wish to thank my parents and friends for their encouragement, which allowed me to successfully complete this study.

Abstract

Active maneuvering devices improve the maneuverability of a vessel during departure and arrival, reducing the need for tug assistance. However, their operation in significant oblique flow conditions leads to complex flow behaviors, posing challenges in predicting the ship's response within the port environment.

This thesis develops an advanced maneuvering model that accounts for asymmetric flow interactions between the hull and maneuvering devices. An offshore supply vessel equipped with two stern azimuth thrusters and one bow thruster serves as the application case. The hydrodynamic performance of the vessel is evaluated using Reynolds-Averaged Navier-Stokes equations (RANS) simulations.

Azimuth thrusters, being directly exposed to external flow, are highly sensitive to oblique inflow conditions. Under such conditions, the deformed propeller slipstream can result in the generation of thrust in excess of that observed under bollard pull conditions. This study identifies critical operating ranges to mitigate propulsion system failure through a systematic analysis of azimuth angles (from 0° to $\pm 180^\circ$), azimuth speeds, and ship speeds. The results of numerical simulation also support the development of an Artificial Neural Network (ANN) model for fast predicting the performance of thruster.

In contrast, the bow tunnel propeller is shielded from external flow. As a result, the oblique flow may not have a significant effect on the performance of the propeller. However, the effects of the slipstream-hull interaction are taken into account. To evaluate these interactions, static simulations are performed on a vessel equipped with a single bow thruster at varying ship speeds and inflow angles. The transient effects of the slipstream are further analyzed by numerical Planar Motion Mechanism (PMM) tests. These tests not only capture transient phenomena, but also determine hydrodynamic derivatives which are subsequently integrated into the maneuvering model. To fully extract the interaction effects, the PMM tests are performed separately for the ship with and without tunnel thruster.

Finally, a maneuvering model is developed for ships equipped with two azimuth thrusters and one bow thruster. Using this model, turning circle simulations under various azimuth speeds, azimuth angles, and wake-field conditions demonstrate its effectiveness in predicting the ship's maneuvering performance.

Zusammenfassung

Manövrierorgane verbessern die Manövrierfähigkeit eines Schiffes beim An- und Ablegen und reduzieren den Bedarf an Schlepperhilfe. Bei starker Schräganströmung verursachen sie jedoch ein komplexes Strömungsphänomen, das die Vorhersage des Schiffsverhaltens im Hafenbereich stark einschränkt.

In der vorliegenden Arbeit wird ein erweitertes Manövriermodell entwickelt, welches die asymmetrischen Strömungsinteraktionen zwischen Schiffsrumpf und Manövrierorganen berücksichtigt. Als Anwendungsfall dient ein Offshore-Versorgungsschiff mit zwei Azimutantrieben am Heck und einem Querstrahlruder am Bug. Das hydrodynamische Verhalten des Schiffes wird mithilfe von RANS-Simulationen untersucht.

Azimutantriebe, die direkt der Außenströmung ausgesetzt sind, reagieren empfindlich auf Schräganströmung. Unter bestimmten Bedingungen kann der Propellerschub den Pfahlzug übersteigen. Um Ausfälle des Antriebssystems zu vermeiden, identifiziert die vorliegende Studie kritische Betriebsbereiche, indem Azimutwinkel von $0°$ bis $\pm 180°$ sowie Azimut- und Schiffsgeschwindigkeiten systematisch analysiert werden. Die numerischen Simulationen unterstützen zudem die Entwicklung eines Künstliche-Intelligenz (KI)-Modells für die schnelle Vorhersage der Auswirkungen des Antriebssystems.

Im Gegensatz zum Azimutantrieb ist das Bugstrahlruder durch den Schiffsrumpf vor der Außenströmung geschützt, sodass seine Wirkung durch Schräganströmung nicht wesentlich beeinflusst wird. Die Wechselwirkung zwischen dem Propellerstrahl und dem Schiffsrumpf muss jedoch berücksichtigt werden. Daher werden statische Simulationen für ein Schiff mit einem Bugstrahlruder bei verschiedenen Schiffsgeschwindigkeiten und Anströmwinkeln durchgeführt.

Zusätzlich werden die dynamischen Effekte des Propellerstrahls mithilfe numerischer PMM-Versuche analysiert. Diese ermöglichen nicht nur die Erfassung instationärer Strömungsphänomene, sondern auch die Ermittlung von Manövrierkoeffizienten, die anschließend in das Manövriermodell integriert werden. Zur vollständigen Erfassung der Wechselwirkung werden die PMM-Versuche sowohl mit als auch ohne Querstrahler durchgeführt.

Schließlich wird ein Manövriermodell für das Schiff mit zwei Azimutantrieben und einem Bugstrahlruder entwickelt. Mithilfe dieses Modells wird die Manövrierfähigkeit des Schiffes bei Drehkreismanövern unter verschiedenen Azimutgeschwindigkeiten, Azimutwinkeln und Strömungsbedingungen bewertet.

Contents

List of Figures

List of Tables

Nomenclature

General Variables

f	Azimuth speed	[Hz]
n	Propeller revolutions per second	[Hz]
t	Thrust deduction factor	[−]
u	Longitudinal velocity component in ship-fixed Cartesian Coordinate System (COS) (ship-COS)	[m/s]
v	Transverse velocity component in ship-COS	[m/s]
w	Wake fraction	[−]
x, y, z	Space variable in ship-COS	[−]
x_0, y_0, z_0	Space variable in space-fixed Cartesian-COS (space-COS)	[−]
x_G	Longitudinal position of center of gravity in ship-COS	[m]
A	Area of the tunnel cross section	[m^2]
D	Propeller diameter	[m]
I_{zz}	Moment of inertia	[kgm^2]
L_{pp}	Ship length between perpendiculars	[m]
P/D	Propeller pitch ratio	[−]
R_t	Total ship resistance	[N]
U_0	Ship speed	[m/s]

Flow Quantities

v_a	Inflow axial velocity	[m/s]
v_∞	Free stream velocity	[m/s]
v_{ix}	Axial component of propeller induced velocity	[m/s]
v_p	Averaged axial velocity inside the tunnel	[m/s]

v_q	Cross flow velocity	[m/s]
Dimensional Forces and Moments		
F_x	Thruster longitudinal force in thruster-fixed Cartesian COS (thruster-COS)	[N]
F_y	Thruster transverse force in thruster-COS	[N]
P	Power	[W]
Q	Propeller torque	[Nm]
Q_z	Thruster vertical moment in thruster-COS	[Nm]
T	Thrust of propeller: $T = 2\rho A v_{ix}\sqrt{v_{ix}^2 + 2v_\infty v_{ix}\cos(\delta) + v_\infty^2}$	[N]
Y_p	Tunnel propeller force: $Y_p = 0.5\rho A v_p^2$	[N]
Y_r	Tunnel jet reaction force: $Y_r = \rho A v_p^2$	[N]
Y_s	Suction force induced by the slipstream on the hull	[N]
Dimensionless Forces and Moments		
kF_x	Thruster longitudinal force in thruster-COS: $kF_x = F_x/(\rho n^2 D^4)$	[−]
kF_y	Thruster transverse force in thruster-COS: $kF_y = F_y/(\rho n^2 D^4)$	[−]
kQ_z	Thruster vertical moment force in thruster-COS: $kQ_z = Q_z/(\rho n^2 D^5)$	[−]
k_x	Thruster longitudinal force at x_G in ship-COS	[−]
k_y	Thruster transverse force at x_G in ship-COS	[−]
k_n	Thruster yaw moment at x_G in ship-COS	[−]
k_t	Thrust coefficient of propeller: $k_t = T/(\rho n^2 D^4)$	[−]
k_q	Torque coefficient of propeller: $k_q = Q/(\rho n^2 D^5)$	[−]
Dimensionless Values		
j	Advance ratio: $j = v_a/(\rho n D)$	[−]
C_M	Merit coefficient: $C_M = k_t/\pi^{3/2}/k_q$	[−]
F_n	Froude number: $F_n = U_0/(\sqrt{gL_{\text{pp}}})$	[−]
η	Propeller efficiency: $\eta = (j/2\pi)(k_t/k_q)$	[−]
λ	Thrust ration between Y_p and Y_r, for ideal condition: $\lambda = Y_p/Y_r = 0.5$	[−]

Hydrodynamic Derivatives		
X_*, Y_*, N_*	Hydrodynamic derivatives at x_G in ship-COS	[Variable]
X'_*, Y'_*, N'_*	Non-dimensional form of hydrodynamic derivatives	[−]
Artificial Neural Network		
l	Number of weights	[−]
w	Weight	[−]
E_D	Sum of squared errors	[−]
E_W	Sum of squared weights	[−]
$F(w)$	Cost function: $F(w) = \beta E_D + \alpha E_W$	[−]
M	Probabilistic model	[−]
P	Probability	[−]
γ	Effective number of parameters weights	[−]
σ	Variance	[−]
Planar Motion Mechanism		
r	Yaw rate at x_G	[rad/s]
u	Surge velocity at x_G	[m/s]
v	Sway velocity at x_G	[m/s]
X, Y	Total longitudinal force and total transverse force at x_G in ship-COS	[N]
N	Total yaw moment at x_G in ship-COS	[Nm]
ψ	Yaw angle	[rad]
ω	Ship circular frequency	[rad/s]
$\overrightarrow{T}$	Vector containing X, Y, and N	[Variable]
Angles		
β	Ship drift angle: $\beta = \arctan(-v/u)$	[rad]
δ	Inflow angle	[rad]
δ_{eff}	Effective inflow angle, $\delta_{\text{eff}} = \arctan(v_q/v_a)$	[rad]
δ_R	Rudder steering angle	[rad]

ψ	Heading angle; yaw angle	[rad]

Other Variables

$\overrightarrow{A_*}$	Fourier coefficients of velocity	[Variable]
$\overrightarrow{B_*}$	Fourier coefficients of acceleration	[Variable]
g	Gravity	[m/s^2]
ρ	Density of water	[kg/m^3]

Acronyms

ANN Artificial Neural Network

CFD Computational Fluid Dynamics

COS Coordinate System

DES Detached Eddy Simulation

DNS Direct Numerical Simulation

IMO International Maritime Organization

ITTC International Towing Tank Conference

LES Large Eddy Simulation

MC Merit Coefficient

MMG Maneuvering Modeling Group

MP Most Probable

MRM Multiple Run Method

MSE Mean Squared Error

OP Operation Point

PMM Planar Motion Mechanism

RANS Reynolds-Averaged Navier-Stokes equations

SRM Single Run Method

1 Motivation

1.1 Introduction

The International Maritime Organization (IMO) has issued rules and regulations to evaluate the maneuverability of ships; however, the regulations have focused only on the safe maneuvering of conventional ships under typical operating conditions. Other important aspects such as shallow-water maneuvering, low-speed maneuvering, and steering under extreme environmental conditions are not considered, where the direction of forward motion may no longer be the ship's primary direction of motion. During low-speed maneuvers, many effects can have a considerable influence on the motion behavior of the ship. For example, Artyszuk [10], Gierusz [11], and Reichel [12] conducted experiments that showed that the bow thruster changes the position of the pivot point by increasing the ship's speed. This shift in the position of the pivot point can make it difficult for the ship to maneuver in confined spaces.

In addition, when a ship has forward speed or encounters an oblique flow while the bow thruster is operating, the slipstream of the bow thruster is bent, and this portion of the bent flow creates a suction force on the hull. The resulting transverse force will induce a yaw and a roll motion. Fig. (1.1) shows a simple schematic representation of the effect of the bow thruster on the hull of the ship. Y_s is the force due to the interference of the bow thruster slipstream with the ship's hull. Therefore, in harbor areas, self-propelled vessels require a thorough evaluation of the hydrodynamic forces generated by their steering devices to reduce the risk of accidents.

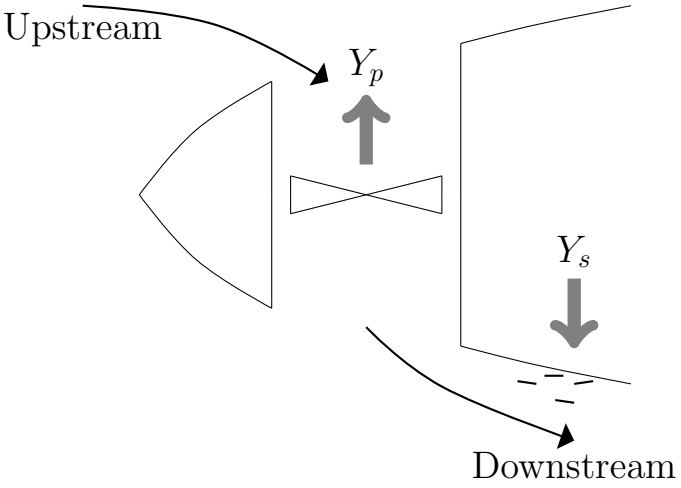

Figure 1.1: Degradation of transverse forces (adapted from Brix [1]).

1.2 Mathematical Models and Their Limitations

Most of the mathematical models used to simulate and evaluate the maneuverability of the ship have been developed based on three assumptions (Mucha [13], el Moctar et al. [14] and Cura-Hochbaum [15]):

1. Symmetry of forces: It is assumed that the ship's hull is symmetric and experiences symmetric forces when traveling straight ahead. However, the ship may experience asymmetric hydrodynamic forces in certain situations, such as during berthing and unberthing maneuvers.

2. Operation at design speed: Models typically assume that ships operate at design speeds, but ships often navigate at lower speeds in harbors where conventional rudders may not provide sufficient steering force. In this case, active devices such as steerable thrusters are frequently employed, as depicted in Fig. (1.2). During harbor maneuvers, a complex interaction can occur when an azimuth thruster is positioned downstream of another, changing the efficiency of a downstream thruster (Gierusz [16]). In addition, as a result of the diffusion of the propeller slipstream, there is notable interaction between the slipstreams of the azimuth thrusters and the ship's hull.

3. Neglect of non-linear terms: Many models ignore higher-order nonlinear terms, which become significant at off-design speeds due to increased cross-flow drag (Hooft [17]). A careful consideration of the non-linear contributions of the hydrodynamic characteristics of the flow is essential.

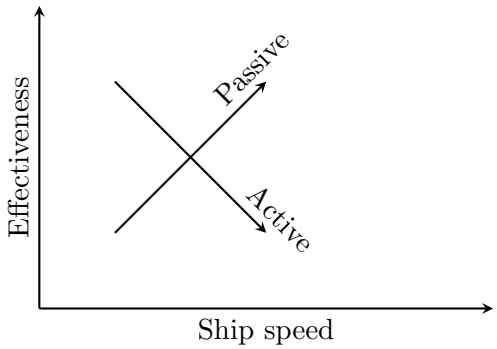

Figure 1.2: Application of active and passive control devices to ship speed (adapted from Brix [1]).

1.3 Aim of the Work

The objective of this thesis is to develop a maneuvering model to simulate the maneuvers of ships that use active steering devices to perform their maneuvers in confined areas. The model has to be able to take into account the asymmetry caused by tunnel thrusters or other active maneuvering devices.

1.4 Approach

1.4.1 Selection of ship maneuvering model

Different models can be applied to simulate ship maneuvers. The most commonly used maneuvering models are Abkowitz and Maneuvering Modeling Group (MMG), both are discussed in detail in Section (2.1). The fundamental difference between the two models is how they deal with the decomposition of forces and moments. For example, in the Abkowitz model, the interaction terms are automatically taken into account, since the decomposition is based on the Taylor expansion. In the MMG model, the effect of the interaction must be considered in the model developed for the bare hull, propeller, and rudder (Yasukawa [18]). In the absence of a reported maneuvering model that considers tunnel thruster-hull interactions, the Abkowitz formulation is more appropriate than the MMG model. However, since the regression coefficients apply globally to a fully appended ship, it becomes difficult to derive the effect of a single parameter on the maneuverability characteristics (Eminente and Coppola [19]). This limitation leads to inappropriate use in the ship design process. Therefore, to isolate the interaction effects, it is essential to perform an additional PMM test for the bare hull without the tunnel thruster. Both sets of captive model tests can be performed numerically.

1.4.2 Numerical approach

The interaction between an azimuth thruster (Fig. (1.3)) and the ship's hull may be less significant at ship design speed. During low-speed maneuvers, the high drift angle of the ship can result in high dynamic loads on the thrusters. Therefore, it is important to use accurate prediction methods to identify high-loading conditions to avoid the adverse effects of overloading and the potential failure of the propulsion unit. For this reason, fully discrete propellers are considered in the numerical simulations conducted within the thesis. A solver for RANS is applied to calculate the viscous flow properties on the ship with a working propeller.

1.4.3 Machine learning approach

Although RANS is a simplified Navier-Stokes equation, using it as a fast prediction tool may be inefficient in terms of computational time. Instead, a predictive model is needed to characterize the relationship between external conditions and the response of the propeller. The relationship is considered non-linear because of the complexity of the flow at large inflow angles experienced by the propellers. A general mathematical description may quickly face a bottleneck. In such a case, ANN is more appropriate to describe this non-linear relationship. The results of RANS simulations have been used to build an ANN model that can respond quickly and provide the appropriate results for a real-time monitoring system.

Figure 1.3: SCHOTTEL steerable thruster ([2]).

1.5 Outline of the Work

- Chapter 2 provides an overview of various methods for predicting ship maneuverability, including a summary of previous investigations on bow and azimuth thrusters. In addition, a brief overview of essential theoretical concepts is given as a prerequisite for the developed model. The chapter begins with a discussion of various maneuverability prediction techniques, such as database methods, model testing, and computational simulations. It then discusses the operational characteristics of tunnel thrusters and active devices such as podded propulsor and azimuth thruster. The chapter also covers important theoretical concepts, including the application of momentum theory and Bernoulli's equation to predict thruster performance, and the expansion of forces and moments for symmetric hulls using the Abkowitz-type maneuvering model. It also discusses recent experimental and numerical investigations of thruster performance under various conditions.

- Chapter 3 focuses on the simulation of turbulent flows using the RANS method in Computational Fluid Dynamics (CFD). It explains the importance of accurate turbulence modeling, especially near-wall regions, and discusses different simulation approaches such as Direct Numerical Simulation (DNS), Large Eddy Simulation (LES), and Detached Eddy Simulation (DES). The RANS method, chosen for its balance between accuracy and computational requirements, is used to model viscous fluid flow by solving the continuity and Navier-Stokes equations. It also discusses various numerical grids, highlighting structured and unstructured meshes, and introduces dynamic mesh techniques such as sliding mesh, remeshing, adaptive mesh refinement, overset mesh, and mesh deformation. ANSYS CFX solver is used for the simulations, using hybrid k-ω and k-ϵ models for better performance.

The structured mesh is preferred in this thesis for its control of boundary layers and critical flow gradients, with separate domains for the propeller, tunnel, and hull to optimize mesh quality and computational efficiency.

- Chapter 4 presents a detailed analysis of the hydrodynamic performance and maneuvering capabilities of an offshore vessel equipped with azimuth and bow thrusters. The study uses RANS calculations to investigate the interactions and performance of these thrusters. The performance of an azimuth thruster during maneuvers is analyzed considering factors such as the direction of propeller rotation and dynamic versus static simulation conditions. The use of ANN and data analysis to predict thruster longitudinal and transverse forces is also explored.

- Chapter 5 presents ship maneuvering simulations where hydrodynamic derivatives are obtained by virtual PMM tests. The model setup for the forced harmonic motions (surge, sway, yaw, and combined sway-yaw) is included in the numerical computation. The corresponding mesh deformation for these motions is briefly explained. An example of a ship turning maneuver based on the maneuvering coefficients is validated by comparison with the free-running test.

- Chapter 6 illustrates the steps in the development of maneuvering models, starting with the bare hull and progressing to the incorporation of thruster impacts. It proposes a generalized method for determining hydrodynamic coefficients. This method is based on a direct regression analysis of the hydrodynamic derivatives. The method allows the determination of the hydrodynamic derivatives for a wide range of maneuvering applications, e.g., during operation at off-design speed or by berthing and unberthing maneuvers in harbors. It also includes several simulations of turning maneuvers using the developed models.

- Chapter 7 emphasizes the importance of accurate modeling to improve ship maneuverability and performance in various operational scenarios. It also summarizes important results, such as how the tunnel thruster has a large effect on the lateral force and how ANN can be used to estimate thruster forces in complex flow situations. It suggests further research on the effects of thruster slipstreams on hull performance, the effects of ducts on maneuverability, and the expanded use of predictive models using ANN.

2 Literature Review

This chapter begins with an introduction to the prediction methods used to evaluate ship maneuverability. The operational characteristics of the azimuth and tunnel thrusters are then reviewed. In addition, a brief overview of essential theoretical concepts is provided as a prerequisite for the developed model.

2.1 Methods of Maneuvering Prediction

The various maneuverability prediction techniques have been thoroughly addressed in the first SIMMAN workshop (Stern et al. [20]). The purpose of the workshop was the validation of different maneuverability prediction methods. According to ITTC 2008 [3], the most relevant approaches for prediction include database methods, model tests, and computational simulations, which are concisely illustrated in Fig. (2.1).

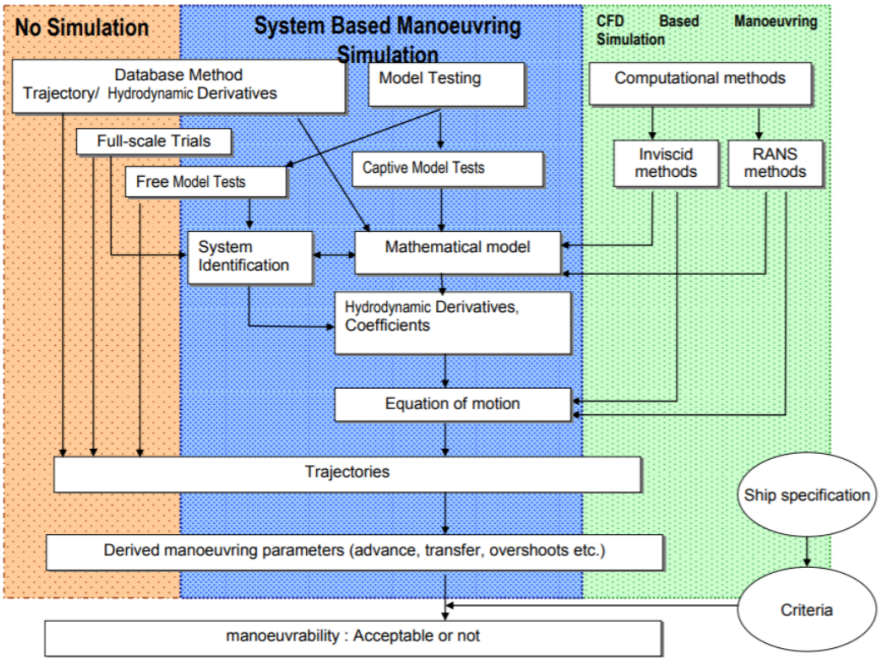

Figure 2.1: Overview of maneuvering prediction methods ([3]).

Methods based on an empirical database are mostly efficient. The approximate formulas are usually developed by analyzing the results of model experiments (Kijima et al. [21], Yoshimura and Masumoto [22]), due to the rapid changes in ship dimensions in

recent years, the accuracy of the prediction is limited if no ship with similar dimensions is available in the database.

System identification techniques typically use maneuvering coefficients derived from free-running data to build mathematical models (Araki et al. [23], Hajizadeh et al. [24] and Xue et al. [25]). This process optimizes the hydrodynamic coefficients within a mathematical model, ensuring that the model accurately reproduces maneuvers. The least squares estimation (Yin et al. [26]) and the recursive prediction error (Zhou and Blank [27]) are mostly used for the identification of the maneuvering coefficients. However, the prediction is highly dependent on the number of samples. A series of tests that cover a wide range of vessel speeds, drift angles, rudder angles, and rotation rates ITTC 2008 [3] may be required to obtain the desired results.

Free-running or captive model tests can perform maneuver prediction. While free-running tests are the most reliable and take advantage of the independence of a mathematical maneuvering model. For parametric studies, they are not suitable. Alternatively, a method based on hydrodynamic derivatives can be used to predict a variety of ship maneuvers, including zigzag, turning circle, and spiral tests. These derivatives can be determined through captive model tests, such as steady straight-line tests, harmonic motion tests using a PMM, and steady circular tests. In particular, the PMM test (Gertler [28]) provides comprehensive hydrodynamic derivatives involving damping and acceleration-related coefficients. After that, by resolving the equations of motion, it is possible to derive the ship's trajectory using the hydrodynamic derivatives from the PMM tests. The PMM test has practical advantages, as demonstrated by satisfactory agreement with the full-scale measurements reported by Chislett and Strøm-Tejsen [29] and Wolff [30]. However, there are two major challenges with model testing: First, scaling problems due to the inconsistency of the Reynolds number between model and full-scale; and second, excessive demands on the dimensions of the test basin due to the need to perform ship maneuvering tests without influences from the basin walls. The experimental costs associated with using a full-scale ship would be prohibitively high.

CFD-based RANS methods have gained considerable popularity in recent years. Mofidi [31] performed a direct CFD simulation with fully discretized moving propeller and rudder. The results show excellent agreement with the measurements. In his work, a coupled inviscid/viscous method is also implemented, where the propeller is treated with a boundary element method, while the propeller interaction with the hull is resolved using viscous flow methods, as implemented by Wökner et al. [32], Krasilnikov [33] and Neizel et al. [34]. However, good agreement can be achieved only in the vicinity of the design condition. The underlying reason is the limited accuracy of the potential code; under off-design conditions, the boundary element method fails to capture the blade leading edge separation. Cura-Hochbaum [15] has developed and applied a RANS code to simulate the maneuverability of a twin screw ship model. Compared with experiments, the results are generally satisfactory. However, the results showed overestimated overshoot angles in the $20°/20°$ zig-zag test, the simplified propeller model used was assumed to be the reason for the discrepancy. When the associated coefficients are extracted completely from the measurements, the difference in the overshoot angles disappears. Maneuvering experiments at low speeds have not been as widely published as design speeds. Hooft

[17] demonstrated that slow-moving ships exhibit considerable drift angles and that the effect of cross-flow drag on ship maneuvering can be significant. Some researchers, such as Le and Nguyen [35] and Kang and Hasegawa [36], simulated ship maneuvering at low speeds using the MMG model. Although their results agree well with the experimental results, the mathematical description can be very costly due to the regression analysis involving a large number of experimental samples. Therefore, an Abkowitz-type mathematical model seems appropriate in the case of limited information on the interaction parameter. An illustration of the Abkowitz type, derived from the Taylor expansion of the longitudinal force, is provided by Abdel-Maksoud [9],

$$\begin{aligned} X &= X_0 + [X_u\Delta u + X_v v + X_p p + X_r r + X_{\dot{u}}\dot{u} + X_{\dot{v}}\dot{v} + X_{\dot{p}}\dot{p} + X_{\dot{r}}\dot{r} + X_\delta\delta_R] \\ &+ \frac{1}{2}[X_{uu}\Delta u^2 + X_{vv}v^2 + ... + X_{\delta\delta}\delta_R^2 + 2X_{uv}\Delta uv + 2X_{ur}\Delta ur + ... + 2X_{\dot{r}\delta}\dot{r}\delta_R] \\ &+ \frac{1}{3}[X_{uuu}\Delta u^3 + X_{vvv}v^3 + ... + X_{\delta\delta\delta}\delta_R^3 + 3X_{uuv}\Delta u^2 v + 3X_{uur}\Delta u^2 r + ... + 3X_{\dot{r}\delta\delta}\dot{r}\delta_R^2 \\ &+ 6X_{uvr}\Delta uvr + 6X_{uv\dot{u}}\Delta uv\dot{u} + ... + 6X_{\dot{v}\dot{r}\delta}\dot{v}\dot{r}\delta_R]. \end{aligned} \tag{2.1}$$

The longitudinal force, denoted X, is a function of various velocities (u, v, p, r), accelerations ($\dot{u}$, $\dot{v}$, $\dot{p}$, $\dot{r}$), and rudder angles (δ_R). Abkowitz recommends using a third-order Taylor expansion, which is considered sufficient for many maneuvering simulations. The term Δu represents the change in ship speed, expressed as $u - U_0$, where U_0 is the constant speed of a ship in equilibrium before beginning the maneuver, resulting in a zero resultant longitudinal force (X_0).

Fig. (2.2) illustrates the relationship between X and v. If X depends only on velocity v, the expression can be formulated as follows:

$$X = X_v v + \frac{1}{2}X_{vv}v^2 + \frac{1}{3}X_{vvv}v^3. \tag{2.2}$$

The figure illustrates three possible relationships between the longitudinal force X and the transverse velocity v. Each of the three curves is symmetric about the X axis. Eq. (2.2) is required to satisfy the condition $X(-v) = X(v)$:

$$\begin{aligned} X(-v) &= X(v), \\ -X_v v + \frac{1}{2}X_{vv}v^2 - \frac{1}{3}X_{vvv}v^3 &\stackrel{!}{=} X_v v + \frac{1}{2}X_{vv}v^2 + \frac{1}{3}X_{vvv}v^3. \end{aligned} \tag{2.3}$$

obviously, the v-related odd terms are either zero or are treated as absolute values, i.e.,

$$X(v) = \begin{cases} \frac{1}{2}X_{vv}v^2, & \text{if } X_v = X_{vvv} = 0. \\ X_{|v|}|v| + \frac{1}{2}X_{vv}v^2 + \frac{1}{3}X_{|v|vv}|v|v^2, & \text{otherwise.} \end{cases} \tag{2.4}$$

The use of the absolute formulation could be expected in cases where the curve deviates from simple adherence to the relation $X(v) = \frac{1}{2}X_{vv}v^2$. However, certain publications (e.g., Mucha [13], el Moctar et al. [14], Cura-Hochbaum [15]) show that a simple

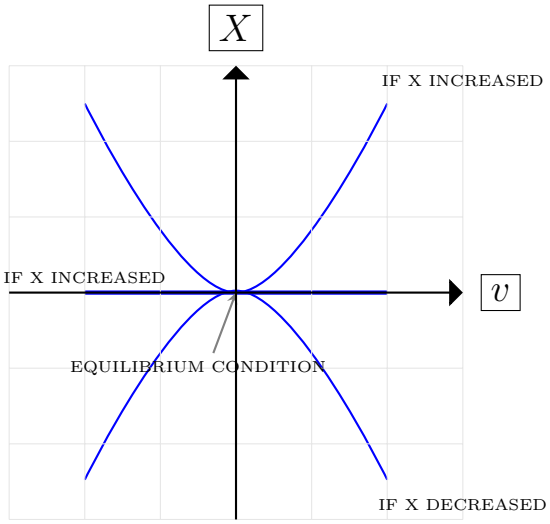

Figure 2.2: Three possible relationships between X and v (adapted from Crane [4]).

approximation can still give satisfactory results for standard ship maneuvers. The expansion of forces and moments for a symmetric hull in the horizontal plane, focusing only on X, Y, and N on the body axis, can therefore be formulated as follows:

$$\begin{aligned} X &= X_{\dot{u}}\dot{u} + X_u\Delta u + X_{uuu}\Delta u^3 + X_{vv}v^2 + X_{rr}r^2 \\ &+ X_{\delta\delta}\delta_R^2 + X_{vvu}vv\Delta u^2 + X_{rru}rr\Delta u + X_{\delta\delta u}\delta_R^2\Delta u \\ &+ X_{v\delta}v\delta_R + X_{r\delta}r\delta_R + X_{vru}vr\Delta u + X_{v\delta u}v\delta_R\Delta u + X_{r\delta u}r\delta_R\Delta u + X_{r\delta v}r\delta_R v, \end{aligned} \tag{2.5}$$

$$\begin{aligned} Y &= Y_0 + Y_{\dot{v}}\dot{v} + Y_{\dot{r}}\dot{r} + Y_{uu}\Delta u^2 + Y_v v + Y_{vvv}v^3 + Y_{vrr}vr^2 \\ &+ Y_{v\delta\delta}v\delta_R^2 + Y_{vu}v\Delta u + Y_{vuu}v\Delta u^2 + Y_r r + Y_{rrr}r^3 + Y_{rvv}rv^2 \\ &+ Y_{r\delta\delta}r\delta_R^2 + Y_{ru}r\Delta u + Y_{ruu}r\Delta u^2 + Y_\delta\delta_R^2 + Y_{\delta\delta\delta}\delta_R^3 \\ &+ Y_{\delta vv}\delta_R v^2 + Y_{\delta rr}\delta_R r^2 + Y_{\delta u}\delta_R\Delta u + Y_{\delta uu}\delta_R\Delta u^2 + Y_{vr\delta}vr\delta_R, \end{aligned} \tag{2.6}$$

$$\begin{aligned} N &= N_0 + N_{\dot{v}}\dot{v} + N_{\dot{r}}\dot{r} + N_{uu}\Delta u^2 + N_v v + N_{vvv}v^3 + N_{vrr}vr^2 \\ &+ N_{v\delta\delta}v\delta_R^2 + N_{vu}v\Delta u + N_{vuu}v\Delta u^2 + N_r r + N_{rrr}r^3 + N_{rvv}rv^2 \\ &+ N_{r\delta\delta}r\delta_R^2 + N_{ru}r\Delta u + N_{ruu}r\Delta u^2 + N_\delta\delta_R^2 + N_{\delta\delta\delta}\delta_R^3 \\ &+ N_{\delta vv}\delta_R v^2 + N_{\delta rr}\delta_R r^2 + N_{\delta u}\delta_R\Delta u + N_{\delta uu}\delta_R\Delta u^2 + N_{vr\delta}vr\delta_R. \end{aligned} \tag{2.7}$$

The presence of Y_0 and N_0 is due to asymmetric effects, such as the Hovgaard effect on a ship equipped with a single screw propulsion system. Note that the hydrodynamic derivatives in Eq. (2.5) already include the factor introduced in Eq. (2.1).

To facilitate the comparison between the model and the full-scale ship, the hydrodynamic derivatives are usually nondimensionalized. For example, the term $Y_v v$ has unit [N] and can be expressed as

$$
\begin{aligned}
v'Y'_v &= \frac{Y_v v}{0.5\rho U_0^2 L_{pp}^2} \\
&= \frac{v}{U_0}\frac{Y_v}{\frac{1}{U_0}0.5\rho U_0^2 L_{pp}^2} \\
&= \underbrace{\frac{v}{U_0}}_{v'}\underbrace{\frac{Y_v}{0.5\rho U_0 L_{pp}^2}}_{Y'_v}.
\end{aligned} \tag{2.8}
$$

Here U_0 represents the reference velocity, typically derived from the vessel speed before the start of a maneuver.

For an existing tunnel thruster, the formulation might require modification. Thus, the conventional equations (Eq. (2.5), Eq. (2.6) and Eq. (2.7)), should be appropriately revised. The development of the maneuvering model is discussed later in Section (6.4).

2.2 Performance of Tunnel Thruster

The primary auxiliary device for improving maneuverability at low ship speeds is the tunnel thruster. Tunnel thrusters can be classified according to the location of the installation in the bow or in the stern. At low speeds, bow thrusters are efficient in facilitating transverse motion of a ship. With increasing ship speed, the pivot point moves forward and in this case, the stern thrusters will deliver more yaw moment.

Applying the momentum theorem, which states that the thruster's force is equal to the flow's changing momentum, allows for the prediction of the thruster's performance. Based on Rankine's work on axial momentum, Eqs. (2.10) and (2.11) describe the relationship between the forces and the velocity inside the tunnel (see Appendix (A)):

$$Y_r = \rho A v_p^2 \tag{2.10}$$

and

$$Y_p = \frac{1}{2}\rho A v_p^2, \tag{2.11}$$

where the jet reaction Y_r is governed by the momentum equation and the tunnel propeller thrust Y_p is derived from the Bernoulli equation. The equations are established under the conditions of zero inflow velocity and constant cross section area inside the tunnel (A), as shown in Fig. (2.3).

The propeller force Y_p has only half the thrust of the jet reaction force Y_r, i.e., the thrust acting on the tunnel duct (Fig. (2.3)) must be equal to the propeller thrust, as discussed by Oosterveld [37]. However, it is important to recalculate the relationship between these two forces, taking into account the flow losses caused by friction and flow expansion, as shown in Fig. (2.4). These losses occur as a result of the change in the

lateral direction of the flow with respect to the main flow, a consequence of the diffusion of the free shear flow.

An accurate estimation of flow velocity is essential for reliable force prediction. This requires a series of experimental or numerical investigations to establish the relationship between the inflow and the slipstream velocity, as well as the propeller and the hull characteristics.

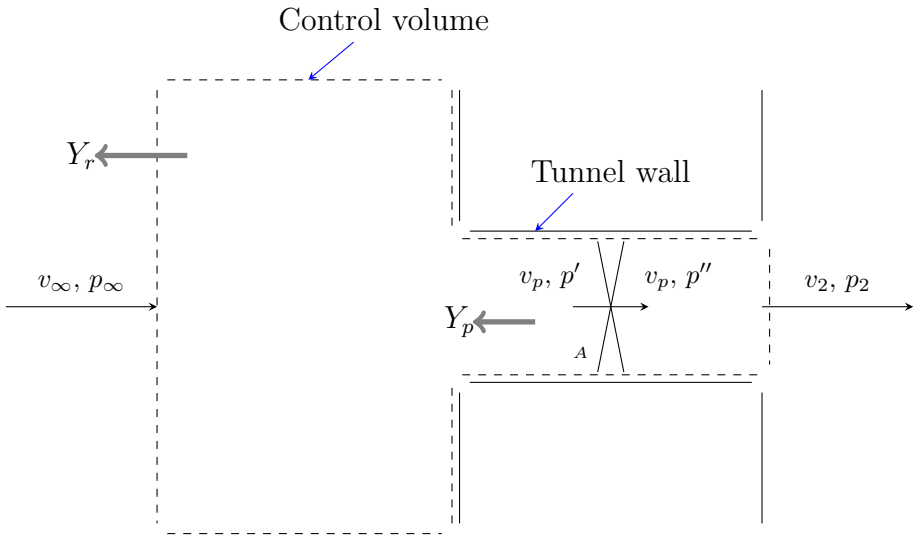

Figure 2.3: Simplified tunnel section. The transverse force on the tunnel wall is equal to the force on the propeller according to Eq. (2.10) and Eq. (2.11).

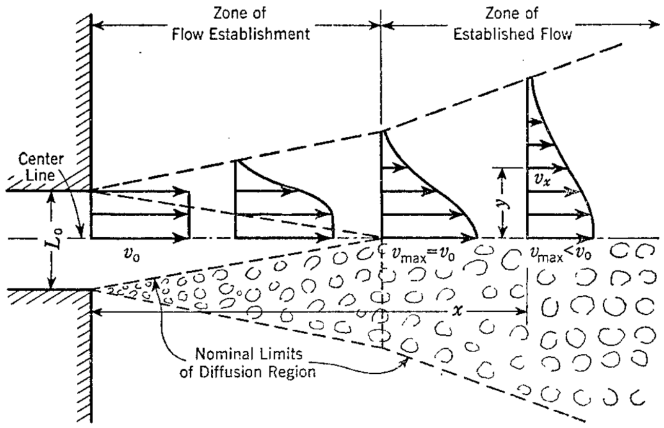

Figure 2.4: Turbulence free jet on jet exit side of a lateral thruster (Albertson et al. [5]).

Nienhuis [7] conducted tests on vessels equipped with a tunnel thruster. In the study, variations in total transverse forces as a function of ship speed and heading angle are investigated with the bow thruster in operation. The results indicated that the propeller

thruster had limited sensitivity to changes in external flow conditions. The trend of the propeller torque corresponded to that of the propeller thrust. The decrease in total transverse force was attributed to the suction force on the hull induced by the propeller slipstream.

The same aspect was experimentally investigated by Norrby [38]. The results showed that the propeller thrust does not really change with changing ship speed. The reason for the change in the resultant force is mainly due to the altered pressure distribution on the hull induced by the propeller slipstream. This conclusion is consistent with the findings of Chislett and Björheden [39], who also found that the center of the suction force Y_s, as shown in Fig. (1.1), changes linearly with increasing ship speed. In addition, the tendency of the resultant force to decrease is noticeable only up to a certain speed, after which a slight increase occurs, as reported by Taniguchi et al. [40].

Lübcke and Krüger [41] conducted experiments on a ship equipped with three bow thrusters and two stern thrusters operating at zero ship speed. Their observations revealed that the relationship of the resultant force with the propeller thrust, Y_r/Y_p, tends to remain constant at around 1.2, showing a minimal dependence on the number of active bow thrusters. This finding contrasts with the ratio of 2 as suggested by Eq. (2.10) and Eq. (2.11). The lower ratio is mainly attributed to flow losses, which are more pronounced for stern thrusters. The study concluded that both the shape of the hull and the length of the tunnel significantly influence the performance of the tunnel thruster.

The effect of bow thrusters under dynamic conditions remains understudied. Taniguchi et al. [40] conducted free-running tests to evaluate the effectiveness of bow thrusters compared to rudders. Their results showed that bow thrusters resulted in a lower drift angle compared to rudders, indicating a smaller reduction in longitudinal speed during their operation. In addition, Reichel [12] conducted model tests on three ships equipped with bow thrusters and found that these thrusters can initiate longitudinal motion, a phenomenon likely due to centrifugal force.

Feng et al. [42] performed a thorough hydrodynamic analysis of bow thrusters using the RANS numerical method. Their study considered various factors, including the effects of the hull, the angle of inflow, and the radius of the tunnel opening fillet. In addition, the interaction between multiple thrusters was investigated. Comparison with experiments shows that numerical simulations can provide sufficient accuracy.

Brix [43] introduced several design recommendations for bow thrusters, including the installation of a passive anti-suction tunnel for the purpose of pressure equalization, optimization of the tunnel arrangement to minimize thruster interactions, and orientation of the protective grid to reduce vortex formation. An updated review of this topic is presented by Baniela [44].

To describe the efficiency of a bow thruster, Merit Coefficient (MC) is often used, which characterizes the power ratio,

$$C_M = \frac{T v_p}{P}. \tag{2.12}$$

Substituting v_p as defined in Eq. (2.10) for the total thrust yields:

$$
\begin{aligned}
C_M &= \frac{T}{2\pi Qn}\sqrt{\frac{T}{\rho\frac{\pi}{4}D^2}} \\
&= \frac{k_t}{2\pi k_q Dn}(2nD)\sqrt{\frac{k_t}{\pi}} \\
&= \frac{(k_t/\pi)^{3/2}}{k_q}.
\end{aligned} \tag{2.13}
$$

MC is applicable to propellers operating at bollard pull (Beveridge [45]), eliminating the dependence on the propeller advance ratio j.

2.3 Performance of Steering Devices

A rudder is commonly used as a passive steering device for vessels, but can be insufficient for vessels navigating at low speeds. This inadequacy is due to a decrease in the flow velocity to the rudder and an abrupt reduction in the lifting force when the stall angle is reached. Considering these factors, it is necessary to replace the conventional propeller-rudder configuration with an active device to improve maneuverability during low-speed maneuvers.

The active device can be a podded propulsor or an azimuth thruster unit. The difference between them is in the placement of the propulsion machinery. According to Carlton [46], it is outside the hull in the podded propulsor but inside the hull in the azimuth thruster. These propulsion systems are widely used in tugs, offshore supply vessels, anchor handling vessels, drilling vessels, ferries, and fast transport vessels, specifically chosen for their ability to provide a high degree of maneuverability.

There are basically two configurations of maneuverable devices: the pulling and pushing modes, which differ in the arrangement of the housing. In the pushing mode, the propeller suffers from the housing's wake field, whereas in the pulling mode, the housing is behind the propeller and is therefore subject to the propeller slipstream. The operation conditions of both configurations are totally different. In pulling mode, the ship's transverse, yaw, or combined motions of the ship significantly affect the propeller slipstream during low-speed maneuvers, resulting in unstable forces on the housing. In contrast, in pushing mode, the effect of the housing wake field on the propeller may be minor compared to the effect of the housing on the propeller at high speeds. Therefore, the pushing mode is often used for a vessel operating at low speeds.

At the ship's design speed, comparable maneuverability can be expected between the conventional and pod configurations, as illustrated in Fig. (2.5). The pod housing produces less lateral force F_{yr} than the rudder at the same steering angle, but considering the contribution of the pod propeller to the lateral force, the difference in total lateral force may be negligible.

Frequent operation of the podded propulsor at high inflow angles can result in frequent damage to the bearings of the thruster units (Carlton [47]). It is essential to estimate

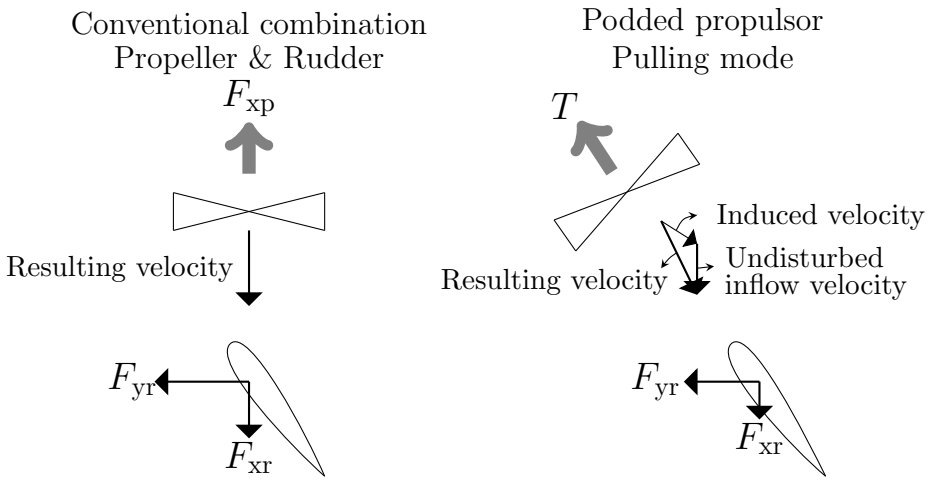

Figure 2.5: The difference in operating principle between a podded propulsor and a conventional shafted propeller with rudder (adapted from Krüger [6]).

the thruster forces with respect to the oblique flow. The propeller thrust can be derived from the classical momentum theory (see Appendix (B)):

$$T = 2\rho A v_{ix}(v_\infty \cos(\delta) + v_{ix}), \tag{2.14}$$

where v_∞ is the undisturbed inflow and v_{ix} is the propeller induced velocity perpendicular to the propeller disc. The angle between the oblique flow and the propeller shaft is defined as δ.

Maximum thrust is typically achieved under bollard pull conditions characterized by zero free stream velocity ($v_\infty = 0$ m/s). This thrust condition is also represented in Eq. (2.14) at $\delta = 90°$. However, in practical situations, the maximum thrust usually occurs near $\delta = 90°$, exceeding the thrust observed in the bollard pull condition. This difference occurs because the classical momentum theory does not account for the wake effect of the propeller.

A valid momentum theory for the oblique-flow conditions may meet the following two requirements:

- at $\delta = 0°$, the formulation should be back to the classical momentum equation, and
- at $\delta = 90°$, the model should provide the maximum thrust.

Glauert [48] proposed a mathematical formulation such as

$$\begin{aligned} T &= 2\rho A v_{ix}\sqrt{(v_{ix} + v_\infty \cos(\delta))^2 + (v_\infty \sin(\delta))^2} \\ &= 2\rho A v_{ix}\sqrt{v_{ix}^2 + 2v_\infty v_{ix}\cos(\delta) + v_\infty^2}. \end{aligned} \tag{2.15}$$

Stettler [49] demonstrated the feasibility of Glauert's hypothesis. Theoretical insight into the solution of the induced velocity v_{ix} involves the application of the blade element and the momentum approach combined with Glauert's assumption. The implementation, which accounts for propeller wake skew effects, number of blades, and pod wake effects, is described in detail. The method provides an acceptable estimate, consistent with the measurements, in the range of inflow angles between $-50°$ and $+50°$. A similar investigation of applicability was performed by Amini and Steen [50].

Recent experimental studies have investigated both the pulling and the pushing modes in open and ducted configurations over a wide range of inflow angles and loading conditions.

Akinturk et al. [51] investigated the propulsion characteristics of a puller-podded propulsor with an open propeller operating in an oblique flow, under static and dynamic conditions. A comparative analysis revealed consistent values between the static and dynamic cases. The maximum load is observed at approximately $120°$ and $110°$ for positive and negative azimuth speeds, respectively. This load asymmetry is attributed to variations in the direction of the propeller and thruster unit.

Islam et al. [52] conducted thorough investigations on azimuth velocity variations. The measurements showed that azimuth velocity has a negligible effect on longitudinal force, transverse force, and steering moment at both the investigated advance coefficients of $j = 0.2$ and $j = 0.8$. In contrast, Amini and Steen [53] found that azimuth velocity predominantly affects the transverse force and has a minor effect on the longitudinal force. This conclusion is drawn from experimental results obtained by an azimuth thruster with an open propeller.

Dang et al. [54] conducted an experimental study of a pushing thruster with a ducted propeller. The results show apparent fluctuations in the propeller thrust and unit moments after reaching the azimuth angle around $\pm 90°$, where the thrust is highest. A similar statement is made for other propeller pitch angles and operating conditions with respect to the advance ratios.

Islam [55] argued that the RANS-based CFD code effectively predicts results comparable to the measured data at high azimuth angles. In particular, the deviation of the RANS-based predictions from the measured results is in the range of 1% to 5% for azimuth angles ranging from $-180°$ to $180°$ under dynamic conditions.

Schiller et al. [56] performed RANS calculations for a ducted azimuth thruster. The study shows a consistent observation of a critical azimuth angle of approximately $90°$. In addition, azimuth velocity is observed to have a significant effect on transverse force, compared to longitudinal force, as denoted by Amini and Steen [53]. The authors provide insight into the underlying flow mechanisms.

Berchiche et al. [57] investigated the effect of a free surface on the performance of ducted azimuth thrusters using the RANS method. In general, thrust losses increase with decreasing azimuth thruster immersion. Ventilation occurs in a depth/diameter ratio of 0.9 for trawling ($j = 0.2$) and 0.8 for bollard conditions ($j = 0$). The loss of thrust in free sailing conditions ($j = 0.6$) in a depth/diameter ratio of 0.8 is only 3% compared to the value for the case without considering the free water surface.

The interaction between the thruster and the hull becomes critical when the jet attempts to interfere with the hull, especially since the flow follows the curved bilge radius out of the hull, a phenomenon known as the Coanda effect (Kumar and Das [58]). Fig. (2.6) illustrates the jet expansion of an azimuth thruster operating under unconfined conditions at $j = 0$, adapted from the study by Nienhuis [7]. The solid and dashed lines represent the maximum velocity U_m and the jet width of expansion, respectively. By x/D=6 downstream, the position of U_m falls on the x-axis. The free stream exhibits symmetry on the x-axis. However, if a plate is introduced parallel to the propeller shaft, the maximum speed profile changes. However, the difference in maximum speed between the two cases is minimal. In the presence of a plane boundary, Wei et al. [59] pointed out that three regions are expected to form, namely the free jet region (I), the impingement region (II), and the wall jet region (III). In region I, the jet exhibits free jet characteristics with symmetric upper and lower streams. As the jet enters Region II, its expansion in the lower stream is restricted when it encounters the boundary, forcing it to flow parallel to the boundary. Finally, in region III, the jet undergoes a classical wall jet formation.

Brandner [60] studied the interaction between the thrusters. During tests, the starboard thruster operated ahead of the port thruster. The influence of the interaction was observed only in the port thruster, while the starboard thruster remained unaffected by the presence of the port thruster. A mathematical model was formulated based on the estimation of the wake trajectory of the starboard thruster. The wake of the starboard thruster and the free inflow formed the inflow to the port thruster. The thruster-thruster interaction was calculated by adding up the contributions of these two flows. Satisfactory agreement with the experimental results was found only for azimuth angles below 90°. However, a notable deviation from the predictions occurred when the port thruster operated completely behind the wake of the starboard thruster.

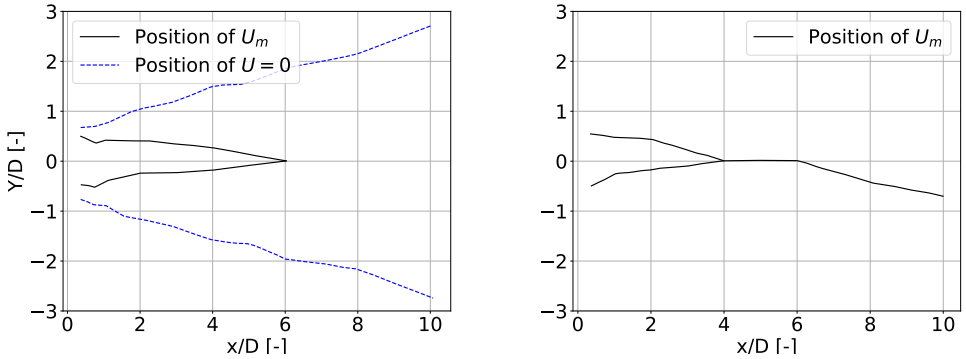

Figure 2.6: Evolution of maximum velocity and jet width downstream of a propeller at $j = 0.0$. Left: free unbounded condition; right: bounded condition under plate (adapted from Nienhuis [7]).

3 Numerical Computations

3.1 Introduction

The simulation of turbulent flows around complex geometries has become very well established in the field of computational fluid dynamics in recent decades. Turbulence is characterized by erratic and stochastic variations in pressure and velocity that are difficult to predict. The turbulent flows have different mixing layer scales, and the larger scales have a greater influence on the distribution of energy, whereas the smaller scales are responsible for dissipation. Accurate turbulence modeling is critical in CFD because it greatly affects the accuracy of the whole simulation, especially the flow at small scales in the region near the wall.

Direct Numerical Simulation (DNS) numerically solves the Navier-Stokes equations without utilizing a turbulence model, since all scales of motion are captured. Large Eddy Simulation (LES) directly simulates large-scale flow structures while modeling smaller scales. The RANS approach, which solves time-averaged equations of motion, is less effective in simulating flows with anisotropic behavior. A more accurate method is Detached Eddy Simulation (DES), which combines RANS and LES methods, using RANS near solid boundaries and LES elsewhere in the flow field. However, DES requires high computational resources due to the need for a refined mesh to accurately represent local turbulence.

Considering the balance between computational resources and accuracy, the RANS model remains widely used in industrial applications.

3.2 Viscose Fluid Flow Modeling

In the present work, the RANS method is applied. The continuity equation and the Reynolds-averaged Navier-Stokes equations for an incompressible Newtonian medium are solved. The conservation equations for mass and momentum are the following:

$$\rho \frac{\partial}{\partial x_j}\left(U_j\right) = 0 \tag{3.1a}$$

and

$$\rho \frac{\partial U_i}{\partial t} + \rho \frac{\partial}{\partial x_j}\left(U_i U_j\right) = -\frac{\partial p}{\partial x_j} + \frac{\partial}{\partial x_j}\left[\mu_{\text{eff}}\left(\frac{\partial U_i}{\partial x_j} + \frac{\partial U_j}{\partial x_i}\right)\right] + S_M, \tag{3.1b}$$

where S_M is the body force, and μ_{eff} is the effective viscosity, consisting of the laminar and turbulent viscosities, denoted as μ and μ_{t}, respectively. The definitions of turbulent

kinetic energy k, turbulence dissipation rate ϵ, and specific dissipation rate ω are shown below:

$$k : \left[\frac{m^2}{s^2}\right] = \overline{u_i' u_i'}/2 \tag{3.2a}$$

$$\epsilon : \left[\frac{m^2}{s^2}\frac{1}{\mathrm{s}}\right] = \nu \overline{\frac{\partial u_i'}{\partial x_j}\left(\frac{\partial u_i'}{\partial x_j} + \frac{\partial u_j'}{\partial x_i}\right)} \tag{3.2b}$$

$$\tag{3.2c}$$

$$\omega : \left[\frac{1}{\mathrm{s}}\right] = \frac{\epsilon}{k}, \tag{3.2d}$$

where the superscript $'$ denotes the fluctuation in the velocity deviating from their mean values. The turbulence viscosity is given by

$$\mu_\mathrm{t} \sim \rho\frac{k^2}{\epsilon} \tag{3.3a}$$

and

$$\mu_\mathrm{t} \sim \rho\frac{k}{\omega}. \tag{3.3b}$$

In some cases, it is not necessary to resolve all the turbulent properties of the flow. In this case, the two-equation models k-ω and k-ϵ are often considered sufficient and are used to connect the turbulent viscosity μ_t, which is the same in both models and does not depend on the direction. It might be possible to obtain more accurate results from a computer simulation if a more advanced RANS model is used, such as the Reynolds stress model, to calculate the Reynolds stress tensor $-\rho\overline{u_i' u_j'}$. However, simulation would require much more effort. Furthermore, the validation of anisotropic models is not as widely practiced as both k-ϵ and k-ω.

The main limitation of the k-ϵ model is its inability to accurately calculate the turbulence dissipation rate near the wall and to effectively model flow separation. In contrast, the major drawback of the k-ω model is its high sensitivity to the characteristics of the inlet free stream, a factor that can significantly affect the results. Menter [61] has suggested a hybrid model using the k-ϵ model in the farfield and k-ω in near the wall region. The blending function explained in the ANSYS [62] accomplishes the transition between the two models as follows:

$$\mu_\mathrm{t} = \frac{\rho a_1 k}{\max(a_1\omega, SF_2)}, \tag{3.4}$$

where S is the magnitude of the strain rate and corresponds to $\sqrt{2S_{ij}S_{ij}}$. F_2 is a blending function. Its value is 0 in the free shear layers and 1 in the attached boundary layers. a_1

is an empirical coefficient used to improve the performance when flow separation takes place. This hybrid k-ω model is applied in this work to represent the flow properties.

In all simulations, the ANSYS CFX solver is applied and provides second-order accuracy for the advection term in flow regions with low variable gradients. In regions with high variable gradients, it switches smoothly to a first-order upwind scheme for improved robustness. For the transient term, the default setting is the second-order backward Euler scheme, a robust and implicit time-stepping scheme.

3.3 Numerical Grid

The continuous fluid domain can be discretely divided into small cells, and for each cell, the Navier-Stokes equations can be solved numerically.

3.3.1 Type of grids

There are two primary types of numerical mesh: structured and unstructured. Structured meshes consist of regularly arranged cells, typically in the form of hexahedra. They offer better control over aspect ratios and less numerical diffusion in areas with critical flow gradients. However, they are generally suitable for simpler geometries and require considerable effort to produce high-quality meshes for complex domains. Unstructured meshes, on the other hand, have cells that are shaped like triangles or tetrahedra, and they allow for more local refinement in places where flow behaviors need to be accurately represented, like where there are sharp changes in velocity or pressure. In contrast, structured meshes apply refinement globally, extending to less critical regions.

Given the limitations of structured meshes and the less controlled nature of unstructured meshes in certain areas, a hybrid mesh that combines both types may be used to take advantage of their respective benefits.

3.3.2 Dynamic mesh

Five primary dynamic mesh techniques are commonly used to simulate fluid flow in domains with time-varying changes: sliding mesh, remeshing, adaptive mesh refinement, overset mesh, and mesh deformation.

The sliding mesh approach typically involves connecting rotating and stationary domains by a sliding interface to exchange flow quantities in order to simulate rotating machinery. However, this approach does not allow for relative motion between domains. In contrast, the overset mesh approach allows for relative motion between multiple bodies by interpolating flow quantities in overlapping domains. This method is highly flexible and can accommodate complex motions, but it requires consistent mesh resolution in overlapping domains to minimize numerical interpolation errors.

Mesh deformation is suitable for moderate boundary displacements until mesh degradation occurs. For larger deformations that threaten mesh quality, remeshing can be used to maintain mesh quality by re-configuring the numerical mesh domain. However,

this mesh refinement process can slow the computational efficiency in simulations with large numbers of cells.

Adaptive mesh refinement is beneficial for areas where more detail is needed to represent complicated flow features, such as vortical flows. It does this by refining the mesh in certain areas based on mesh refinement criteria. Compared to remeshing, mesh deformation is a more efficient method, especially for moderate boundary movements. This approach significantly reduces the number of cells compared to an overlapping mesh due to the involvement of a background mesh.

ANSYS CFX uses the "Displacement Diffusion" model, where displacements at domain boundaries are propagated to other mesh points by solving the following equation:

$$\nabla \cdot (\Gamma_{\text{disp}} \nabla \delta) = 0. \tag{3.5}$$

In this equation, δ represents the displacement relative to previous mesh locations, and Γ_{disp} is the stiffness of the mesh.

When a uniform stiffness value is applied to the mesh, the assigned displacements are evenly distributed throughout the mesh. However, if the stiffness of the mesh varies throughout the domain, the nodes in the regions with higher stiffness will have very little relative motion and will tend to move together. The use of varying mesh stiffness is particularly useful for maintaining the distribution and quality of the mesh around sharp edges or in the boundary layers. Therefore, accurate meshing coupled with appropriate stiffness assignment is required for this model.

3.3.3 Illustration of meshes applied in the numerical study

In this thesis, the RANS simulations use only structured meshes to improve the control of the boundary layer, focusing on critical factors such as cell aspect ratio and mesh orthogonality. These are essential for an accurate representation of flow gradients. Furthermore, in narrow spaces, especially in the gap between the propeller tip and adjacent walls (tunnel wall and nozzle), the mesh is designed to be of high quality and resolution to effectively capture the circulating flow around the propeller tip.

In addition, the propeller, tunnel, and hull are modeled as separate mesh domains to optimize the total number of cells. This approach ensures that refining the mesh in one domain does not affect the mesh resolution in the other domains. The rotational motion of the propeller requires its domain to be defined independently. Sliding interfaces are used to smoothly connect the rotating and stationary domains.

The main features of the mesh are shown in Fig. (3.1), with the interface mesh highlighted in red. It is important to note that within the rotating domain, the mesh is generated for a single blade. This mesh can then be periodically replicated to generate the full mesh for the propeller. Therefore, it is important to ensure that the periodic interfaces have the same mesh resolution and topology to minimize unnecessary interpolation errors.

A mesh-sensitive study for the bare hull has been carried out and can be found in Appendix (C).

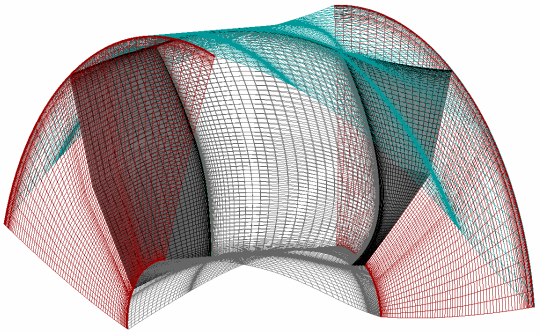

(a) Azimuth thruster: blade mesh.

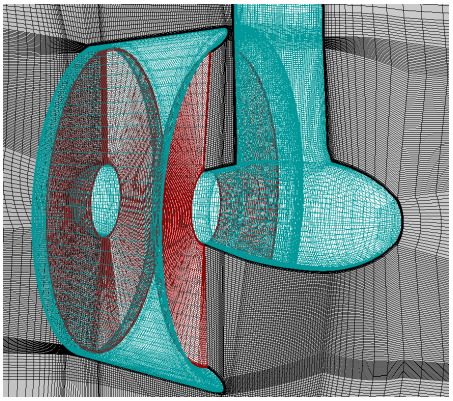

(b) Azimuth thruster: housing mesh.

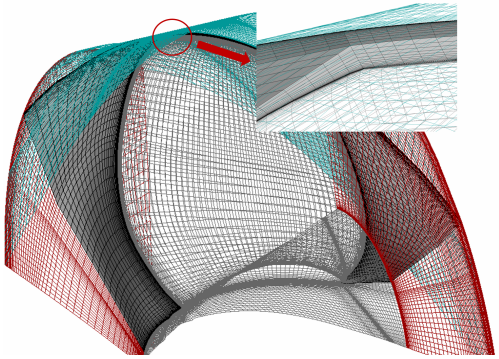

(c) Tunnel thruster: blade mesh.

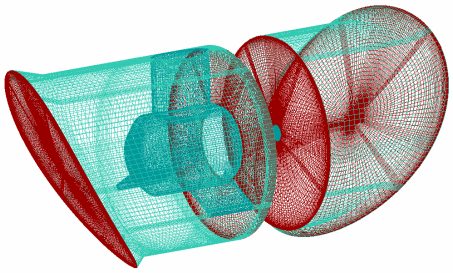

(d) Tunnel thruster: housing mesh.

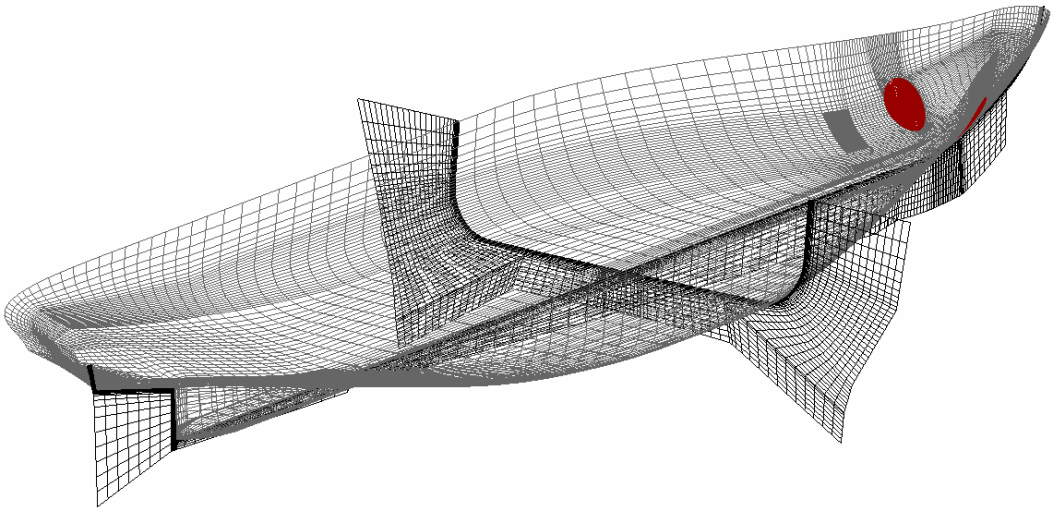

(e) Hull mesh

Figure 3.1: Mesh view of the ship.

4 Numerical Investigations of the Maneuvering Devices

4.1 Introduction

In this chapter, extensive RANS calculations were conducted on the azimuth thruster performance to identify the correlations between the parameters studied. Subsequently, a study of a bow thruster flow characteristics was carried out, primarily to determine the effects of interaction parameters on the forces exerted on different parts of the ship, taking into account variations in speed and inflow angle.

4.2 Main Propulsion

In the present study, the hydrodynamic characteristics of an offshore vessel are investigated. The ship was initially equipped with three bow thrusters and two stern podded thrusters, Krasilnikov [63]. For increasing computational efficiency, the configuration of the propulsion and steering devices of the ship is modified accordingly, so that it comprises only one bow thruster and two stern azimuth thrusters.

The main particulars of the ship are given in Tab. (4.1).

Table 4.1: Main specification of ship's hull.

Length between perpendiculars	L_{pp}	74.4	[m]
Draught mean	T	5	[m]
Beam	B	17.6	[m]
Moment of inertia	I_{zz}	1.66×10^9	[kgm^2]
Design speed	v_{s}	14	[knots]

The ship has a draft of 5 m (see Tab. (4.1)), therefore, which means that different aspects must be considered when selecting the diameter of its azimuth thrusters. The most relevant factors include:

- occurrence of cavitation and ventilation and
- thrust losses due to thruster-hull and thruster-thruster interactions.

To mitigate thrust losses caused by ventilation, as discussed in Section (2.3), it is crucial to maintain a depth-to-diameter ratio greater than $h/D = 0.8$. Here, the depth

h refers to the vertical distance from the free surface to the propeller shaft. Additionally, significant interaction between azimuth thrusters occurs only when the slipstream induced by one thruster impinges directly on the other. Brandner [60] notes that for a ship at rest, this interaction usually occurs when the angle of attack of the downstream thruster exceeds 60°.

Considering the above factors, the diameters of the two azimuth thrusters and the vertical distance between the propeller axis and the hull are chosen as $D = 2.4$ m and 1.5 times the diameter, respectively. The ratio of submerged depth to diameter is approximately $h/D = 0.9$.

During slow maneuvers, both stern thrusters operate primarily in the first quadrant, where the hull has a predominant influence on the azimuth thrusters. Each azimuth thruster is considered an individual device in the numerical simulation, as shown in Fig. (4.1). The asymmetry effect typically associated with single-screw vessels can be ignored in the maneuvering model for twin-skew vessels, as discussed in Section (2.1), i.e., the value of the transverse force (Y_0) or the yaw moment (N_0) is zero. The complete thruster unit is shown in Fig. (4.2).

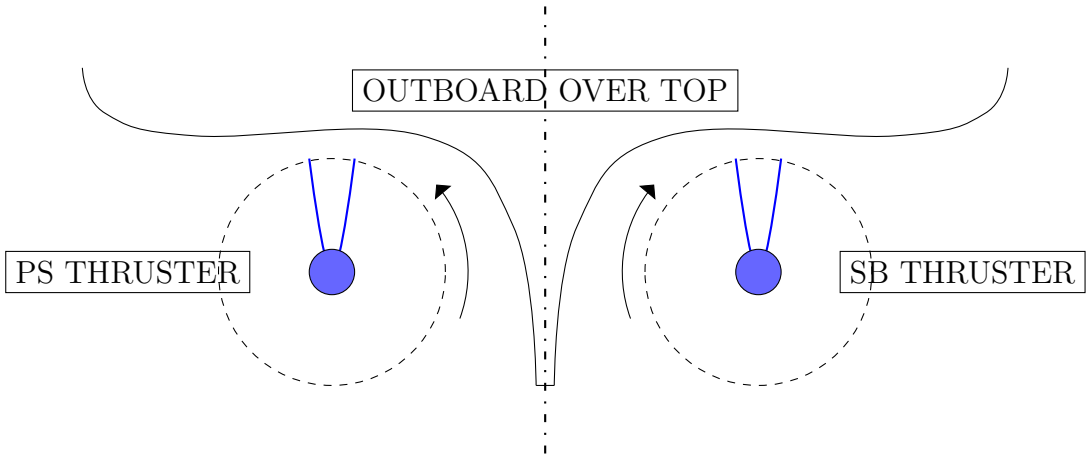

Figure 4.1: The arrangement of the stern azimuth thrusters.

4.2.1 Propeller geometry

Dang [64] points out the importance of maintaining a constant pitch and non-zero tip chord length in ducted propellers to achieve high MC, as shown in Eq. (2.13). For this reason, the Ka 4-70 propeller was selected.

Oosterveld [65] gives a description of the geometry and hydrodynamic characteristics of the Kaplan propeller in combination with the 19A duct. The blade section length is normalized by the chord length at the 0.6R section, while the maximum thickness distribution is related to the propeller diameter. The chord length distributions, denoted as y_{back} and y_{face}, represent the coordinates of the back of the blade (suction side) and the face (pressure side), respectively. The precision of the profile geometry was verified by

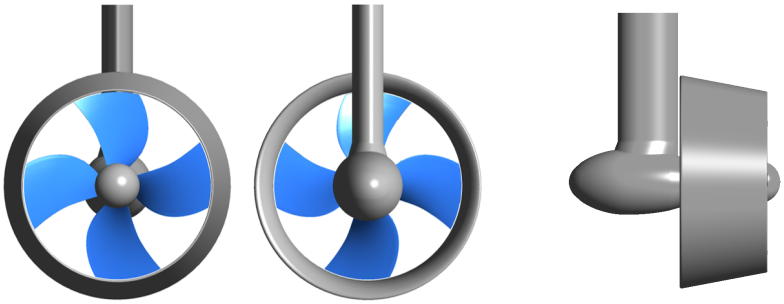

Figure 4.2: View of the starboard azimuth thruster. From left to right: front view, back view and side view.

conducting open-water tests on the Ka 4-70 with a nozzle No.19A ducted propeller. The experimental results, including k_t, k_{tn}, and k_q, were represented as polynomial functions of j and P/D. Tab. (4.2) shows the differences between the simulated and experimental data, showing high differences at high advance ratios. These discrepancies are primarily the result of the blades' relatively low loading compared to their high loading conditions at low advance ratios.

Good agreement between the calculated and measured results confirms the accurate reproduction of the blade geometry. The study then focuses on the pushing mode configuration during low-speed ship operations. The major challenge in this case is the continuous exposure of the propeller to the wake of the housing. To improve performance in such an inhomogeneous wake field, modern propellers often have a skew, as shown in Fig. (4.3). Therefore, a skew is introduced, its distribution is oriented to that of the KCS propeller [66], but with a reduced skew toward the outer radius (see Fig. (4.4)). This design concept follows the idea that the pressure peak at 12 o'clock can be more effectively distributed across the wider chord length at blade tip of the ducted propeller compared to a non-ducted propeller. Additionally, the negative skew near the root balances out the spindle torque induced by the positive skew of the upper section.

Using the geometry specified above, Schiller et al. [67] conducted an investigation to determine the effect of the scale on the performance of the pushing mode, as outlined in Tab. (4.3) and in Fig. (4.5). Notable differences were observed between the flow on the model and the full-scale propellers, mainly attributed to variations in flow separation, a phenomenon extensively analyzed by Müller [68]. However, the performance curves for the two full-scale propellers are similar. Therefore, subsequent discussions will focus on the results based on the propeller with a diameter (D) of 4.2 m.

In oblique flow conditions, simulations were performed with a predefined azimuth speed f, covering azimuth angles from 0° to ±180°. This range corresponds to the typical operation of azimuth thrusters, e.g., during crash stop and harbor maneuvers.

The computational flow field is divided into three domains: the far-field domain for setting boundary conditions, the cylindrical domain to consider the rotation of the thruster unit, and a rotating domain for the propeller, as shown in Fig. (4.6). In static simulations ($f = 0$ rpm), the azimuth angles range mainly from $-30°$ to 30°, extending every

Table 4.2: Comparison of simulated and experimental results for ducted propeller Ka 4-70 with nozzle no.19A under open-water condition.

Open Water Test Ka 4-70 with nozzle no. 19A (D = 240 mm, P/D = 1.2, n = 3.59 Hz)							
j	k_t **(propeller sim)**	k_t **(propeller exp)**	**sim/exp [%]**		k_{tn} **(nozzle sim)**	k_{tn} **(nozzle exp)**	**sim/exp [%]**
0.1	0.641	0.626	102		0.305	0.296	103
0.3	0.510	0.504	101		0.187	0.188	100
0.5	0.388	0.388	100		0.101	0.103	98
0.7	0.264	0.257	103		0.034	0.030	114
0.9	0.092	0.094	99		-0.042	-0.050	86

j	k_q **(propeller sim)**	k_q **(propeller exp)**	**sim/exp [%]**		η **(sim)**	η **(exp)**	**sim/exp [%]**
0.1	0.064	0.066	96		0.160	0.150	106
0.3	0.062	0.063	98		0.394	0.380	104
0.5	0.056	0.057	98		0.550	0.540	102
0.7	0.047	0.047	99		0.627	0.607	103
0.9	0.031	0.033	94		0.430	0.410	105

Table 4.3: Three sizes of azimuth thruster units.

Size	**D [m]**	**n (Hz)**
Model scale (MS)	0.25	11
Full scale (FS24)	2.4	3.45
Full scale (FS42)	4.2	2.1

30° up to 120° for the identification of critical loads. The combinations of advance ratio j and azimuth angle δ are detailed in Tab. (4.4).

A body-fixed coordinate system is applied at the thruster mounting point on the hull (see Fig. (4.7)). The dimensionless coefficients kF_{x} and kF_{y} represent the longitudinal and transverse forces. These coefficients are averaged over a number of propeller revolutions at a constant azimuth angle. Their standard deviations account for the variation of the thrust and torque coefficients. The static simulations indicate that critical operation conditions often occur between azimuth angles of 60° and 120° at high advance ratios, as shown in Fig. (4.8).

Table 4.4: Calculation matrix for the full-scale propeller with 4.2 m diameter.

static simulation (f = 0 rpm)	
j	δ [°]
0, 0.2, 0.4 0.6, 0.8, 1.0	-30, -15 0, 15, 30 60, 90, 120

dynamic simulation	
j	f [rev/min]
0	1, 2, 3, 6
0.1	2, 3, 6
0.6	2, 3, 6
1	2, 3, 6

During ship maneuvers, adjustment of the azimuth angle requires changing the azimuth speed f, which in turn affects both the longitudinal force kF_{x} and the transverse

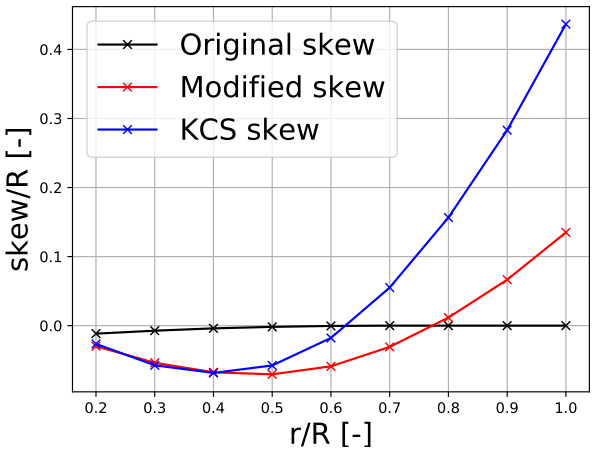

Figure 4.3: The modified skew distribution.

force kF_y. Therefore, in this thesis, the effects of varying the azimuth speed f will be focused.

As shown in Fig. (4.9), kF_x remains relatively steady with changes in f for angles up to 120° at a constant advance ratio j. In contrast, kF_y shows a significant correlation with variations in f. The response of these forces to j in a given f (f=3 rpm) is shown in Fig. (4.10), consistent with the static results.

The above results are derived from the cases where the thruster is turned to starboard. For a turn to starboard of the ship, the thrusters have to rotate in the opposite direction, resulting in a different force prediction, as shown in Fig. (4.11). This change is mainly due to the different rotation directions of the propeller and the thruster unit, with a more noticeable effect on kF_x than on kF_y.

The comparative results, as depicted in Fig. (4.12), illustrate two simulation situations: one with azimuth speed and the other without it. Up to 120°, the longitudinal force plots are nearly identical. However, the transverse forces are significantly lower in static simulations. The pronounced differences at larger angles are due to variations in propeller slipstream formation; unlike in dynamic conditions, the slipstream is fully developed in static simulations. These differences in slipstream behavior result in significant differences in force predictions between both cases.

Therefore, the performance characteristics of the azimuth thruster under oblique flow conditions can be outlined as follows:

- The maximum values of kF_x and kF_y in an advance ratio $j = 0.6$ are about five and two times higher, respectively, than the thrust under the bollard pull condition, contributing significantly to the increase in the bending moment.

- Critical conditions are observed when the azimuth angle δ is between 60° and 120°. Although kF_x shows limited sensitivity to changes in azimuth speed, kF_y

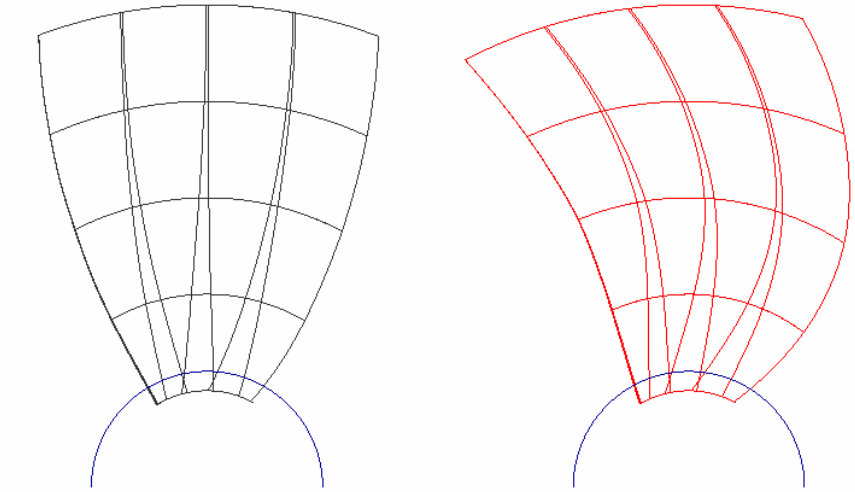

Figure 4.4: Propelelr blades with modified skew mounted in the 19A shape duct.

is strongly affected. This difference is mainly due to the influence of the duct on kF_y, as rotation of the thruster unit causes an additional velocity component. As the azimuth speed increases, this additional velocity component changes, altering the pressure distribution inside the duct. For a detailed investigation, see Section (F.1) in Chapter (F).

- The direction of rotation of a propeller has a significant effect on the performance of the thruster unit. A right-handed propeller generates higher loads when the thruster unit is turned to starboard than when it is turned to port side.
- Dynamic simulations reflect real operating conditions more accurately and provide results that are more representative. In addition, from a computational efficiency standpoint, the time required for dynamic computations is substantially less than the cumulative time required for computations at each azimuth angle.
- Forces under static and dynamic conditions exhibit significant inconsistency, particularly at azimuth angles higher than 90°, due to the different appearances of the slipstream.

4.2.2 Mathematical modeling

The goal of the following part is to predict the longitudinal and transverse forces based on the results of the calculations performed. The results presented are obtained from many RANS simulations, each takes about two weeks of run time on a 32-core computer, depending on the value of f. Two approaches are followed, one of which involves analyzing the forces to identify the correlations between the variables. Another approach is to use an ANN to determine the relationship between the variables.

Both approaches are explained in the following sections.

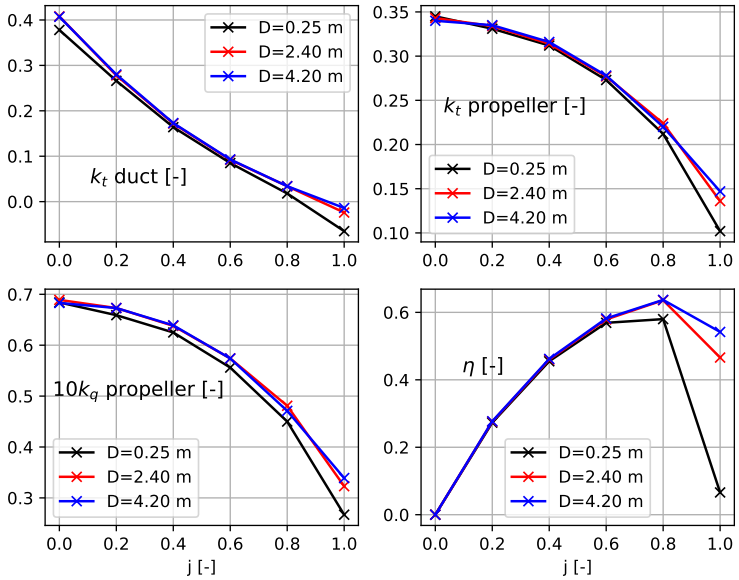

Figure 4.5: Comparison of the coefficients in the open water condition.

4.2.2.1 Data analysis

The mathematical model is developed based on numerical results, considering both longitudinal and transverse forces. In the RANS computations, three variables potentially affect kF_{x} and kF_{y}: the advance ratio j, the azimuth angle δ, and the azimuth speed f. It is observed that kF_{x} remains consistent up to approximately $\delta = 120°$, beyond which it exhibits a highly oscillatory behavior. Therefore, the mathematical model is formulated only up to the azimuth angle where maximum loads occur, which is approximately 120° for kF_{x} and 90° for kF_{y}.

The first focus of model development was on the outer rotation of the starboard thruster unit. This involves a clockwise rotating propeller with positive azimuth speed. The numerical simulations indicate that the difference in kF_{x} is less pronounced compared to kF_{y}. The curves representing the variable kF_{y} have a certain tendency. For data analysis purposes, the value of kF_{y} at $\delta = 30°$ is utilized as an illustrative example. The respective values of kF_{y} in the static and dynamic situations are given in Tab. (4.5).

The coefficients at zero azimuth speed are the static coefficients, denoted as $kF_{y_{\underline{s}}}$. The total kF_y can be divided into two parts: the static component $kF_{y_{\underline{s}}}$ and a correction component $\mathrm{kF}_{y_{\underline{c}}}$, which is adjusted with respect to the azimuth speed f. This relation can be formulated as the following equation:

$$kF_{\mathrm{y(f)}} \quad = \quad kF_{\mathrm{y_s}} + kF_{\mathrm{y_c}}. \tag{4.1}$$

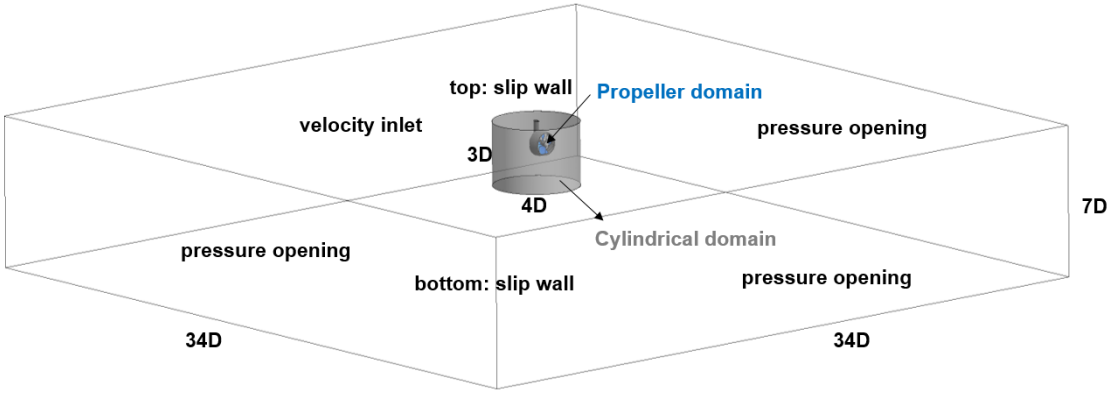

Figure 4.6: Computational domain for the simulation of the azimuth thruster.

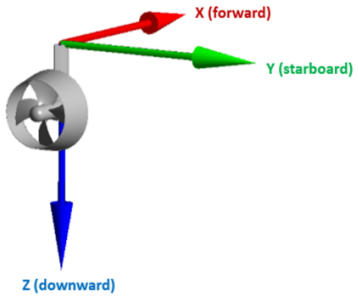

Figure 4.7: Definition of thruster-fixed coordinate system.

Tab. (4.5) provides a strong relation between static transverse force and dynamic force with a correction of $2.5f$. Eq. (4.1) can be rewritten as follows:

$$kF_{\mathrm{y(f)}} \quad = \quad kF_{\mathrm{y_s}} + 2.5f, \tag{4.2}$$

where $2.5f$ is the correction component ($kF_{\mathrm{y_c}}$).

In addition, kF_{y} should be considered as a function of the azimuth angle δ. After data analysis, referring to Fig. (4.13), the behavior of kF_{y} can be effectively modeled by a second-order polynomial, which can be expressed as follows:

$$kF_{\mathrm{y}}(\delta, j, f) \quad = \quad \underbrace{-0.53j\delta^2 + 1.62j\delta}_{\text{static}} + \underbrace{2.5f}_{\text{corrector}} \quad \forall \ 0^\circ < \delta < 90^\circ. \tag{4.3}$$

An excessive longitudinal force has been reported by a number of studies (Glauert [48], Stettler [49], Akinturk et al. [51], and Amini and Steen [53]). This phenomenon is

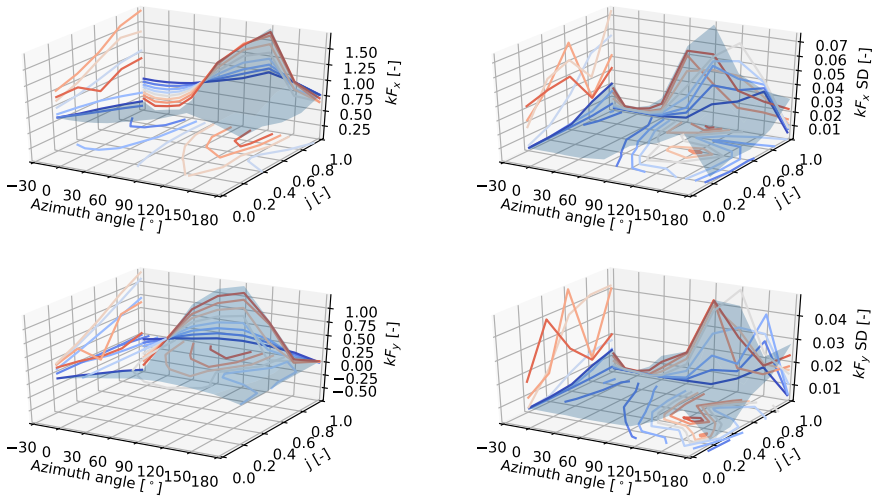

Figure 4.8: Critical cases observed from the force coefficients (first row, from left to right: kF_x and its standard deviation; second row, from left to right: kF_y and its standard deviation) in the static tests ($f = 0$ rpm).

Table 4.5: Change of kF_y over the advance ratio j and the azimuth speed f at the azimuth angle of 30°.

kF_y for azimuth angle of 30°				
j [-]	f = **0 rps**	f = **0.033 rps (2 rpm)**	f = **0.05 rps (3 rpm)**	f = **0.1 rps (6 rpm)**
0.0	0	0.08726	0.12958	0.25012
0.1	-	0.15796	0.20248	0.33005
0.6	0.37814	0.46241	0.50521	0.63404
1.0	-	0.84961	0.90440	1.06639

caused by the velocity induced by the skewed wake of the propeller. Glauert [48] derived a mathematical equation to describe this phenomenon, see Eq. (2.15):

$$T = 2\rho A_p v_{ix}\sqrt{v_{ix}^2 + v_\infty^2 + 2v_{ix}v_\infty\cos(\delta)}. \tag{4.4}$$

The objective of utilizing Eq. (4.4) is to determine the value of v_{ix} by a provided thrust T. Specifically, when the highest value of T is obtained at an azimuth angle of $\delta = 90°$, Eq. (4.4) can be reduced as follows:

$$T = 2\rho A_p v_{ix}\sqrt{v_\infty^2 + v_{ix}^2}. \tag{4.5}$$

T should be nondimensionalized by propeller rotation rate n and diameter D, such as

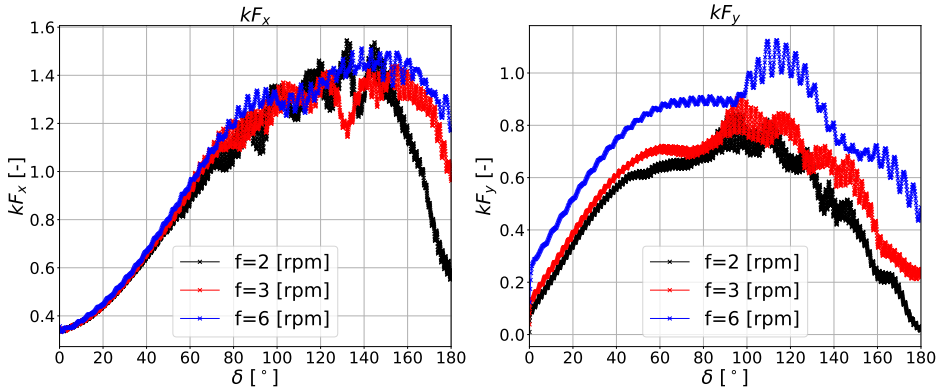

Figure 4.9: Correlations of kF_{x} and kF_{y} with variations of f at $j = 0.6$.

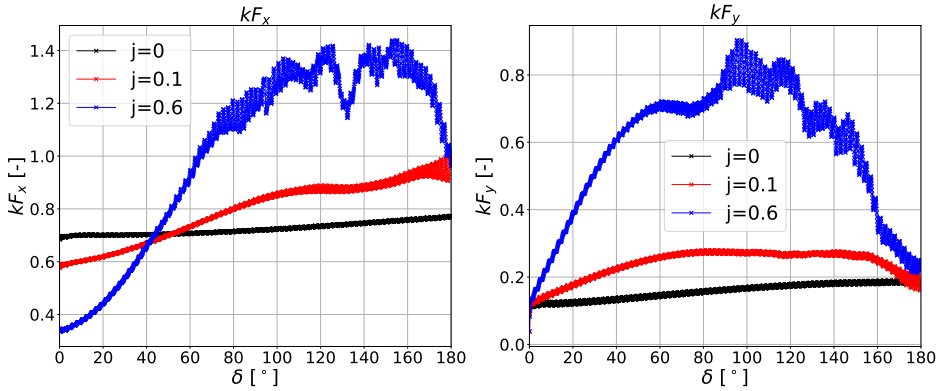

Figure 4.10: Correlations of kF_{x} and kF_{y} with variations of j at $f = 3$ rpm.

$$\begin{aligned} kF_{\mathrm{x}} &= \frac{T}{\rho n^2 D^4} \\ &= \frac{\pi}{2n^2 D^2} v_{\mathrm{ix}} \sqrt{v_\infty^2 + v_{\mathrm{ix}}^2}. \end{aligned} \tag{4.6}$$

However, while v_{ix} and v_∞ are still given in [m/s], it would be more convenient to change them into comparable representations based on the well-defined advance ratios. This conversion can be depicted as follows:

$$\begin{aligned} kF_{\mathrm{x_{max}}} &= \frac{\pi}{2n^2 D^2} v_{\mathrm{ix}} \sqrt{v_\infty^2 + v_{\mathrm{ix}}^2} \\ &= \frac{\pi}{2n^2 D^2} \frac{j_i}{nD} \sqrt{(\frac{j}{nD})^2 + (\frac{j_i}{nD})^2} \quad \forall \ \delta = 90°. \end{aligned} \tag{4.7}$$

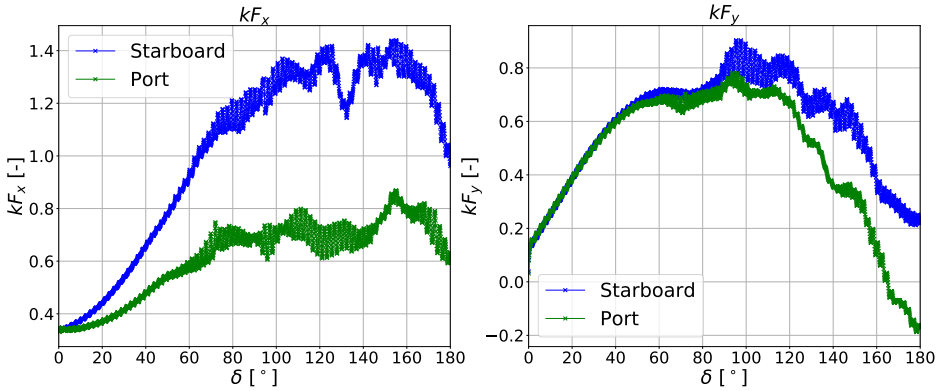

Figure 4.11: Correlations of kF_{x} and kF_{y} with variations of rotating direction of thruster unit at $j = 0.6$ and $f = 3$ rpm.

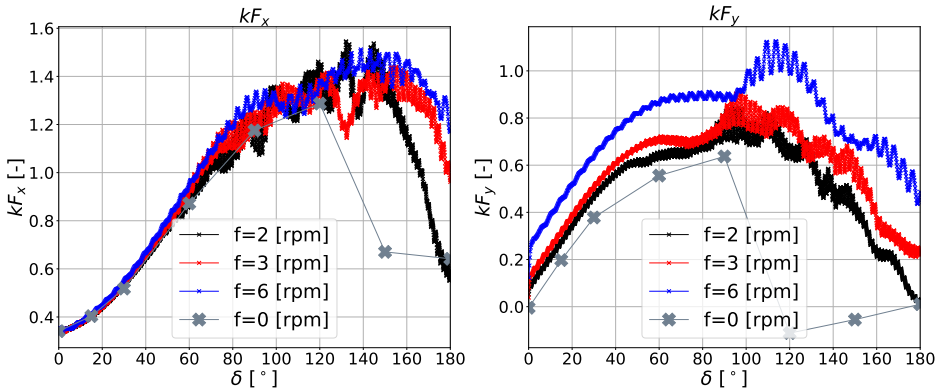

Figure 4.12: Comparison between the results from static and dynamic conditions at $j = 0.6$.

Using the data from RANS simulations, the longitudinal force T and the inflow velocity v_∞ are already available. The unknown variable is the induced velocities, which can be derived from Eq. (4.5). j_i in Eq. (4.7) can be defined as

$$v_{\mathrm{ix}}/(nD)$$

and is represented by a second-order polynomial. This polynomial is expressed as a function of the commonly defined advance ratio $j = v_\infty/(nD)$:

$$j_i \quad = \quad -0.4j^2 + 0.5j + 0.7. \tag{4.8}$$

The maximum value of kF_{x} can be determined using Eq. (4.7), which serves as one of the requirements for curve regression.

The curves of kF_{x} can be divided at an azimuth angle by 45° (see Fig. (4.10)), where all j-curves converge. The first part includes azimuth angle from 0° to 45°, and the

Table 4.6: Determination of the induced velocity after Eq. (4.6).

j [-]	kF_x (120°) [-]	v_∞ [m/s]	v_{ix} [m/s]	j_i [-]
0.0	0.727	0.000	5.999	0.68
0.1	0.859	0.882	6.491	0.74
0.6	1.370	5.292	7.435	0.84
1.0	1.595	8.820	7.011	0.79

second from 45° to 120°. Using a second-order polynomial requires three conditions to be met: The bollard pull and its first derivative at 45° satisfy the first two conditions. The third condition is defined by the values at 0°, based on open water tests for the first part, and by the maximum value predicted by Eq. (4.7) for the second part.

The regression curves for kF_x and kF_y are shown as dashed curves in Fig. (4.13).

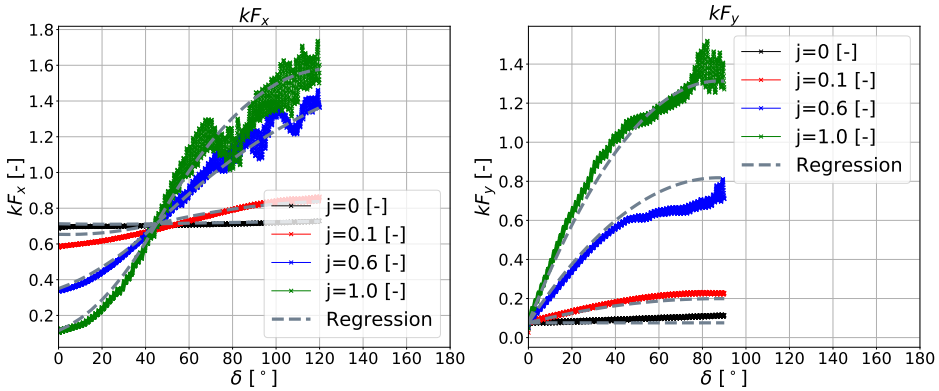

Figure 4.13: Comparison of the regression curves and raw data obtained from the RANS simulation for various advance ratios.

The observed variation of kF_y, illustrated in Fig. (4.11), indicates that the equation for kF_y in Eq. (4.3) remains valid due to the different rotation direction of the thruster unit. However, it is necessary to reevaluate kF_x in the following way:

$$kF_{x_{max}} = \frac{\pi}{2n^2D^2}\frac{j_i}{nD}\sqrt{(\frac{j}{nD})^2+(\frac{j_i}{nD})^2} - (0.9j+0.1) \quad \forall \ \delta = 90°. \tag{4.9}$$

This predictive model needs the open-water test results and Glauert's approach. It takes into account the effect of the oblique flow on the force exceeding the thrust of the bollard pull. However, a drawback of this model is the challenge of accurately characterizing the forces at high azimuth angles. To address this issue, the following section presents the use of ANN for improved and extended force prediction.

4.2.2.2 Machine Learning

Bayesian approach

ANN, first proposed by McCulloch and Pitts [69], are widely used in regression problems. The basic concept of an ANN model involves connecting neurons across different layers to establish a relationship between inputs and outputs. This model uses nonlinear activation functions to implement nonlinear relationships. The complexity of the problem can be addressed by adjusting the number of neurons and layers within the network. The primary challenge for ANN is overfitting, where the model performs well on training data but poorly on test data. This problem is related to the bias-variance tradeoff, as discussed by Kohavi and Wolpert [70]. A common strategy to mitigate overfitting is to limit the weights in the error function, a technique often referred to as "weight decay", as described by Tikhonov [71], Krogh and Hertz [72], and Bos and Chug [73]. Determining the parameters that control this regularization process can be challenging. Bayesian regularization networks address this problem by automatically tuning the optimal regularization parameters. A process for optimizing these hyperparameters is known as Mackay's Bayesian technique, based on the work of MacKay [74].

In the error function $F(w)$, as shown in Eq. (4.10), a second term E_W, representing the sum of squares of the network weights[1], is added to the sum of squares errors. Each term is multiplied by its corresponding hyperparameters, β and α. The minimization of $F(w)$ employs the backpropagation algorithm, as proposed by Rumelhart et al. [75]:

$$\begin{aligned} F(w) &= \beta E_D + \alpha E_W \\ &= \beta(\sum_{i=1}^{N}(e_i)^2) + \alpha(\sum_{i=1}^{l} {w_i}^2), \end{aligned} \tag{4.10}$$

where N is the sample size in the training set and l is the total number of weights.

In the Bayesian framework, network weights are considered as random variables. The weights must be chosen to maximize the conditional probability of the weights for a given range of datasets D. The mathematical expression for the conditional probability of w is

$$P(w|D,\alpha,\beta,M) = \frac{P(D|w,\beta,M)P(w|\alpha,M)}{P(D|\alpha,\beta,M)}, \tag{4.11}$$

where $P(w|\alpha,M)$ is the prior density, $P(D|w,\beta,M)$ is the likelihood function, M stands for a selected probabilistic model (here Gaussian probabilistic model is used) and $P(D|\alpha,\beta,M)$ is evidence for α and β.

When assuming zero-mean Gaussian distributions for both the prior distribution of weights and the likelihood distribution of noise in the training data, their respective density functions can be expressed as follows:

[1] The weights here already contain biases.

$$P(D|w,\beta,M) = \frac{1}{Z_D(\beta)}\exp(-\beta E_D) \tag{4.12a}$$

$$P(w|\alpha,M) = \frac{1}{Z_W(\alpha)}\exp(-\alpha E_W) \tag{4.12b}$$

with

$$Z_D(\beta) = (\frac{\pi}{\beta})^{\frac{N}{2}} \tag{4.13a}$$

$$Z_W(\alpha) = (\frac{\pi}{\alpha})^{\frac{l}{2}}, \tag{4.13b}$$

where

$$\beta = \frac{1}{2\sigma^2_{\text{noise}}}, \tag{4.14a}$$

$$\alpha = \frac{1}{2\sigma^2_{\text{weights}}}. \tag{4.14b}$$

σ^2_{noise} and $\sigma^2_{\text{weights}}$ are the variance of the noise and weights, respectively.

Using Eq. (4.12), the posterior density of Eq. (4.11) can be obtained as follows:

$$\begin{aligned} P(w|D,\alpha,\beta,M) &= \frac{P(D|w,\beta,M)P(w|\alpha,M)}{P(D|\alpha,\beta,M)} \\ &= \frac{\frac{1}{Z_D(\beta)}\frac{1}{Z_W(\alpha)}}{P(D|\alpha,\beta,M)}\exp(-\beta E_D - \alpha E_W) \\ &= \frac{1}{Z_F(\alpha,\beta)}\exp(-F(w)). \end{aligned} \tag{4.15}$$

Based on Eq. (4.14), the variable β exhibits an inverse relationship with the noise variance in the training data. Consequently, a higher variance of noise, denoted σ^2_{noise}, will lead to a reduced value of β. On the other hand, as α increases, the variance of the weights decreases, leading to a more uniform network response. When the value of α is extremely small, it essentially annuls the "weight decay" effect, thus decreasing the influence of regularization. Typically, a higher regularization ratio α/β results in a smoother network function, while a lower ratio increases the variability of w, hence increasing the risk of overfitting the network (see Hagen et al. [76]).

In order to determine the values of α and β, the Bayes' method can be reapplied to both regularization parameters,

$$P(\alpha,\beta|D,M) = \frac{P(D|\alpha,\beta,M)P(\alpha,\beta|M)}{P(D|M)}. \tag{4.16}$$

Maximizing the posterior term $P(\alpha, \beta|D, M)$ means maximizing the likelihood density ($P(D|\alpha, \beta, M)$), which is the evidence in Eq. (4.11),

$$P(D|\alpha, \beta, M) = \frac{P(D|w, \beta, M)P(w|\alpha, M)}{P(w|D, \alpha, \beta, M)}. \tag{4.17}$$

Using Eq. (4.12) and Eq. (4.15), Eq. (4.17) can be obtained by

$$\begin{aligned} P(D|\alpha, \beta, M) &= \frac{P(D|w, \beta, M)P(w|\alpha, M)}{P(w|D, \alpha, \beta, M)} \\ &= \frac{\frac{1}{Z_D(\beta)}\frac{1}{Z_W(\alpha)}}{\frac{1}{Z_F(\alpha,\beta)}\exp(-F(w))}\exp(-\beta E_D - \alpha E_W) \\ &= Z_F(\alpha, \beta)\frac{1}{Z_D(\beta)}\frac{1}{Z_W(\alpha)}. \end{aligned} \tag{4.18}$$

According to Foresee and Hagan [77], $Z_F(\alpha, \beta)$ is approximated to

$$Z_F \approx (2\pi)^{\frac{l}{2}}(\det(H^{MP})^{-1})^{1/2}\exp(-F(w^{MP})), \tag{4.19}$$

where w^{MP} means Most Probable (MP) weights and H is the Hessian matrix approximated by the cross product of Jacobian J as follows:

$$H = 2\beta J^T J + 2\alpha I, \tag{4.20}$$

where I is the identity matrix and J is the Jacobian matrix, which has the form:

$$J = \begin{bmatrix} \frac{\partial e(x_1,w)}{\partial w_1} & \cdots & \frac{\partial e(x_1,w)}{\partial w_l} \\ \vdots & \ddots & \vdots \\ \frac{\partial e(x_N,w)}{\partial w_1} & \cdots & \frac{\partial e(x_N,w)}{\partial w_l} \end{bmatrix}. \tag{4.21}$$

The Levenberg-Marquardt algorithm [78] enables the determination of the change in the weights, δw, through the following equation:

$$(H + \lambda I)\delta w = \beta(J^T e) + \alpha w. \tag{4.22}$$

The symbol λ represents the damping factor, which may vary from one iteration to the next.

The updated weights allow for the calculation of the regularization parameters α and β in Eq. (4.23). This equation is derived from the zero derivative of Eq. (4.18).

Once α and β have been updated, the Hessian matrix (Eq. (4.20)) can be recalculated to change the weights again, as shown in Eq. (4.22). This is an iterative process that continues until all parameters have converged.

$$\alpha^{\mathrm{MP}} = \frac{\gamma}{2E_W(w^{\mathrm{MP}})} \tag{4.23a}$$

$$\beta^{\mathrm{MP}} = \frac{N-\gamma}{2E_D(w^{\mathrm{MP}})}. \tag{4.23b}$$

γ indicates the effective number of parameters (weights):

$$\gamma = l - 2\alpha^{\mathrm{MP}}\mathrm{tr}(H^{\mathrm{MP}})^{-1}, \tag{4.24}$$

where $\mathrm{tr}(\mathrm{H}^{\mathrm{MP}})^{-1}$ is the trace of the inverse Hessian matrix.

A simple example

The process of training a neural network can be divided into two main phases: the forward pass and the backpropagation algorithm. In the context of Bayesian regularization, the input value is the advance ratio j, and the target value is the propeller's k_t. Forward propagation and backpropagation are used to adjust the weights to fit the model to the data, minimizing the error between the predicted and actual k_t values.

Fig. (4.14) shows a simple neural network consisting of three layers: an input layer, a hidden layer, and an output layer (1x1x1).

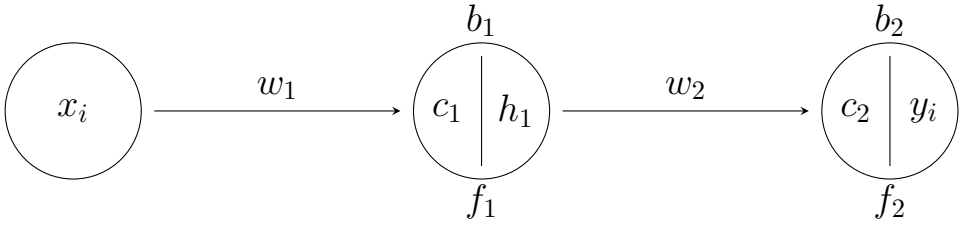

Figure 4.14: A simple network structure.

The objective of this network is to illustrate the mechanism of the regularization algorithm. A detailed description of the notation used in this example is provided below:

- x_i: Input ($x_1 = 0.1$, $x_2 = 0.3$, $x_3 = 0.5$, $x_4 = 0.7$, $x_5 = 0.9$).
- w_1: Weight between the input layer and the hidden layer.
- b_1: Bias in the hidden layer.
- c_1: Input into the hidden layer.
- f_1: Activation function in hidden layer.
- h_1: Output after activation in the hidden layer.

- w_2: Weight between the hidden layer and the output layer.
- b_2: Bias in the output layer.
- c_2: Input into the output layer.
- f_2: Activation function in the output layer.
- y_i: Output after activation.
- t_i: Target output (y_1 =0.626, y_2=0.504, y_3=0.388, y_4=0.257, y_5=0.094).
- e_i: t_i - y_i.

In the context of the forward pass, the relationship between the parameters can be expressed as follows:

$$\begin{aligned} w_1 x_i + b_1 &= c_1 && \text{(4.25a)} \\ h_1 &= f_1(c_1) && \text{(4.25b)} \\ w_2 h_1 + b_2 &= c_2 && \text{(4.25c)} \\ y_i &= f_2(c_2) && \text{(4.25d)} \\ e_i &= t_i - y_i. && \text{(4.25e)} \end{aligned}$$

In the backpropagation pass, the partial derivative of e_i with respect to weights and biases can be calculated by applying the chain rule. If only the first element in the input vector is considered, the partial derivative of e_1 with respect to the second weight (w_2) can be written as

$$\frac{de_1}{dw_2} = \frac{\partial e_1}{\partial y_1}\frac{\partial y_1}{\partial c_2}\frac{\partial c_2}{\partial w_2}. \tag{4.26}$$

Using the relationship in Eq. (4.25), we get

$$\frac{de_1}{dw_2} = -1 \cdot f_2{}' \cdot h_1. \tag{4.27}$$

Similarly, the partial derivative of e_1 with respect to the first weight (w_1) is given by

$$\begin{aligned} \frac{de_1}{dw_1} &= \frac{\partial e_1}{\partial y_1}\frac{\partial y_1}{\partial c_2}\frac{\partial c_2}{\partial h_1}\frac{\partial h_1}{\partial c_1}\frac{\partial c_1}{\partial w_1} && \text{(4.28a)} \\ &= -1 \cdot f_2{}' \cdot w_2 \cdot f_1{}' \cdot x_1. && \text{(4.28b)} \end{aligned}$$

The Jacobian matrix for the five values entered is calculated as follows:

$$\begin{matrix} \frac{de_i}{dw_1} & \frac{de_i}{db_1} & \frac{de_i}{dw_2} & \frac{de_i}{db_2} \end{matrix}$$
$$\begin{bmatrix} -w_2 f_2{}' f_1{}' x_1 & -w_2 f_2{}' f_1{}' & -h_1 f_2{}' & -f_2{}' \\ -w_2 f_2{}' f_1{}' x_2 & -w_2 f_2{}' f_1{}' & -h_1 f_2{}' & -f_2{}' \\ -w_2 f_2{}' f_1{}' x_3 & -w_2 f_2{}' f_1{}' & -h_1 f_2{}' & -f_2{}' \\ -w_2 f_2{}' f_1{}' x_4 & -w_2 f_2{}' f_1{}' & -h_1 f_2{}' & -f_2{}' \\ -w_2 f_2{}' f_1{}' x_5 & -w_2 f_2{}' f_1{}' & -h_1 f_2{}' & -f_2{}' \end{bmatrix}$$

If the activation function applied in the hidden layer is the hyperbolic tangent function, as defined as

$$\tanh(\mathrm{x}) \quad = \quad \frac{2}{1+\exp(-2x)} - 1 \tag{4.29}$$

and no transfer function is applied in the output layer, the Jacobian matrix can be calculated as follows:

$$\begin{matrix} \frac{de_i}{dw_1} & \frac{de_i}{db_1} & \frac{de_i}{dw_2} & \frac{de_i}{db_2} \end{matrix}$$
$$\begin{bmatrix} -w_2(1-\tanh^2(w_1x_1+b1))x_1 & -w_2(1-\tanh^2(w_1x_1+b1)) & -\tanh(w_1x_1+b1) & -1 \\ -w_2(1-\tanh^2(w_1x_2+b1))x_2 & -w_2(1-\tanh^2(w_1x_2+b1)) & -\tanh(w_1x_2+b1) & -1 \\ -w_2(1-\tanh^2(w_1x_3+b1))x_3 & -w_2(1-\tanh^2(w_1x_3+b1)) & -\tanh(w_1x_3+b1) & -1 \\ -w_2(1-\tanh^2(w_1x_4+b1))x_4 & -w_2(1-\tanh^2(w_1x_4+b1)) & -\tanh(w_1x_4+b1) & -1 \\ -w_2(1-\tanh^2(w_1x_5+b1))x_5 & -w_2(1-\tanh^2(w_1x_5+b1)) & \tanh(w_1x_5+b1) & -1 \end{bmatrix}$$

The initial weights and biases are randomly assigned using a normal distribution. The specific values for the weights are: w_1 = -0.125, b_1 = 0.451, w_2 = 0.232, and b_2 = 0.099.

The value of γ is 4, which represents the total number of parameters in the initial step. The values of α and β are determined by employing Eq. (4.23), where E_D and E_W represent the sums of the squares of the weights, including biases, and the total of squared errors, as illustrated in Eq. (4.10). The values of α and β are determined to be 7.08 and 1.47, respectively.

The updated weights and biases can be obtained by utilizing Eq. (4.22). The damping factor (λ) is assumed to be equal to 20. It should be noted that the value of λ is not required to be constant. Following the first iteration, the updated weights and biases are as follows: w_1 = -0.097, b_1 = 0.366, w_2 = 0.201, and b_2 = 0.121. After re-evaluating the weights, it is necessary to adjust the Jacobian matrix as well as the α, β, and γ parameters.

Tab. (4.7) presents the changes in weights and biases, together with the regularization parameters, throughout an iterative procedure. The table shows that γ implies an effective parameter count of 3, which is less than the total number of weights and biases (l = 4). It may be advisable to drop out b_2.

The findings of Foresee and Hagan [77] indicate that the value of γ remains relatively stable even as the number of weights increases. This result was used to guide the investigation into the effect of different numbers of nodes in the hidden layer. Tab. (4.8) illustrates the variation of γ based on the number of nodes in the hidden layer. As the number of nodes increases, the value of γ remains relatively stable. One of the advantages of this method is that the network remains unaffected by the overfitting problem even as the network structure expands.

Table 4.7: Parameter changes during an iterative process in Bayesian network.

	Iteration						
	1	2	3	...	50	100	200
	Weights and biases						
w_1	-0.125	-0.097	-0.098	...	-0.746	-0.743	-0.742
b_1	0.451	0.366	0.356	...	0.619	0.728	0.728
w_2	0.232	0.201	0.217	...	0.949	1.014	1.016
b_2	0.099	0.121	0.187	...	0.155	0.040	0.040
	Regularization parameters						
α	7.081	1.406	2.371	...	0.802	0.721	0.721
β	1.474	6.401	8.352	...	3254.273	4625.765	4631.947
γ	4.000	0.557	1.035	...	2.991	3.048	3.047

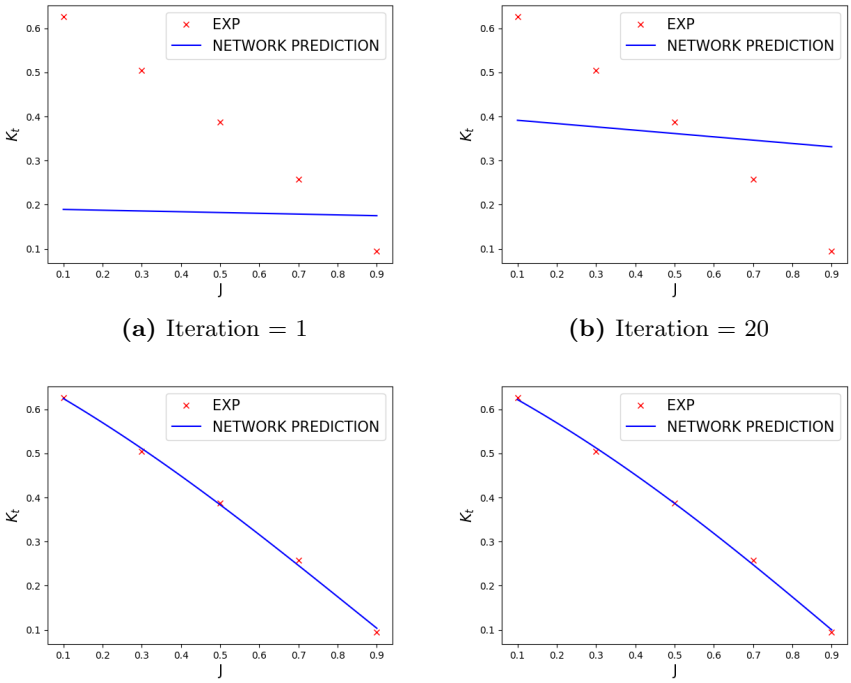

(a) Iteration = 1 **(b)** Iteration = 20

(c) Iteration = 50 **(d)** Iteration = 200

Figure 4.15: Predicted results at different iterations.

Table 4.8: Effective number of parameters.

Number of nodes at hidden layer	Total number of w inc. b	γ
1	4	3.047
5	16	3.106
10	31	3.112
50	151	3.117
100	301	3.118

Application

Tab. (4.9) contains 12 RANS simulations, representing 20% of the total units in the table. The goal is to employ approximately 20% of the available data to predict the remaining 80% of the unknown results. 66.7% of the data from the 12 simulations were used for training, while the remaining portion (33.3%) was allocated as the validation dataset. Since the validation data and training data are derived from the same dataset, the performance of the trained neural network on the validation dataset is generally satisfactory. The network's robustness needs to be assessed by evaluating its performance on the hidden data. In this case, the RANS results for $f = 5, j = 0.5$ are selected as the test dataset, indicated by the symbol "o" in Tab. (4.9). The results shown below were performed using the MATLAB toolbox in commercial software [79].

Table 4.9: Summary of the calculated RANS simulations for the azimuth thruster operating under oblique flow condition.

f/j	0	0.1	0.2	0.3	0.4	0.5	0.6	0.7	0.8	0.9	1
2	x	x					x				x
3	x	x					x				x
4											
5						o					
6	x	x					x				x

Before starting training, it is necessary to preprocess the data. The presence of separated flows at significant angles results in a substantial oscillatory force. The Fourier series is used to eliminate the high frequency force and simplify the network. An eighth-order Fourier series expansion has been selected for this purpose. The solid line represents the regression result obtained from the expansion of the Fourier series, as depicted in Fig. (4.16).

However, it is important to note that δ varies between 0° and 180°, but the highest value of j is limited to 1. Consequently, the network will only take into account the impact of the angle and will disregard the variation of j. Thus, normalizing the input data is essential. The chosen normalization range spans from -1 to 1. The activation function is represented by the hyperbolic tangent function, see Eq. (4.29).

The second phase involves determining the structure of the network. If the structure is excessively complex, even if the Bayesian network has the capability to reduce parameters through γ, see Eq. (4.24), an excessive number of weights and biases will result in a

reduction in computing time. In case the network structure is too simple, it could reduce the accuracy of the fit.

In the network, the number of input variables is three, namely δ, j, and f. The number of neurons in the hidden layer is assumed to be a multiple of 3, with an upper limit of 21. The number of such test combinations is 7. Since the initial variables of the weights are random, the Mean Squared Error (MSE) from one combination is not persuasive, so a total of 500 samples is performed, i.e., 500 networks calculated for each combination. MSEs of the output is shown in Fig. (4.17). For both kF_x and kF_y, networks based on three neurons produce relatively large MSE. As the number of neurons increases, the MSEs become smaller and the improvement of the network tends to level off, so 12 and 9 are finally used as the number of neurons in the hidden layer of the neural network for kF_x and kF_y, respectively.

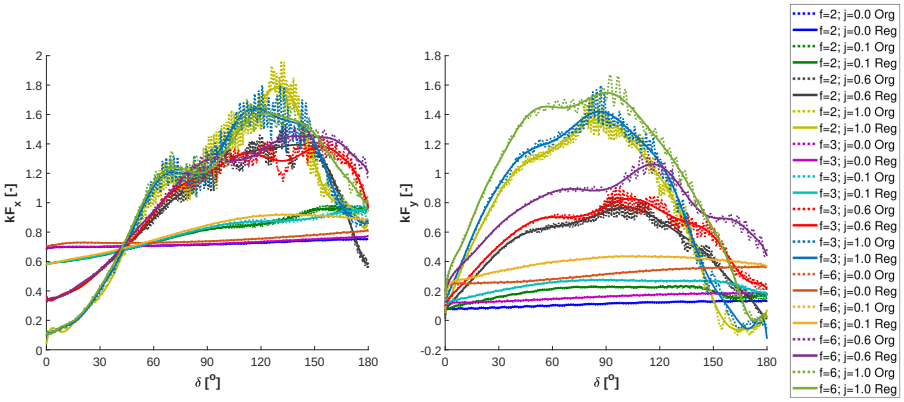

(a) Regression curve for kF_x **(b)** Regression curve for kF_y

Figure 4.16: Fourier series expansion of 8th order for the original RANS data.

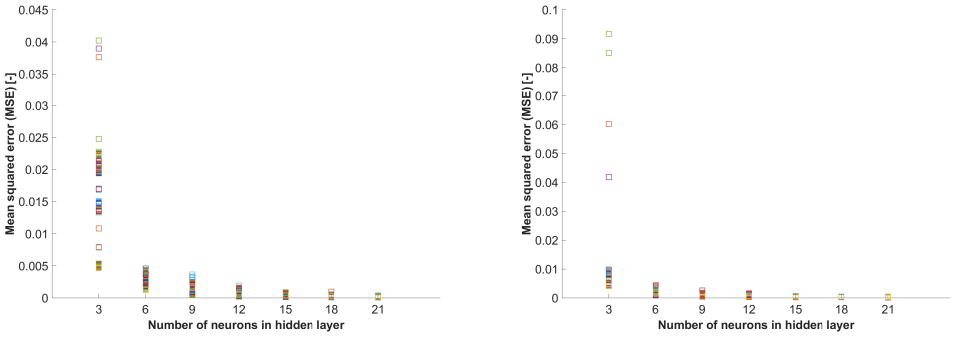

(a) kF_x **(b)** kF_y

Figure 4.17: Study of number of nodes in hidden layer for the net structure.

In Bayesian networks, it is assumed that the weight distribution follows a Gaussian distribution, at least in terms of its previous distribution ($P(w|\alpha\, M)$ in Eq. (4.12). The

advantage of randomly assigning the initial weights is that it increases the possibility of combining different weights. The disadvantage is that the number of combinations must be increased as much as possible in the process of finding the optimal value. Here, the total number of combinations is set to 10,000, divided into 1000 groups, each group consisting of 10 individuals. If 10,000 networks are calculated directly, there will inevitably be poor networks with large MSE. They will have a huge impact on the normalization of MSE, and will cause other networks with small MSE to have a value around -1 after normalization. For this reason, a best network should be extracted from a group that includes 10 networks to reduce the risk of the occurrence of high MSE. This is the reason for dividing the 10,000 networks into 1000×10.

The joint MSE of the seen and unseen datasets is used as a metric and the network with the smallest MSE will be selected as the best-weighted network. In particular, the dataset under the working conditions of $f = 5$ and $j = 0.5$ is not involved in the training of the network and is hidden from the network. Fig. (4.18) shows the MSE distribution of these 1000 best performing individuals. As expected, the MSEs in the validation dataset performed much better than the MSEs in the test dataset. Clearly, the average MSE of the two datasets is not convenient as an evaluation, and it is necessary to normalize the individual MSEs. The best individual shown in the figure is derived from the minimum of the mean of the normalized MSEs from both validation and test datasets.

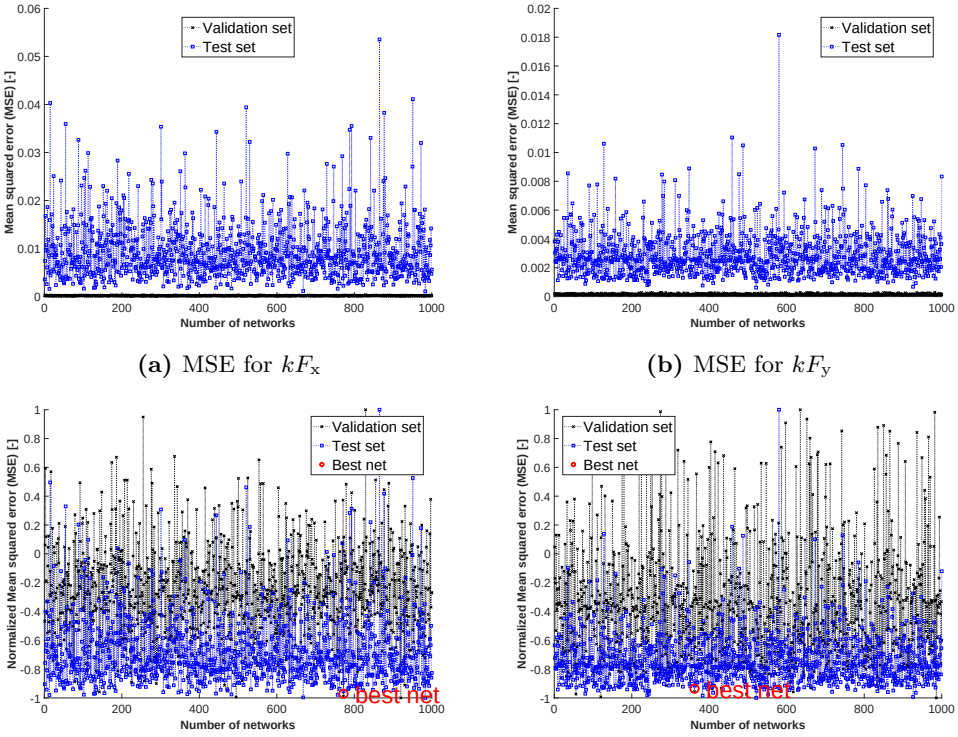

(a) MSE for kF_{x}

(b) MSE for kF_{y}

(c) Normalized MSE for kF_{x}

(d) Normalized MSE for kF_{y}

Figure 4.18: Performance of error in the 1000 networks.

Fig. (4.19) shows the probability distribution of the weights between the input and hidden layers in these 1000 networks. The input has three variables, and the hidden layer has 12 neurons, so the total number of weights is 12x3. The weights in the first column connect the first variable in the input layer, i.e., the azimuth angle to the 12 neurons in the hidden layer. The weights in the second and third columns represent the relationship of j and f to the hidden layer, respectively.

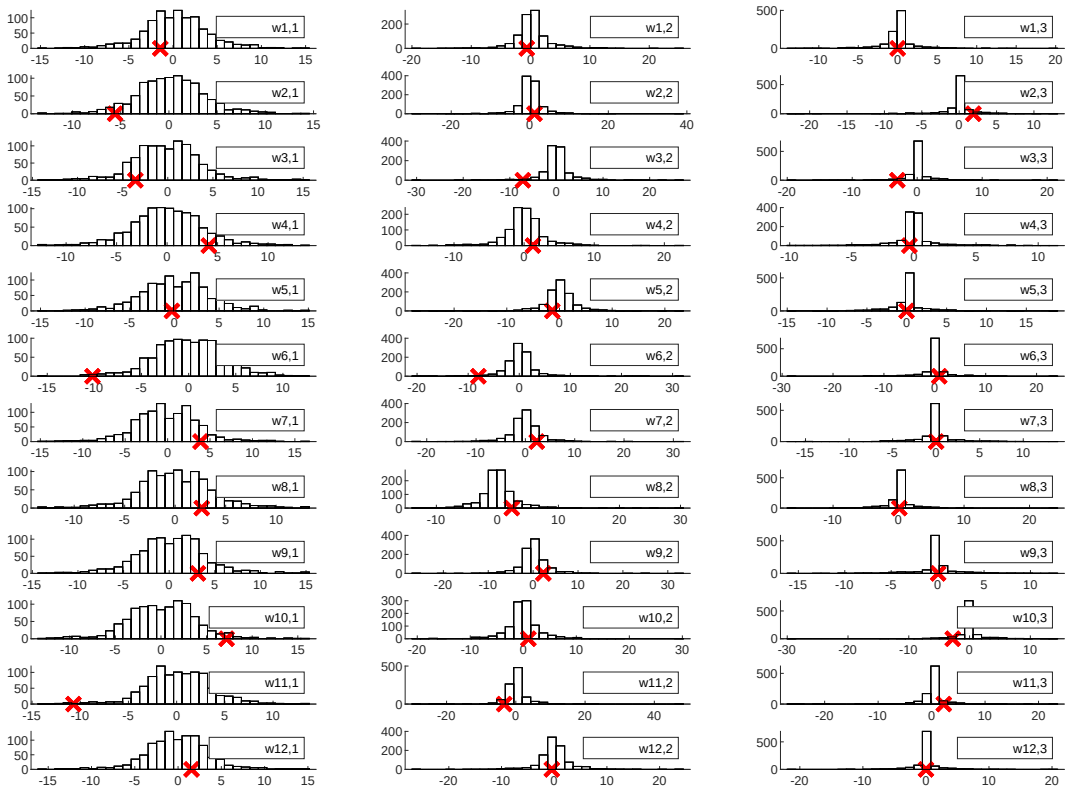

Figure 4.19: The range of values of weights connected to input and hidden layers in the 1000 networks. Symbol "x" denotes the weights being applied to the best network.

The densities of these weights correspond to their posterior distributions. Their values were centered around zero, closely resembling the zero-mean Gaussian distribution. The weight posterior distribution aligns with its prior distribution. The figure also illustrates a strong correlation between the variance of the weights and the range of values for the variables. Specifically, the variable δ has 181 different values, while j and f have only four and three different values, respectively. The weight distribution of the angles is broad, while the densities of j and f are narrow.

The network demonstrates high accuracy in the visible dataset, providing results that are comparable to those achieved by RANS in the validation dataset depicted in Fig. (4.20). Nevertheless, the network's predictive capacity is notably diminished, particularly for kF_{x}, with respect to $f = 5$ and $j = 0.5$ in the test dataset, as depicted in Fig. (4.21). However, in the absence of enough training data, the neural network has a rather impressive prediction capacity.

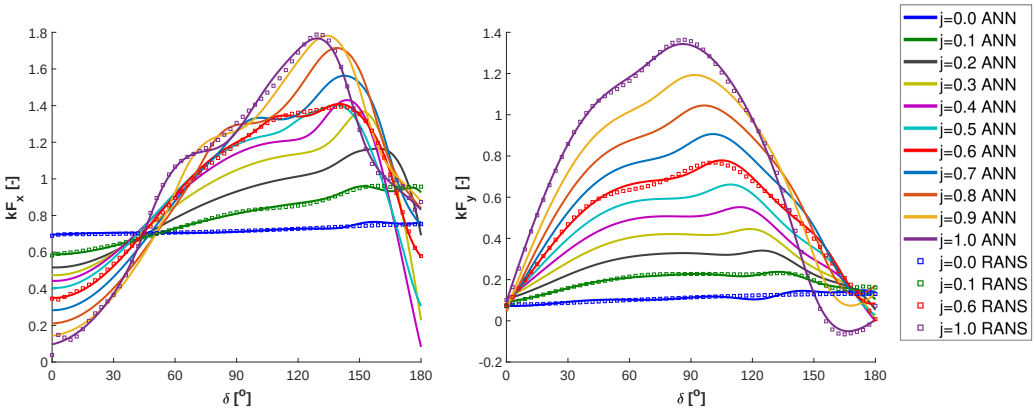

(a) kF_{x}: $f = 2$ **(b)** kF_{y}: $f = 2$

Figure 4.20: Performance of the best network in the validation dataset. □: RANS simulations. Solid lines: Prediction by the trained network. The network structure of kF_{x} is 3-12-1 and that of kF_{y} is 3-9-1.

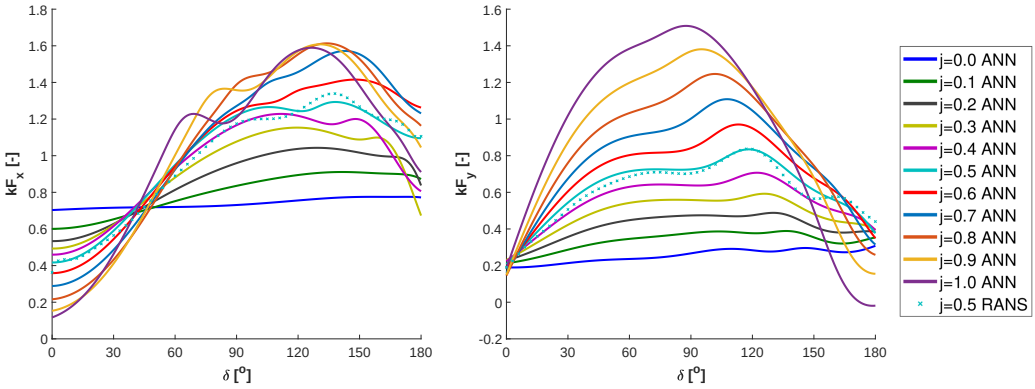

(a) kF_{x}: $f = 5$ **(b)** kF_{y}: $f = 5$

Figure 4.21: Performance of the best network in the test dataset. x: RANS simulations in the working condition of $f = 5$, $j = 0.5$. The network structure of kF_{x} is 3-12-1 and that of kF_{y} is 3-9-1.

As indicated in Tab. (4.9), the network lacks sufficient data for training in the range of $j = 0.2$ to 0.6. In order to enhance the precision of the network, it is necessary to

provide the network with additional training data while increasing the complexity of the network to capture the complex curve patterns observed at high azimuth angles. The extended training data is shown in Tab. (4.10). As an additional test dataset, $j = 0.9$ is also included. The number of neurons in the first hidden layer is kept constant, i.e., kF_x has 12 neurons and kF_y has 9 neurons. The number of neurons in the second hidden layer of both nets is 3. Keeping the structure simple can reduce computation time.

Table 4.10: Summary of updated calculated RANS simulations for the azimuth thruster operating in the dynamic condition.

f/j	0	0.1	0.2	0.3	0.4	0.5	0.6	0.7	0.8	0.9	1
2	x	x			x		x		x		x
3	x	x		x	x		x		x		x
4				x	x						
5						o				o	
6	x	x			x		x		x		x

As more training data are fed into the network, the level of uncertainty within the network decreases, resulting in better accuracy when predicting previously unseen data. The precision of the network predictions for both kF_x and kF_y is obvious. The predictions related to kF_y give excellent results in both the validation dataset (Fig. (4.22)) and the test dataset (Fig. (4.23)). However, there are still slight discrepancies in the prediction for kF_x on the test dataset in the large azimuth angle region, and the solid lines do not exactly match the RANS curve.

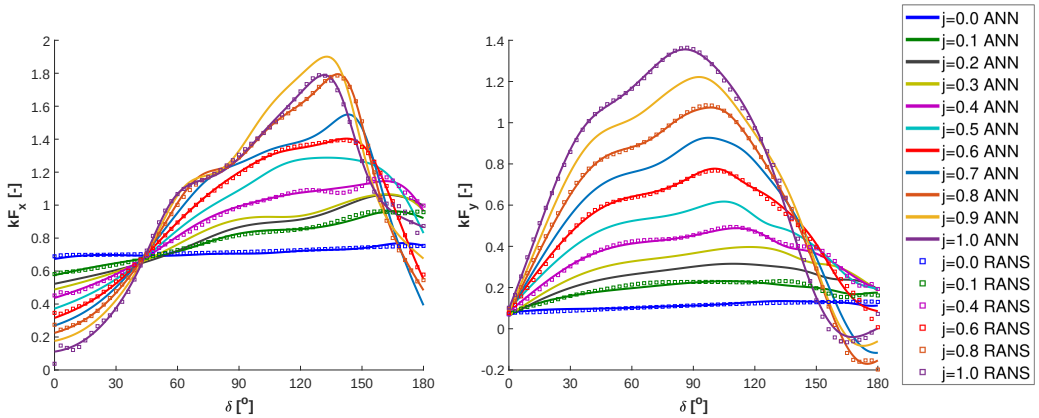

(a) kF_x: $f = 2$ **(b)** kF_y: $f = 2$

Figure 4.22: Performance of the best network with two hidden layers for the validating dataset. □: RANS computation. Solid lines: Prediction by the trained network. The network structure of kF_x is 3-12-3-1 and that of kF_y is 3-9-3-1.

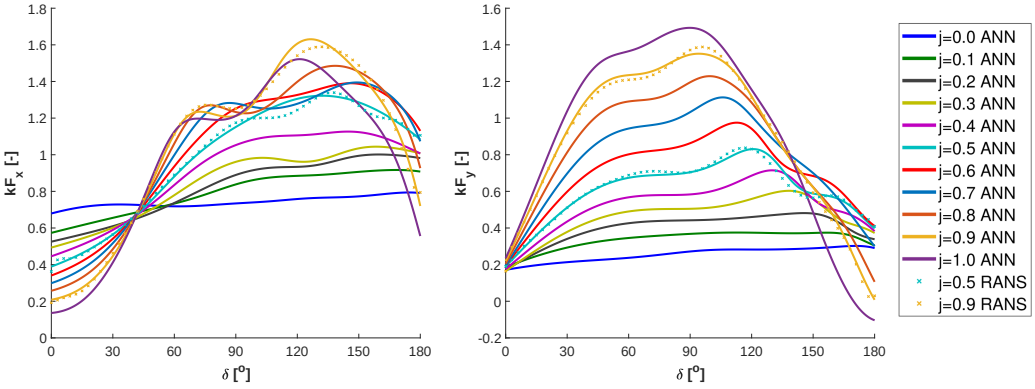

(a) kF_{x}: $f = 5$ **(b)** kF_{y}: $f = 5$

Figure 4.23: Performance of the best network with two hidden layers for the testing dataset. x: RANS computation in the working condition of $j = 0.5$ and 0.9 at $f = 5$. The test data remains hidden from the network during training. The network structure of kF_{x} is 3-12-3-1 and that of kF_{y} is 3-9-3-1.

In general, the current network's predictions did not exhibit any signs of overfitting. The network's prediction accuracy for new data is found to be closely correlated with the amount of data it has acquired. The training data for this investigation consisted of 23 cases estimated using RANS, which accounted for 40% of the total number of cases presented in Tab. (4.10). However, the utilization of less than 50% of the data to predict the remaining 60% or more is particularly attractive in real scenarios due to the probability that the input data are random numbers. For additional prediction results of the network, see Appendix (D).

4.3 Tunnel Thruster

Regarding the tunnel thruster, it is essential that the tunnel should be sufficiently deep to mitigate the risk of thruster loss due to ventilation. At ship zero speed, the relation between tunnel immersion and propeller diameter, as proposed by Brix [43], should be more than

$$\frac{e}{D} = 1.2 \cdot \frac{0.7}{D} \sqrt{\frac{Y_r}{\pi g \rho D}}, \tag{4.30}$$

where e describes the distance between the upper edge of the tunnel and the water surface. Y_r stands for the resulting transverse force. The minimum required immersion calculated by Eq. (4.30) is $e_{\mathrm{min}} = 1.33$ m, which is less than the current selected value of 1.93 m, so the appearance of ventilation may not be of concern.

Illustrations of the tunnel propeller, the tunnel, including the tunnel wall and housing, and the hull are shown in Fig. (4.24).

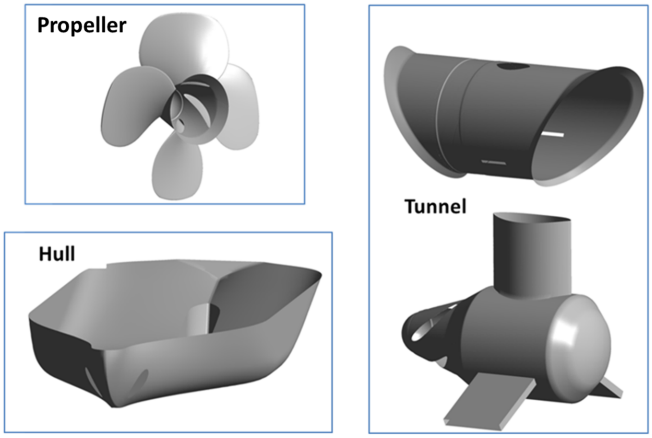

Figure 4.24: View of the ship bow thruster in the numerical computation.

4.3.1 Geometry

The primary function of the bow thruster is to generate transverse thrust. The blades are often symmetric to produce equal thrust in both directions of operation. The achievement of a high MC is attributed to the maintenance of a constant pitch, as described in Section (2.2). The selection of the blade shape was based on the empirical results of Taniguchi et al. [40], which showed that the Kaplan blade shape outperformed the elliptical shape. To minimize the occurrence of massive cavitating flow, it is common practice to limit the blade tip circumferential speed to a range of 30 to 35 m/s (Brix [43]). The propeller rotation rate, diameter, and tunnel configuration can be found in Tab. (4.11).

Table 4.11: Specification of tunnel thruster configuration.

Number of tunnel thruster	1	[-]
Diameter of thruster	1.93	[m]
Diameter of tunnel	1.96	[-]
Tunnel length (averaged)	2.747	[m]
Propeller rpm	317.5	[rev/min]

JASTRAM, SINTEF and TUHH conducted a numerical investigation in the InterThrust research project to investigate the effect of changing design parameters on the flow field generated by the thruster. The results of the RANS-based simulation provide a comprehensive understanding of the influence of the design parameters, including tunnel length, hull frame angle, waterline angle, tunnel entry shape, and gear housing shape. The simulations focused on the analysis of a basic hull block, rather than an actual ship under zero current speed conditions. Several aspects can be briefly described as follows:

- The total transverse thrust decreases with increasing tunnel length at a fixed frame angle. The increase in frictional force can play a considerable role in reducing the total transverse thrust.

- If the frame angle increases while the tunnel length remains constant, the two transverse forces can compensate each other; that is, the increase in propeller force due to the separated flow at the 6 o'clock position at the tunnel entrance and the decrease in hull force at the tunnel exit due to the change in pressure distribution. Therefore, the change in total transverse force is not significant.
- Changes in both the waterline angle and the frame angle affect the amount of the separated flow at the 9 o'clock and 6 o'clock positions, respectively. Both high frame angle and waterline angle increase the fluctuation of the force amplitude, which can amplify the vibrations experienced by a ship.
- The shape of the tunnel entrance prioritizes the reduction of vibrations caused by flow separation over consideration of propeller efficiency.

4.3.2 Mathematical modeling

The model relies on the velocity of the flow in the tunnel, and if this velocity is known, the propeller force can be predicted by Eq. (2.11). When the ship is at rest, the propeller force is half the total transverse force, which can be represented by the parameter $\lambda = 0.5$:

$$\lambda = \frac{Y_p}{Y_r}. \tag{4.31}$$

The value of λ is greater than 0.5 in practice due to flow losses caused by factors such as the geometry of the vessel, including the hull frame angle and waterline angle, and the diffusion of the propeller jet. The propeller force can be calculated as follows:

$$\begin{aligned} Y_p &= \lambda Y_r \\ &= \lambda \rho A (v_p)^2. \end{aligned} \tag{4.32}$$

The thrust coefficient for a propeller is then given by

$$\begin{aligned} k_t &= \frac{Y_p}{\rho n^2 D^4} \\ &= \lambda \frac{1}{4} \pi j^2, \end{aligned} \tag{4.33}$$

where $\mathrm{j} = \mathrm{v_p}/(\mathrm{nD})$. On the other hand, k_t can also be formulated as a function of j, which can be defined based on the measurements or the CFD simulation results, and it yields,

$$k_t = mj + n, \tag{4.34}$$

where m and n correspond to the slope and bias of the k_t curve, respectively. Different values of these variables indicate different blade characteristics, including pitch distribution, number of blades, and blade area ratio. The OP for determining the unknown

advance ratio j is derived from the intersection of the two k_t curves, as illustrated in Fig. (4.25). The OP can vary depending on how the ship motions affect the velocity inside the tunnel.

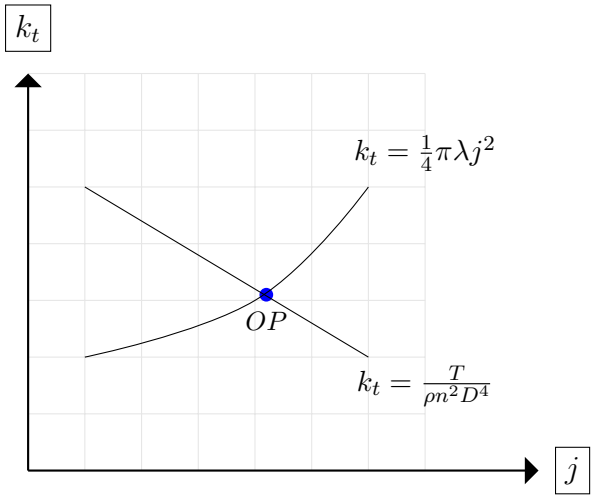

Figure 4.25: Solution of the velocity inside the tunnel.

Example for a simplified case

The Kaplan propeller model has a diameter of 240 mm, which scales to a real diameter of 1.92 m using a factor of 8. The gap between the propeller tip and the tunnel wall is approximately 1% of the propeller diameter, suggesting a tunnel diameter of 1.94 m. This dimension closely matches the tunnel propeller dimensions referenced in Tab. (4.11). The Kaplan type of Ka 4-70 was chosen, but without the skew modification, as described in Section (4.2).

Manufacturers often prefer propellers with smaller diameters and higher speeds for cost effectiveness. However, this strategy can reduce efficiency and cause cavitation at the blade tip. To keep the blade tip speed in the range of 30 to 34 m/s for a 1 m propeller radius, the optimum rotation rate should be approximately 5 Hz. The purpose of this analysis is to calculate the value of the parameter λ, as detailed in Eq. (4.33).

Fig. (4.26) shows the dimensions of the computational domain with the propeller positioned in the tunnel, equidistant from the entrance and exit. The domain size is chosen to mimic the conditions of the tunnel thruster operating in an unconfined environment. Non-slip wall conditions are applied to the propeller, tunnel walls, and propeller hub.

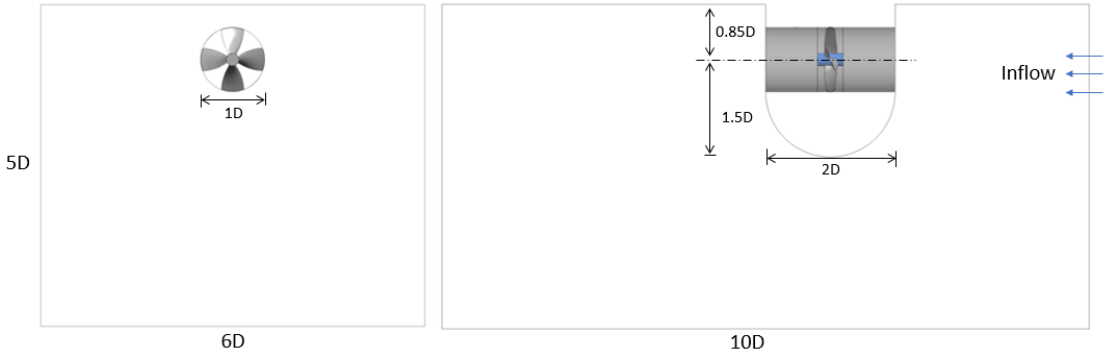

Figure 4.26: Simulation domain.

During the ship's berthing and unberthing maneuvers, transverse motion significantly affects the velocity inside the tunnel. This effect is simulated in the RANS simulation by adjusting the inflow velocity at the boundary. The inflow velocities analyzed in the study are 0 m/s, 1 m/s, 2 m/s, 3 m/s, and 4 m/s.

Fig. (4.27) shows the simulated average axial velocities on the three cross sections. At the propeller plane (x/R=0: a constricted cross-section), the axial velocity is increased due to the blocking effect of the propeller. At the downstream station of x/R=-2.02, which is located at the tunnel exit, the axial velocity is comparatively lower. In the upstream section of x/R=0.3, the velocity differs from the velocity at x/R=-2.02 (the tunnel exit) due to the influence of the propeller hub.

The tunnel exit velocity is assumed to represent the flow velocity within the tunnel, denoted by v_p. Under varying inflow conditions, both v_p and j change accordingly. Using the propeller thrust coefficient k_t extracted from the simulations, the relationship between j and v_p can be illustrated in Fig. (4.28). Where j varies from 0.91 to 1.01, corresponding to inflow velocities of 0 to 4 m/s in steps of 1 m/s. In the bollard pull condition without inflow velocity ($v_\infty = 0$), the value of λ is interpolated to be 0.68 at $j = 0.91$. In Bladt's [80] documentation, this factor is referred to as the "Schubanteilziffer (thrust ratio)" and an empirical estimate of this parameter is provided. The value given in his example is 0.649. It should be noted that different tunnel configurations and blade characteristics can lead to different results when determining this factor. An accurate estimate of this factor requires additional support from experimental data or numerical simulations.

Particular attention must be paid to understanding how the ship's speed affects the behavior of the propeller slipstream in relation to the hull. The following section provides a detailed illustration of the interactions between the bow thruster and the hull.

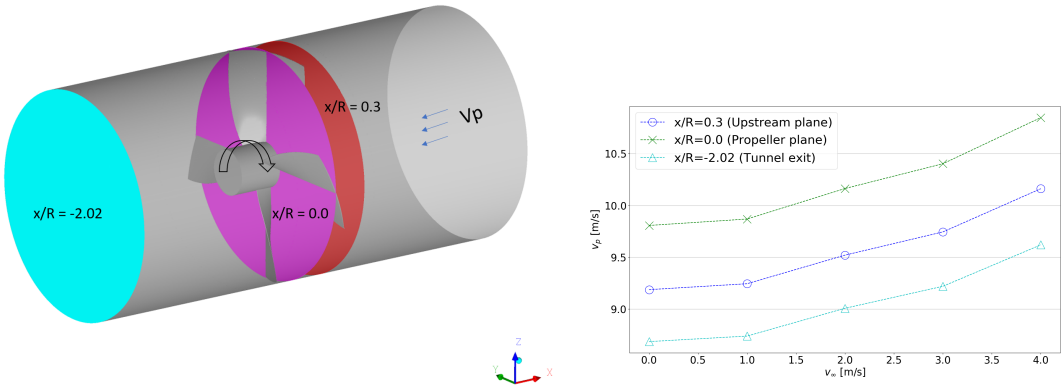

(a) Plane stations to capture the averaged disc velocity.

(b) Relationship between the inflow velocity and the velocity in the tunnel.

Figure 4.27: Average axial velocity across the sampled planes.

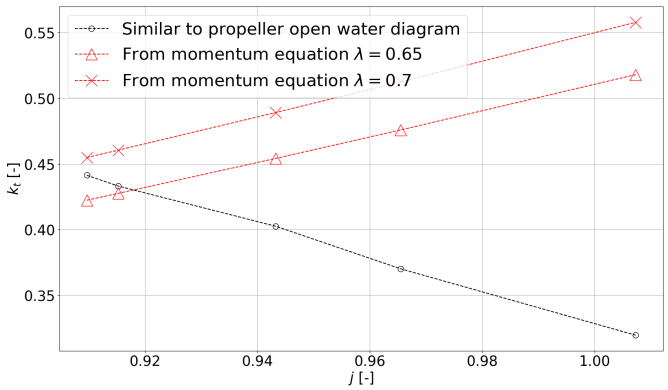

Figure 4.28: OP related to the average axial velocity across the tunnel exit plane.

4.4 Interactions

Numerical simulations were performed to investigate the effects of different ship speeds and inflow orientations on thruster-hull interactions. One set of simulations considered different Froude numbers (F_n), while another set considered different inflow angles at a constant F_n number. In subsequent analysis, the forces produced by the propeller, the tunnel, and the hull, as shown in Fig. (4.24), will be presented as different components to give a general view of the effect of a bow thruster.

Figs. (4.30) through (4.31) show the results of these simulations. The main points to be discussed are as follows:

- The propeller thrust and torque have shown a minor reduction in response to varying ship speeds, as observed in the numerical simulations and discussed by

Norrby [38]. The primary factor influencing the change in total transverse force is the transverse force acting on the hull. The combined resistance of the tunnel wall and fairing is the primary factor influencing the total longitudinal force, while the propeller contributes a positive force.

- It is generally expected that the total transverse force will decrease consistently as the ship's speed increases. However, the observation in Fig. (4.29b) indicates that the total transverse force shows a decreasing trend only up to $F_n = 0.111$, after which it begins to increase. This finding is consistent with the results of Taniguchi et al. [40] as documented in their research. This phenomenon is considered to be related to the changing relative position between the hull and the slipstream generated by the bow thruster.

- The propeller thrust is slightly higher when the heading angle is positive than when it is negative, as shown in Fig. (4.30b), due to the variation in the inflow conditions. The variation in the hull transverse force is the main factor influencing the variation in the total transverse force.

- The similar tendency of the propeller thrust and torque (Fig. (4.31)), indicates that the MC is insensitive to the changing speeds and heading angles.

- The separated flow at 6 o'clock and at 9 o'clock can be intensified while ship speed increases, as shown in Fig. (4.29a).

Any change in the hull shape compared to the one studied can lead to significant changes in the interaction between the propeller slipstream and the ship's hull, even if the conditions remain the same. However, the propeller force is only moderately affected by the given conditions, which allows the use of the model to predict the propeller force. A separate module can be developed to account for the interaction between the thruster and the hull. However, it is not easy to accurately determine the interaction during the maneuvering tests because it is strongly correlated with the instantaneous position of the ship. The effect of the propeller on the ship during PMM tests will be described in great detail in Chapter (6).

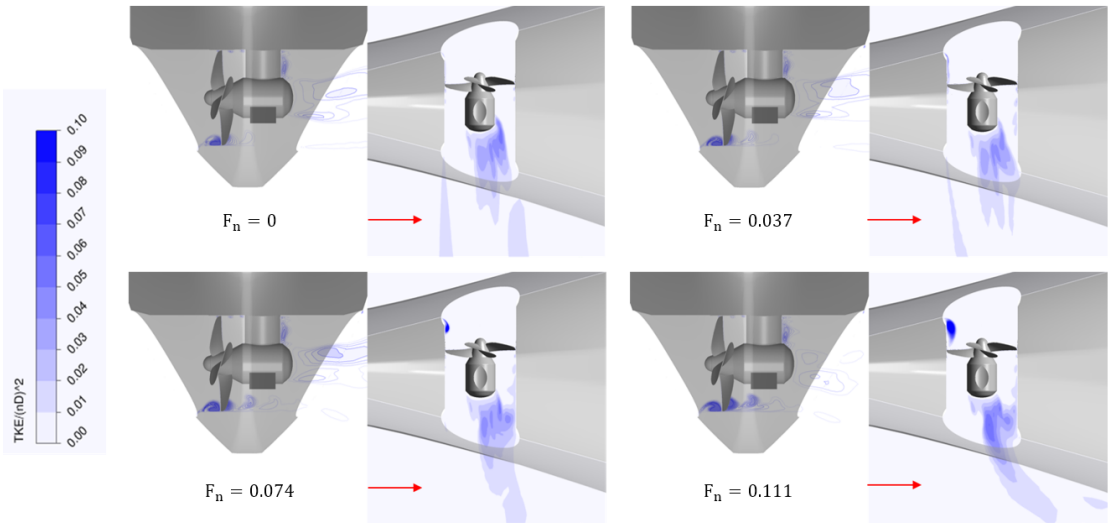

(a) The flow behavior within the tunnel. The vortex due to flow separation can be seen at the 6 and 9 o'clock positions. The intensity of the vortex increases with the increase of ship speed.

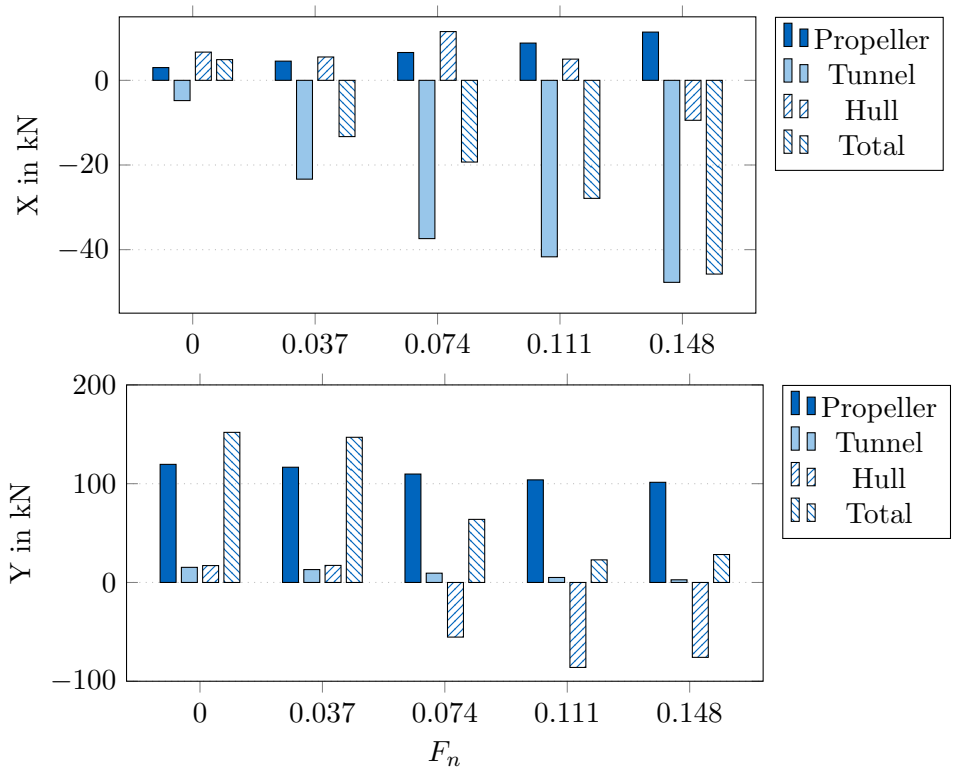

(b) Variation of forces on different components, as shown in Fig. (4.24).

Figure 4.29: Variation of ship speed at zero ψ.

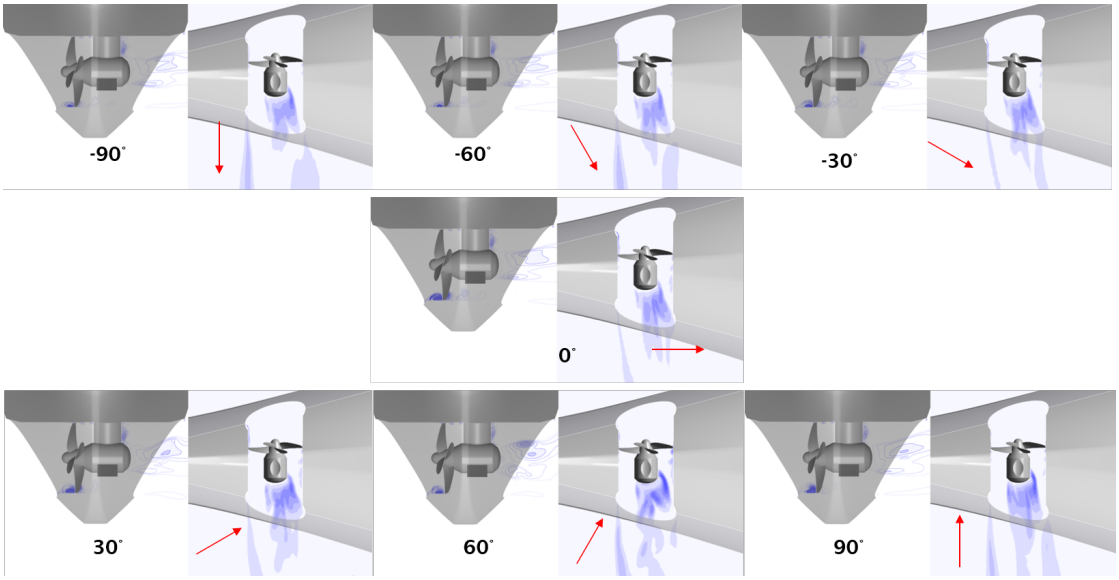

(a) Flow behavior within the tunnel.

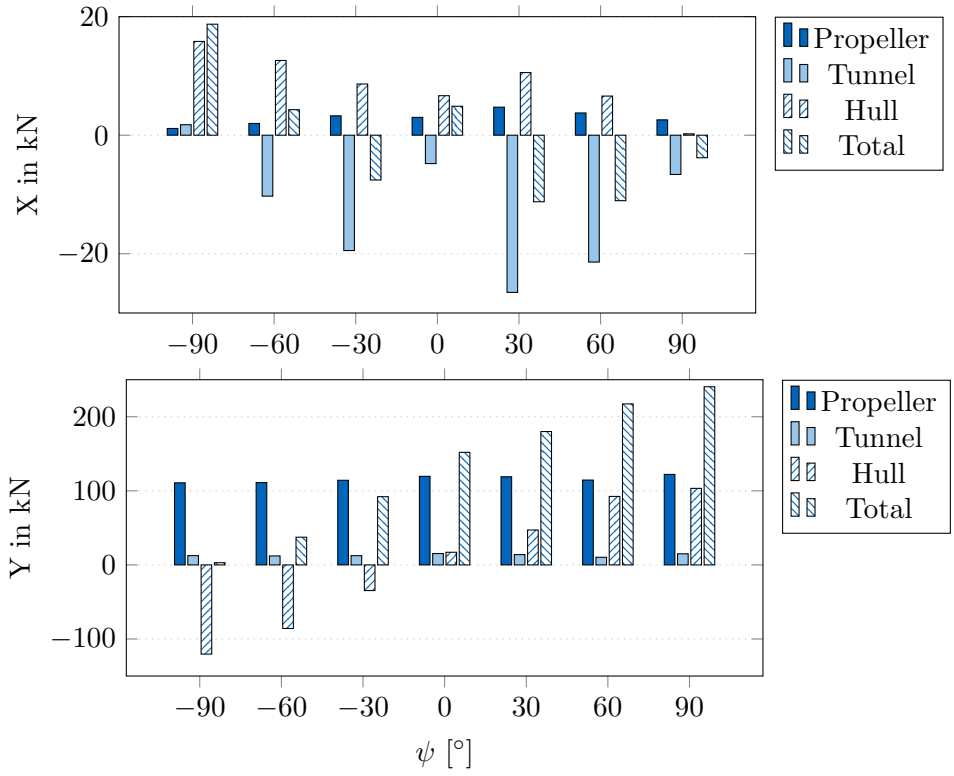

(b) Variation of forces on different components, as shown in Fig. (4.24).

Figure 4.30: Variation of heading angle at $F_n = 0.037$.

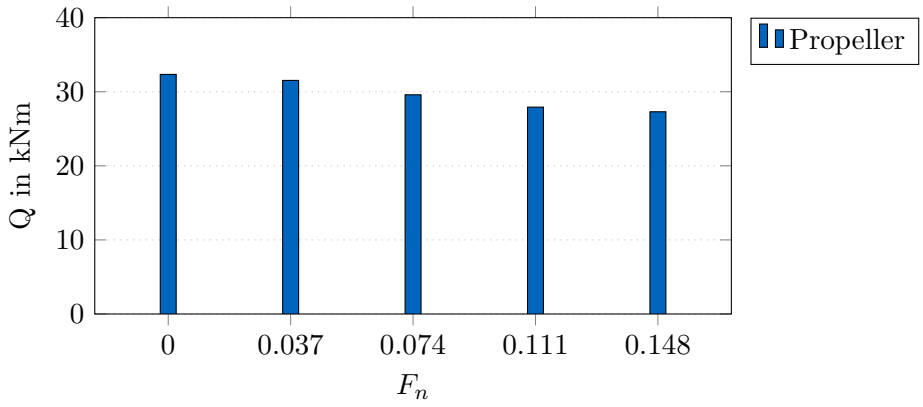

(a) $Q(F_n)$.

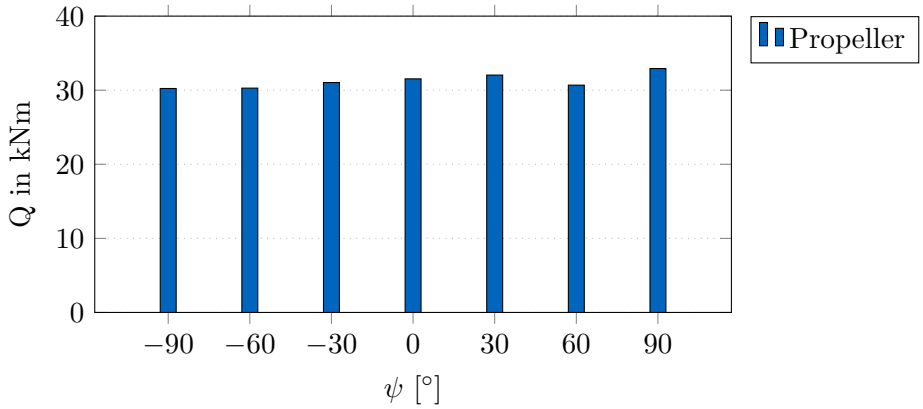

(b) $Q(\psi)$.

Figure 4.31: Variation of propeller torque Q.

5 Ship Maneuvering

The International Maritime Organization (IMO [81]) has issued rules and regulations to test the maneuverability of ships. The standards have been developed for ships with conventional propulsion systems and rudders, and they apply to ships longer than 100 m at their design speed. The maneuverability tests should be carried out without the use of non-continuously operating auxiliary assistance under normal operating conditions, including deep water, unrestricted water, calm environment, full load, even keel, and steady approach at test speed. It should be at least 90 percent of the ship's speed, which corresponds to 85 percent of the maximum engine rating.

For ships designed for specific purposes or operating permanently within a limited area where conditions are beyond IMO standards, the shipowners are then required to determine maneuvering characteristics.

5.1 Overview of Maneuvering Simulations

In general, the maneuverability of a ship can be divided into three categories, namely maintaining course, changing course, and changing speed. For the first, the ship is required to maintain a steady course without the use of steering control devices, which, however, are also used to identify the ability of the ship to change course. Speed change is the ability of a ship to change its speed. According to MSC.137(76) [81], the assessment of the ship's maneuverability is taken into account by the following standard maneuvers:

- The turning ability describes the ability of a ship to leave its course into a turning circle. The advance and the tactical diameter are evaluated on the basis of the turning maneuver with the maximum possible rudder deflection.

- The initial turning ability, the purpose of this maneuver is to check the distance covered by a ship when she reaches a certain heading deviation reacted by a moderate deflected rudder.

- The yaw-checking and course-keeping abilities are the abilities to change heading in response to the rudder actions. Evaluation can be performed by the zig-zag maneuver.

- The stopping ability is intended to check the ship's stopping ability to avoid a possible collision. The ability is characterized by the track reach, time to dead in water, and lateral deviations.

The fact that a ship has good turning ability does not mean that it has good course keeping ability, as discussed by Kobylinski [82]. The criteria described above are evaluated via the geometrical parameters; for example, the *advance* and the *tactical diameter* in the turning circle maneuver should not exceed 4.5 and 5 ship lengths, respectively, see Fig. (5.1). Bertram [83] provides a detailed description of the maneuvering tests.

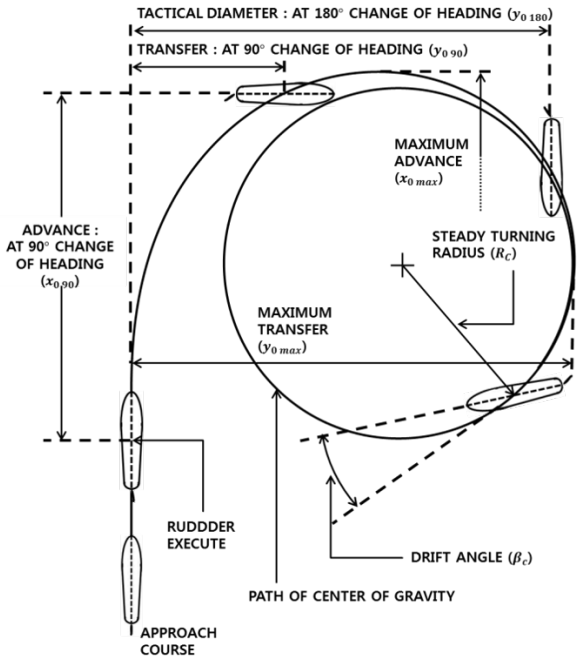

Figure 5.1: The geometrical measures on turning circle (ITTC [8]).

5.2 Coordinate Systems

A body-fixed right-handed Cartesian coordinate system is applied. The axes x, y, and z move relative to the earth-fixed one (x_0,y_0, and z_0), as shown in Fig. (5.2)). The x-axis is positive in forward direction, the y-axis is positive toward starboard, and the z-axis is positive downward. The resulting velocity U is the magnitude velocity, consisting of u and v in the form of

$$U = \sqrt{u^2 + v^2}. \tag{5.1}$$

The drift angle β is the angle between u and U as defined in

$$\beta = \arctan\frac{-v}{u}, \tag{5.2}$$

where $-$ stands for the negative β as the angle is counted from u to U (negative about z-axis). The rudder angle δ is positive when the rudder is deflected to the port side

around positive z-axis. The notation of the course angle ψ and the center of gravity O are also defined in Fig. (5.2).

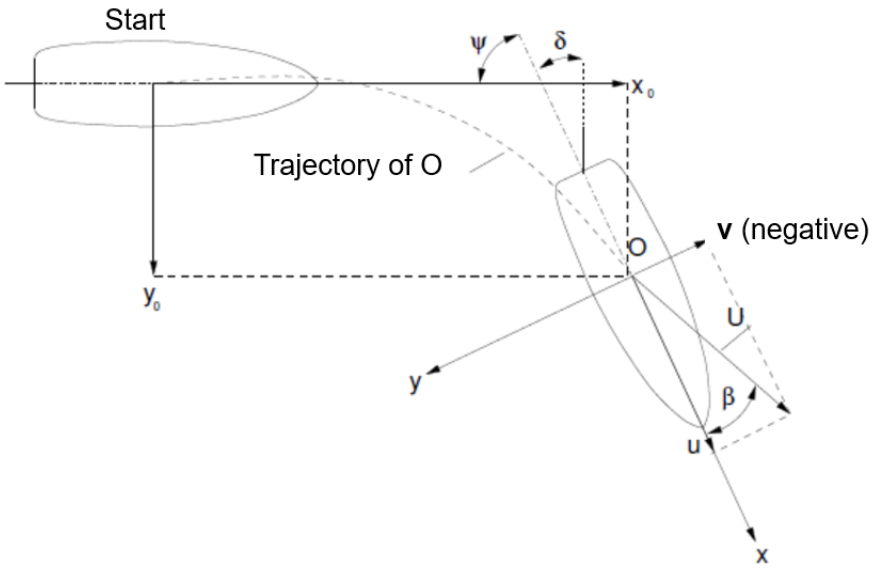

Figure 5.2: Definition of the coordinate system during ship maneuver (Abdel-Maksoud [9]).

5.3 Dimensionless Numbers

Usually, the forces and moment are nondimensionalized by using the characteristic scales such as L_{pp}, U_0 and ρ as shown in Tab. (5.1). Since velocities and circular frequency will also be employed in the equations for forces and moments, they must also be nondimensionalized, as shown in Tab. (5.2). Further additional dimensionless hydrodynamic derivatives used in the maneuvering model are listed in Appendix (E).

Table 5.1: Definition of dimensionless forces and moment.

$X' = \frac{X}{0.5\rho U_0^2 L_{pp}^2}$	$Y' = \frac{Y}{0.5\rho U_0^2 L_{pp}^2}$	$N' = \frac{N}{0.5\rho U_0^2 L_{pp}^3}$

Table 5.2: Definition of dimensionless velocities and circular frequency.

$\omega' = \frac{\omega L_{\mathrm{pp}}}{U_0}$	$v' = \frac{v}{U_0}$	$r' = \frac{r L_{pp}}{U_0}$	$u' = \frac{u}{U_0}$

5.4 Maneuvering Modeling

Several factors must be taken into account in the development of the maneuvering model. For considering the interaction between the thrusters and the ship's hull, the maneuvering model must be able to account for the asymmetric force generated by a bow thruster and not follow the mathematical expressions for a symmetric ship described in Section (2.1). In addition, general applicability should be a priority when developing such a model.

The effectiveness of the bow thruster is most noticeable at low ship speeds, where surge, sway, and yaw motions are primarily involved, while heave, pitch, and roll are less significant. Lewandowski [84] describes the relevant equation for a rigid body in a horizontal plane, relative to the body's fixed frame, as follows:

$$
\begin{aligned}
X &= m(\dot{u} - vr - r^2 x_G) && \text{(5.3a)}\\
Y &= m(\dot{v} + ur + \dot{r} x_G) && \text{(5.3b)}\\
N &= I_{zz}\dot{r} + m(ur + \dot{v}) x_G. && \text{(5.3c)}
\end{aligned}
$$

Meanwhile, the hydrodynamic forces (X, Y) and moment (N) are a function of the ship's motion parameters u, v, r, $\dot{u}$, $\dot{v}$, and $\dot{r}$. The vector $\overrightarrow{T}$, containing X, Y, and N can be expressed as

$$
\begin{aligned}
\overrightarrow{T} &= \begin{pmatrix} X \\ Y \\ N \end{pmatrix} \\
&\cong \overrightarrow{T_0} \\
&+ \overrightarrow{T_u}\Delta u + \overrightarrow{T_{uu}}\Delta u^2 + \overrightarrow{T_{uuu}}\Delta u^3 + \overrightarrow{T_{\dot{u}}}\dot{u} + \overrightarrow{T_{\dot{u}u}}\dot{u}\Delta u + \overrightarrow{T_{\dot{u}uu}}\dot{u}\Delta u^2 \\
&+ \overrightarrow{T_v} v + \overrightarrow{T_{vv}} v^2 + \overrightarrow{T_{vvv}} v^3 + \overrightarrow{T_{\dot{v}}}\dot{v} + \overrightarrow{T_{\dot{v}v}}\dot{v}v + \overrightarrow{T_{\dot{v}vv}}\dot{v}v^2 \\
&+ \overrightarrow{T_r} r + \overrightarrow{T_{rr}} r^2 + \overrightarrow{T_{rrr}} r^3 + \overrightarrow{T_{\dot{r}}}\dot{r} + \overrightarrow{T_{\dot{r}r}}\dot{r}r + \overrightarrow{T_{\dot{r}rr}}\dot{r}r^2 \\
&+ \overrightarrow{T_{vu}} v\Delta u + \overrightarrow{T_{ru}} r\Delta u \\
&+ \overrightarrow{T_{vvu}} v^2\Delta u + \overrightarrow{T_{rru}} r^2\Delta u + \overrightarrow{T_{vru}} vr\Delta u \\
&+ \overrightarrow{T_{vuu}} v\Delta u^2 + \overrightarrow{T_{ruu}} r\Delta u^2 \\
&+ \overrightarrow{T_{vr}} vr + \overrightarrow{T_{rrv}} r^2 v + \overrightarrow{T_{vvr}} v^2 r, && \text{(5.4)}
\end{aligned}
$$

using Taylor-series expansions under three assumptions:

1. Acceleration terms of the first order,
2. velocity terms up to the third order, and
3. no cross-coupling between acceleration and velocity such as $\dot{r}v$.

In Eq. (5.3) X, Y, and N are the external forces. The acceleration-related terms can be moved to the left side. Accelerations can be determined based on the velocities

u, v and r and the related forces and moments. The calculated accelerations can be integrated over time using Euler's method to calculate the actual ship speed, which is integrated again after the coordinate transformation to get the trajectory of the ship in the earth-fixed frame. An example is presented in Section (5.6) based on the research by Wolff [30].

Note that Eq. (5.4) is not the final maneuvering model. A model will be presented after discussing the results of the sensitivity study of the hydrodynamic derivatives in Section (6.4).

5.5 Virtual PMM Tests

5.5.1 Description of ship motion

During the PMM test, the ship model moves forward at a constant speed. In addition, forced motions are applied in a controlled manner at two specific points on the ship: one near the bow and the other near the stern, both located equidistant from the main section of the ship. For a more detailed description, see Crane et al. [4]. The forced motion allows for adjustment of the oscillation phase of the relative motion between the two points. In the virtual simulation of the PMM test, a sinusoidal motion is applied in the ship-fixed frame (x, y, z) relative to the earth-fixed one (x_0, y_0, z_0), as shown in Fig. (5.3). During PMM tests, the velocity components (u, v, r) that represent the center of gravity of the ship are subjected to periodic oscillations. To simplify computational simulation, a constant velocity u_0 is used as the inlet boundary condition to replace the ship's forward speed U_0 in the x_0-direction.

To determine the coefficients in Eq. (5.4), different tests must be performed for each set of coefficients. For example, to obtain the coefficients associated with the oscillation velocity v, it is crucial to suppress the ship motion with respect to u and r. A detailed description of the forced hull motion is provided below.

5.5.1.1 Pure surge

The ship will only perform longitudinal oscillations along the x-axis, with no motions in other degrees of freedom,

$$u = \hat{u}\cos(\omega t) \tag{5.5a}$$
$$v = 0 \tag{5.5b}$$
$$r = 0. \tag{5.5c}$$

The symbol $\hat{}$ indicates the velocity amplitude. Displacements and yaw angle within the ship's frame are derived by integrating these velocities,

$$x = \hat{x}\sin(\omega t) + \text{constant} \tag{5.6a}$$

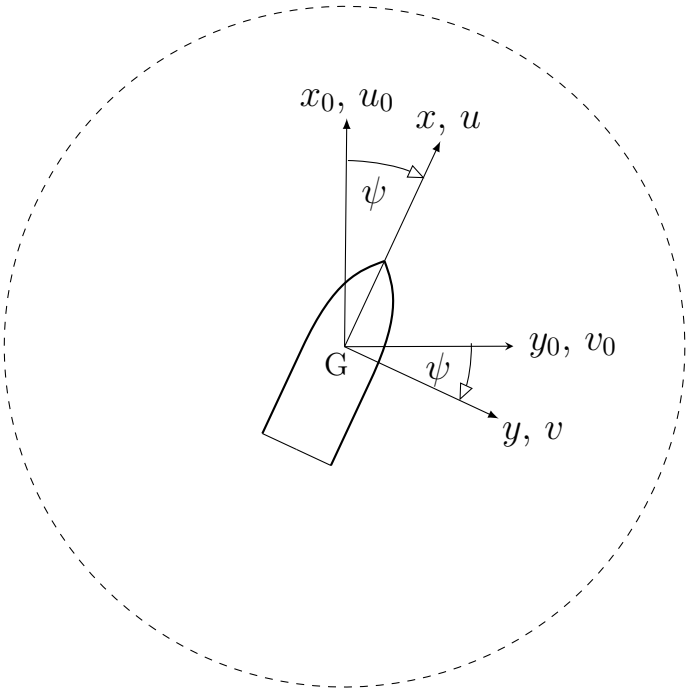

Figure 5.3: Definition of coordinate systems and motion parameters.

$$y = \text{constant} \tag{5.6b}$$
$$\psi = \text{constant}. \tag{5.6c}$$

The initial position of the ship-fixed frame is aligned with the earth-fixed frame, and the constants in the equations are set to zero.

In the earth-axis system, the displacements are as follows:

$$x_0 = x + u_0 t \tag{5.7a}$$
$$y_0 = y \tag{5.7b}$$
$$\psi = 0. \tag{5.7c}$$

5.5.1.2 Pure sway

The ship performs transverse oscillations along the y-axis. Movements in the other degrees of freedom do not take place. In the body frame, the velocities are

$$u = 0 \tag{5.8a}$$
$$v = \hat{v}\cos(\omega t) \tag{5.8b}$$

$$r = 0. \tag{5.8c}$$

The displacements and the yaw angle are

$$x = 0 \tag{5.9a}$$
$$y = \hat{y}\sin(\omega t) \tag{5.9b}$$
$$\psi = 0. \tag{5.9c}$$

In the earth-axis system, the displacements and yaw angle have the same formulation as in Eq. (5.7).

5.5.1.3 Pure yaw

The ship performs pure rotational oscillations around the z-axis, without movements along the y-axis. The velocity v is zero,

$$u = 0 \tag{5.10a}$$
$$v = 0 \tag{5.10b}$$
$$r = \hat{r}\cos(\omega t). \tag{5.10c}$$

The displacement y_0 is obtained by integrating v_0 as follows:

$$y_0 = \int v_0 dt = \int u_0 \frac{v_0}{u_0} dt. \tag{5.11}$$

The relations between v, u_0, and v_0, as found in Fig. (5.3), can be written as

$$u_0 \sin\psi - v_0 \cos(\psi) = v = 0 \tag{5.12a}$$
$$\Rightarrow \frac{v_0}{u_0} = \tan(\psi). \tag{5.12b}$$

Finally, y_0 becomes

$$y_0 = \int u_0 \tan(\psi) dt, \tag{5.13}$$

and the yaw angle ψ is

$$\psi = \hat{\psi}\sin(\omega t). \tag{5.14}$$

Note that the oscillation velocity u in the pure yaw motion is not exactly zero. When only the yaw oscillation angle ψ is small, u_s can be simplified to u_0 as shown

in Eq. (5.15a), where u_s stand for the longitudinal velocity component in the ship-fixed frame (x, y, z):

$$\begin{aligned} u_s &= u_0 \cos\psi + v_0 \sin\psi && (5.15a) \\ &\approx u_0. && (5.15b) \end{aligned}$$

5.5.1.4 Combined sway-yaw

The ship performs a combined transverse and rotational oscillation. The oscillating velocity u is zero:

$$\begin{aligned} u &= 0 && (5.16a) \\ v &= \hat{v} \cos(\omega t) && (5.16b) \\ r &= \hat{r} \cos(\omega t). && (5.16c) \end{aligned}$$

From the same figure (Fig. (5.3)), the relation between v, u_0, and v_0 can be obtained:

$$u_0 \sin\psi + v \cos\omega t = v_0 \cos\psi. \tag{5.17}$$

It follows that

$$y_0 = \int \frac{\hat{v} \cos(\omega t) + u_0 \sin(\psi)}{\cos(\psi)} dt \tag{5.18}$$

with

$$\psi = \hat{\psi} \sin(\omega t). \tag{5.19}$$

Tab. (5.3) presents an overview of the motion parameters. The integrals are calculated numerically through the Runge-Kutta integration scheme. By applying these motion parameters, the desired coefficients are obtained. A detailed methodology for calculating these coefficients is described in the following sections.

5.5.2 Determination of hydrodynamic derivatives

First, the determination of the hydrodynamic derivatives derived from the sway motion is introduced; other hydrodynamic derivatives from the surge and the yaw motion are handled in the same way.

For the sway test, the vector $\overrightarrow{T}$ is only a function of v. Using a third-order Taylor-series expansion about $\overrightarrow{T}$, yields the following:

$$\overrightarrow{T}(v, \dot{v}) \cong \overrightarrow{T_0} + \overrightarrow{T_v} v + \overrightarrow{T_{vv}} v^2 + \overrightarrow{T_{\dot{v}v}} \dot{v} v + \overrightarrow{T_{vvv}} v^3 + \overrightarrow{T_{\dot{v}vv}} \dot{v} v v$$

Table 5.3: Displacement set in the earth-fixed coordinate system.

		Surge	Sway	Yaw	Sway + Yaw
PMM motion	u	$\hat{u}\cos(\omega t)$	0	0	0
	v	0	$\hat{v}\cos(\omega t)$	0	$\hat{v}\cos(\omega t)$
	r	0	0	$\hat{r}\cos(\omega t)$	$\hat{r}\cos(\omega t)$
Displacement	x_0	$\hat{x}_0\sin(\omega t)+u_0 t$	$u_0 t$	$u_0 t$	$u_0 t$
	y_0	0	$\hat{y}_0\sin(\omega t)$	$\int u_0\tan(\psi)dt$	$\int \frac{\hat{v}\cos(\omega t)+u_0\sin(\psi)}{\cos(\psi)}\mathrm{dt}$
	ψ	0	0	$\hat{\psi}\sin(\omega t)$	$\hat{\psi}\sin(\omega t)$

$$
\begin{aligned}
&= \overrightarrow{T_0} + \overrightarrow{T_v}\hat{v}\cos(\omega t) + \overrightarrow{T_{\dot{v}}}(-\hat{v}\omega\sin(\omega t)) \\
&+ \overrightarrow{T_{vv}}\hat{v}^2\cos^2(\omega t) + \overrightarrow{T_{\dot{v}v}}(\hat{v}^2\omega\sin(\omega t)\cos(\omega t)) \\
&+ \overrightarrow{T_{vvv}}\hat{v}^3\cos^3(\omega t) + \overrightarrow{T_{\dot{v}vv}}(-\hat{v}^3\omega\sin(\omega t)\cos^2(\omega t)). \qquad (5.20)
\end{aligned}
$$

Using trigonometric relations in Tab. (5.4),

Table 5.4: Some useful trigonometric relations.

$\sin^2(\omega t) = \frac{1}{2} - \frac{1}{2}\cos(2\omega t)$
$\sin^3(\omega t) = \frac{3}{4}\sin(\omega t) - \frac{1}{4}\sin(3\omega t)$
$\cos^2(\omega t) = \frac{1}{2} + \frac{1}{2}\cos(2\omega t)$
$\cos^3(\omega t) = \frac{3}{4}\cos(\omega t) + \frac{1}{4}\cos(3\omega t)$

Eq. (5.20) is then converted to

$$
\begin{aligned}
\overrightarrow{T} \;\cong\; & (\overrightarrow{T_0} + \frac{1}{2}\overrightarrow{T_{vv}}\hat{v}^2) \\
+ \;& (\overrightarrow{T_v}\hat{v} + \frac{3}{4}\overrightarrow{T_{vvv}}\hat{v}^3)\cos(\omega t) + (-\overrightarrow{T_{\dot{v}}}\hat{v}\omega - \frac{1}{4}\overrightarrow{T_{\dot{v}vv}}\omega\hat{v}^3)\sin(\omega t) \\
+ \;& (\frac{1}{2}\overrightarrow{T_{vv}}\hat{v}^2)\cos(2\omega t) + (-\frac{1}{2}\overrightarrow{T_{\dot{v}v}}\hat{v}^2\omega\sin(2\omega t)) \\
+ \;& (\frac{1}{4}\overrightarrow{T_{vvv}}\hat{v}^3)\cos(3\omega t) + (-\frac{1}{4}\overrightarrow{T_{\dot{v}vv}}\hat{v}^3\omega)\sin(3\omega t), \qquad (5.21)
\end{aligned}
$$

or in matrix notation;

$$
\begin{pmatrix}
1 & 0 & 0 & \frac{1}{2}\hat{v}^2 & 0 & 0 & 0 \\
0 & \hat{v} & 0 & 0 & 0 & \frac{3}{4}\hat{v}^3 & 0 \\
0 & 0 & -\hat{v}\omega & 0 & 0 & 0 & -\frac{1}{4}\omega\hat{v}^3 \\
0 & 0 & 0 & \frac{1}{2}\hat{v}^2 & 0 & 0 & 0 \\
0 & 0 & 0 & 0 & -\frac{1}{2}\omega\hat{v}^2 & 0 & 0 \\
0 & 0 & 0 & 0 & 0 & \frac{1}{4}\hat{v}^3 & 0 \\
0 & 0 & 0 & 0 & 0 & 0 & -\frac{1}{4}\omega\hat{v}^3
\end{pmatrix}
\begin{pmatrix}
\overrightarrow{T_0} \\ \overrightarrow{T_v} \\ \overrightarrow{T_{\dot{v}}} \\ \overrightarrow{T_{vv}} \\ \overrightarrow{T_{\dot{v}v}} \\ \overrightarrow{T_{vvv}} \\ \overrightarrow{T_{\dot{v}vv}}
\end{pmatrix}
=
\begin{pmatrix}
\overrightarrow{A_0} \\ \overrightarrow{A_1} \\ \overrightarrow{B_1} \\ \overrightarrow{A_2} \\ \overrightarrow{B_2} \\ \overrightarrow{A_3} \\ \overrightarrow{B_3}
\end{pmatrix}. \qquad (5.22)
$$

The coefficients on the right-hand side of Eq. (5.22) are the Fourier coefficients obtained from the time history of forces and moment during a period. The unknown variables ($\overrightarrow{T_0}$, $\overrightarrow{T_v}$, $\overrightarrow{T_{\dot{v}}}$, $\overrightarrow{T_{vv}}$, $\overrightarrow{T_{\dot{v}v}}$, $\overrightarrow{T_{vvv}}$, and $\overrightarrow{T_{\dot{v}vv}}$) can be estimated from Eq. (5.22).

In the surge and yaw tests $\overrightarrow{T}$ is the function of u and r, respectively. The unknown variables $\overrightarrow{T_u}$, $\overrightarrow{T_{\dot{u}}}$, $\overrightarrow{T_{uu}}$, $\overrightarrow{T_{\dot{u}u}}$, $\overrightarrow{T_{uuu}}$, $\overrightarrow{T_{\dot{u}uu}}$ or $\overrightarrow{T_r}$, $\overrightarrow{T_{\dot{r}}}$, $\overrightarrow{T_{rr}}$, $\overrightarrow{T_{\dot{r}r}}$, $\overrightarrow{T_{rrr}}$, $\overrightarrow{T_{\dot{r}rr}}$ can be estimated similarly in these cases.

The method used in this thesis is called a Single Run Method (SRM) because the PMM test is run only once for each input parameter $\hat{u}$, $\hat{v}$, or $\hat{r}$. A Multiple Run Method (MRM) means multiple runs of a PMM test over a range of input parameters $\hat{u}$, $\hat{v}$, and $\hat{r}$. To explain the MRM, the first term in the second row of Eq. (5.21) is selected and defined as

$$(\overrightarrow{T_v}\hat{v} + \frac{3}{4}\overrightarrow{T_{vvv}}\hat{v}^3)\cos(\omega t) \quad = \quad c_1(\hat{v})\cos(\omega t), \tag{5.23}$$

where c_1 is assumed to be the amplitude of the first harmonic cosine function from the Fourier series and depends on the amplitude of the transverse velocity $\hat{v}$. After multiple runs for different $\hat{v}$, a polynomial between c_1 and $\hat{v}$ can be established as follows:

$$c_1(\hat{v}) \quad = \quad a_1\hat{v} + b_1\hat{v}^3. \tag{5.24}$$

Substituting $c_1(\hat{v})$ into Eq. (5.23), one obtains

$$\overrightarrow{T_v}\hat{v} + \frac{3}{4}\overrightarrow{T_{vvv}}\hat{v}^3 \quad = \quad a_1\hat{v} + b_1\hat{v}^3. \tag{5.25}$$

By comparing both sides of Eq. (5.25), the unknown coefficients T_v and $\overrightarrow{T_{vvv}}$ will be calculated. Yoon [85] found that the MRM could provide better predictions for nonlinear hydrodynamic derivatives than the SRM. However, it is very time consuming for numerical computation, and perhaps it is more practical for tests performed in a towing tank.

The coupled terms $\overrightarrow{T_{rv}}$, $\overrightarrow{T_{rrv}}$, and $\overrightarrow{T_{rvv}}$ are determined from the combined sway-yaw test. The third-order Taylor-series expansion for the combined vector $\overrightarrow{T}$ is:

$$\begin{aligned}
\overrightarrow{T}(v, r, \dot{v}, \dot{r}) \quad \cong \quad & \overrightarrow{T_0} \\
+ \quad & \overrightarrow{T_r}r + \overrightarrow{T_{\dot{r}}}\dot{r} + \overrightarrow{T_{rr}}r^2 + \overrightarrow{T_{rrr}}r^3 + \overrightarrow{T_{\dot{r}r}}\dot{r}r + \overrightarrow{T_{\dot{r}rr}}\dot{r}rr \\
+ \quad & \overrightarrow{T_v}v + \overrightarrow{T_{\dot{v}}}\dot{v} + \overrightarrow{T_{vv}}v^2 + \overrightarrow{T_{vvv}}v^3 + \overrightarrow{T_{\dot{v}v}}\dot{v}v + \overrightarrow{T_{\dot{v}vv}}\dot{v}vv \\
+ \quad & \overrightarrow{T_{rv}}rv + \overrightarrow{T_{rrv}}rrv + \overrightarrow{T_{vvr}}vvr.
\end{aligned} \tag{5.26}$$

The terms referring to pure sway and pure yaw in Eq. (5.26) are collected and defined as $\overrightarrow{T_k}$ which can be brought to the left-hand side of Eq. (5.26), one obtains

$$\begin{aligned}
\overrightarrow{T} - \overrightarrow{T_k} \quad \cong \quad & \overrightarrow{T_0} + \overrightarrow{T_{rv}}rv + \overrightarrow{T_{rrv}}rrv + \overrightarrow{T_{vvr}}vvr \\
= \quad & \overrightarrow{T_0}
\end{aligned}$$

$$
\begin{aligned}
&+ \quad \frac{1}{2}\overrightarrow{T_{rv}}\hat{r}\hat{v} \\
&+ \quad \frac{3}{4}\overrightarrow{T_{rrv}}\hat{r}\hat{r}\hat{v}\cos(\omega t) + \frac{3}{4}\overrightarrow{T_{vvr}}\hat{v}\hat{v}\hat{r}\cos(\omega t) \\
&+ \quad \frac{1}{2}\overrightarrow{T_{rv}}\hat{r}\hat{v}\cos(2\omega t) \\
&+ \quad \frac{3}{4}\overrightarrow{T_{rrv}}\hat{r}\hat{r}\hat{v}\cos(3\omega t) + \frac{1}{4}\overrightarrow{T_{vvr}}\hat{v}\hat{v}\hat{r}\cos(3\omega t),
\end{aligned} \tag{5.27}
$$

or in matrix notation, such as:

$$
\begin{pmatrix}
1 & \frac{1}{2}\hat{r}\hat{v} & 0 & 0 \\
0 & 0 & \frac{3}{4}\hat{r}\hat{r}\hat{v} & \frac{3}{4}\hat{v}\hat{v}\hat{r} \\
0 & \frac{1}{2}\hat{r}\hat{v} & 0 & 0 \\
0 & 0 & \frac{1}{4}\hat{r}\hat{r}\hat{v} & \frac{1}{4}\hat{v}\hat{v}\hat{r}
\end{pmatrix}
\begin{pmatrix}
\overrightarrow{T_0} \\ \overrightarrow{T_{rv}} \\ \overrightarrow{T_{rrv}} \\ \overrightarrow{T_{vvr}}
\end{pmatrix}
=
\begin{pmatrix}
\overrightarrow{A_0} \\ \overrightarrow{A_1} \\ \overrightarrow{A_2} \\ \overrightarrow{A_3}
\end{pmatrix}, \tag{5.28}
$$

where A_n are the Fourier coefficients of $\overrightarrow{T} - \overrightarrow{T_k}$. The system shown in Eq. (5.28) is an under-estimated system for determining $\overrightarrow{T_{rrv}}$ and $\overrightarrow{T_{vvr}}$. In order to close the system, a second amplitude has to be introduced for the velocities of sway and yaw (Abdel-Maksoud [9]), as illustrated in the following equations:

$$
\begin{pmatrix}
1 & \frac{1}{2}\hat{r}_{(1)}\hat{v}_{(1)} & 0 & 0 \\
0 & \frac{1}{2}\hat{r}_{(1)}\hat{v}_{(1)} & 0 & 0 \\
0 & 0 & \frac{1}{4}\hat{r}_{(1)}\hat{r}_{(1)}\hat{v}_{(1)} & \frac{1}{4}\hat{v}_{(1)}\hat{v}_{(1)}\hat{r}_{(1)} \\
0 & 0 & \frac{1}{4}\hat{r}_{(2)}\hat{r}_{(2)}\hat{v}_{(2)} & \frac{1}{4}\hat{v}_{(2)}\hat{v}_{(2)}\hat{r}_{(2)}
\end{pmatrix}
\begin{pmatrix}
\overrightarrow{T_0} \\ \overrightarrow{T_{rv}} \\ \overrightarrow{T_{rrv}} \\ \overrightarrow{T_{vvr}}
\end{pmatrix}
=
\begin{pmatrix}
\overrightarrow{A_{0(1)}} \\ \overrightarrow{A_{1(1)}} \\ \overrightarrow{A_{3(1)}} \\ \overrightarrow{A_{3(2)}}
\end{pmatrix}. \tag{5.29}
$$

The surge-coupled hydrodynamic derivatives such as $\overrightarrow{T_{vu}}, \overrightarrow{T_{vur}}, \overrightarrow{T_{vvu}}, \overrightarrow{T_{ru}}, \overrightarrow{T_{ruu}}, \overrightarrow{T_{rru}}$, $\overrightarrow{T_{\dot{v}u}}$, $\overrightarrow{T_{\dot{v}r}}$, $\overrightarrow{T_{\dot{v}vu}}$, and $\overrightarrow{T_{\dot{r}ru}}$ are determined by repeating the tests (surge, sway, yaw, coupled sway and yaw) several times at different ship speeds U. The number of repetitions depends on the order of u in the specific hydrodynamic derivatives. For example, $\overrightarrow{T_{vuu}}$ is the second derivation of $\overrightarrow{T_v}$ to u; the number of repetitions is then three in order to obtain a second-order polynomial.

The solution of complete hydrodynamic derivatives is given in Tab. (5.5), where the Fourier coefficients $\overrightarrow{A_n}$ and $\overrightarrow{B_n}$ are different according to the different dynamic tests.

Table 5.5: Determination of hydrodynamic derivatives in relation to Fourier coefficients using the single-run method.

	Surge	Sway	Yaw		Sway + Yaw
$\overrightarrow{T_0}$	$\overrightarrow{A_0} - \overrightarrow{A_2}$	$\overrightarrow{A_0} - \overrightarrow{A_2}$	$\overrightarrow{A_0} - \overrightarrow{A_2}$	$\overrightarrow{T_0}$	$\overrightarrow{A_{0(1)}} - \overrightarrow{A_{2(1)}}$
$\overrightarrow{T_{u/v/r}}$	$\frac{\overrightarrow{A_1} - 3\overrightarrow{A_3}}{\hat{u}}$	$\frac{\overrightarrow{A_1} - 3\overrightarrow{A_3}}{\hat{v}}$	$\frac{\overrightarrow{A_1} - 3\overrightarrow{A_3}}{\hat{r}}$	$\overrightarrow{T_{rv}}$	$\frac{2\overrightarrow{A_{2(1)}}}{\hat{r}_{(1)}\hat{v}_{(1)}}$
$\overrightarrow{T_{uu/vv/rr}}$	$\frac{2\overrightarrow{A_2}}{\hat{u}^2}$	$\frac{2\overrightarrow{A_2}}{\hat{v}^2}$	$\frac{2\overrightarrow{A_2}}{\hat{r}^2}$	$\overrightarrow{T_{vvr}}$	$\frac{4\overrightarrow{A_{3(1)}}\hat{r}_{(2)}\hat{r}_{(2)}\hat{v}_{(2)} - 4\overrightarrow{A_{3(2)}}\hat{r}_{(1)}\hat{r}_{(1)}\hat{v}_{(1)}}{\hat{v}_{(1)}\hat{v}_{(1)}\hat{r}_{(1)}\hat{r}_{(2)}\hat{r}_{(2)}\hat{v}_{(2)} - \hat{v}_{(2)}\hat{v}_{(2)}\hat{r}_{(2)}\hat{r}_{(1)}\hat{r}_{(1)}\hat{v}_{(1)}}$
$\overrightarrow{T_{uuu/vvv/rrr}}$	$\frac{4\overrightarrow{A_3}}{\hat{u}^3}$	$\frac{4\overrightarrow{A_3}}{\hat{v}^3}$	$\frac{4\overrightarrow{A_3}}{\hat{r}^3}$	$\overrightarrow{T_{rrv}}$	$\frac{4\overrightarrow{A_{3(1)}}\hat{v}_{(2)}\hat{v}_{(2)}\hat{r}_{(2)} - 4\overrightarrow{A_{3(2)}}\hat{v}_{(1)}\hat{v}_{(1)}\hat{r}_{(1)}}{\hat{r}_{(1)}\hat{r}_{(1)}\hat{v}_{(1)}\hat{v}_{(2)}\hat{v}_{(2)}\hat{r}_{(2)} - \hat{r}_{(2)}\hat{r}_{(2)}\hat{v}_{(2)}\hat{v}_{(1)}\hat{v}_{(1)}\hat{r}_{(1)}}$
$\overrightarrow{T_{\dot{u}/\dot{v}/\dot{r}}}$	$-\frac{\overrightarrow{B_1} - \overrightarrow{B_3}}{\omega\hat{u}}$	$-\frac{\overrightarrow{B_1} - \overrightarrow{B_3}}{\omega\hat{v}}$	$-\frac{\overrightarrow{B_1} - \overrightarrow{B_3}}{\omega\hat{r}}$		
$\overrightarrow{T_{\dot{u}u/\dot{v}v/\dot{r}r}}$	$-\frac{2\overrightarrow{B_2}}{\hat{u}^2\omega}$	$-\frac{2\overrightarrow{B_2}}{\hat{v}^2\omega}$	$-\frac{2\overrightarrow{B_2}}{\hat{r}^2\omega}$		
$\overrightarrow{T_{\dot{u}uu/\dot{v}vv/\dot{r}rr}}$	$-\frac{4\overrightarrow{B_3}}{\hat{u}^3\omega}$	$-\frac{4\overrightarrow{B_3}}{\hat{v}^3\omega}$	$-\frac{4\overrightarrow{B_3}}{\hat{r}^3\omega}$		
Number of Simulations	1	1	1		2

5.6 Example of Ship Turning in a Circle Based on Hydrodynamic Derivatives

Wolff [30] examined five model ships: a tanker, a Serie 60 bulker, a mariner, a container vessel, and a ferry. Their hydrodynamic derivatives are available for validation in comparison to the freely maneuvering model. The bulker was chosen here for demonstration purposes.

The Taylor-series expansions for the forces and moment using the hydrodynamic derivatives given by Wolff are expressed as

$$X = X_{\dot{u}}\dot{u} + X_{\dot{u}uu}\dot{u}uu + X(\mathrm{d}) \tag{5.30a}$$
$$Y = Y_{\dot{v}}\dot{v} + Y_{\dot{v}vv}\dot{v}vv + Y_{\dot{r}}\dot{r} + Y_{\dot{r}rr}\dot{r}rr + Y(\mathrm{d}) \tag{5.30b}$$
$$N = N_{\dot{v}}\dot{v} + N_{\dot{v}vv}\dot{v}vv + N_{\dot{r}}\dot{r} + N_{\dot{r}rr}\dot{r}rr + N(\mathrm{d}), \tag{5.30c}$$

where $X(d)$, $Y(d)$, and $N(d)$ stand for the damping-related terms without accelerations. By substituting Eq. (5.3) into Eq. (5.30), one obtains:

$$m\dot{u} - X_{\dot{u}}\dot{u} - X_{\dot{u}uu}\dot{u}uu = mvr + mr^2x_G + X(\mathrm{d}) \tag{5.31a}$$
$$m\dot{v} - Y_{\dot{v}}\dot{v} - Y_{\dot{v}vv}\dot{v}vv - Y_{\dot{r}}\dot{r} - Y_{\dot{r}rr}\dot{r}rr + m\dot{r}x_G = -mur + Y(\mathrm{d}) \tag{5.31b}$$
$$-N_{\dot{v}}\dot{v} - N_{\dot{v}vv}\dot{v}vv + m\dot{v}x_G + I_{zz}\dot{r} - N_{\dot{r}}\dot{r} - N_{\dot{r}rr}\dot{r}rr = -murx_G + N(\mathrm{d}). \tag{5.31c}$$

The matrix notation of Eq. (5.31) is

$$\begin{pmatrix} m - X_{\dot{u}} - X_{\dot{u}uu}uu & 0 & 0 \\ 0 & m - Y_{\dot{v}} - Y_{\dot{v}vv}vv & -Y_{\dot{r}} - Y_{\dot{r}rr}rr + mx_G \\ 0 & -N_{\dot{v}} - N_{\dot{v}vv}vv + mx_G & I_{zz} - N_{\dot{r}} - N_{\dot{r}rr}rr \end{pmatrix} \begin{pmatrix} \dot{u} \\ \dot{v} \\ \dot{r} \end{pmatrix} = \begin{pmatrix} mvr + mr^2x_G + X(\mathrm{d}) \\ -mur + Y(\mathrm{d}) \\ -murx_G + N(\mathrm{d}) \end{pmatrix}. \tag{5.32}$$

The solution of u, v, and r is based on the Euler integration method. The information of the subsequent time is taken from the previous time. The initial values are set to zero,

except for u due to the non-zero velocity U_0 before the ship maneuver. The expressions of the velocities can be written as

$$u_{[i+1]} = u_{[i]} + \Delta u_{[i]} + U_0 \tag{5.33a}$$
$$v_{[i+1]} = v_{[i]} + \Delta v_{[i]} \tag{5.33b}$$
$$r_{[i+1]} = r_{[i]} + \Delta r_{[i]} \tag{5.33c}$$

with

$$\Delta u_{[i]} = \dot{u}_{[i]}\Delta t \tag{5.34a}$$
$$\Delta v_{[i]} = \dot{v}_{[i]}\Delta t \tag{5.34b}$$
$$\Delta r_{[i]} = \dot{r}_{[i]}\Delta t, \tag{5.34c}$$

respectively, Δt stands for the time step. $\dot{u}$, $\dot{v}$, and $\dot{r}$ are obtained from matrix (5.32).

The velocity in the earth-fixed coordinate system at the ith time step is obtained according to Fig. (5.2). The velocities u, v, and r are the velocities in the ship-fixed axis, that is

$$u_{0[i]} = u_{[i]}\cos(\psi_{[i]}) - v_{[i]}\sin(\psi_{[i]}) \tag{5.35a}$$
$$v_{0[i]} = u_{[i]}\sin(\psi_{[i]}) + v_{[i]}\cos(\psi_{[i]}). \tag{5.35b}$$

The trajectory of the ship can be obtained by the numerical integration of Eq. (5.35) over time, that is:

$$x_{0[i+1]} = x_{0[i]} + \Delta t(u_{[i]}\cos(\psi_{[i]}) - v_{[i]}\sin(\psi_{[i]})) \tag{5.36a}$$
$$y_{0[i+1]} = y_{0[i]} + \Delta t(u_{[i]}\sin(\psi_{[i]}) + v_{[i]}\cos(\psi_{[i]})), \tag{5.36b}$$

where $\psi_{[i]}$ is the heading angle of the ship at the ith time step and is assumed to be

$$\psi_{[i+1]} = \psi_{[i]} + \frac{1}{2}(r_{[i]} + r_{[i+1]})\Delta t. \tag{5.37}$$

As shown in Fig. (5.4), the result based on the coefficients (solid curve) is in full agreement with the freely maneuvering model indicated by the red symbol "x".

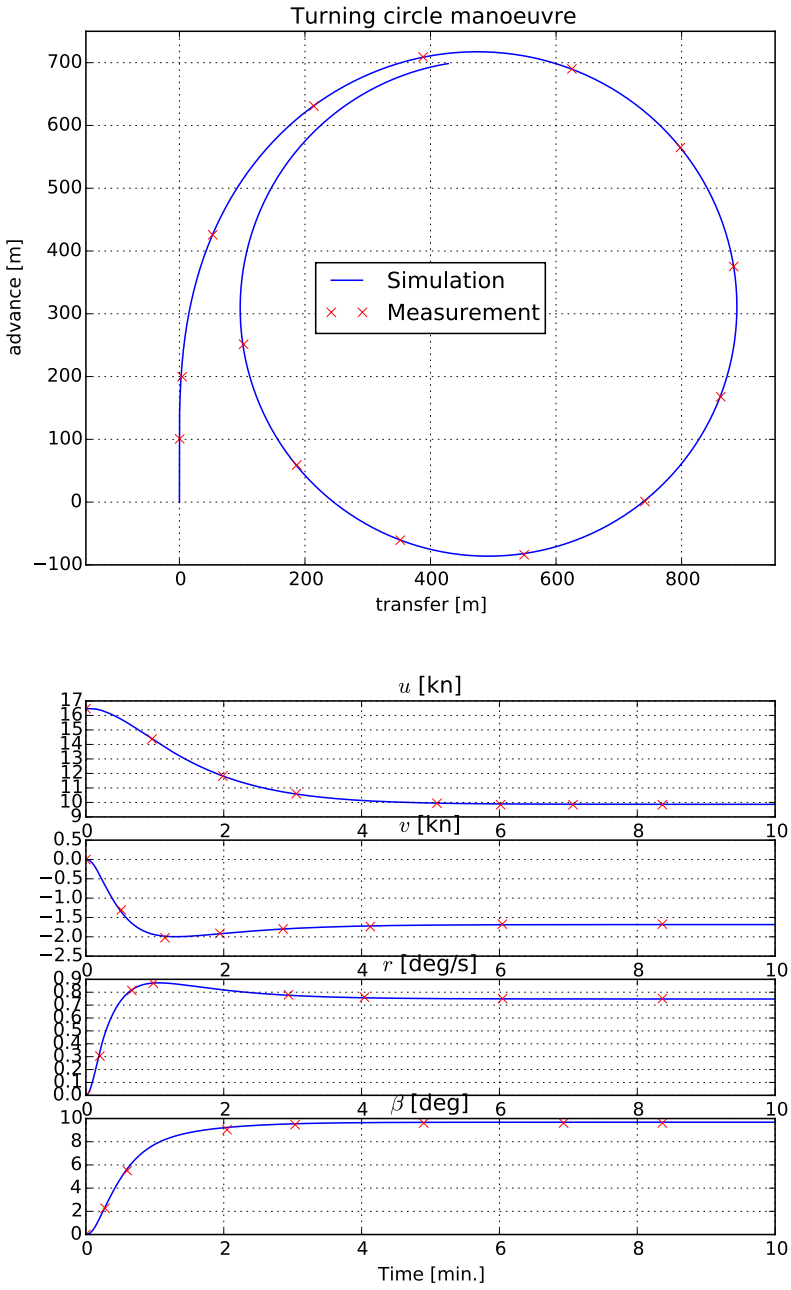

Figure 5.4: Simulation of a turning maneuver with rudder angle $\delta = -35°$ for the Series 60 bulker. Top: trajectory of the ship. Bottom: time history of the turning maneuvering parameters.

6 Numerical Captive Maneuvering Tests

6.1 Introduction

In Section (4.4), the interaction between the slipstream of the tunnel thruster and the hull primarily affects the total transverse force exerted on the ship. Static simulations, while useful, often have difficulty accurately capturing dynamic flow behavior.

In this chapter, numerical captive maneuvering tests are presented to evaluate significant differences in hydrodynamic derivatives between simulations with and without a tunnel propeller. Through comparative analysis, relevant derivatives are identified for the development of a maneuvering model.

The expansions X, Y, and N can be decomposed into components that include the bare hull, the azimuth thruster, and the bow thruster. To formulate the mathematical model that characterizes the interaction between the bow thruster and the hull, it is essential to perform simulations of the ship under two conditions: with and without the tunnel propeller, as shown in Fig. (6.1). The two sets of numerical captive model tests were performed independently to determine the additional effect of the interaction.

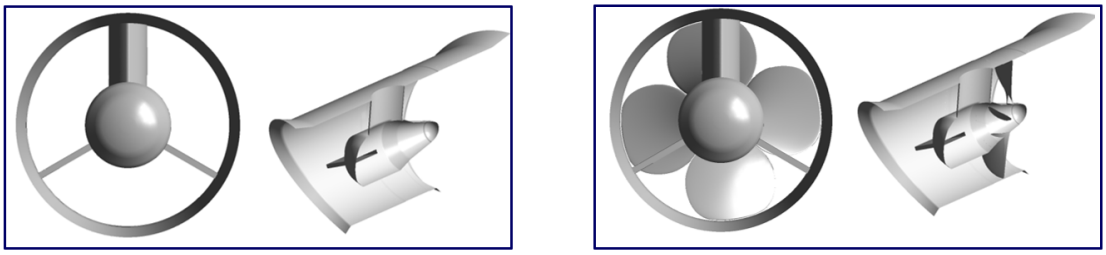

Figure 6.1: Numerical captive tests without (left) and with propeller (right) inside the tunnel.

6.2 Numerical Settings

6.2.1 Initial and boundary conditions

For the determination of the coupling terms for u, such as $\overrightarrow{T_{vuu}}$, the flow simulations must be carried out at three ship speeds. The time step for the rotating propeller of the thruster is selected as a function of the propeller rotation rate n. At each time step, the propeller rotates 10°.
In the simulation of the case without a rotating propeller, the time step is modified to maintain the Courant number within the computations for the three ship speeds.

The phenomenon of the memory effect must be considered by choosing ω', as oscillatory motion can produce a force oscillating at a frequency different from its own, as studied by Chislett and Strøm-Tejsen [29]. When the ship navigates through the wake created by its own motion, the predicted maneuvering derivatives will no longer be reliable. Vantorre and Eloot [86] show that as ω' increases, the error in the acceleration-related derivatives decreases, while the error in the velocity-related derivatives increases. The minimum and maximum values of ω' recommended by ITTC (7.5-02-06-02) [87] are $\omega' = 0.25$ and $\omega' = 4$, respectively. A typical value is 2 to 4 in the yaw test and 0.25 to 2 in the sway test to possibly avoid memory effects.

Tab. (6.1) shows the selected motion parameters based on ITTC (7.5-03-04-01) [88].

To minimize the reflection effect of the boundaries, it is advisable to define the size of the entire domain as large as possible. ITTC (7.5-03-04-01) [88] has suggested that the size of the numerical domain should be 3-5 times the length of the vessel in the longitudinal direction, 2-3 times the length in the transverse direction, and as same as the length in the vertical direction. The domain imposed in this case is much larger than the recommendations, as shown in Fig. (6.2).

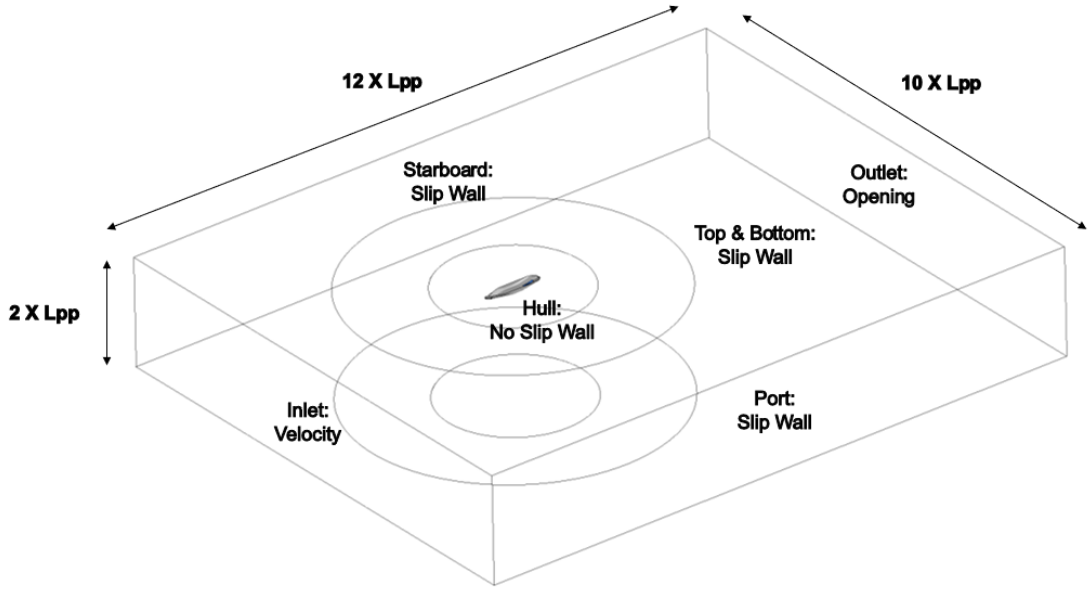

Figure 6.2: Boundary conditions of the computational domain.

The side and bottom boundaries can be treated as slip walls when considering boundary conditions. The ship speed is represented by setting a constant inflow velocity at the entrance boundary. The modeling of the free surface is neglected due to the reduced effect of wave excitation during moderate ship motion.

There is a phase shift between the parameters y_0 and ψ for pure yaw and combined yaw-sway motions. This can be seen in Tab. (5.3) as well as Figs. (6.7) through (6.8).

The initial position of the ship is adjusted to zero y_0 or to zero ψ. A well-converged steady solution has to be available to be able to start the dynamic motion simulations.

Table 6.1: Motion parameters in PMM tests.

Dynamic Motions	Speed [m/s]	$\hat{u}$ [m/s]	$\hat{v}$ [m/s]	$\hat{r}$ [deg./s]	$\hat{x}$ [m]	$\hat{y}$ [m]	$\hat{\psi}$ [deg.]
Surge ($u' = 0.1$)	2	0.20	0	0	3.72	0	0
	3	0.30	0	0	3.72	0	0
	4	0.40	0	0	3.72	0	0
Sway ($v' = 0.35$)	2	0	0.70	0	0	13.02	0
	3	0	1.05	0	0	13.02	0
	4	0	1.40	0	0	13.02	0
Yaw ($r' = 0.3$)	2	0	0	0.46	0	5.61	8.6
	3	0	0	0.69	0	5.61	8.6
	4	0	0	0.92	0	5.61	8.6
Coupled 1	2	0	-0.70	0.46	0	14.22	8.6
($v' = -0.35$)	3	0	-1.05	0.69	0	14.22	8.6
($r' = 0.3$)	4	0	-1.40	0.92	0	14.22	8.6
Coupled 2	2	0	-0.40	0.46	0	9.34	8.6
($v' = -0.2$)	3	0	-0.60	0.69	0	9.34	8.6
($r' = 0.3$)	4	0	-0.60	0.69	0	9.34	8.6

6.2.2 Moving mesh

The motion of the vessel must follow the displacements calculated in Tab. (5.3) for pure translation (surge, sway) and combined rotation and translation (yaw, coupled sway-yaw). Furthermore, the motion of the propeller mesh around its axis inside the tunnel must be further specified.

The computation domain for the volume mesh is divided into three parts: the first part contains the propeller domain, the second part contains the tunnel domain, and the third domain extends from the hull to the outer limits. The primary implementation of mesh deformation is carried out in the third part, which can be further divided into three distinct subdomains, as shown in Fig. (6.3). This procedure allows the deformations to be carried out independently within each subdomain. During a pure yaw test, subdomain I experiences a rotation that requires the absence of mesh deformation to preserve mesh quality. However, subdomain II and subdomain III allow for most of the deformation caused by rotation and translation, respectively.

The settings apply to the cell stiffness (see Eq. (3.5) in Section (3.3)), which affects its ability to deform and is inversely proportional to its size. Therefore, the mesh sizes in the subdomains are organized in increasing order from I to III. This gradation ensures that the domains farther away from the hull have more space and a greater capacity for distortion than those closer to the hull.

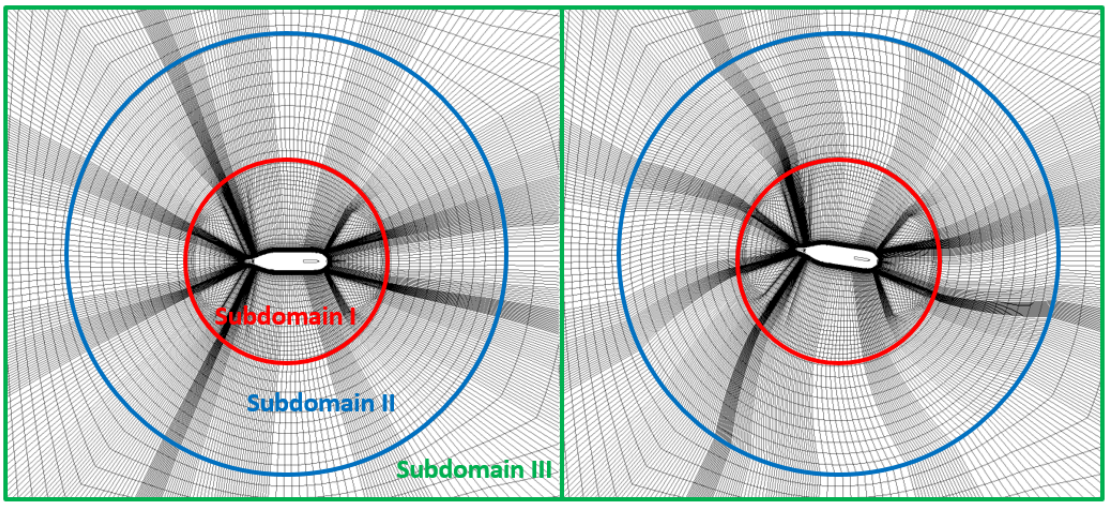

Figure 6.3: Mesh deformation during a yaw motion.

6.3 Numerical Results

6.3.1 Evaluation

In the simulation, the solver uses the origin of the earth coordinate system (x_0, y_0, z_0 as shown in Fig. (5.3)) as the default point to evaluate forces and moments. However, because of the dynamic oscillation of a ship, its center of gravity varies over time. Therefore, it is necessary to transform the moments from the solver's default origin to a fixed origin on the ship. The calculation of the moment with respect to the origin of the ship-fixed system can be achieved as follows:

- Surge: $N = N_0$ - $Y_0 \cdot \hat{x} \cdot \sin(\omega t)$
- Sway: $N = N_0 + X_0 \cdot \hat{y} \cdot \sin(\omega t)$
- Yaw: $N = N_0 + (X_0 \cdot \cos(\psi) + Y_0 \cdot \sin(\psi)) \cdot \hat{y} \cdot \sin(\omega t)$,

where the subscript 0 represents the value with respect to the solver default origin. In addition, there is no correction for the in-plane forces in the case of surge and sway motion, while in the case of yaw motion, a transformation of the in-plane forces due to the existence of the angle ψ should also be considered.

6.3.2 Captive model tests for a ship without an tunnel propeller

The calculation of the hydrodynamic derivatives requires only the data obtained during the last period of the ship's motion. To obtain a convergent solution, it is necessary to run the simulations for many periods. The duration of the calculation depends on the evolution of forces and moments. Fig. (6.4) shows the last three periods, indicating that the simulation has reached a state of strong convergence.

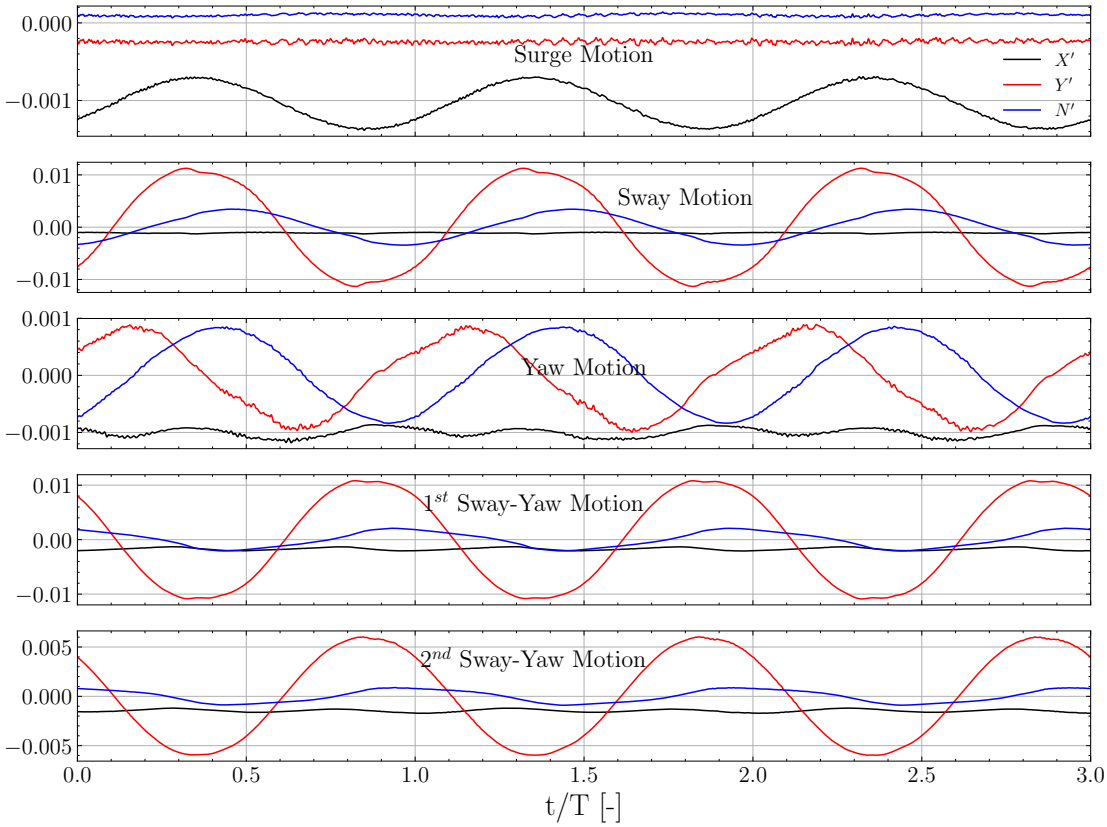

Figure 6.4: Time history of forces and moment for the five dynamic tests during last three periods at $F_n = 0.074$.

The last period at three different ship speeds can be observed in Fig. (6.5a). Significant variations in Y and N are observed during the surge test. The most likely cause is the asymmetry of the tunnel housing geometry. The amplitude of these variations increases as the ship's speed increases. However, the range of changes is limited. To facilitate comparison, Fig. (6.5b) shows the results in a nondimensional way. Clearly, the main focus of the analysis must be on the discrepancy in the longitudinal force.

Considering the ship as a slender body, the oblique flow causes an increase in drag during the oscillatory motion. The difference can be seen in the results derived from the five dynamic motions. In Fig. (6.6a), the mean value of X', denoted X'_0, can be considered as the longitudinal resistance of the ship. The difference in X'_0 is more evident in the combined sway-yaw motions than in the pure dynamic motions. In addition, resistance increases further as a result of the increased sway amplitude set in the first combined motion (see Tab. (6.1)).

The variation of longitudinal forces at different ship speeds is shown in Fig. (6.6b) for each dynamic test. In general, the value of X'_0 tends to decrease as F_n increases. The maximum decrease of X'_0 is about 6%, seen in the yaw test. The decrease in X'_0 can be attributed to the decreasing effect of the viscous force as F_n increases.

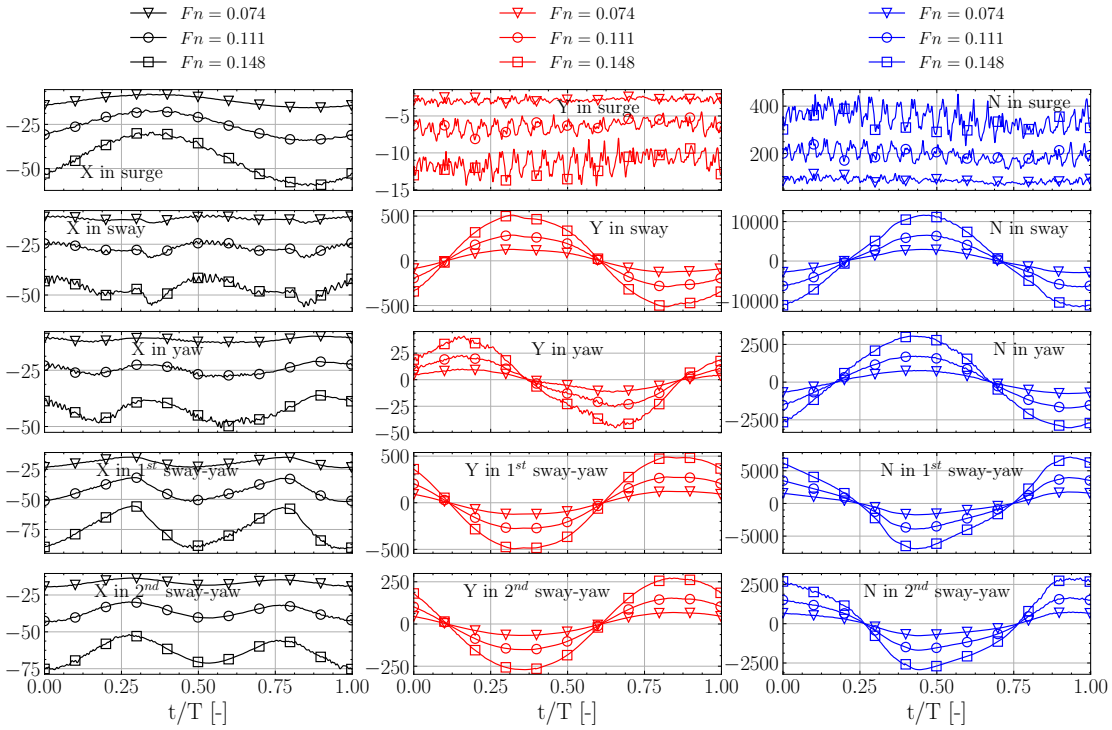

(a) X [N], Y [N], and N [Nm].

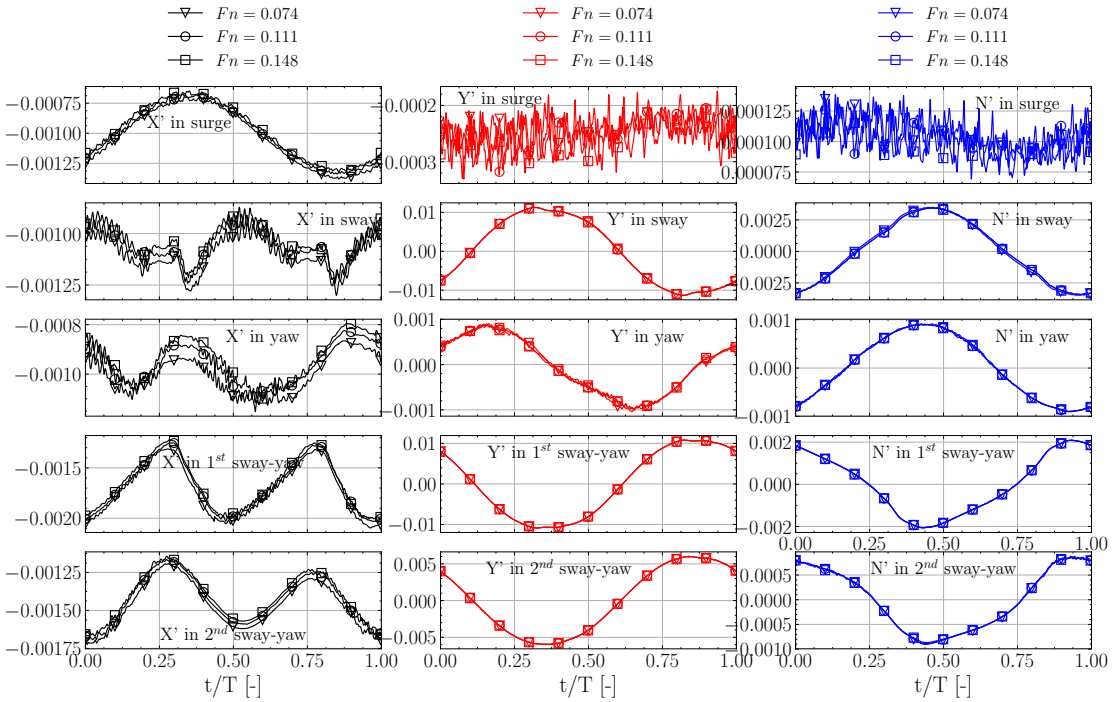

(b) X', Y', and N'.

Figure 6.5: Comparison of forces and moment for the three speeds without propeller during one period of surge, sway, yaw, first and second combined sway-yaw test.

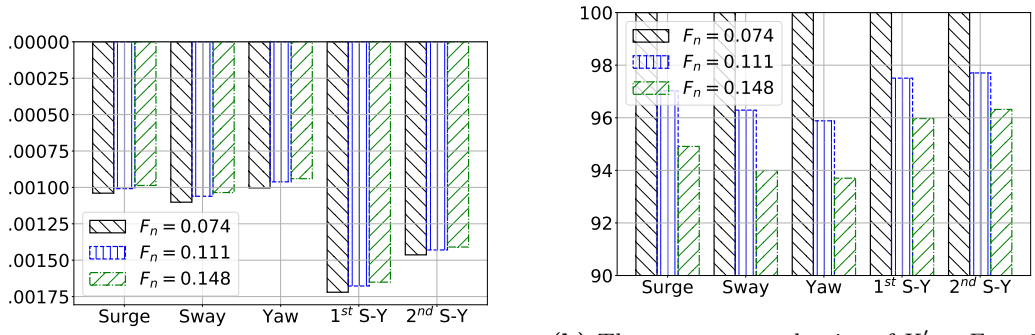

(a) X'_0.

(b) The percentage reduction of X'_0 at $F_n = 0.148$ compared to the value at $F_n = 0.074$.

Figure 6.6: The mean values of longitudinal force X' with varying F_n in the dynamic tests.

Apart from the discrepancies in the surge test, the observations of the remaining curves in the other tests are not remarkable. Therefore, two main points can be drawn from these results:

1. Cross-coupled terms with u such as $\overrightarrow{T_{vu}}, \overrightarrow{T_{vru}}, \overrightarrow{T_{vvu}}, \overrightarrow{T_{ru}}, \overrightarrow{T_{ruu}}$, and $\overrightarrow{T_{rru}}$ can be ignored.

2. The curves in the non-dimensionalized illustration show minimal variation within each dynamic test. For a more thorough analysis, a detailed study of the hydrodynamic derivatives identification is performed, focusing on the ship's speed at 2 kn ($F_n = 0.074$).

The evolution of the forces acting on the hull correlates with the forced motion of the ship. If the ship is periodically oscillating, the forces acting on it will also exhibit periodic oscillations. The left side of Fig. (6.7) shows the predefined hull motion, while the right side shows the hull response. The dashed regression curves are obtained by applying the Fourier series up to the third order using Eq. (5.21).

In the yaw oscillation, the phase shift between the yaw angle and the sway, as determined by Eq. (5.13), is 90°. The time history of the yaw angle remains the same in both combined sway-yaw tests because of the same value of $\hat{r}$, as shown in Tab. (6.1). Thus, the difference is recognized only in the transverse displacement, as determined by Eq. (5.18) and shown in Fig. (6.8).

The ship contains an asymmetric gearbox inside the tunnel, which can result in non-zero values for Y_0 and N_0.

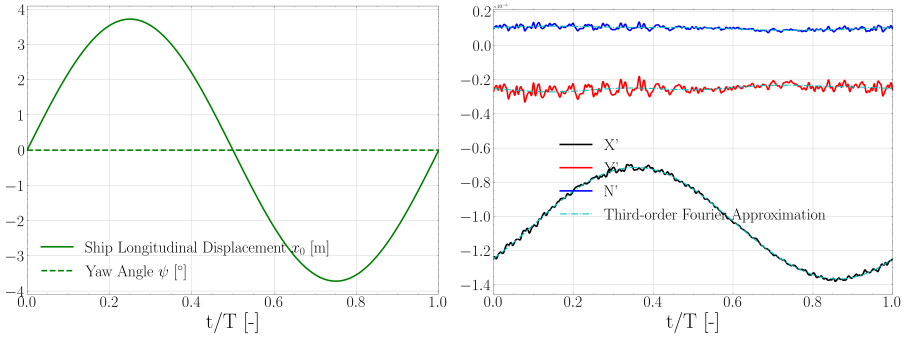

(a) Surge

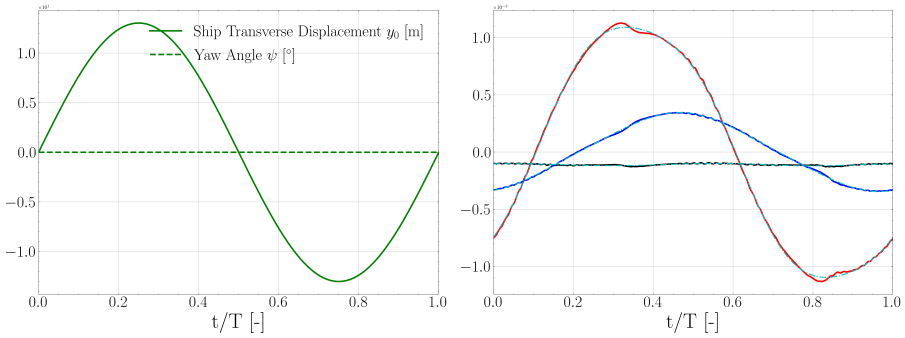

(b) Sway

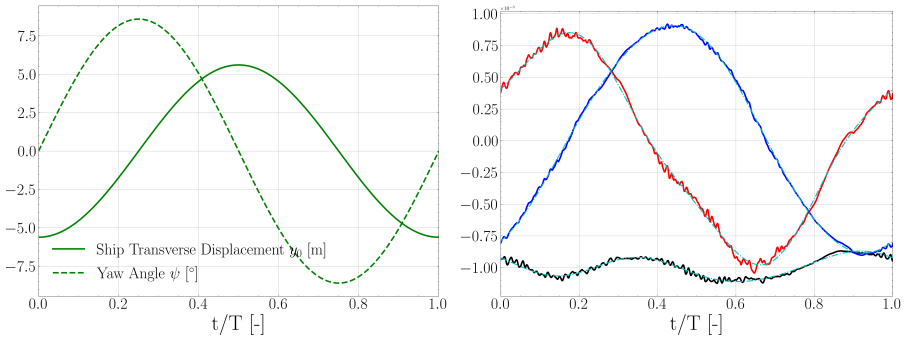

(c) Yaw

Figure 6.7: Time history of the nondimensional forces and moment during last period of dynamic tests (w/o propeller) at $F_n = 0.074$.

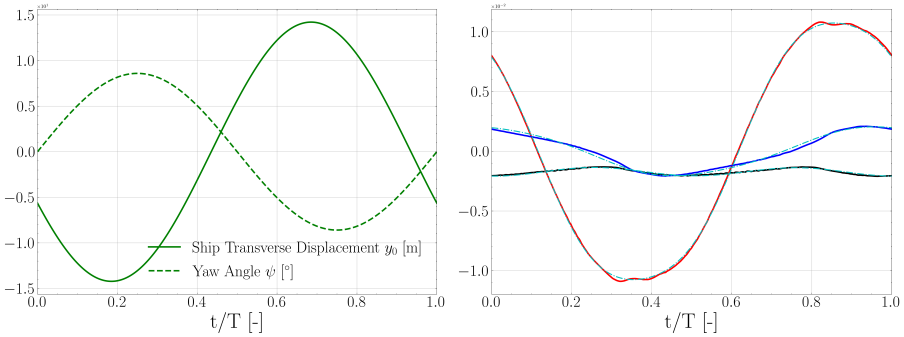

(a) First sway-yaw test

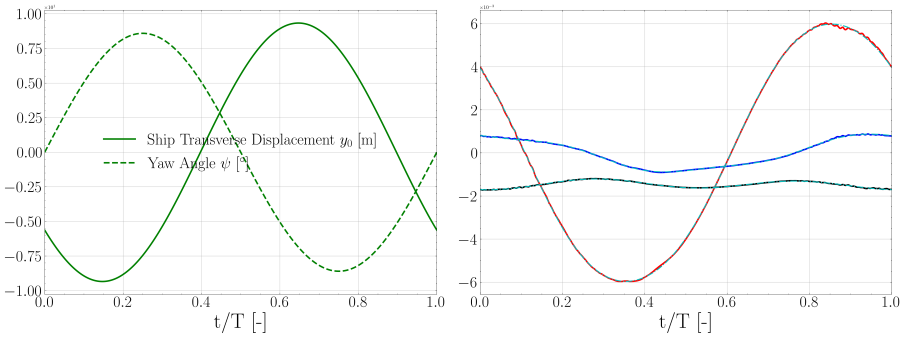

(b) Second sway-yaw test

Figure 6.8: Time history of the nondimensional forces and moment during last period of sway-yaw test (without propeller) at $F_n = 0.074$.

Since the hydrodynamic derivatives in Eq. (5.27) are associated with the $\overrightarrow{T}$-$\overrightarrow{T_k}$ curves, the Fourier coefficients cannot be obtained from the sway-yaw curves (Fig. (6.8)); instead, they must be derived from Fig. (6.9).

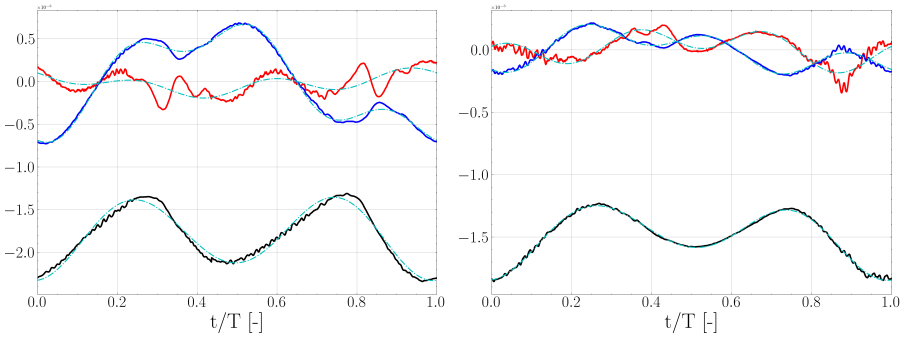

Figure 6.9: Time history of differences of forces and moment for the first combined sway-yaw test (left) and the second one (right) during last period of sway-yaw test (w/o propeller) at $F_n = 0.074$.

The hydrodynamic derivatives are calculated using the approach described in Section (5.5.2) and presented in Tab. (6.2) for the ship's speed at $F_n = 0.074$.

Table 6.2: Hydrodynamic derivatives $\times 10^5$ for the ship without the propeller at $F_n = 0.074$.

X_0	-137.175	Y_0	-4.162	N_0	0.45
X_u	-197.804	Y_u	-17.605	N_u	5.052
X_{uu}	-84.989	Y_{uu}	-97.501	N_{uu}	53.295
X_{uuu}	-519.082	Y_{uuu}	2087.980	N_{uuu}	-455.318
$X_{\dot{u}}$	-127.948	$Y_{\dot{u}}$	6.584	$N_{\dot{u}}$	-5.085
$X_{\dot{u}u}$	-14.186	$Y_{\dot{u}u}$	54.864	$N_{\dot{u}u}$	-17.803
$X_{\dot{u}uu}$	-344.769	$Y_{\dot{u}uu}$	25.859	$N_{\dot{u}uu}$	-3.596
X_v	-6.585	Y_v	-1578.367	N_v	-845.845
X_{vv}	124.150	Y_{vv}	-15.289	N_{vv}	-0.055
X_{vvv}	43.355	Y_{vvv}	-4401.338	N_{vvv}	-924.524
$X_{\dot{v}}$	-0.324	$Y_{\dot{v}}$	-1378.843	$N_{\dot{v}}$	-126.357
$X_{\dot{v}v}$	-43.943	$Y_{\dot{v}v}$	-7.762	$N_{\dot{v}v}$	-0.677
$X_{\dot{v}vv}$	26.093	$Y_{\dot{v}vv}$	2273.011	$N_{\dot{v}vv}$	-256.437
X_r	-0.712	Y_r	244.689	N_r	-256.791
X_{rr}	15.592	Y_{rr}	-24.812	N_{rr}	20.249
X_{rrr}	244.095	Y_{rrr}	-1029.989	N_{rrr}	-170.673
$X_{\dot{r}}$	-2.407	$Y_{\dot{r}}$	-119.206	$N_{\dot{r}}$	-67.764
$X_{\dot{r}r}$	93.476	$Y_{\dot{r}r}$	40.242	$N_{\dot{r}r}$	-18.935
$X_{\dot{r}rr}$	46.650	$Y_{\dot{r}rr}$	324.497	$N_{\dot{r}rr}$	50.973
X_{rv}	811.918	Y_rv	-42.946	N_{rv}	13.959
X_{rrv}	363.425	Y_{rrv}	-4512.177	N_{rrv}	301.680
X_{vvr}	86.761	Y_{vvr}	-3739.200	N_{vvr}	-1269.099

6.3.3 Captive model tests for a ship with a working tunnel propeller

The forced motion of the vessel remains unaffected by the operation of the tunnel propeller and is determined based on the approach outlined in Tab. (5.3). The blade frequency is clearly visible in the time history of ship response. However, the blade frequency-related local fluctuation cannot be accurately represented by the regression curves obtained from the third-order Fourier series. The dashed curves provide an approximate representation of the time histories of X', Y', and N' as shown in Figs. (6.10) through (6.12).

During the surge test, the variables Y' and N' are correlated with the surge motion. The dashed lines on Y' and N' indicate that the related hydrodynamic derivatives cannot be ignored compared to the case of the bare hull. In the sway test, the force evolution is comparable to the situation without a tunnel propeller, with only minor variations in specific areas within the t/T interval of 0.3 to 0.4. However, in the yaw test, the simulation results in the two situations (with and without propeller) yield significantly different Y' forces. This indicates that their Hydrodynamic derivatives must be significantly different. A detailed discussion of the evolution of the transverse forces during the sway and yaw tests is provided in Appendix (F).

Tab. (6.3) shows the determined coefficients for the situation with a working tunnel thruster propeller. It should be noted that the mean values of Y and N (Y_0 and N_0) are significantly higher than the corresponding values of the bare hull due to the effect of the operating thruster propeller. The interaction between the slipstream and the hull is characterized by the difference in the hydrodynamic derivatives listed in the tables.

A detailed comparison of the curves between the ship with and without the propeller is discussed in Section (6.4).

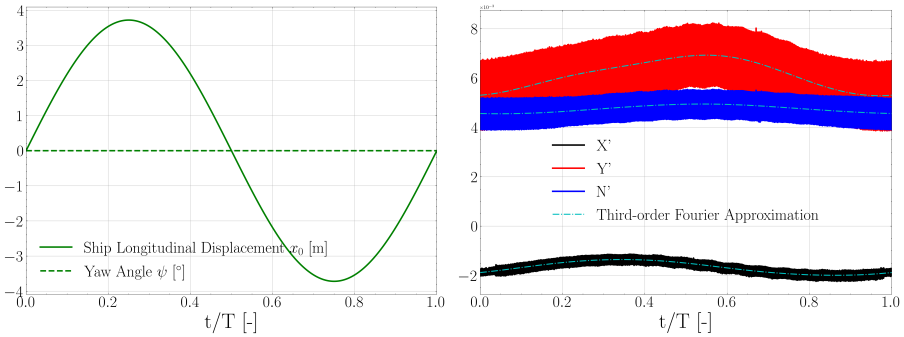

(a) Surge

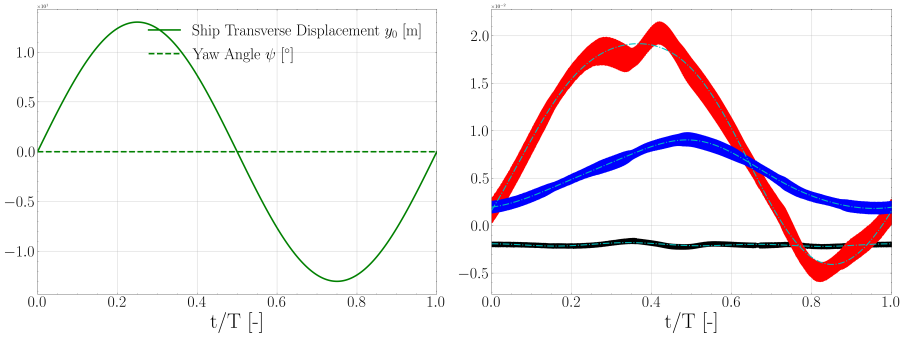

(b) Sway

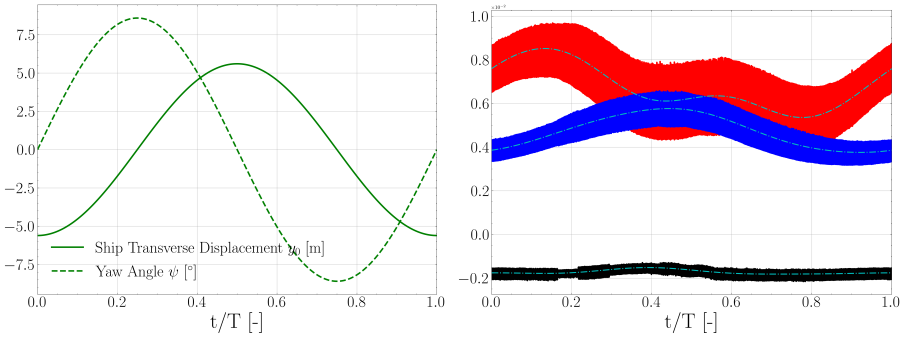

(c) Yaw

Figure 6.10: Time history of the nondimensional forces and moment during last period of dynamic tests (w/ tunnel propeller).

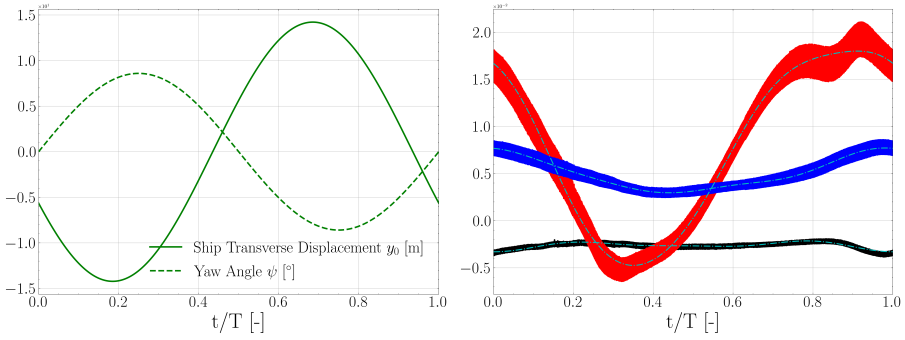

(a) First sway-yaw test

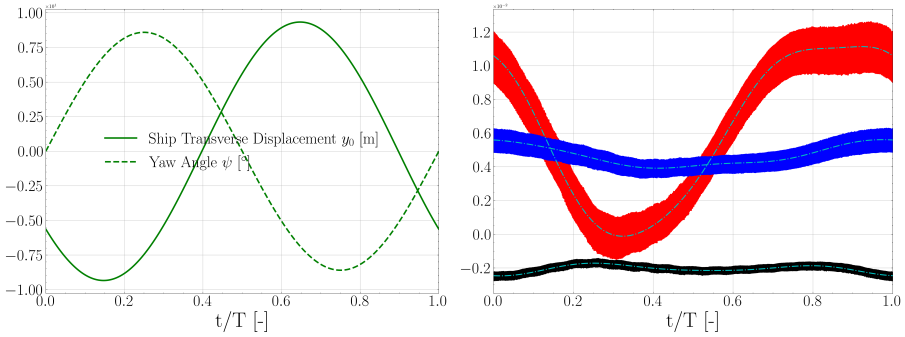

(b) Second sway-yaw test

Figure 6.11: Time history of the nondimensional forces and moment during last period of sway-yaw test (w/ tunnel propeller).

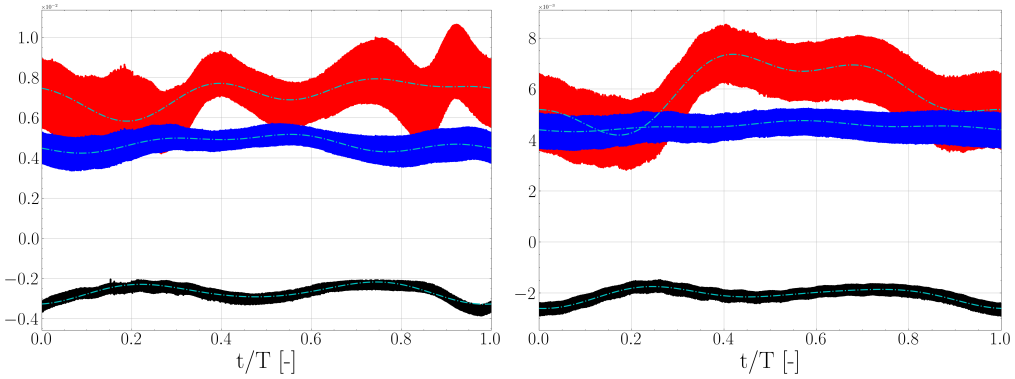

Figure 6.12: Time history of differences of forces and moment for the first combined sway-yaw test (left) and the second one (right) during last period of sway-yaw test (w/ tunnel propeller).

Table 6.3: Hydrodynamic derivatives $\times 10^5$ for a working propeller at $F_n = 0.074$. Each X_0, Y_0 and N_0 has five values in five dynamic tests, and the values shown here are taken from the first sway-yaw test, because its motion is probably closest to the real maneuvering test.

X_0	-224.408	Y_0	707.975	N_0	461.544
X_u	-170.377	Y_u	-749.303	N_u	-186.994
X_{uu}	-198.091	Y_{uu}	-902.017	N_{uu}	45.566
X_{uuu}	-1979.192	Y_{uuu}	-3904.446	N_{uuu}	-171.976
$X_{\dot{u}}$	-130.290	$Y_{\dot{u}}$	-8.454	$N_{\dot{u}}$	23.424
$X_{\dot{u}u}$	34.34	$Y_{\dot{u}u}$	-1197.090	$N_{\dot{u}u}$	19.272
$X_{\dot{u}uu}$	-616.997	$Y_{\dot{u}uu}$	2607.747	$N_{\dot{u}uu}$	470.432
X_v	-119.854	Y_v	-1977.322	N_v	-877.360
X_{vv}	13.463	Y_{vv}	757.359	N_{vv}	460.536
X_{vvv}	1207.072	Y_{vvv}	-1241.450	N_{vvv}	-1085.545
$X_{\dot{v}}$	-8.201	$Y_{\dot{v}}$	-1331.561	$N_{\dot{v}}$	-122.069
$X_{\dot{v}v}$	32.154	$Y_{\dot{v}v}$	-792.184	$N_{\dot{v}v}$	-101.606
$X_{\dot{v}vv}$	-25.114	$Y_{\dot{v}vv}$	436.552	$N_{\dot{v}vv}$	203.668
X_r	-40.466	Y_r	276.187	N_r	-272.376
X_{rr}	61.130	Y_{rr}	441.458	N_{rr}	120.869
X_{rrr}	214.808	Y_{rrr}	-505.71	N_{rrr}	-362.711
$X_{\dot{r}}$	-10.635	$Y_{\dot{r}}$	-198.47	$N_{\dot{r}}$	-81.600
$X_{\dot{r}r}$	74.097	$Y_{\dot{r}r}$	-616.119	$N_{\dot{r}r}$	11.746
$X_{\dot{r}rr}$	-136.780	$Y_{\dot{r}rr}$	644.398	$N_{\dot{r}rr}$	99.618
X_{rv}	796.692	Y_{rv}	-190.902	N_{rv}	-167.407
X_{rrv}	1954.658	Y_{rrv}	-11682.707	N_{rrv}	1299.872
X_{vvr}	879.882	Y_{vvr}	-6796.332	N_{vvr}	1371.747

6.4 Development of Maneuvering Models

The maneuvering model is a hybrid model that combines Taylor expansions, namely of the Abkowitz form, to build the bow thruster and hull models. Additionally, a separate module is built for the azimuth thruster model, which aligns closely with the MMG type.

In this section, the model development for the ship without an tunnel propeller is presented first, and then the model is expanded to include the influence of the operating tunnel propeller. The maneuvering model for the azimuth thruster is based on achieving equilibrium of the longitudinal forces with respect to the azimuth angles.

6.4.1 Maneuvering model of hull

In Section (6.3.2), the hydrodynamic coefficients for a bare hull are presented in Tab. (6.2). It is necessary to reduce the number of these coefficients to simplify the extension of the model to a ship equipped with an operating tunnel propeller.

Filtering the coefficients in Tab. (6.2) is directly challenging because each force term is a product of the maneuvering coefficient and, for example, an associated velocity term. The force component, characterized by a high coefficient value, can be multiplied by a small velocity value, thus reducing its contribution to the total forces.

One method of evaluating these coefficients is to convert the data from force versus time to force versus velocity. This allows the polynomial coefficients to be determined by fitting a polynomial to the data. To determine the relationship between force and velocity, it is necessary to have a time history of the force during each dynamic test. For example, the sway motion is exposed. According to Eq. (5.20), Y in the sway motion can be expressed as

$$Y \cong Y_v v + Y_{vv} v^2 + Y_{vvv} v^3 + Y_{\dot{v}} \dot{v} + Y_{\dot{v}v} \dot{v} v + Y_{\dot{v}vv} \dot{v} v^2. \tag{6.1}$$

During one period, the ship reaches twice the same velocity, where the force is distinguished by Y_1 and Y_2, and we have

$$Y_1 \cong Y_v v_1 + Y_{vv} v_1^2 + Y_{vvv} v_1^3 + Y_{\dot{v}} \dot{v}_1 + + Y_{\dot{v}v} \dot{v}_1 v_1 + Y_{\dot{v}vv} \dot{v}_1 v_1^2 \tag{6.2}$$

$$Y_2 \cong Y_v v_2 + Y_{vv} v_2^2 + Y_{vvv} v_2^3 + Y_{\dot{v}} \dot{v}_2 + + Y_{\dot{v}v} \dot{v}_2 v_2 + Y_{\dot{v}vv} \dot{v}_2 v_2^2. \tag{6.3}$$

The ship performs a harmonic oscillation; Eq. (6.2) and Eq. (6.3) can be expressed as

$$\begin{aligned} Y_1 \cong\ & Y_v y_0 \omega \cos(\omega t_1) + Y_{vv} (y_0 \omega)^2 (\cos(\omega t_1))^2 + Y_{vvv} (y_0 \omega)^3 (\cos(\omega t_1))^3 + \\ & Y_{\dot{v}} (-\omega^2 y_0 \sin(\omega t_1)) + Y_{\dot{v}v} (-\omega^3 y_0^2 \sin(\omega t_1) \cos(\omega t_1)) + \\ & Y_{\dot{v}vv} (-\omega^4 y_0^3 \sin(\omega t_1) \cos^2(\omega t_1)) \end{aligned} \tag{6.4}$$

$$\begin{aligned} Y_2 \cong\ & Y_v y_0 \omega \cos(\omega t_2) + Y_{vv} (y_0 \omega)^2 (\cos(\omega t_2))^2 + Y_{vvv} (y_0 \omega)^3 (\cos(\omega t_2))^3 + \\ & Y_{\dot{v}} (-\omega^2 y_0 \sin(\omega t_2)) + Y_{\dot{v}v} (-\omega^3 y_0^2 \sin(\omega t_2) \cos(\omega t_2)) + \\ & Y_{\dot{v}vv} (-\omega^4 y_0^3 \sin(\omega t_2) \cos^2(\omega t_2)). \end{aligned} \tag{6.5}$$

With the relation of $\omega t_1 + \omega t_2 = 2\pi$, i.e., $\cos(\omega t_2) = \cos(\omega t_1)$ and $\sin(\omega t_2) = -\sin(\omega t_1)$, Eq. (6.5) becomes

$$\begin{aligned} Y_2 \cong\ & Y_v y_0 \omega \cos(\omega t_1) + Y_{vv} (y_0 \omega)^2 (\cos(\omega t_1))^2 + Y_{vvv} (y_0 \omega)^3 (\cos(\omega t_1))^3 + \\ & Y_{\dot{v}} (\omega^2 y_0 \sin(\omega t_1)) + Y_{\dot{v}v} (\omega^3 y_0^2 \sin(\omega t_1) \cos(\omega t_1)) + \\ & Y_{\dot{v}vv} (\omega^4 y_0^3 \sin(\omega t_1) \cos^2(\omega t_1)). \end{aligned} \tag{6.6}$$

Eliminating the acceleration terms can be done by the sum of Eq. (6.4) and Eq. (6.6) to obtain

$$Y_1 + Y_2 = 2(Y_v y_0 \omega \cos(\omega t_1) + Y_{vv} (y_0 \omega)^2 (\cos(\omega t_1))^2) + Y_{vvv} (y_0 \omega)^3 (\cos(\omega t_1))^3)$$

$$\frac{Y_1 + Y_2}{2} = Y_v v_1 + Y_{vv} v_1^2 + Y_{vvv} v_1^3 \tag{6.7}$$

$$Y(v_1) = Y_v v_1 + Y_{vv} v_1^2 + Y_{vvv} v_1^3. \tag{6.8}$$

Eq. (6.7) states that the mean values of Y related to the same location can represent the distribution of Y in v. As shown in Fig. (6.13), the curves on the left should be mirrored to the right at the point $t/T = 0.5$, where the minimum sway velocity occurs. The average value at each velocity from $t/T = 0.5$ to $t/T = 1.0$ (from $v_{\min}$ to $v_{\max}$) forms the distribution of forces and moments ($X(v')$, $Y(v')$, and $N(v')$) in the sway test, as shown in Fig. (6.15).

This approach provides a procedure for obtaining hydrodynamic derivatives from surge, sway, and yaw tests, as shown in Figs. (6.13) through (6.16).

Tab. (6.4) shows the coefficients associated with the polynomials, which closely match the hydrodynamic derivatives obtained from the Fourier analysis, as listed in Tab. (6.2).

The polynomial indicates that $Y(v)$ is a strictly decreasing function inversely related to v, thus requiring negative coefficients for Y_v and Y_{vvv}. When Y is an odd function of v, the coefficient Y_{vv} must be regarded as $Y_{|v|v}$, as indicated in Fig. (2.2) in Section (2.1). However, the influence of Y_{vv} on the tendency of the polynomial is limited (see Fig. (6.15)).

The calculated values of N_v and N_{vvv} are negative when the forebody is dominant. The profile X with respect to the variables v and r is analyzed in Appendix (F) based on the data obtained from the RANS simulations. In general, numerical simulations provided reasonable results.

For further insight into the physical significance of the possible force-velocity as well as moment-velocity correlation, see Crane et. al. [4].

Table 6.4: Maneuvering coefficients $\times 10^5$ obtained from the polynomials.

	a	**b**	**c**	**d**
$X'(\Delta u')$	-518.038	-85.466	-198.095	-103.524
$Y'(\Delta u')$	2084.806	-97.706	-17.585	-24.546
$N'(\Delta u')$	-457.958	53.156	5.063	10.006
$X'(v')$	43.507	128.282	-6.594	-117.929
$Y'(v')$	-4426.915	-15.474	-1575.467	-1.071
$N'(v')$	-952.466	0.014	-841.802	0.570
$X'(r')$	245.138	15.545	-0.703	-100.142
$Y'(r')$	-1025.987	-24.684	244.033	-2.685
$N'(r')$	-170.962	20.034	-256.947	0.946

The evolution of Y over acceleration $\dot{v}$ can be followed by subtracting Eq. (6.4) from Eq. (6.6) to eliminate the velocity-dependent terms. However, terms combined from velocity and acceleration, such as $Y_{\dot{v}vv}$, can significantly affect the solution of pure accelerated terms, such as $Y_{\dot{v}}$. Therefore, it is advisable to determine the value of the acceleration-related coefficient using a Taylor expansion approach.

To address this issue, the raw data curves are applied again. For example, consider the time history of the sway test shown in Fig. (6.17), which contains three distinct curves of different colors. The black curve represents the raw data output from the simulation. The regression curve, represented by the blue dashed line, is obtained from the hydrodynamic derivatives given in Tab. (6.2). The red dashed curve is generated using the red coefficients obtained from Tab. (6.5). The red coefficients indicate the primary characteristic of the curve profiles and can be used in the maneuvering model built for the bare hull, as shown in Eqs. (6.9) through (6.11).

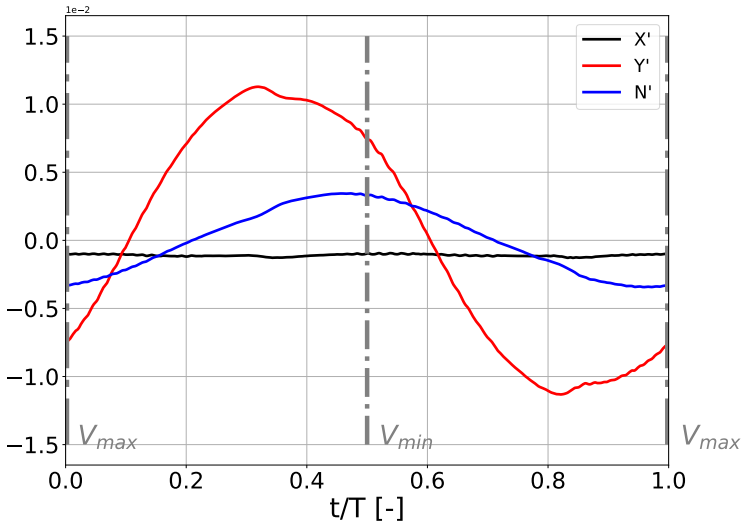

Figure 6.13: Time history of the forces and moment in the sway motion.

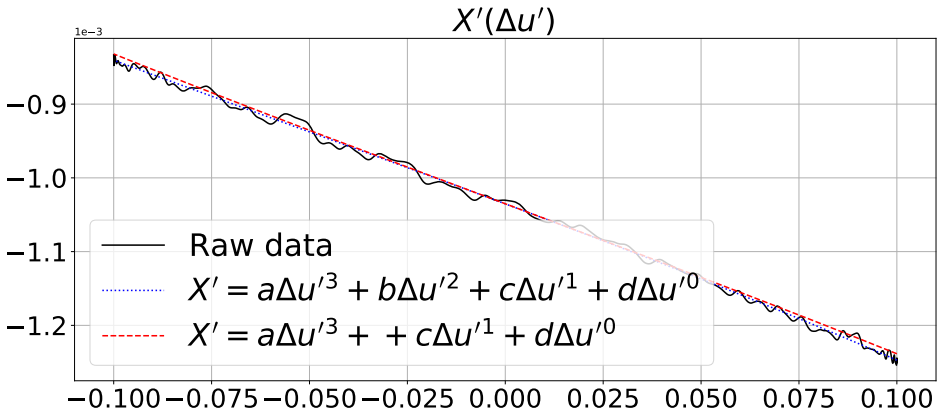

Figure 6.14: Surge related polynomial.

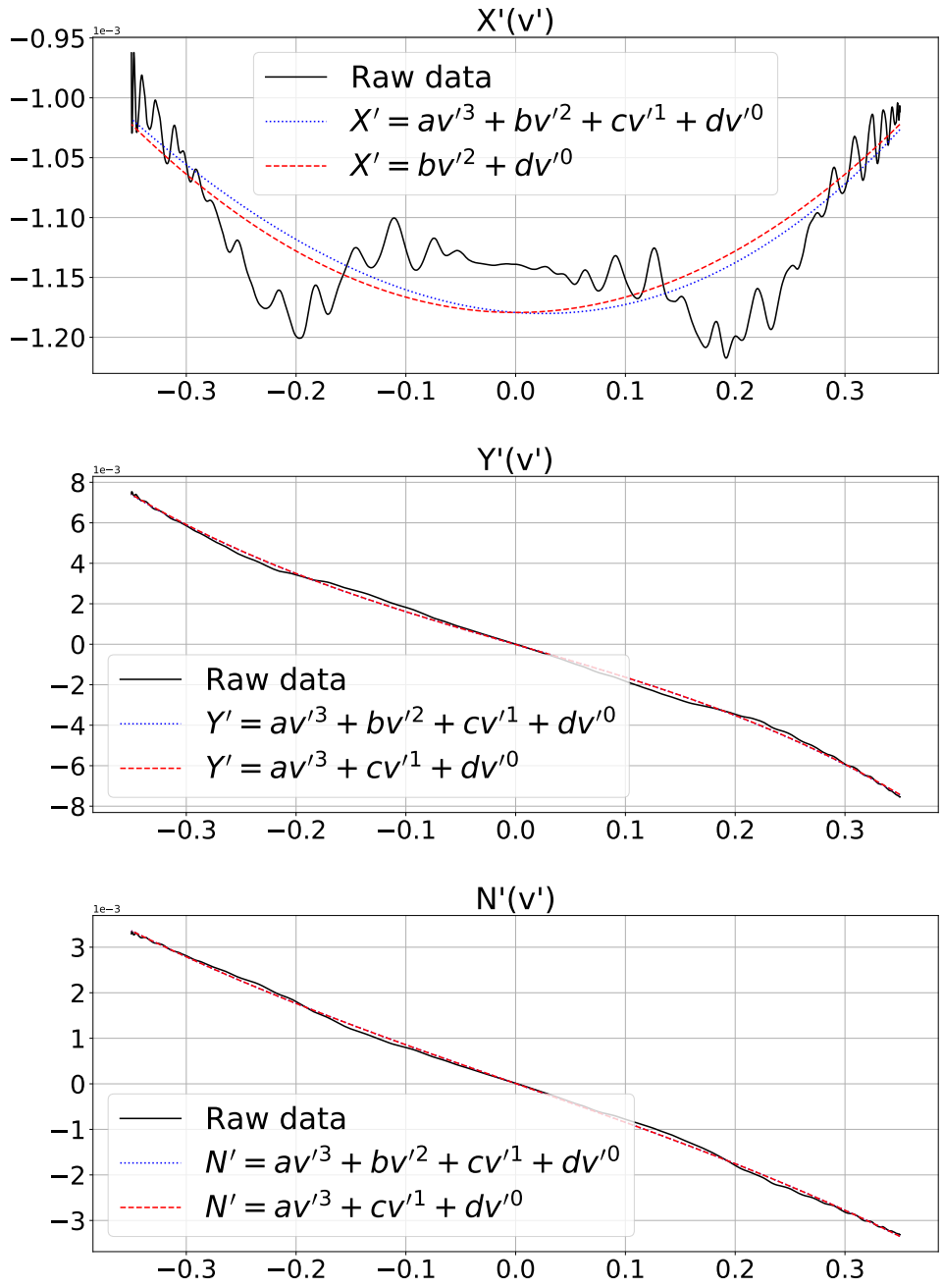

Figure 6.15: Sway related polynomial.

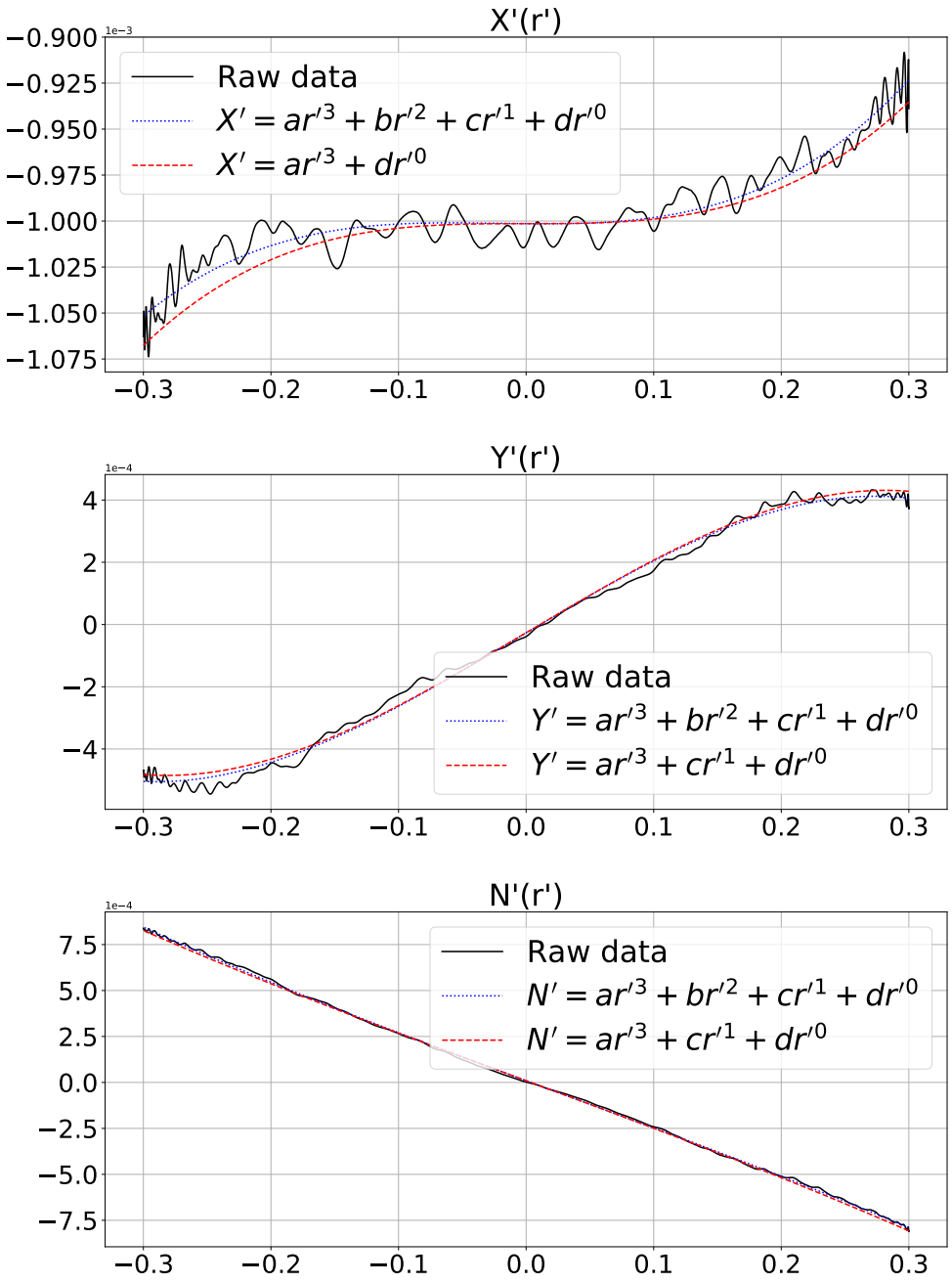

Figure 6.16: Yaw related polynomial.

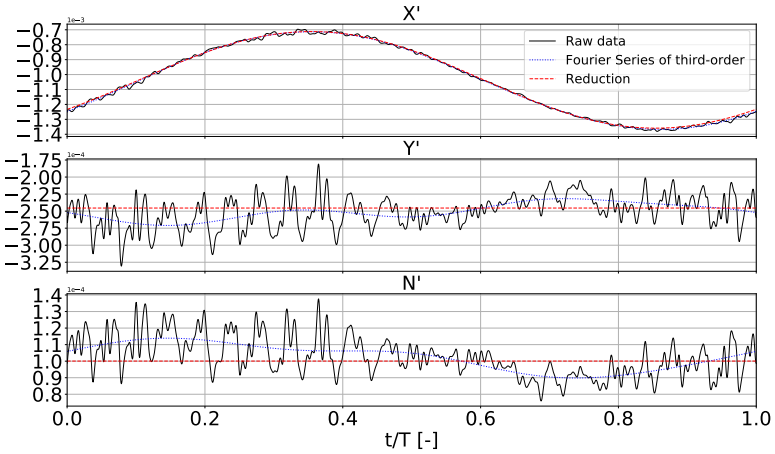

(a) Surge

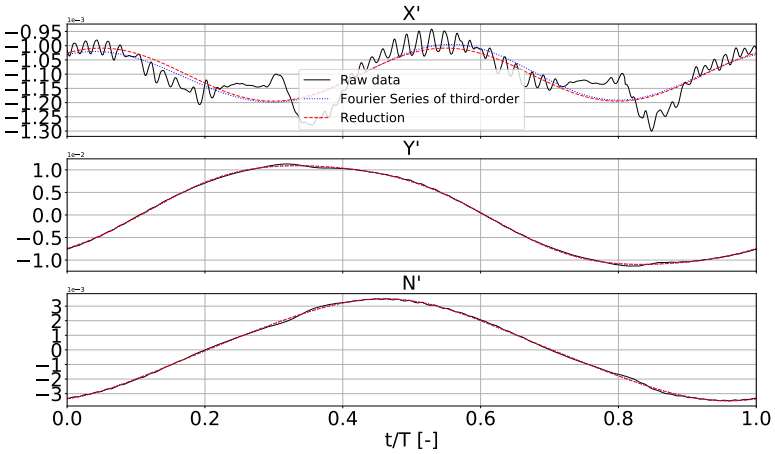

(b) Sway

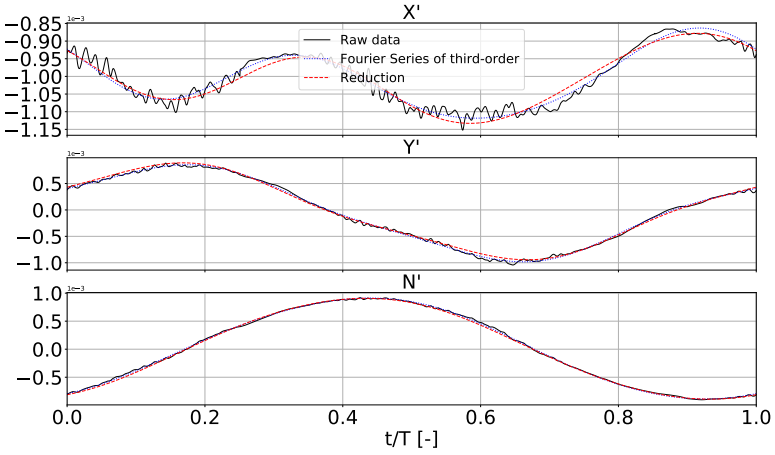

(c) Yaw

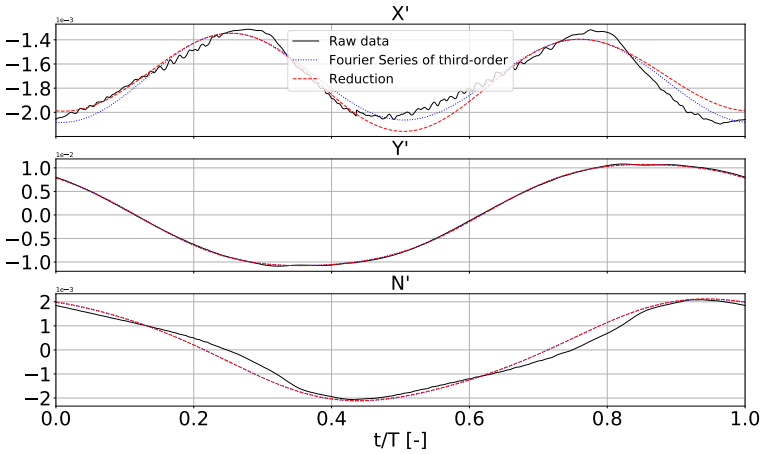

(d) First combined sway and yaw

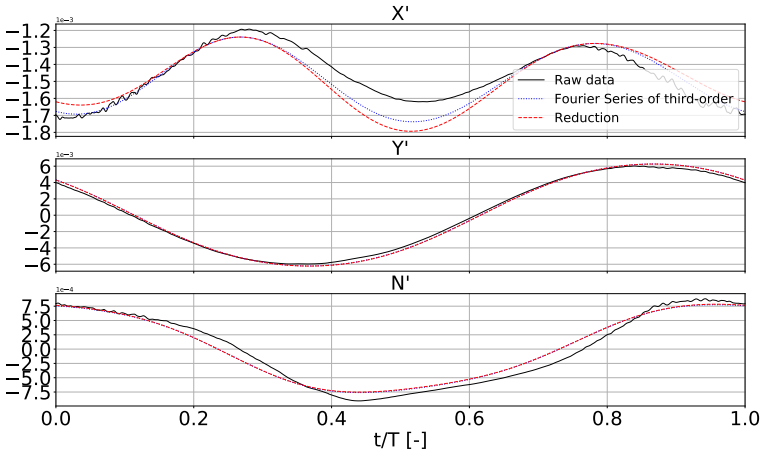

(e) Second combined sway and yaw

Figure 6.17: Comparison of time history of forces X', Y', and moment N' during one period of dynamic tests between original (black), regression (blue), and reduction (red) curve. From top to bottom: Surge, sway, yaw, first combined sway-yaw, and second combined sway-yaw at $F_n = 0.074$.

Table 6.5: Hydrodynamic derivatives for the bare hull (significant terms in red).

u			v			r			rv		
X_u	Y_u	N_u	X_v	Y_v	N_v	X_r	Y_r	N_r	X_{rv}	Y_{rv}	N_{rv}
X_{uu}	Y_{uu}	N_{uu}	X_{vv}	Y_{vv}	N_{vv}	X_{rr}	Y_{rr}	N_{rr}	X_{rrv}	Y_{rrv}	N_{rrv}
X_{uuu}	Y_{uuu}	N_{uuu}	X_{vvv}	Y_{vvv}	N_{vvv}	X_{rrr}	Y_{rrr}	N_{rrr}	X_{vvr}	Y_{vvr}	N_{vvr}
$X_{\dot{u}}$	$Y_{\dot{u}}$	$N_{\dot{u}}$	$X_{\dot{v}}$	$Y_{\dot{v}}$	$N_{\dot{v}}$	$X_{\dot{r}}$	$Y_{\dot{r}}$	$N_{\dot{r}}$			
$X_{\dot{u}u}$	$Y_{\dot{u}u}$	$N_{\dot{u}u}$	$X_{\dot{v}v}$	$Y_{\dot{v}v}$	$N_{\dot{v}v}$	$X_{\dot{r}r}$	$Y_{\dot{r}r}$	$N_{\dot{r}r}$			
$X_{\dot{u}uu}$	$Y_{\dot{u}uu}$	$N_{\dot{u}uu}$	$X_{\dot{v}vv}$	$Y_{\dot{v}vv}$	$N_{\dot{v}vv}$	$X_{\dot{r}rr}$	$Y_{\dot{r}rr}$	$N_{\dot{r}rr}$			

$$
\begin{aligned}
X \cong\ & X_0 \\
+\ & X_u \Delta u + X_{uuu} \Delta u^3 + X_{\dot{u}} \dot{u} \\
+\ & X_{vv} v^2 \\
+\ & X_{\dot{r}r} \dot{r} r + X_{rrr} r^3 \\
+\ & X_{rv} r v
\end{aligned}
\tag{6.9}
$$

$$
\begin{aligned}
Y \cong\ & Y_0 \\
+\ & Y_v v + Y_{vvv} v^3 + Y_{\dot{v}} \dot{v} + Y_{\dot{v}vv} \dot{v} v^2 \\
+\ & Y_r r + Y_{rrr} r^3 + Y_{\dot{r}} \dot{r} + Y_{\dot{r}rr} \dot{r} r^2 \\
+\ & Y_{rrv} r^2 v + Y_{vvr} v^2 r
\end{aligned}
\tag{6.10}
$$

$$
\begin{aligned}
N \cong\ & N_0 \\
+\ & N_v v + N_{vvv} v^3 + N_{\dot{v}} \dot{v} + N_{\dot{v}vv} \dot{v} v^2 \\
+\ & N_r r + N_{rrr} r^3 + N_{\dot{r}} \dot{r} + N_{\dot{r}rr} \dot{r} r^2 \\
+\ & N_{rrv} r^2 + N_{vvr} v^2 r
\end{aligned}
\tag{6.11}
$$

6.4.2 Maneuvering model of hull with an operating tunnel thruster

As stated previously, both methods can be applied to determine the coefficients associated with velocity. However, only the Taylor expansion method can determine the terms associated with acceleration. Polynomials have the advantage of providing a clear representation of the force-velocity relationship. In this section, a study of the time history curves is conducted to identify cases where there are significant changes in the evolution of the curves. The polynomial approach is then used to analyze the differences. The primary coefficients of interest are further identified. Finally, the maneuvering model is derived from the mathematical model of the bare hull.

Fig. (6.18) shows the time history of X', Y', and N' for two situations: one with a working tunnel propeller and one without. Since the mean values of these variables remain constant over time, the curves shown in the figure exclude X'_0, Y'_0, and N'_0.

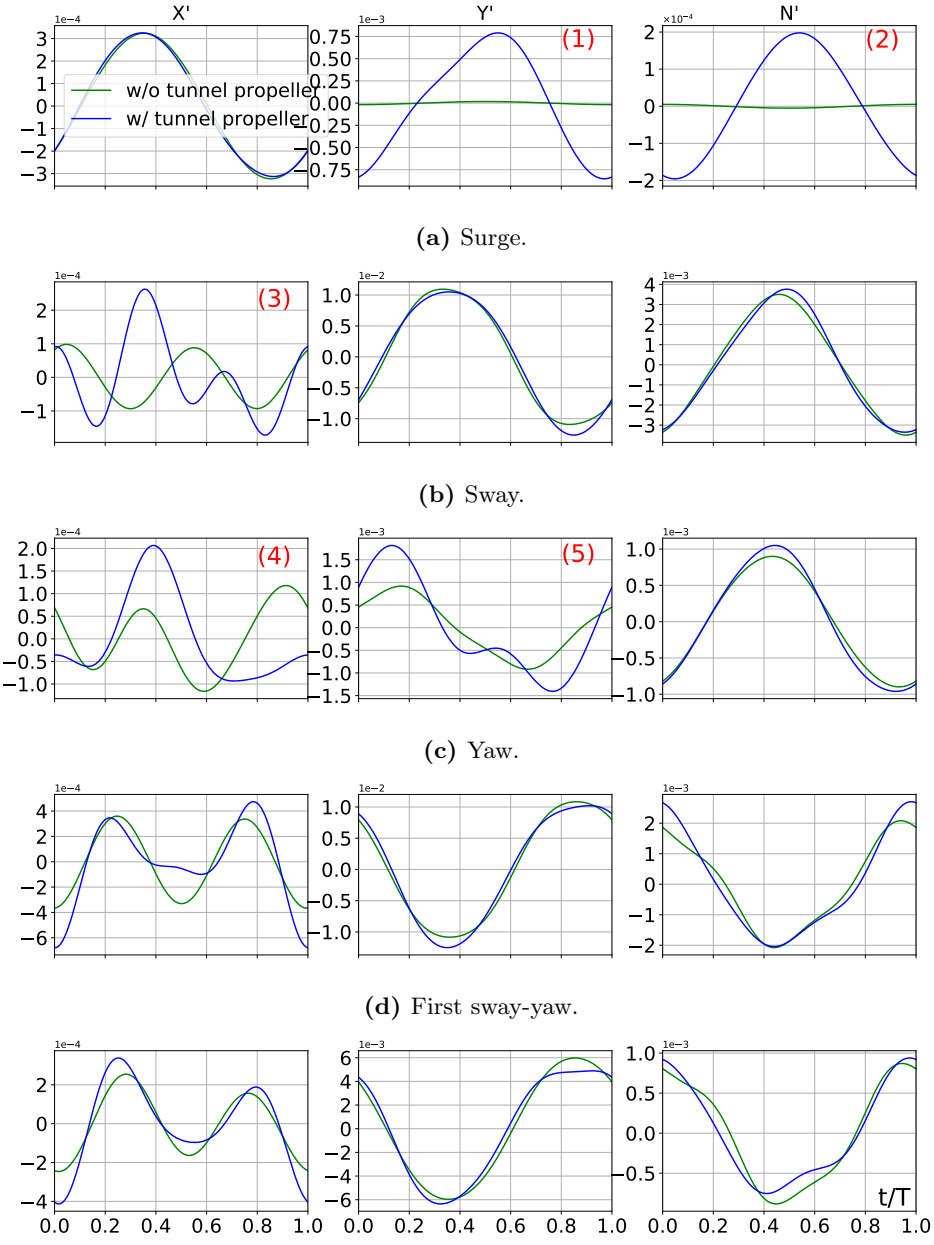

(a) Surge.

(b) Sway.

(c) Yaw.

(d) First sway-yaw.

(e) Second sway-yaw.

Figure 6.18: Comparison of non-dimensional forces and moment between a ship with and without tunnel propeller at the five forced dynamic tests during the last period (from top to bottom: surge, sway, yaw, first and second combined sway-yaw test).

Numbers 1 through 5 represent the considered cases where there is a significant difference between the two situations. This discrepancy is observed in the pure surge tests in subplots 1 and 2, the pure sway tests in subplot 3, and the pure yaw tests in subplots 4 and 5. The corresponding polynomials can be seen in Figs. (6.19) through (6.21).

Regarding subfigures 1-2 of the surge test, Y' and N' represent the odd function of the velocity $\Delta u'$ (see Fig. (6.19)). They indicate a reduction of the effect of the bow thruster as the ship's speed increases. This result is also consistent with the performance of the bow thruster. To account for the effect of the thruster in this situation, it is necessary to include $Y'(\Delta u')$ and $N'(\Delta u')$ as additional terms in the bare hull maneuvering model.

The oscillation X' in the sway test, when the tunnel thruster propeller is in operation, appears to be an odd function with respect to the change in v', as shown in Fig. (6.20) on the left. However, $X'(r)$ is neither an odd nor an even function with respect to r', see the same figure on the right. The polynomial should be given as $X'(r') = X'_r \cdot r' + X'_{rr} \cdot r'^2 + X'_{rrr} \cdot r'^3$, where X'_{rrr} may have a more significant contribution than the other terms, resulting in an increase in longitudinal force as the yaw rate increases. During ship starboard turn, it is important to evaluate the positive range r'. In the investigated case, the curve shows that the significant differences in $X'(r')$ occur at the minimum and maximum yaw rates. Their contribution to resistance X'_0, as seen in Tab. (6.3), can vary from 6.7% to -4.4%. In general, when comparing the curves with the maximum positive velocity, the force in the $X'(v')$ curve is approximately similar, but in the $X'(r')$ curve, the force is reduced in the absence of a tunnel thruster propeller. However, the curves with the tunnel thruster propeller operating in both sway and yaw motions still have a limited effect on X'.

The difference in Y' in the yaw test shown in Fig. (6.21) is significant. As r' increases to about 0.18, the two curves show divergent patterns that move further apart. At the peak value of r' (0.3), the value of Y' on the blue curve exceeds 12% of Y'_0.

However, the difference in N' cannot be considered significant. The proximity between the point of application of slipstream-induced suction (Y_s in Fig. (1.1)) and the center of gravity of the ship may explain this phenomenon.

Every change in each hydrodynamic derivative can affect the ship maneuvering simulation parameters to certain degrees. Given the previous discussion, a more thorough investigation of Y in yaw test will be a priority.

The hydrodynamic derivatives of Y associated with r and $\dot{r}$, namely Y_r, Y_{rrr}, $Y_{\dot{r}}$, $Y_{\dot{r}rr}$, $Y_{\dot{r}rr}$, Y_{rrv}, and Y_{vvr}, will be studied in the next step. A simple way is to substitute the corresponding coefficients in the maneuvering model with a new set of coefficients.

Tab. (6.6) presents a comparison between the original hydrodynamic coefficients from Tab. (6.3) and the reduced coefficients, focusing on the differences in the turning parameters. Based on the results, the reduced model is considered suitable for ship maneuvering simulations.

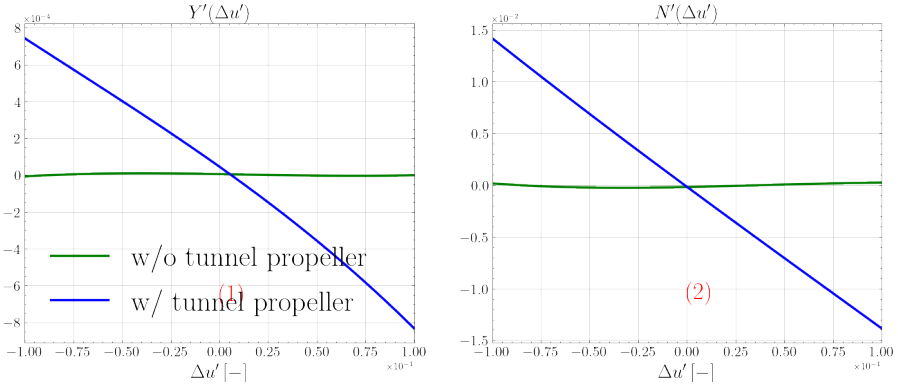

Figure 6.19: The development of Y' (left) as well as N' (right) about changing longitudinal velocity $\Delta u'$.

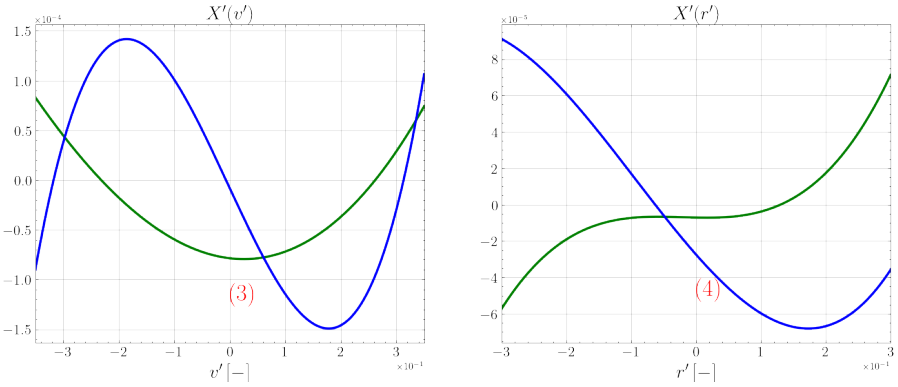

Figure 6.20: The development of X' about changing transverse velocity (left) and yaw velocity (right) v' both with and without propeller.

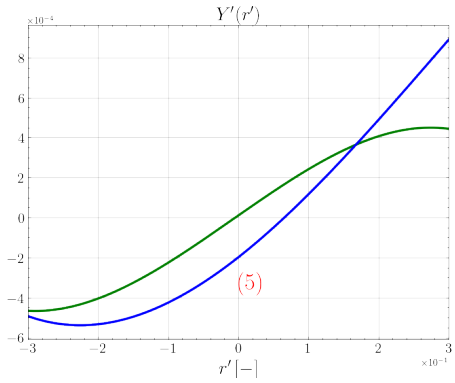

Figure 6.21: The development of Y' about changing yaw velocity r' both with and without propeller.

Furthermore, to determine the significant hydrodynamic derivatives among these coefficients, a method proposed by Mucha [13] is used. This method consists in systematically increasing one of the hydrodynamic derivatives by a constant percentage while leaving the others unchanged. When the turning parameters exceed a threshold, this coefficient is regarded as the primary one.

An illustration is given in Tab. (6.7). The errors are calculated by taking the sum of each deviation, where each deviation is assigned a weight. When simulating a turning circle, the advance and tactical diameter may be more important than the turning diameter. The corresponding contributions for advance diameter, tactical diameter, and turning diameter are 0.4, 0.4, and 0.2, respectively. According to the data in the table, both Y_{rrr} and Y_{rrv} have an error rate greater than 5%, indicating that they can be attributed to the extended impact caused by the operating propeller of the tunnel thruster.

The maneuvering model of the ship can be formulated considering the effects of the bow thruster, as expressed in Eqs. (6.12) through (6.14). The components highlighted in red represent the effects caused by the bow thruster.

Table 6.6: Change of turning parameters after the replacement of the Y-related terms.

	Advance/Lpp	**Tactical Diameter/Lpp**	**Turning Diameter/Lpp**	β [°]
original	1.358	1.851	1.643	5.410
replaced	1.378	1.835	1.510	8.272

Table 6.7: Sensitivity study of hydrodynamic derivatives in terms of turning parameters.

	Advance/Lpp	w=0.4	**Tactical D/Lpp**	w=0.4	**Turning D/Lpp**	w=0.2	**Error [%]**
Y_r	1.378	0.593	1.900	1.054	1.648	0.057	1.704
Y_{rrr}	1.391	0.967	1.736	2.492	1.271	4.527	7.987
$Y_{\dot{r}}$	1.353	0.155	1.780	1.542	1.508	1.645	3.342
$Y_{\dot{r}rr}$	1.390	0.944	1.895	0.961	1.514	1.573	3.478
Y_{rrv}	1.356	0.056	1.977	2.726	2.052	4.979	7.761
Y_{vvr}	1.382	0.698	1.820	0.679	1.461	2.213	3.589

$$
\begin{aligned}
X &\cong X_0 + \Delta X_0 \\
&+ X_u \Delta u + X_{\dot{u}} \dot{u} \\
&+ X_{vv} v^2 \\
&+ X_{\dot{r}r} \dot{r} r + X_{rrr} r^3 \\
&+ X_{rv} r v
\end{aligned}
\tag{6.12}
$$

$$
\begin{aligned}
Y &\cong Y_0 + Y_0 \\
&+ Y_u \Delta u \\
&+ Y_v v + Y_{vvv} v^3 + Y_{\dot{v}} \dot{v} + Y_{\dot{v}vv} \dot{v} v^2 \\
&+ Y_r r + Y_{vvr} v^2 r + Y_{\dot{r}} \dot{r} + Y_{\dot{r}rr} \dot{r} r^2
\end{aligned}
\tag{6.13}
$$

$$
\begin{aligned}
& + \quad Y_{rrr} r^3 + Y_{rrv} r^2 v \\
\\
N \quad \cong \quad & N_0 + N_0 \\
& + \quad N_u \Delta u \\
& + \quad N_v v + N_{vvv} v^3 + N_{\dot{v}} \dot{v} + N_{\dot{v}vv} \dot{v} v^2 \\
& + \quad N_r r + N_{rrr} r^3 + N_{\dot{r}} \dot{r} + N_{\dot{r}rr} \dot{r} r^2 \\
& + \quad N_{rrv} r^2 + N_{vvr} v^2 r.
\end{aligned}
\tag{6.14}
$$

6.4.3 Maneuvering model of main propulsion system

The chosen range of azimuth angles is relatively narrow, ranging from -30° to 30°. This limitation is primarily due to the increased complexity associated with thruster-hull and thruster-thruster interactions at larger angles, in which one thruster operated completely behind the wake of another thruster, as denoted in the review section (2.3). Such complexity would present a significant challenge to model development. The use of ANN is expected to extend the model to include interactions, but this will require a larger dataset and the support of appropriate simulations.

6.4.3.1 Main propulsion system without tunnel propeller

The maneuvering model designed for the bare hull requires an extension to consider the main propulsion system. The correlation between the hull and the main propulsion can be approximated by the deduction factor and the wake fraction.

The operating point of the self-propelled vessel is determined by the point where two distinct curves join. One is related to the resistance experienced by a vessel, while the other is related to the propulsion system. The propeller thrust coefficient, denoted k_t, is well known and shown in Fig. (4.5). This section provides a brief overview of the method used to locate the propulsion point. For a detailed description, please refer to the lecture [89].

The propeller must provide a thrust force of T to maintain a given ship's speed. The corresponding thrust coefficient k_t can be written as follows:

$$k_t = \frac{T}{\rho n^2 D^4} \tag{6.15a}$$

$$= \frac{R_t}{(\rho n^2 D^4)(1-t)}. \tag{6.15b}$$

Since the propeller induces an additional suction force in the stern region of the ship, the required propeller thrust T is often higher than the resistance of the ship R_t, so a parameter t, the so-called thrust deduction factor, must be introduced to describe the relationship between them.

In addition, the advance ratio j is introduced in Eq. (6.15) by replacing n^2 through $n^2 = v_a^2/j^2D^2$:

$$k_t = \frac{R_t j^2}{(\rho v_a^2 D^2)(1-t)}, \tag{6.16}$$

where v_a represents the average inflow velocity to the propeller, which is less than the ship's speed U_0. The wake fraction w is used to consider the ratio between v_a and U_0. The relationship between the thrust coefficient k_t needed by the ship and j^2 can be written as follows:

$$k_t = \frac{R_t j^2}{(\rho v_a^2 D^2)(1-t)} = \underbrace{\frac{R_t}{\rho U_0^2 (1-w)^2 D^2 (1-t)}}_{C} j^2, \tag{6.17a}$$

where C should be a constant for ship sailing at a constant speed. The propulsion operating point is determined by the intersection of the k_t curves, which represents the propeller thrust based on the open water test results, and the thrust required for the ship to sustain a straight course at the speed being considered. In the investigated case at $F_n = 0.074$, the intersection point is approximately located at $j = 0.82$, as shown in Fig. (6.22). The propeller rotation rate is then $v_a/(jD) = 0.91$ rps assuming that the port and starboard thrusters contribute the same thrust (half of the total thrust) at $\delta = 0°$.

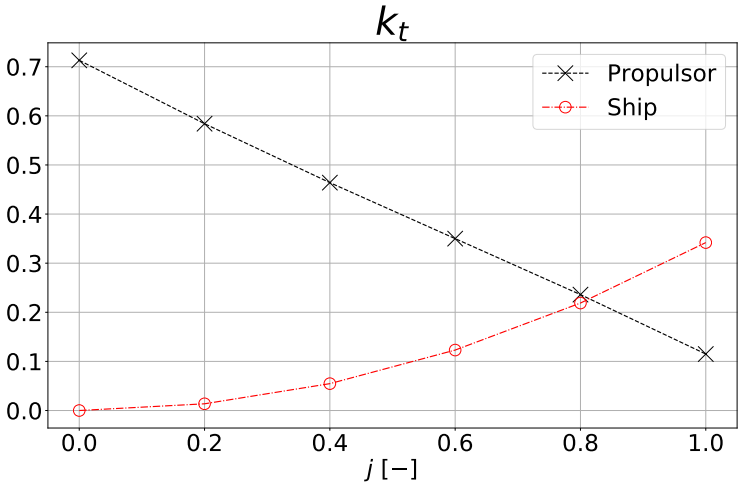

Figure 6.22: Determination of the propulsion point.

Similarly to the approach taken for $\delta = 0°$, additional azimuth angles of $-15°$ and $-30°$, as shown in Fig. (6.23), are necessary to develop a polynomial to determine higher-order hydrodynamic derivatives. A negative azimuth angle indicates the thruster's orientation towards the port side. The results presented in Section (4.2) are based on the thruster fixed coordinate system. These results need to be translated into the ship fixed coordinate system, as demonstrated in Tab. (6.8) and Tab. (6.9). In particular, the difference in coefficients at negative and positive azimuth angles can be attributed to the different interactions between the rotation of the propeller and the azimuth thruster unit, as discussed in Section (4.2).

Table 6.8: The coefficients of the starboard thruster turning to port in thruster-(left) and ship-fixed(right) coordinate systems.

	thruster-fixed coordinate			**ship-fixed coordinate**		
			$\delta = 0°$			
J	kF_x	kF_y	kQ_z	k_x	k_y	k_n
0	0.713	0	0	0.713	0	0
0.2	0.584	0	0	0.584	0	0
0.4	0.464	0	0	0.464	0	0
0.6	0.350	0	0	0.350	0	0
0.8	0.236	0	0	0.236	0	0
1	0.115	0	0	0.115	0	0
			$\delta = -15°$			
0	0.713	0	0	0.689	-0.185	2.653
0.2	0.578	-0.048	-0.006	0.546	-0.196	2.811
0.4	0.455	-0.121	0.003	0.408	-0.234	3.376
0.6	0.346	-0.206	0.020	0.281	-0.289	4.168
0.8	0.222	-0.276	0.034	0.143	-0.324	4.692
1	0.071	-0.350	0.044	-0.022	-0.356	5.168
			$\delta = -30°$			
0	0.713	0	0	0.617	-0.357	5.125
0.2	0.583	-0.090	-0.010	0.460	-0.369	5.301
0.4	0.481	-0.229	0.003	0.302	-0.439	6.311
0.6	0.397	-0.381	0.030	0.153	-0.528	7.627
0.8	0.300	-0.530	0.061	-0.005	-0.609	8.815
1	0.194	-0.700	0.097	-0.182	-0.703	10.206

Table 6.9: The coefficients of the starboard thruster turning to starboard in thruster-(left) and ship-fixed(right) coordinate systems.

	thruster-fixed coordinate			**ship-fixed coordinate**		
			$\delta = 0°$			
J	kF_x	kF_y	kQ_z	k_x	k_y	k_n
0	0.713	0	0	0.713	0	0
0.2	0.584	0	0	0.584	0	0
0.4	0.464	0	0	0.464	0	0
0.6	0.350	0	0	0.350	0	0
0.8	0.236	0	0	0.236	0	0
1	0.115	0	0	0.115	0	0
			$\delta = 15°$			
0	0.713	0	0	0.689	0.185	-2.653
0.2	0.605	0.043	0.001	0.573	0.198	-2.847
0.4	0.507	0.116	-0.006	0.460	0.243	-3.503
0.6	0.414	0.203	-0.023	0.347	0.303	-4.382
0.8	0.292	0.278	-0.039	0.210	0.344	-4.985
1	0.152	0.356	-0.051	0.055	0.383	-5.560
			$\delta = 30°$			
0	0.713	0	0	0.617	0.357	-5.125
0.2	0.636	0.075	0.006	0.513	0.383	-5.499
0.4	0.590	0.226	-0.003	0.398	0.491	-7.057
0.6	0.532	0.388	-0.030	0.267	0.602	-8.684
0.8	0.443	0.548	-0.062	0.110	0.696	-10.068
1	0.344	0.724	-0.096	-0.064	0.799	-11.528

The values of k_y and k_n at different azimuth angles can be derived from the operating points as shown in Fig. (6.23). From Tab. (6.10) it can be seen that the propeller rotation

rate must increase as δ increases to maintain the forward speed of the ship. Fig. (6.24) shows the distribution of the force and moment of the starboard thruster over different azimuth angles. The red dashed line shows the regression analysis using a third-order polynomial. Thus, the azimuth thruster induced transverse force Y and yaw moment N can be seen as an odd function of δ.

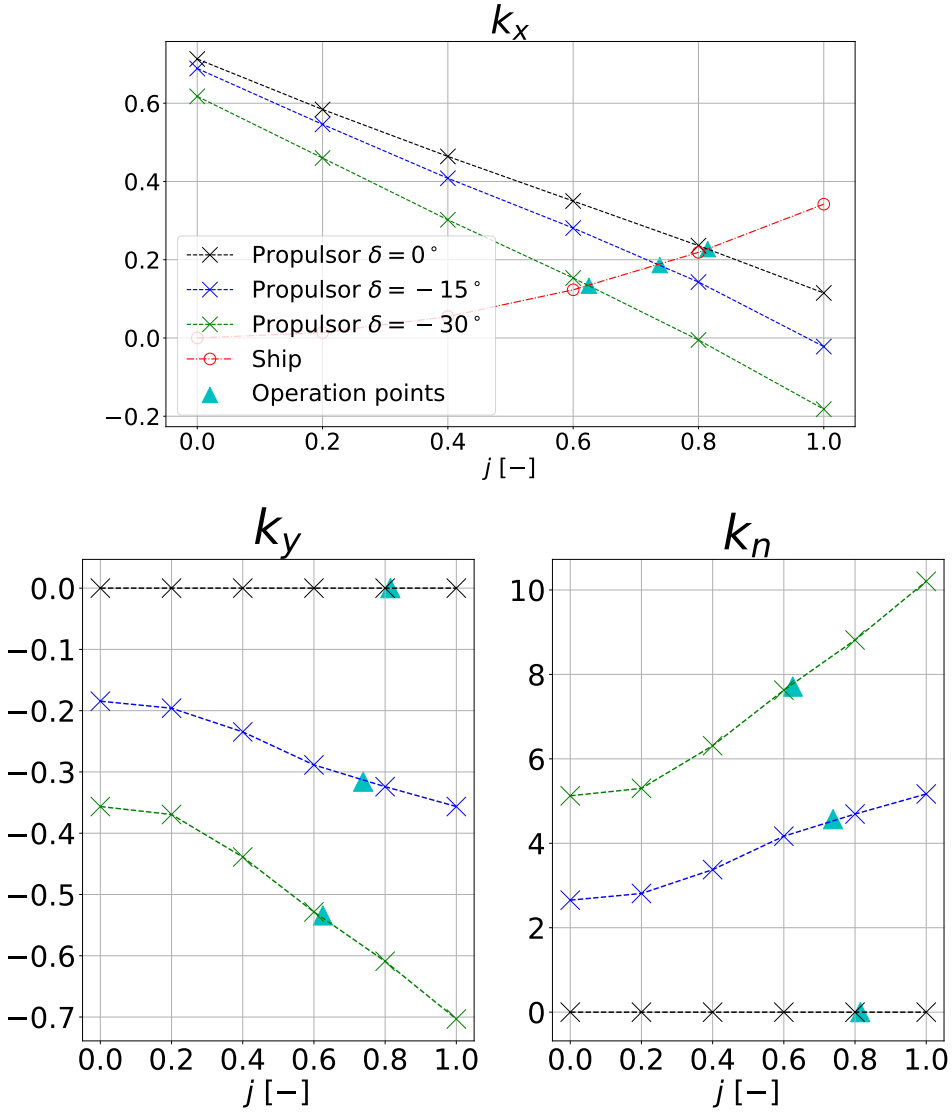

Figure 6.23: Determination of further propulsion points.

Table 6.10: Calculation of the propulsor operation points.

δ [°]	k_x [-]	j [-]	n [Hz]
-30	0.13	0.63	1.19
-15	0.19	0.74	1.01
0	0.23	0.81	0.91
15	0.22	0.79	0.94
30	0.18	0.72	1.04

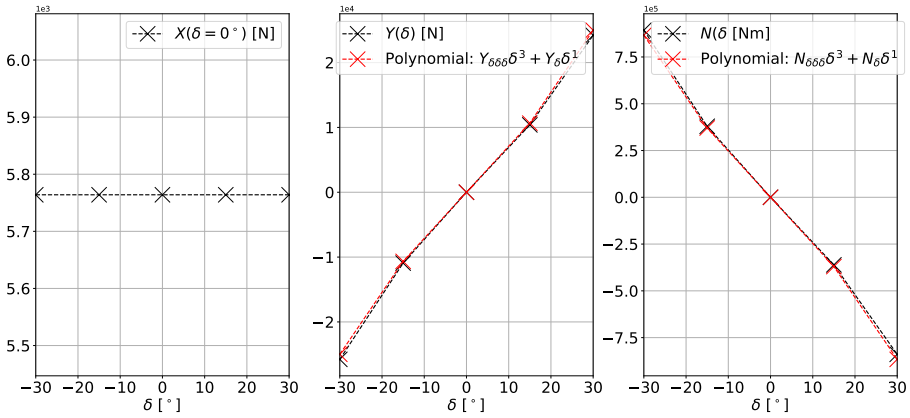

Figure 6.24: Distribution of X, Y, and N on δ in the ship fixed axis from the starboard thruster without the tunnnel propeller.

The expression for azimuth thruster, expanded up to the third order, can be written as:

$$X(\delta) \approx X_0^P \tag{6.18a}$$
$$Y(\delta) \approx Y_0^P + Y_\delta^P \delta + Y_{\delta\delta\delta}^P \delta^3 \tag{6.18b}$$
$$N(\delta) \approx N_0^P + N_\delta^P \delta + N_{\delta\delta\delta}^P \delta^3, \tag{6.18c}$$

where X_0^P, Y_0^P, and N_0^P are the values at $\delta = 0°$.

The development process for the port thruster is identical to that of the starboard thruster. The mathematical model incorporating the effect of the azimuth thrusters is presented below:

$$\begin{aligned} X \cong\ & X_0 + \Delta X_0^P \\ +\ & X_u \Delta u + X_{uuu} \Delta u^3 + X_{\dot{u}} \dot{u} \\ +\ & X_{vv} v^2 \end{aligned} \tag{6.19}$$

$$
\begin{aligned}
&+ \quad X_{\dot{r}r}\dot{r}r + X_{rrr}r^3 \\
&+ \quad X_{rv}rv
\end{aligned}
$$

$$
\begin{aligned}
Y \quad \cong \quad & Y_0 + Y_0^P \\
&+ \quad Y_v v + Y_{vvv}v^3 + Y_{\dot{v}}\dot{v} + Y_{\dot{v}vv}\dot{v}v^2 \\
&+ \quad Y_r r + Y_{rrr}r^3 + Y_{\dot{r}}\dot{r} + Y_{\dot{r}rr}\dot{r}r^2 \\
&+ \quad Y_{rrv}r^2 + Y_{vvr}v^2 r \\
&+ \quad Y_\delta^P \delta + Y_{\delta\delta\delta}^P \delta^3
\end{aligned} \tag{6.20}
$$

$$
\begin{aligned}
N \quad \cong \quad & N_0 + N_0^P \\
&+ \quad N_v v + N_{vvv}v^3 + N_{\dot{v}}\dot{v} + N_{\dot{v}vv}\dot{v}v^2 \\
&+ \quad N_r r + N_{rrr}r^3 + N_{\dot{r}}\dot{r} + N_{\dot{r}rr}\dot{r}r^2 \\
&+ \quad N_{rrv}r^2 + N_{vvr}v^2 r \\
&+ \quad N_\delta^P \delta + N_{\delta\delta\delta}^P \delta^3
\end{aligned} \tag{6.21}
$$

6.4.3.2 Main propulsion system with the operating tunnel propeller

The inclusion of the tunnel propeller results in an increase in the resistance of the ship, leading to a steeper thrust curve compared to that shown in Fig. (6.23). As a result, the advance ratio is reduced and the propeller rotation rate is increased. However, engine overload is unlikely to occur due to the low speed of the ship.

Tab. (6.11) shows the progressive increase in resistance during the sway-yaw test. The production of eddies could potentially increase the forces exerted on the tunnel wall, leading to an increased resistance when the tunnel thruster propeller is in operation.

Tab. (6.12) shows the hydrodynamic derivatives associated with Y' and N' derived from Fig. (6.25). The discrepancy is mainly due to the first-order coefficient. However, the third-order coefficients show a high degree of similarity.

Table 6.11: Comparison of ship resistance in kN between static and dynamic tests with and without a working propeller.

	ship w/o tunnel propeller		ship w/ working tunnel propeller					
F_n	R_t **(static) A**	R_t **(dynamic) B**	R_t **(static) C**	R_t **(dynamic) D**	**B/A**	**D/A**	**D/B**	**D/C**
0.074	-11.528	-15.557	-19.303	-25.448	1.349	2.21	1.64	1.32

Table 6.12: Comparison of dimensionless hydrodynamic derivatives multiplied by 10^5 for the port-side thruster between with and without propeller (in brackets).

X'			**Y'**			**N'**		
		ratio			ratio			ratio
X_0^P	125.57 (56.91)	2.21	Y_δ^P	462.16(338.57)	1.37	N_δ^P	-215.65(-158.29)	1.36
			$Y_{\delta\delta\delta}^P$	303.63 (300.93)	1.01	$N_{\delta\delta\delta}^P$	-138.63 (-138.14)	1.00

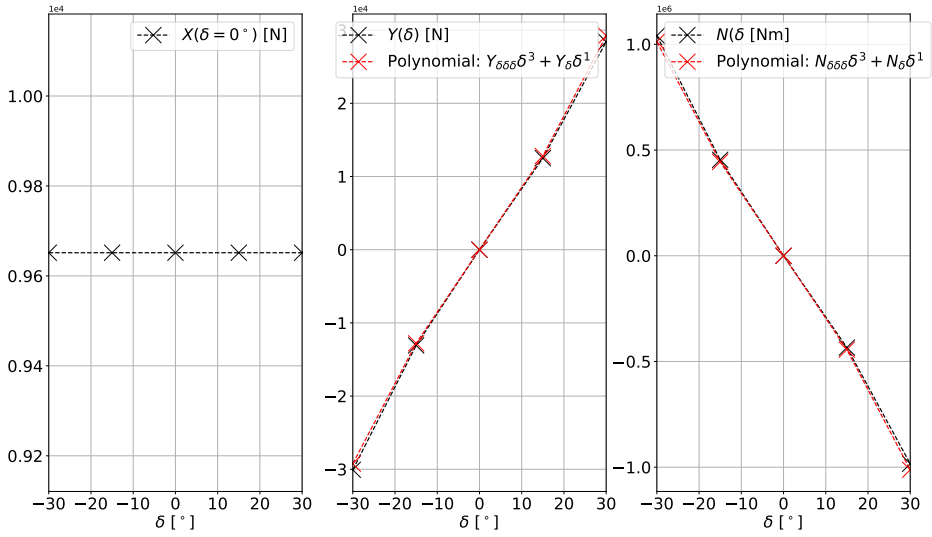

Figure 6.25: Distribution of X, Y, and N with respect to δ in the ship fixed axis from the starboard thruster with the effect of tunnel propeller.

The mean values related to the ship without the tunnel propeller are disregarded, as they are negligible compared to the values caused by the operating tunnel propeller. Behind a twin-screw ship, the flow is symmetric and, thus, the components Y_0^p and N_0^p can also be discarded. Furthermore, before the start of the ship's maneuver, a balance can be found in the longitudinal direction so that the total longitudinal force is zero at a constant ship forward speed. The coefficients $X_{\dot{r}r}$, $Y_{\dot{v}vv}$, and $Y_{\dot{r}rr}$, combined with velocity and acceleration, are used to reconstruct regression curves such as those in Fig. (6.17); as tested, they have little effect on the behavior of the ship turning circle maneuver. The integrated maneuvering model for a ship equipped with two azimuth thrusters and a bow thruster, operating at low speed ($F_n = 0.074$) is expressed as follows:

$$
\begin{aligned}
X &\cong \underbrace{X_0 + \Delta X_0 + \Delta X_0}_{=0} \\
&+ X_u \Delta u + X_{\dot{u}} \dot{u} \\
&+ X_{vv} v^2 \\
&+ X_{rrr} r^3 \\
&+ X_{rv} rv \\
\\
Y &\cong \underbrace{Y_0 + Y_0 + Y_0}_{=Y_0} \\
&+ Y_u \Delta u
\end{aligned}
\tag{6.22}
$$

$$
\begin{aligned}
&+ \quad Y_v v + Y_{vvv} v^3 + Y_{\dot{v}} \dot{v} \\
&+ \quad Y_r r + Y_{vvr} v^2 r + Y_{\dot{r}} \dot{r} \\
&+ \quad Y_{rrr} r^3 + Y_{rrv} r^2 v \\
&+ \quad Y_\delta \delta + Y_{\delta\delta\delta} \delta^3
\end{aligned} \tag{6.23}
$$

$$
\begin{aligned}
N \quad \cong \quad & \underbrace{N_0 + N_0 + N_0}_{N_0} \\
&+ \quad N_u \Delta u \\
&+ \quad N_v v + N_{vvv} v^3 + N_{\dot{v}} \dot{v} \\
&+ \quad N_r r + N_{rrr} r^3 + N_{\dot{r}} \dot{r} \\
&+ \quad N_{rrv} r^2 + N_{vvr} v^2 r \\
&+ \quad N_\delta \delta + N_{\delta\delta\delta} \delta^3 .
\end{aligned} \tag{6.24}
$$

6.5 Discussion of Results

The trajectory of the ship's center of gravity G, as shown in Fig. (6.26), can be effectively simulated using the maneuvering model developed for the ship operating at $F_n = 0.074$. The rotation rate of the tunnel propeller is constant. The direction of rotation of the azimuth thruster causes the ship to move to starboard, thus avoiding a collision with an approaching ship.

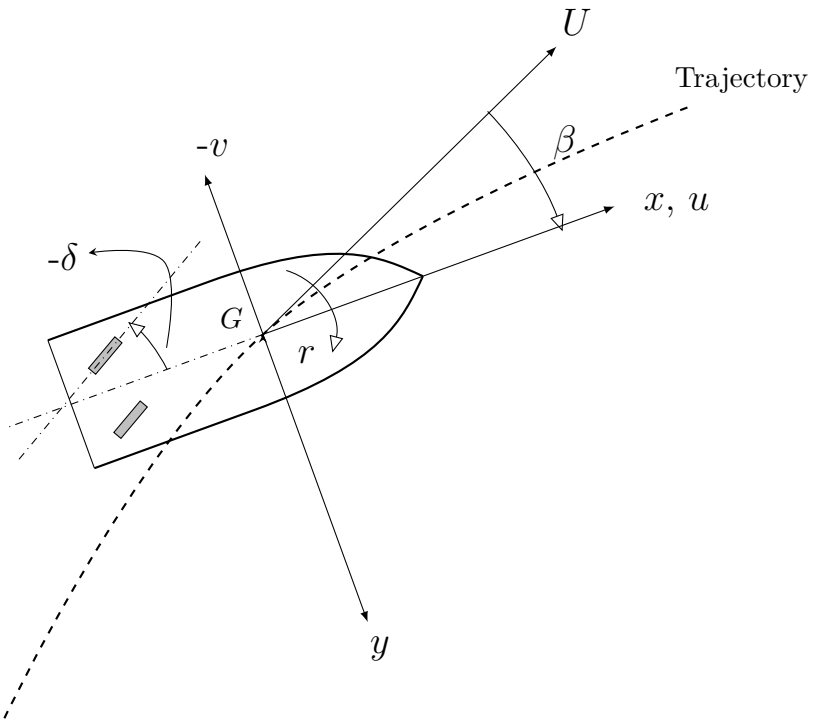

Figure 6.26: The turning circle parameters.

If both thrusters have an azimuth speed of at least 9°/s ($f = 1.5$ Hz) as required by SOLAS regulations (as indicated by Toxopeus [90]), the thrust components in $x-$ and $y-$directions can be expressed as follows:

$$\begin{aligned} k_x &= kF_{\mathrm{x}}\cos(\delta) - (kF_{\mathrm{y}} + 2.5(f+r))\sin(\delta) \\ &= kF_{\mathrm{x}}\cos(\delta) - kF_{\mathrm{y}}\sin(\delta) \underbrace{-2.5(f+r)\sin(\delta)}_{k_{\mathrm{x}}\ \text{corrector}} \qquad (6.25) \\ k_{\mathrm{y}} &= kF_{\mathrm{x}}\sin(\delta) + (kF_{\mathrm{y}} + 2.5(f+r))\cos(\delta) \\ &= kF_{\mathrm{x}}\sin(\delta) + kF_{\mathrm{y}}\cos(\delta) \underbrace{+2.5(f+r)\cos(\delta)}_{k_{\mathrm{y}}\ \text{corrector}}, \qquad (6.26) \end{aligned}$$

where the factor 2.5 is obtained from Eq. (4.3) and r is the instantaneous yaw rate of the ship. Once the azimuth angle is reached, the correction associated with f becomes

negligible. These corrections apply only to the variable r. Specifically, they include $-2.5r\sin(\delta)$ and $2.5r\cos(\delta)$ for the forces in ship-fixed frame k_x and k_y, respectively. As part of the azimuth speed calculation, the ship yaw rate must be taken into account.

The ship trajectories associated with the corrections are shown in Fig. (6.27). If no corrections are applied (r and f equal 0), the performance of the azimuth thrusters is slightly improved, considering the tactical diameter, compared to the case where corrections are applied. The slight degradation of the ship's turning ability is caused by the performance of the duct. When the bow thruster induces a yaw motion in the positive direction, the duct generates a transverse force in the opposite direction. This transverse force degrades the ship's turning ability, especially as the azimuth speed increases. It is important to note that the azimuth speed is the yaw rate of the ship at $\delta = 0$, as mentioned earlier. Appendix (F.1) presents a detailed analysis of the effect of azimuth speed on the duct.

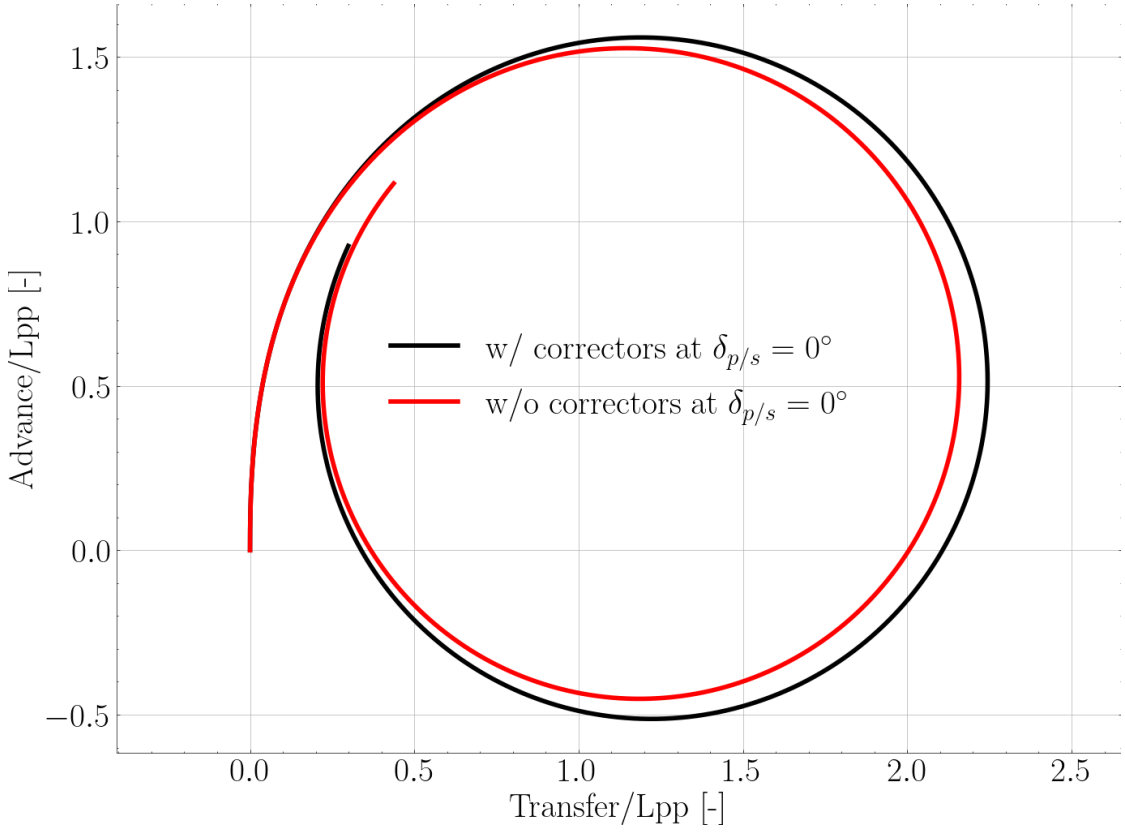

Figure 6.27: The turning circle maneuver with and without the corrector (see Eq. (6.26)).

The results of changes in azimuth speed can be seen in Fig. (6.28). The degradation in performance is observed at slow azimuth speed compared to the other two cases. The time required to reach an azimuth angle of 30° is 30 seconds at slow azimuth speed, 6 seconds at medium azimuth speed, and 3.33 seconds at high azimuth speed. The duration of the displayed circles has been set to 5 minutes. The performance of the

azimuth thruster at medium and high speeds is not remarkable. Turning circle diameters are nearly identical in all three cases.

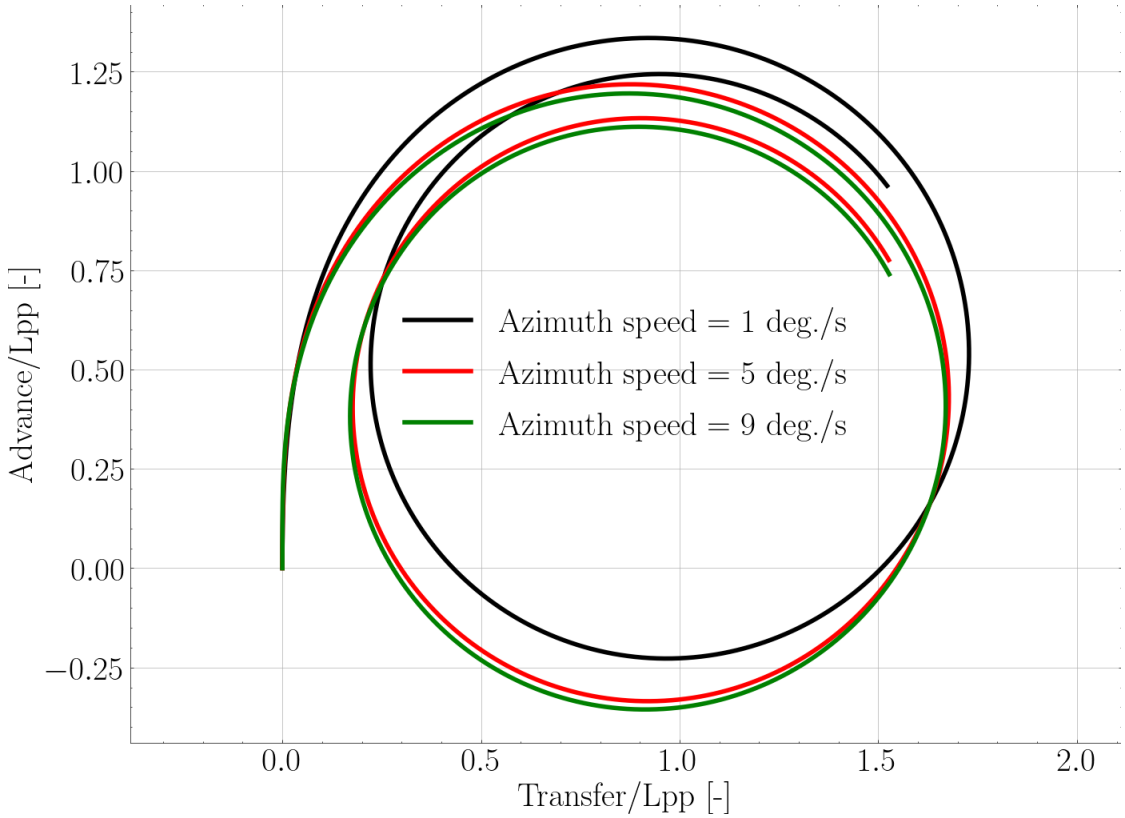

Figure 6.28: The turning circle maneuver at steering angle 30° at different azimuth speeds.

The ship performs both transverse and yaw motions during the ship maneuver. The cross-flow velocity v_q towards the thruster is given by

$$v_q = c_1 v_s + c_2 r x_{\text{prop}}, \tag{6.27}$$

where v_s is the transverse velocity of the ship, x_{prop} is the distance from the azimuth thruster to the ship's center of gravity, r is the ship's yaw rate, and c_1 and c_2 represent the reduction of the transverse velocity caused by the separated flow. The recommendations can be found in Krüger [6]. The effective inflow angle δ_{eff} at zero δ is then

$$\delta_{\text{eff}} = \arctan\left(\frac{v_q}{v_a}\right). \tag{6.28}$$

According to Krüger [6], for a conventional fixed pitch propeller with a steering rudder, the values of c_1 are between 0.35 and 0.4, and the values of c_2 are between 0.65 and

0.70. A slight improvement in the wake field can be observed with a twin-screw vessel. Therefore, the values of c_1 and c_2 are assumed to be 0.45 and 0.75, respectively.

As shown in Tab. (6.13), the cross-flow induced by the yaw rate is more pronounced than the cross-flow induced by the ship's transverse motion. If both factors are considered, they differ from 1, and the angle of inflow to the azimuth thrusters can be reduced. This will result in a decrease in the performance of the azimuth thrusters in terms of the ship's turning circle maneuver. Fig. (6.29) shows a comparison between considering and disregarding the effect of separated cross-flow.

As mentioned earlier, both thrusters will encounter an inflow from the windward side as a result of the positive yaw rate. To assist the bow thruster, the azimuth thruster should be deflected toward the port side. Fig. (6.28) illustrates the variations in the turning circles in response to the steering angles of the two azimuth thrusters. It is expected that the tactical diameter decreases as the steering angle increases. Tab. (6.14) shows that even at a steering angle of $-15°$ the effective inflow angle remains positive. This suggests that the duct has a detrimental effect, as it generates a counteracting transverse force. The presence of the investigated duct in the accelerated type may be inappropriate for the ship's turning ability.

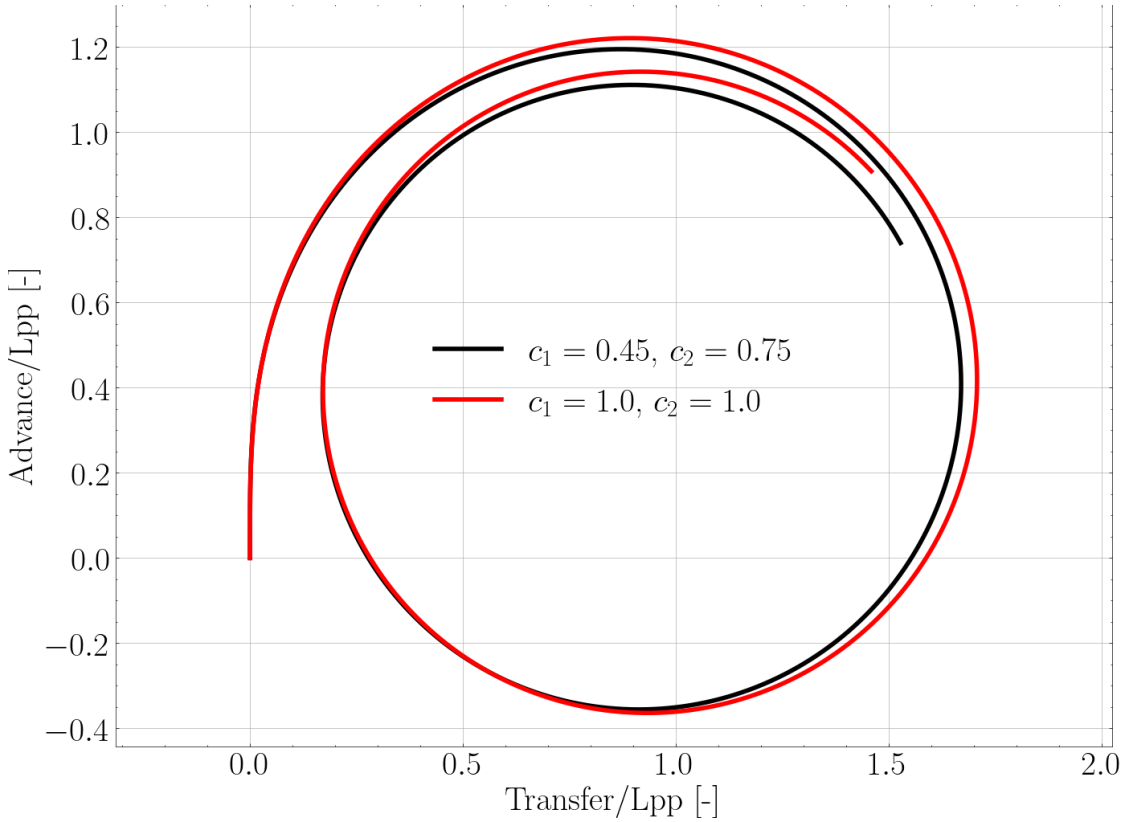

Figure 6.29: The effect of two factors representing the separated cross-flow on the ship's turning maneuver at $\delta = 0°$.

Table 6.13: The resultant cross-flow velocity experienced by the thrusters at $\delta = 0°$.

	Crossing flow		
	Ship transverse velocity [m/s]	Yaw induced transverse velocity [m/s]	Sum [m/s]
c1=1, c2 =1	-0.439	1.989	1.550
c1=0.45, c2=0.75	-0.208	1.541	1.333

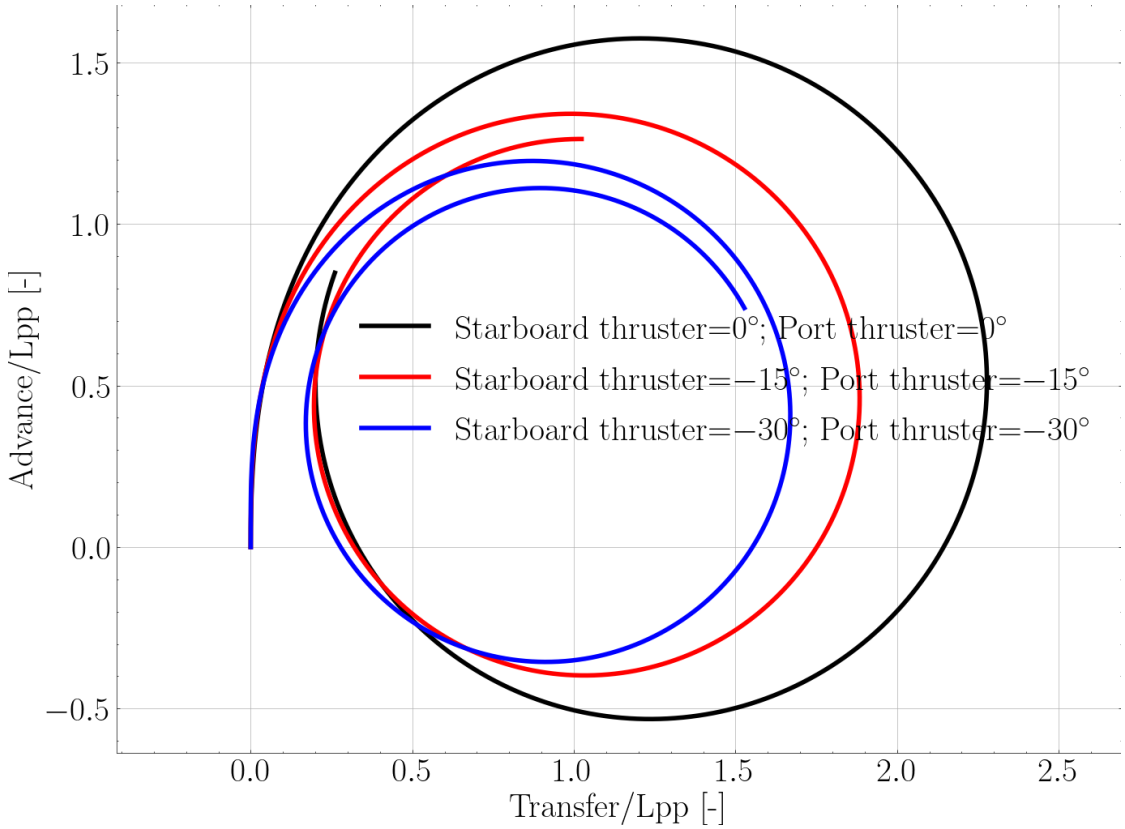

Figure 6.30: Turning circle maneuver at different azimuth angles δ.

Table 6.14: The parameters in the turning circle maneuver at different azimuth angles.

Thruster steering angle [°]	**Crossing flow velocity** [m/s]	**Ship heading angle** [°]	**Thruster inflow angle** [°]
0	1.024	4.613	18.614
-15	1.188	6.715	7.615
-30	1.333	8.336	-4.686

The above findings are based on the assumption that both thrusters have the same steering angle. If one azimuth thruster, for instance, the starboard thruster, does not work adequately, the maneuver can only be assisted by the port side thruster. Fig. (6.31) shows that the port side thruster must be deflected by $-60°$ to achieve a similar turning circle maneuver as both thrusters operating at the steering angle of $-30°$.

It is important to note that if the calculated drift angle of the ship during the maneuver is significantly larger than the angle specified in the yaw and combined sway-yaw tests (see Tab. (6.1)), the hydrodynamic derivatives obtained from both dynamic tests may be considered inappropriate in this circumstance. Thus, the maximum steering angle of both azimuth thrusters is limited. At a steering angle of $-30°$, the drift angle of the ship β is equal to 8.336°, as shown in Tab. (6.14).

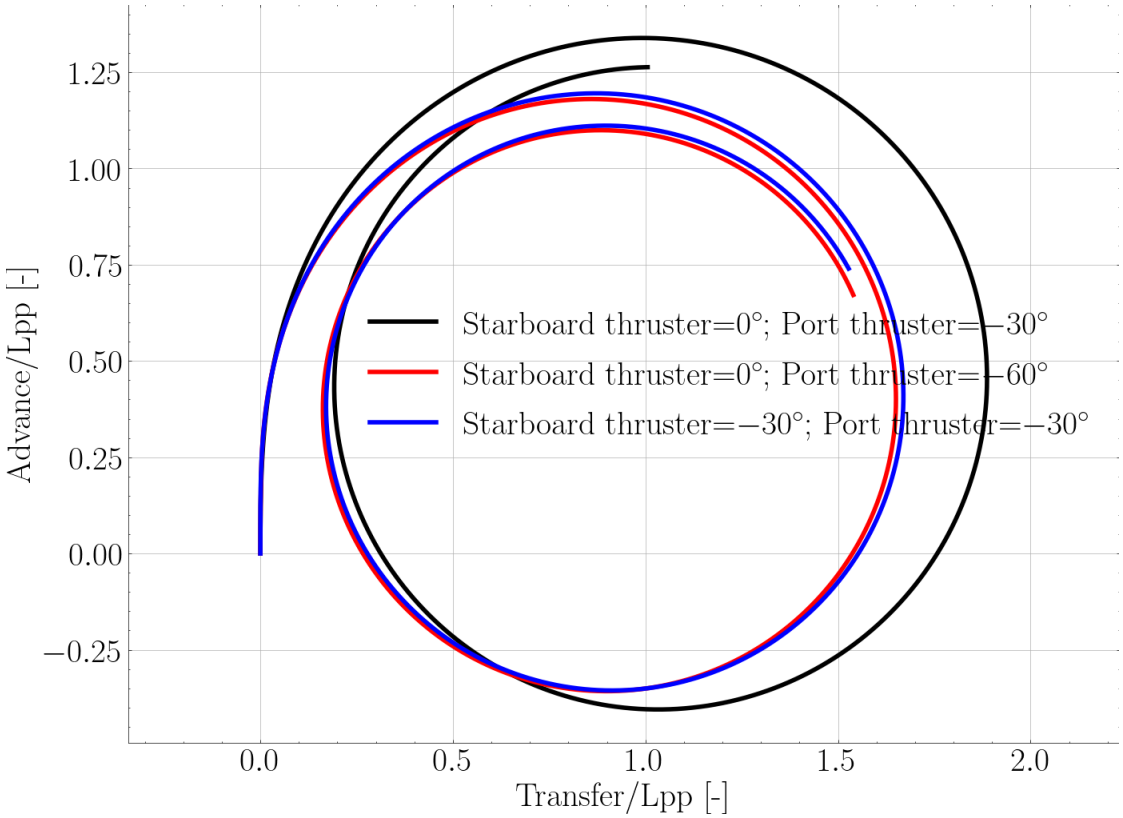

Figure 6.31: Turning circle maneuver supported by one azimuth thruster.

Fig. (6.32) shows the time-varying behavior of the velocities (u, v, r) and the ship drift angle β when both thrusters are set at an azimuth angle of $-30°$. The non-dimensional velocities after 5 minutes can be found in Tab. (6.15). Comparing the ITTC recommendations in Tab. (6.1), it is evident that the sway velocity amplitude is overestimated, while the yaw velocity amplitude is underestimated.

If the value of the yaw rate amplitude r' is set to 1, the oscillation frequency ω' must be adjusted accordingly. Fig. (6.33) shows different combinations of ω' and r'. The last combination seems to be suitable for the pure yaw test, but the value of ω' can lead to errors caused by the undesired memory effect.

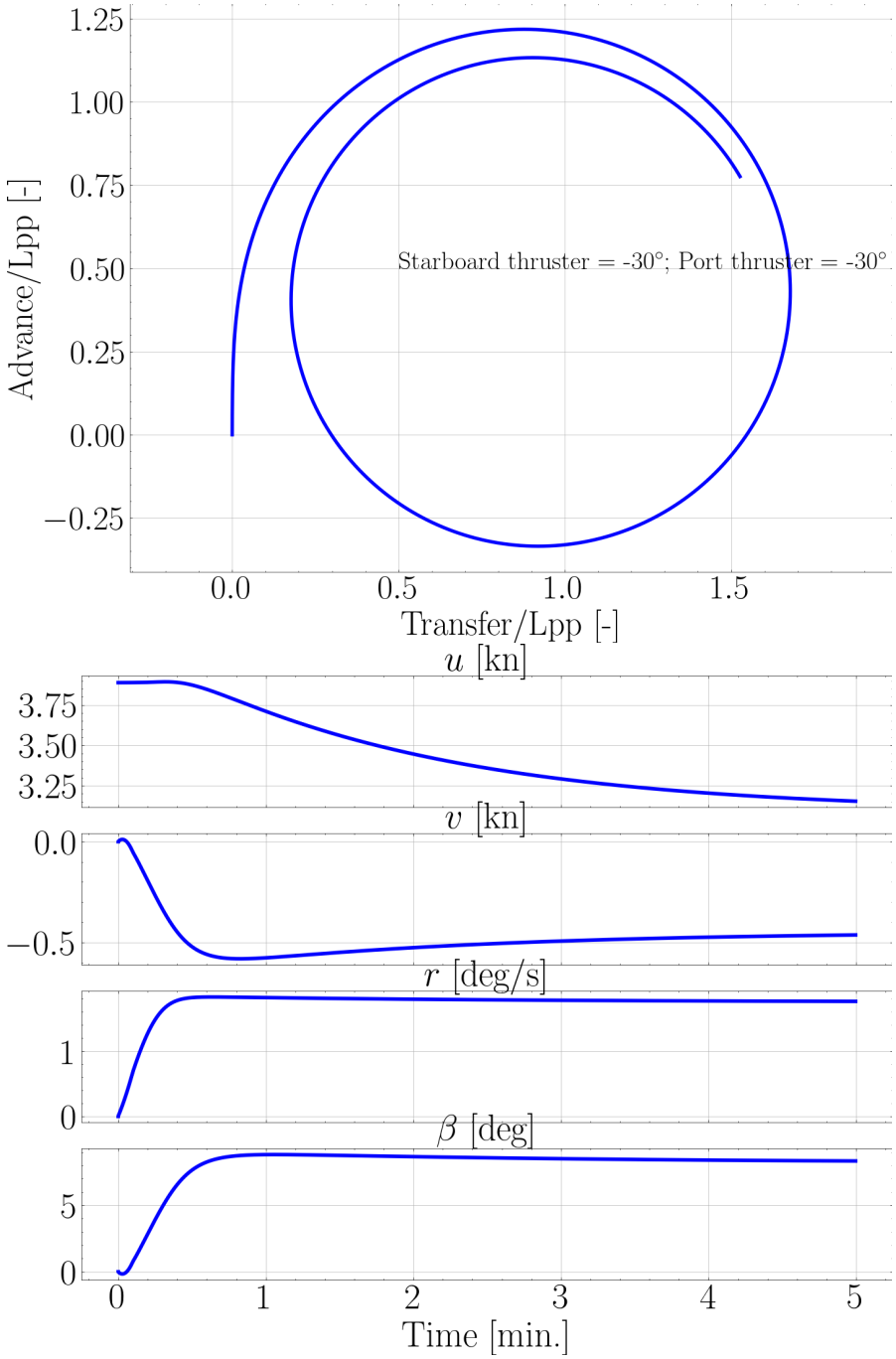

Figure 6.32: The time response of the maneuvering parameters at the steering angle of $\delta = -30°$.

Table 6.15: The dimensionless velocities after 5 minutes of the turning circle maneuver at $\delta = 30°$.

δ	u' [-]	v' [-]	r' [-]
30 [°]	0.811	-0.119	1.139

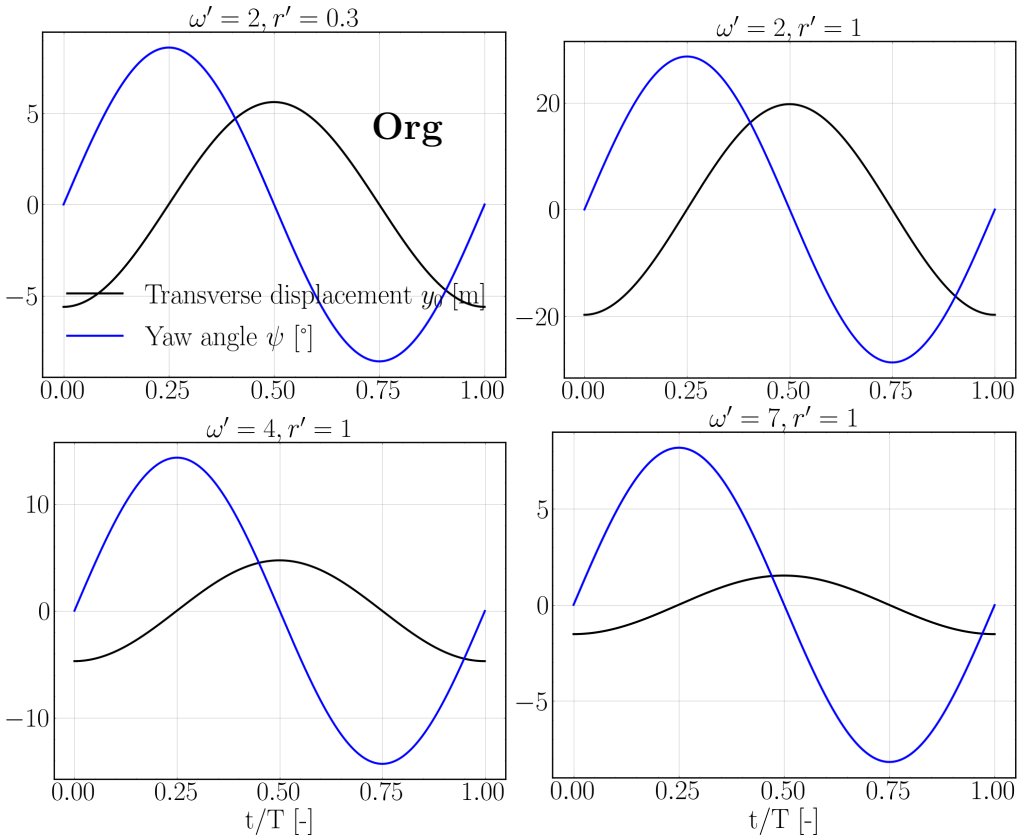

Figure 6.33: The time history of the transverse and the yaw oscillations of the ship with modified ω' and r' at $F_n = 0.074$.

7 Discussion and Conclusions

7.1 Summary

The combined effectiveness of maneuvering systems significantly affects the ability of a ship to maneuver at low speeds. In this work, a ship maneuvering model was developed that integrates the effects of the bow thruster and two azimuth thrusters using hydrodynamic derivatives obtained from PMM tests. The model was developed through a bare-hull study, in which the determination of the critical hydrodynamic coefficients was performed using two different approaches. Several turning maneuvers were performed under different operating conditions, such as changes in azimuth speed, steering angle, and influence of the wake field of the hull.

The following main points are addressed:

- The coefficients obtained from the operation of the tunnel thrusters were compared to those of the bare hull, providing insight into the impact of the thrusters on the vessel's maneuvering performance.
- Significant maneuvering coefficients were identified through numerical turning circle simulations.
- An azimuth thruster model was developed based on the longitudinal force equilibrium, and it was shown that the relationship between the transverse force and the azimuth angle is an odd function. The operating tunnel thruster was found to mainly affect the first-order maneuvering coefficients of this odd function, while the third-order coefficients show a remarkable similarity.
- A thorough investigation of the behavior of a tunnel thruster has been conducted, with particular emphasis on its interaction with the ship's hull.
- ANN has been used to facilitate the development of predictive models for azimuth thruster forces, especially under off-design conditions.

Furthermore, the ANN approach provided remarkably reasonable estimates to predict loads in complex flow behaviors, especially in large, separated flow areas. The accuracy of the model is related to both the amount and the quality of the training data. Bayesian regularization was applied to mitigate the negative effects of data noise on the network.

7.2 Conclusion

In azimuth thruster simulations, critical conditions have been found to occur when the azimuth angle δ is in the range of 60° to 120°. Changes in azimuth speed have a minimal effect on the longitudinal force, whereas the transverse force is significantly affected, primarily due to the effect of the duct. During the rotation of the propulsion unit, which induces an additional velocity component that changes the pressure distribution within the duct. The increasing forces can significantly exceed the forces experienced under the bollard pull condition, leading to higher bending moments and an increased risk of mechanical failure. In addition, the direction of the propeller rotation has a significant effect on the performance of the propulsion unit. When the propulsion unit is rotated to starboard, a right-handed propeller generates more loads than when it is rotated to port. Furthermore, forces in static and dynamic situations have been compared and found to have significant discrepancies at azimuth angles greater than about 90°, due to different appearances of the slipstream. Dynamic simulations provide a more accurate representation of real-world operational conditions and yield more accurate results. From a computational efficiency perspective, dynamic simulations take significantly less time than cumulative simulations at each azimuth angle.

In bow thruster simulations, changes in both the waterline angle and the frame angle affect the amount of separated flow at the 9 o'clock and 6 o'clock positions, respectively. The separated flow there becomes stronger as the ship's speed increases. Higher waterline and frame angles can result in greater variations in force amplitude, increasing thus the vibrations experienced by a ship. The main factor affecting the total lateral force is the suction force that the bow thruster slipstream exerts on the hull. The total lateral force decreases until a certain speed is reached, after which it begins to increase. This phenomenon is related to the changing relative position between the hull and the slipstream created by the bow thruster. However, the variation in tunnel propeller thrust is negligible. The thrust can be represented by calculating the thrust ratio (λ). The tunnel propeller torque follows a similar trend, indicating that the MC is not greatly affected by variations in external conditions.

During PMM test simulations, the hydrodynamic derivatives can only be considered accurate within a certain range of yaw amplitudes. There may be inaccuracies in predicting the hydrodynamic derivatives beyond this range. Increasing the circular frequency ω' can reduce the yaw amplitude. However, this also increases the influence of the memory effect. A smaller circular frequency means a longer period, especially at a lower speed. This longer period increases the computational time of the simulation. A trade-off must be made between the memory effect and circular frequency, taking into account both computational accuracy and computational time.

7.3 Future Work

For future work, several aspects should be considered.

- In the numerical investigations conducted, both azimuth thrusters are still operating in the first quadrant. The influence of the hull on the azimuth thruster is crucial. The interaction effects of the slipstream of the azimuth thrusters on the hull, such as the Coanda effect, should be further investigated in various operating situations such as dynamic positioning.
- The flow behavior on the hull, such as the separation flow, can be directly influenced by the slipstream induced by the bow thruster. The changing wake field in turn can have a direct effect on the performance of the main propulsion systems. The interaction between the bow thruster and the main propulsion systems is therefore a very important issue for overall ship performance.
- The duct has a detrimental effect on turning ability, as it generates opposing transverse force and moment, as shown in Appendix (F.1). This effect may become significant at reduced ship speeds. Future studies should evaluate the performance of propulsion devices without the duct.
- The suction force generated by the bow thruster's slipstream creates a negative yaw moment relative to the ship's center of gravity, resulting in a small drift angle compared to the effect of the rudder. The location where this suction force acts varies with the ship's speed. Therefore, it is recommended to extend and further verify the maneuvering model developed in Eqs. (6.22) through (6.24) at even lower speeds.
- For low-speed maneuvers, the coefficient-based method may not be practical due to multiple interactions and a long simulation time. A free running test should be more appropriate to simulate the motion of the ship at low speeds.
- Due to the relatively small steering azimuth angles involved in the simulation of the turning circle, the investigations carried out within this thesis do not fully demonstrate the wide capabilities of using ANN. However, the neural network-based model could also be used to predict the operating performance of the main propulsion systems in dynamic positioning systems where larger steering angles are applied. Furthermore, it could effectively predict the loading regarding the complex flow characteristics resulting from thruster-hull and thruster-thruster interactions.

Bibliography

[1] J. Brix. *Manoeuvring Technical Manual*. Seehafen Verlag, Hamburg, 1993.

[2] Schottel rudder propeller (srp) [online]. 2021. URL: https://www.schottel.de/en/portfolio/products/product-details/srp-schottel-rudderpropeller [last checked 2021-8-12].

[3] ITTC. Proceedings of 25th ittc - volume i. *The Manoeuvring Committee - Final Report and Recommendations to the 25th ITTC*, 2008.

[4] C. Crane, J. Eda, and A. Landsburg. *Principles of Naval architecture III: Motion in Waves and Controllability*. The Society of Naval Architects and Marine Engineers, second revision edition, 1989.

[5] M. L. Albertson, R. A. Jensen, and H. Rouse. Diffusion of submerged jets. *American Society of civil engineers*, 2409:132–142, 1950. doi:https://doi.org/10.1061/TACEAT.0006302.

[6] S. Krueger. *Lecture: Abschätzung der Eigenschaften von Azimuth-Antrieben in der Projektphase*. Hamburg, 2001.

[7] U. Nienhuis. Analysis of thruster effectivity for dynamic positioning and low speed manoeuvering. URL: https://repository.tudelft.nl/islandora/object/uuid%3Afdbb1863-e656-48b5-b669-d5ad12580016.

[8] ITTC. Full scale manoeuvring trials. *The International Towing Tank Conference*, 2017.

[9] M. Abdel-Maksoud. *Lecture: Manövrierfähigkeit von Schiffen*. Hamburg University of Technology, Hamburg, 2011.

[10] J. Artyszuk. Pivot point in ship manoeuvring. *Scientific Journals*, pages 13–24, 2010.

[11] W. Gierusz. Simulation model of the LNG carrier with podded propulsion, Part II: Full model and experimental results. 123:28–44. URL: https://linkinghub.elsevier.com/retrieve/pii/S0029801816302037, doi:10.1016/j.oceaneng.2016.06.024.

[12] M. Reichel. Longitudinal motion due to action of tunnel thrusters. *Polish Maritime Research*, 25:74–79, 05 2018. doi:10.2478/pomr-2018-0026.

[13] P. Mucha and O. El Moctar. Revisiting mathematical models for manoeuvring prediction based on modified Taylor-series expansions. 62(2):81–96. URL: http://www.tandfonline.com/doi/full/10.1179/0937725515Z.00000000015, doi:10.1179/0937725515Z.00000000015.

[14] B. el Moctar, U. Lantermann, and P. Mucha. Numerische methoden zum manövrierverhalten von schiffen. *Kolloquium Wechselwirkung Schiff/Wasserstraße mit Auswirkungen auf Nautik und schiffsinduzierte Belastungen*, pages 93–100, 2015.

[15] A. Cura-Hochbaum. Virtual pmm tests for manoeuvring prediction. 11 2006.

[16] W. Gierusz. Simulation model of the LNG carrier with podded propulsion Part 1: Forces generated by pods. 108:105–114. URL: https://linkinghub.elsevier.com/retrieve/pii/S0029801815003443, doi:10.1016/j.oceaneng.2015.07.031.

[17] J. Hooft. The cross-flow drag on a manoeuvring ship. 21(3):329–342. URL: https://linkinghub.elsevier.com/retrieve/pii/0029801894900043, doi:10.1016/0029-8018(94)90004-3.

[18] H. Yasukawa and Y. Yoshimura. Introduction of MMG standard method for ship maneuvering predictions. 20(1):37–52. URL: https://link.springer.com/10.1007/s00773-014-0293-y, doi:10.1007/s00773-014-0293-y.

[19] C. Eminente and C. Coppola. Computational evaluation of ship manoeuvring performance based on scale model tests. 25:195–198, 1990.

[20] F. Stern, K. Agdraup, S. Y. Kim, A. C. Hochbaum, K. P. Rhee, F. Quadvlieg, P. Perdon, T. Hino, R. Broglia, and J. Gorski. Experience from SIMMAN 2008—The First Workshop on Verification and Validation of Ship Maneuvering Simulation Methods. 55(02):135–147. URL: https://onepetro.org/JSR/article/55/02/135/173675/Experience-from-SIMMAN-2008-The-First-Workshop-on, doi:10.5957/jsr.2011.55.2.135.

[21] K. Kijima, T. Katsuno, Y. Nakiri, and Y. Furukawa. On the manoeuvring performance of a ship with the parameter of loading condition. *Journal of The Society of Naval Architects of Japan*, 168:141–148, 1990.

[22] Y. Yoshimura and Y. Masumoto. Hydrodynamic database and manoeuvring prediction method with medium high-speed merchant ships and fishing vessels. 04 2012.

[23] M. Araki, H. Sadat-Hosseini, Y. Sanada, K. Tanimoto, N. Umeda, and F. Stern. Estimating maneuvering coefficients using system identification methods with experimental, system-based, and CFD free-running trial data. 51:63–84. URL: https://linkinghub.elsevier.com/retrieve/pii/S002980181200162X, doi:10.1016/j.oceaneng.2012.05.001.

[24] S. Hajizadeh, M. Seif, and H. Mehdigholi. Determination of ship maneuvering hydrodynamic coecients using system identication technique based on free-running model test. 23(5):2154–2165. URL: http://scientiairanica.sharif.edu/article_3945.html, doi:10.24200/sci.2016.3945.

[25] Y. Xue, Y. Liu, G. Xue, and G. Chen. Identification and Prediction of Ship Maneuvering Motion Based on a Gaussian Process with Uncertainty Propagation. 9(8):804. URL: https://www.mdpi.com/2077-1312/9/8/804, doi:10.3390/jmse9080804.

[26] Y. Jian-Chuan, Z. Zao-Jian, and X. Feng. Parametric Identification of Abkowitz Model for Ship Maneuvering Motion by Using Partial Least Squares Regression. *Journal of Offshore Mechanics and Arctic Engineering*, 137(3), 06 2015. 031301. URL: https://doi.org/10.1115/1.4029827, doi:10.1115/1.4029827.

[27] W. Zhou and M. Blanke. Identification of a class of nonlinear state-space models using RPE techniques. In *1986 25th IEEE Conference on Decision and Control*, pages 1637–1642. IEEE. URL: http://ieeexplore.ieee.org/document/4049054/, doi:10.1109/CDC.1986.267185.

[28] M. Gertler. The dtmb planar-motion-mechanism system. page 47, 07 1967.

[29] M. Chislett and J. Strom-Tejsen. Planar motion mechanism tests and full-scale steering and manoeuvring predictions for a mariner class vessel. *International shipbuilding progress*, 12:201–224, 1965.

[30] K. Wolff. Ermittlung der manövriereigenschaften fünf repraesentativer schiffstypen mit hilfe von cpmc-modellversuchen. *Schriftenreihe Schiffbau 412*, 1981.

[31] A. Mofidi. *Ship maneuvers with discretized propeller and coupled propeller model/CFD*. Doctor of philosophy. URL: https://iro.uiowa.edu/esploro/outputs/doctoral/Ship-maneuvers-with-discretized-propeller-and/9983776940002771?institution=01IOWA_INST.

[32] M. Greve, K. Wöckner-Kluwe, M. Abdel-Maksoud, and T. Rung. Viscous-inviscid coupling methods for advanced marine propeller applications. *International Journal of Rotating Machinery*, 2012, 01 2012. doi:10.1155/2012/743060.

[33] V. Krasilnikov. Self-propulsion rans computations with a single-screw container ship. 2013.

[34] J. C. Neizel, M. Pergande, S. Berger, and M. Abdel-Maksoud. Influence of the numerical propulsion modelling on the velocity distribution behind the propulsion device and maneuvering forces. *Proceedings of the Fourth International Symposium on Marine Propulsors*, 2015.

[35] M.-D. Le and D.-H. Nguyen. Estimation of ship hydrodynamic coefficients in harbor maneuvers and its applications. *IFAC Proceedings Volumes*, 33:227–232, 07 2000. doi:10.1016/S1474-6670(17)39633-7.

[36] D. Kang and K. Hasegawa. Prediction method of hydrodynamic forces acting on the hull of a blunt-body ship in the even keel condition. *Journal of Marine Science and Technology*, 12:1–14, 03 2007. doi:10.1007/s00773-006-0232-7.

[37] O. M. W. C. Wake adapted ducted propellers. *NSMB Wagningen Publication No. 345*, 1973.

[38] R. Norrby. The effectiveness of a bow thruster at low and medium ship speeds. *International Shipbuilding Progress/ISP 14-156-01*, 1967. doi:10.3233/ISP-1967-1415601.

[39] M. Chislett and O. Björheden. *Influence of Ship Speed on the Effectiveness of a Lateral-thrust Unit.* Hydro-og Aerodynamisk Laboratorium. Danish Technical Press, 1966.

[40] K. e. a. Taniguchi. Investigations into the fundamental characteristics and operating performances of side thruster. *Mitsubishi Technical Bulletin No.35, Mitsubishi Heavy Industries Ltd*, page 24, 1966.

[41] A. Lübcke and S. Krüger. Dynamic positioning in early design stages. 2014.

[42] Y. Feng, Z. Chen, Y. Dai, Z. Zhang, and P. Wang. An experimental and numerical investigation on hydrodynamic characteristics of the bow thruster. 209:107348. URL: https://linkinghub.elsevier.com/retrieve/pii/S0029801820303802, doi:10.1016/j.oceaneng.2020.107348.

[43] J. Brix. *Querstrahlsteuer.* Forschungszentrum des Deutschen Schiffbaus, Hamburgische Schiffbauversuchsanstalt GmbH, 1978.

[44] S. I. Baniela. The performance of a tunnel bow thruster with slow speed ahead: A revisited issue. 62(4):631–642. URL: https://www.cambridge.org/core/product/identifier/S0373463309990166/type/journal_article, doi:10.1017/S0373463309990166.

[45] J. L. Beveridge. Design and Performance of Bow Thrusters. 9(04):439–453. URL: https://onepetro.org/MTSN/article/9/04/439/176530/Design-and-Performance-of-Bow-Thrusters, doi:10.5957/mt1.1972.9.4.439.

[46] J. Carlton. *Marine propellers and propulsion third edition.* Elsevier Ltd, 2012.

[47] J. S. Carlton. Podded propulsors: Some results of recent research and full scale experience. 7(1):1–14. URL: https://www.tandfonline.com/doi/full/10.1080/20464177.2008.11020208, doi:10.1080/20464177.2008.11020208.

[48] H. Glauert. A general theory of the autogyro. *ARC R & M*, 1111, 01 1926.

[49] J. W. Stettler. Steady and Unsteady Dynamics of an Azimuthing Podded Propulsor Related to Vehicle Maneuvering. URL: https://dspace.mit.edu/handle/1721.1/33164.

[50] H. Amini and S. Steen. Experimental and theoretical analysis of propeller shaft loads in oblique inflow. *Journal of Ship Research*, 55:268–288, 12 2011. doi:10.5957/JOSR.55.4.100044.

[51] A. Akinturk, M. Islam, B. Veitch, and P. Liu. Performance of dynamic azimuthing podded propulsor. *International Shipbuilding Progress*, 59:83–106, 01 2012. doi:10.3233/ISP-2012-0080.

[52] M. Islam, A. Akinturk, and B. Veitch. Performance aspects of podded propulsor in dynamic operating conditions. 62(3-4):139–160. URL: https://www.medra.org/servlet/aliasResolver?alias=iospress&doi=10.3233/ISP-150119, doi:10.3233/ISP-150119.

[53] H. Amini and S. Steen. Theoretical and experimental investigation of propeller shaft loads in transient conditions. *International Shipbuilding Progress*, 59, 04 2013. doi:10.3233/ISP-2012-0079.

[54] J. dang, J. Koning, J. Brouwer, and J. De Jong. Dynamic loads on mechanical azimuthing thrusters. 10 2013.

[55] M. F. Islam. Modeling techniques of puller podded propulsor in extreme conditions. *Journal of Ship Research*, 61(04):230–255, 12 2017. URL: https://doi.org/10.5957/JOSR.170039, arXiv:https://onepetro.org/JSR/article-pdf/61/04/230/2232352/sname-jsr-2017-61-4-230.pdf, doi:10.5957/JOSR.170039.

[56] P. Schiller, K. Wang, M. Palm, and M. Abdel-Maksoud. Unsteady loads on an azimuth thruster in off-design conditions. *Proceedings of the Fifth International Symposium on Marine Propulsors*, 2017.

[57] N. Berchiche, V. I. Krasilnikov, and K. Koushan. Numerical Analysis of Azimuth Propulsor Performance in Seaways: Influence of Oblique Inflow and Free Surface. 6(2):37. URL: https://www.mdpi.com/2077-1312/6/2/37, doi:10.3390/jmse6020037.

[58] A. Kumar and M. K. Das. Study of a turbulent dual jet consisting of a wall jet and an offset jet. 133(10):101201. URL: https://asmedigitalcollection.asme.org/fluidsengineering/article/doi/10.1115/1.4004823/395019/Study-of-a-Turbulent-Dual-Jet-Consisting-of-a-Wall, doi:10.1115/1.4004823.

[59] M. Wei, Y.-M. Chiew, and S.-C. Hsieh. Plane boundary effects on characteristics of propeller jets. 58(10):141. URL: http://link.springer.com/10.1007/s00348-017-2425-8, doi:10.1007/s00348-017-2425-8.

[60] P. A. Brandner. Performance and effectiveness of omni-directional stern drive tugs. URL: https://figshare.utas.edu.au/articles/thesis/Performance_and_effectiveness_of_omni-directional_stern_drive_tugs/23237402, doi: https://doi.org/10.25959/23237402.v1.

[61] F. Menter, M. Kuntz, and R. Langtry. Ten years of industrial experience with the sst turbulence model. *Heat and Mass Transfer*, 4, 01 2003.

[62] ANSYS. CFX-Solver Theory Guide, Turbulence and Wall Function Theory, Eddy Viscocity Turbulence Models. *ANSYS CFX, Documentation*, 2019.

[63] V. Krasilnikov. Numerical investigation into scale effect on the performance characteristics. *Proceedings of the Fifth International Symposium on Marine Propulsors*, 2017.

[64] J. Dang and H. Laheij. Hydrodynamic aspects of steerable thrusters. *Dynamic Positioning Conference*, 2004.

[65] M. Oosterveld. Wake adapted ducted propellers. URL: https://repository.tudelft.nl/islandora/object/uuid%3A549e4c44-cc16-41e7-9230-55afb799ad06.

[66] Moeri container ship (KCS) [online]. 2021. URL: http://www.simman2008.dk/KCS/kcs_geometry.htm [last checked 2021-8-13].

[67] P. Schiller, K. Wang, and M. Abdel-Maksoud. Flow study on a ducted azimuth thruster. In *International Conference on Computational Methods in Marine Engineering, MARINE 2017*, volume 2017, pages 184–195, 2017. URL: http://hdl.handle.net/11420/4135.

[68] S.-B. Müller. Numerische untersuchung der maßtabseffekte an schiffspropellern. URL: https://duepublico2.uni-due.de/receive/duepublico_mods_00024397.

[69] W. Mcculloch and W. Pitts. A logical calculus of ideas immanent in nervous activity. *Bulletin of Mathematical Biophysics*, 5:127–147, 1943.

[70] R. Kohavi and D. Wolpert. Bias plus variance decomposition for zero-one loss functions. 09 1997.

[71] A. Tikhonov. On the solution of ill-posed problems and the method of regularization. pages 501–504, 09 1963.

[72] A. Krogh and J. Hertz. A simple weight decay can improve generalization. In J. Moody, S. Hanson, and R. P. Lippmann, editors, *Advances in Neural Information Processing Systems*, volume 4. Morgan-Kaufmann, 1992. URL: https://proceedings.neurips.cc/paper/1991/file/8eefcfdf5990e441f0fb6f3fad709e21-Paper.pdf.

[73] S. Bos and E. Chug. Using weight decay to optimize the generalization ability of a perceptron. In *Proceedings of International Conference on Neural Networks (ICNN'96)*, volume 1, pages 241–246 vol.1, 1996. doi:10.1109/ICNN.1996.548898.

[74] D. Mackay. Bayesian interpolation. *Neural Computation*, 4:415–447, 1992.

[75] D. Rumelhart, E. H. Geoffrey, and R. J. Williams. Learning representations by back-propagating errors. *Nature*, 323:533–536, 1986.

[76] M. T. Hagan, H. B. Demuth, and M. H. Beale. Neural network design (2nd edition). pages 13–12–13–17, 2014. URL: https://hagan.okstate.edu/nnd.html.

[77] F. Dan Foresee and M. Hagan. Gauss-newton approximation to bayesian learning. In *Proceedings of International Conference on Neural Networks (ICNN'97)*, volume 3, pages 1930–1935 vol.3, 1997. doi:10.1109/ICNN.1997.614194.

[78] Levenberg–marquardt algorithm [online]. URL: https://en.wikipedia.org/wiki/Levenberg%E2%80%93Marquardt_algorithm [last checked 2024-5-21].

[79] MATLAB. *Bayesian regularization backpropagation.* The MathWorks Inc., Natick, Massachusetts, 2020.

[80] K.-J. Bladt. Beitrag zur auslegung von querschubanlagen mit propeller für schiffe).

[81] IMO. *Report of the maritime safety committee on its seventy-sixth session - Annex 6 - standards for ship maneuvrability.* 2012.

[82] L. Kobylinski and J. Nowicki. Manoeuvring characteristics of full-bodied ships with pod propulsion. *Maritime Transportation and Exploitation of Ocean and Coastal Resources*, pages 199–205, 2005.

[83] V. Bertram. *Practical Ship Hydrodynamics.* Elsevier Ltd, 2012.

[84] E. Lewandowski. *The Dynamics of Marine Craft: Maneuvering and Seakeeping.* World Scientific Publishing Co. Pte.Ltd, 2004.

[85] H. Yoon. Phase-averaged stereo-PIV flow field and force/moment/motion measurements for surface combatant in PMM maneuvers. URL: https://iro.uiowa.edu/esploro/outputs/doctoral/9983776767602771, doi:10.17077/etd.jgq7s29l.

[86] M. Vantorre and K. Eloot. Requirements for standard harmonic captive manoeuvring tests. *IFAC Proceedings Volumes: 4th IFAC Conference on Manoeuvring and Control of Marine Craft (MCMC '97), Briujuni, Croatia, 10-12 September*, 30:123 – 128, 09 1997. doi:https://doi.org/10.1016/S1474-6670(17)46501-3.

[87] ITTC. Captive model test procedure, 7.5-02-06-02. *The International Towing Tank Conference - Recommended Procedures and Guidelines*, 2014.

[88] ITTC. Guideline on use of rans tools for manoeuvring prediction, 7.5-03-04-01. *The International Towing Tank Conference - Recommended Procedures and Guidelines*, 2017.

[89] S. Krueger. *Lecture: Schiffspropeller*. Hamburg University of Technology, Hamburg, 2019.

[90] S. Toxopeus and G. Loeff. Manoeuvring aspects of fast ships with pods. *3rd International Euro Conference on High-Performance Marine Vehicles*, pages 392–406, 2002.

[91] S. B.Pope. *Turbulent Flows*. Cambridge University Press, Cornell University, 2000.

[92] M. T. Schobeiri. *Fluid Mechanics for Engineers*. Springer Berlin Heidelberg. URL: `http://link.springer.com/10.1007/978-3-642-11594-3`, `doi:10.1007/978-3-642-11594-3`.

A Application of Momentum Theorem to Bow Thrusters

The change in momentum flux at the boundaries of a control volume is equal to the force applied to it, since there is no flow across the upper and lower boundaries. As shown in Fig. (A.1), the difference in the momentum fluxes between the entrance and exit corresponds to the required force T in the axial direction.

$$T = \dot{m}(v_{\text{exit}} - v_{\text{entrance}}). \tag{A.1}$$

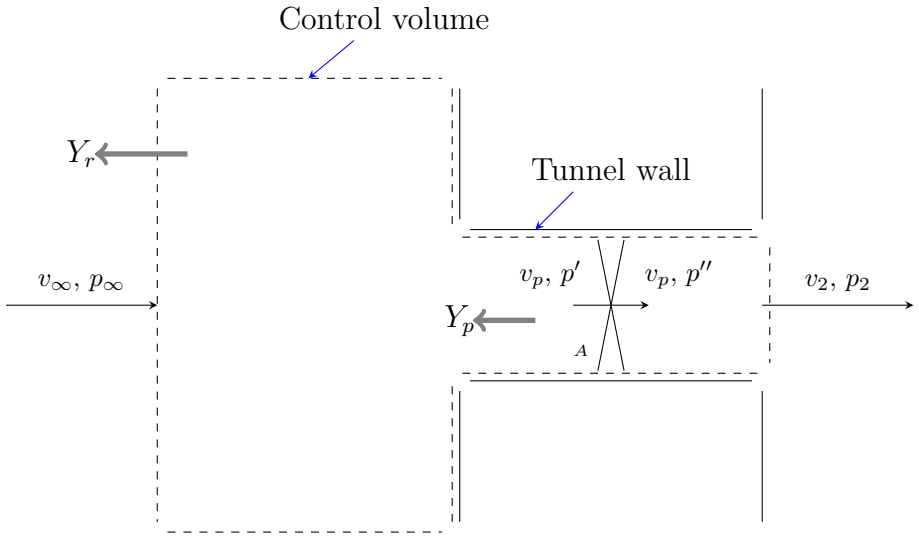

Figure A.1: Simplified geometry for a tunnel section.

The velocity at the tunnel exit is equal to the velocity inside the tunnel, denoted v_p, as a result of the continuity law if the tunnel cross-section area A remains constant. The propeller slipstream reaction force Y_r at rest can be expressed mathematically as

$$\begin{aligned} Y_r &= \dot{m} v_p \\ &= \rho A v_p^2. \end{aligned} \tag{A.2}$$

To determine the force generated by the propeller, we calculate the pressure difference across the propeller disk using Bernoulli's equation; at the front of the disk we have

$$p_\infty + \frac{\rho}{2} v_\infty^2 = p' + \frac{\rho}{2} v_p^2, \tag{A.3}$$

and after the propeller disk:

$$p'' + \frac{\rho}{2} v_p^2 = p_\infty + \frac{\rho}{2} v_p^2. \tag{A.4}$$

The jump of pressure is obtained by using Eq. (A.4) and Eq. (A.3) and yields

$$p'' - p' = -\frac{\rho}{2}(v_p^2 - v_p^2) + \frac{\rho}{2}(v_p^2 - v_\infty^2). \tag{A.5}$$

In the case of zero v_∞, Eq. (A.5) goes to:

$$p'' - p' = \frac{\rho}{2}(v_p^2). \tag{A.6}$$

The propeller thrust Y_p is then multiplied by the pressure jump by the cross area A:

$$\begin{aligned} Y_p &= (p'' - p')A \\ &= \frac{1}{2}\rho A(v_p^2). \end{aligned} \tag{A.7}$$

The average pressure in the free shear flows p_2 on the right side of Eq. (A.4) is assumed to be equal to the reference pressure p_∞. The reason can be explained by the RANS-equations:

$$\frac{\partial \bar{u}_i}{\partial x_i} = 0 \tag{A.8}$$

$$\rho \bar{u}_j \frac{\partial \bar{u}_i}{\partial x_j} = \frac{\partial}{\partial x_j}\left[-\bar{p}\delta_{ij} + \mu\left(\frac{\partial \bar{u}_i}{\partial x_j} + \frac{\partial \bar{u}_j}{\partial x_i}\right) - \rho\overline{u_i' u_j'}\right]. \tag{A.9}$$

The free shear flow is typically axis-symmetric (along the x-axis in which the main flow follows, as shown in Fig. (2.4)). Therefore, the two-dimensional flow is adequate. The mean momentum equations in the y-direction (perpendicular to x) can be obtained from Eq. (A.9) without consideration of the velocity in the z-direction, i.e.,

$$\rho \bar{u}\frac{\partial \bar{v}}{\partial x} + \rho \bar{v}\frac{\partial \bar{v}}{\partial y} = -\frac{\partial \bar{p}}{\partial y} + \mu\left(\frac{\partial^2 \bar{v}}{\partial x^2}\right) + \mu\left(\frac{\partial^2 \bar{v}}{\partial y^2}\right) - \rho\frac{\partial \overline{u'v'}}{\partial x} - \rho\frac{\partial \overline{v'v'}}{\partial y}. \tag{A.10}$$

The convection terms in Eq. (A.10) can be set to zero since the lateral average velocity of v is zero in the boundary layer approximation for the laminar flow. In the case of fully

developed turbulent-free shear flows, the laminar viscosity μ is negligible. Moreover, the axial derivatives of the Reynolds stresses are small compared to the lateral derivatives (see Pope [91]), which leads to simplified mean momentum equations in the y-direction:

$$0 = -\frac{\partial \bar{p}}{\partial y} - \rho \frac{\partial \overline{v'v'}}{\partial y}. \tag{A.11}$$

After the integration to y from 0 to ∞, one obtains

$$\bar{p} = p_\infty - \rho \overline{v'v'}. \tag{A.12}$$

where p_∞ denotes the pressure in the free stream ($y \to \infty$) and the lateral fluctuation $\overline{v'}^2$ is negligible compared to $\overline{u}^2$ contributed to $\bar{p}$ (see Schobeiri [92]). Hence, the averaged pressure in the free jet can be obtained:

$$\bar{p} \approx p_\infty. \tag{A.13}$$

B Application of Momentum Theorem to Azimuth Thruster in Oblique Flow Condition

The derivation of the momentum equation for the oblique flow is similar to the classical momentum theory for axial flow (following Krüger [89]), in which the induced velocity on the propeller plane and at the exit can be defined as $v_{1x}(1+a)$ and $v_{1x}(1+b)$, respectively. The subscript x denotes the axial component. By the momentum theorem (Eq. (A.1)), the axial force acting on the control volume is

$$\begin{aligned} T &= \rho v_{px}(v_{2\mathrm{x}} - v_{1\mathrm{x}}) \\ &= \rho v_\infty \cos(\delta)(1+a)A(v_\infty \cos(\delta)b) \\ &= \rho A(v_\infty \cos(\delta))^2(1+a)b, \end{aligned} \tag{B.1}$$

where v_{px} denotes the component of v_p perpendicular to propeller plane (Fig. (B.1)).

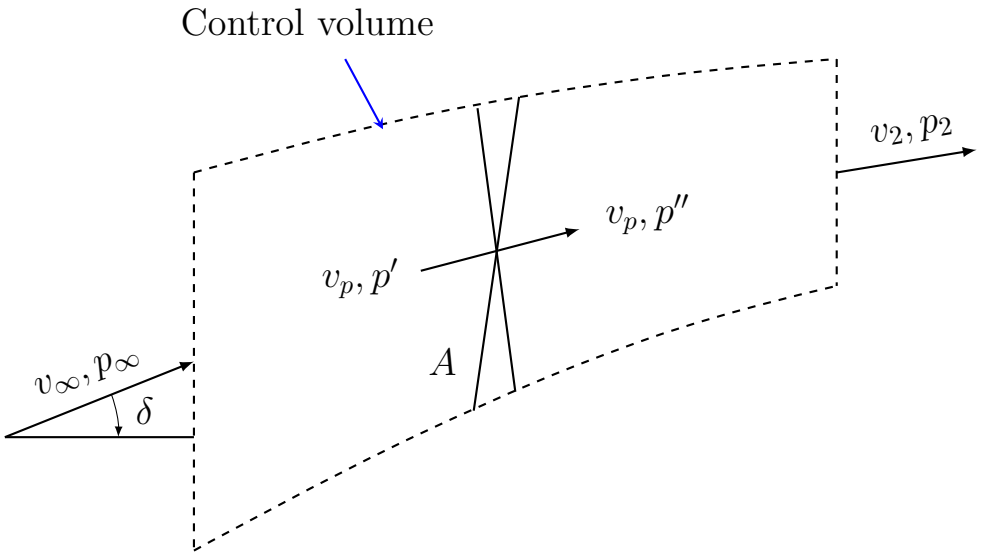

Figure B.1: Propeller disk model in oblique flow.

The thrust T has to be equal to the jump in pressure multiplied by the cross-section area A of the propeller disk. Bernoulli's equation is introduced in front of the propeller disk:

$$p_\infty + \frac{\rho}{2}(v_\infty \cos(\delta))^2 = p' + \frac{\rho}{2}(v_\infty \cos(\delta) + v_\infty \cos(\delta) a)^2, \tag{B.2}$$

and after the propeller disk:

$$p_\infty + \frac{\rho}{2}(v_\infty \cos(\delta) + v_\infty \cos(\delta) b)^2 = p'' + \frac{\rho}{2}(v_\infty \cos(\delta) + v_\infty \cos(\delta) a)^2. \tag{B.3}$$

The jump in pressure on the propeller disk is equal to

$$p'' - p' = \frac{\rho}{2}((v_\infty cos(\delta) + v_\infty \cos(\delta) b)^2 - v_\infty \cos(\delta)^2). \tag{B.4}$$

The propeller thrust is obtained, such as

$$\begin{aligned} T_p &= (p'' - p')A \\ &= A\frac{\rho}{2}((v_\infty \cos(\delta) + v_\infty \cos(\delta) b)^2 - v_\infty \cos(\delta)^2) \\ &= A\frac{\rho}{2}(v_\infty \cos(\delta))^2((1+b)^2 - 1). \end{aligned} \tag{B.5}$$

Using the relation of equality between Eq. (B.1) and Eq. (B.5) one yields

$$\begin{aligned} \rho A(v_\infty \cos(\delta))^2(1+a)b &= A\frac{\rho}{2}(v_\infty \cos(\delta))^2((1+b)^2 - 1) \\ ab &= \frac{b^2}{2}. \end{aligned} \tag{B.6}$$

The solution is $b = 2a$, which coincides with the result of the classical momentum theory for axial flow. By substituting b with $2a$ in Eq. (B.1), one obtains

$$\begin{aligned} T &= \rho A(v_\infty \cos(\delta))^2(1+a)b \\ &= 2\rho A \underbrace{(v_\infty cos(\delta) a)}_{v_{\mathrm{ix}}}(v_\infty cos(\delta) + \underbrace{(v_\infty \cos(\delta) a)}_{v_{\mathrm{ix}}} \\ &= 2\rho A v_{\mathrm{ix}}(v_\infty \cos(\delta) + v_{\mathrm{ix}}), \end{aligned} \tag{B.7}$$

C Mesh Dependence Study for the Hull

In the study of mesh dependence, three meshes with identical resolutions near the wall were generated, each with a y^+ value close to 1 for the full-scale ship. The main differences in mesh resolution are observed in the longitudinal direction of the hull, as shown to the left of Fig. (C.1). On its right side, the variation of the longitudinal force is presented. The x-axis represents the number of cells, while the y-axis shows the resistance normalized to the resistance from the result based on the finest grid. A slight decrease in resistance is observed as the number of cells increases; the maximum deviation is only 1.7% (see Tab. (C.1)). To achieve the most efficient computation, coarse mesh was used for the investigations.

Table C.1: Hull longitudinal force calculated using different mesh resolutions.

Mesh	Total number of nodes [milo.]	$X/X_{\text{fine mesh}}$ [-]
Coarse	5.5	1.017
Medium	9.4	1.005
Fine	14.0	1.000

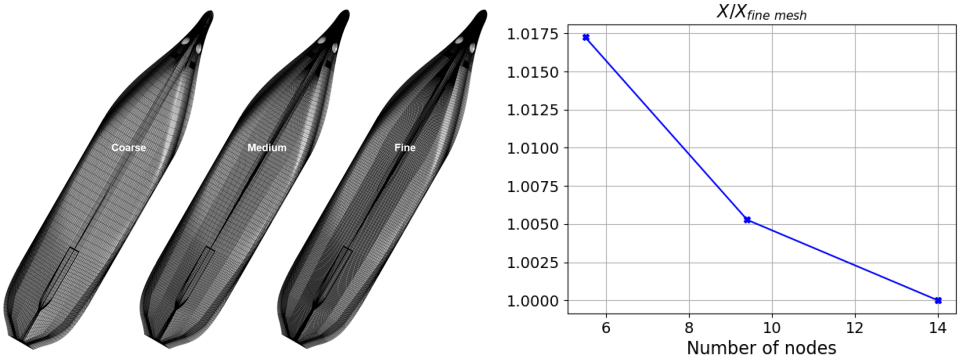

Figure C.1: Mesh sensitivity study at ship design speed.

D Performance of ANN for Force Prediction of Azimuth Thruster in Oblique Flow Condition

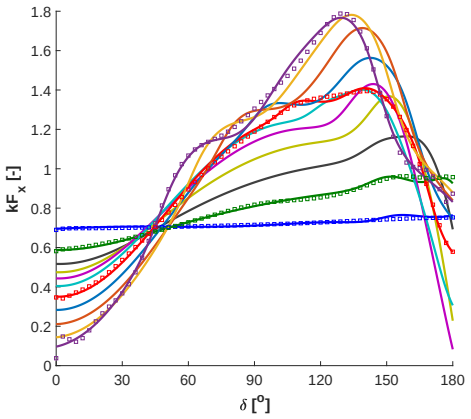

(a) kF_x: $f = 2$

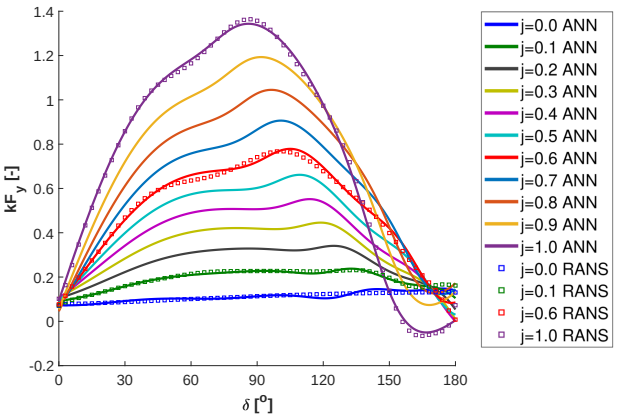

(b) kF_y: $f = 2$

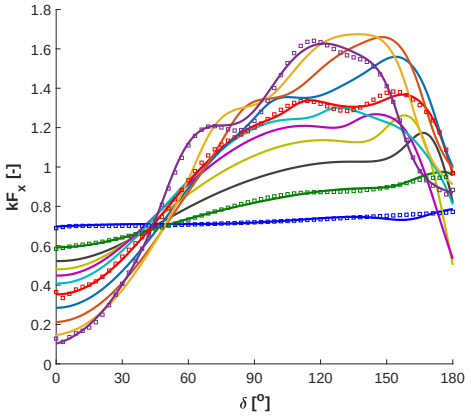

(c) kF_x: $f = 3$

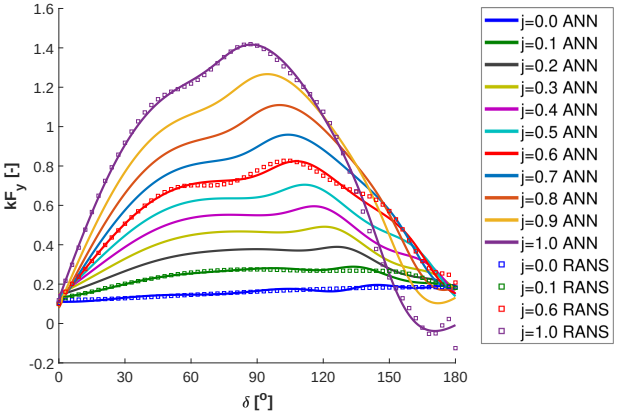

(d) kF_y: $f = 3$

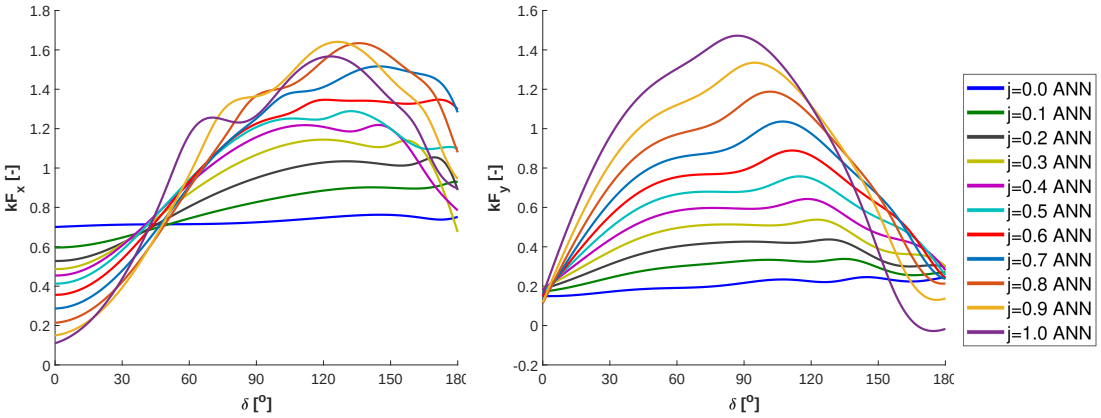

(e) kF_x: $f = 4$ **(f)** kF_y: $f = 4$

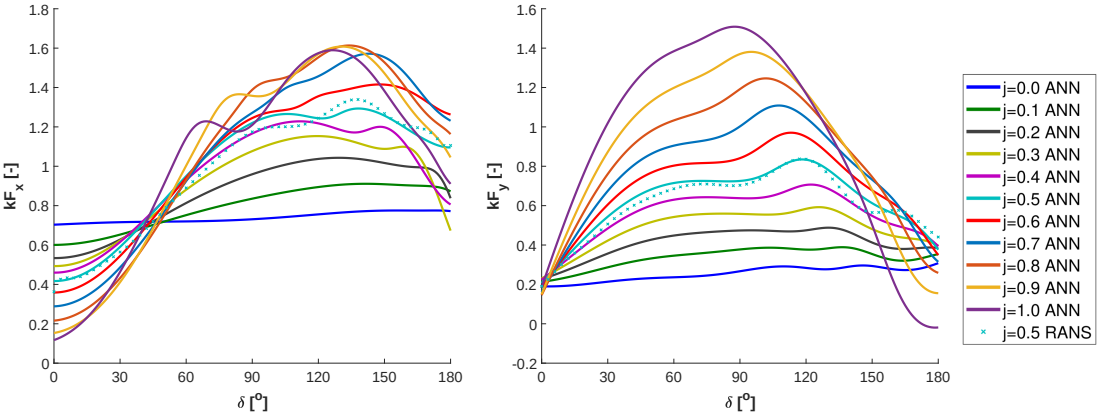

(g) kF_x: $f = 5$ **(h)** kF_y: $f = 5$

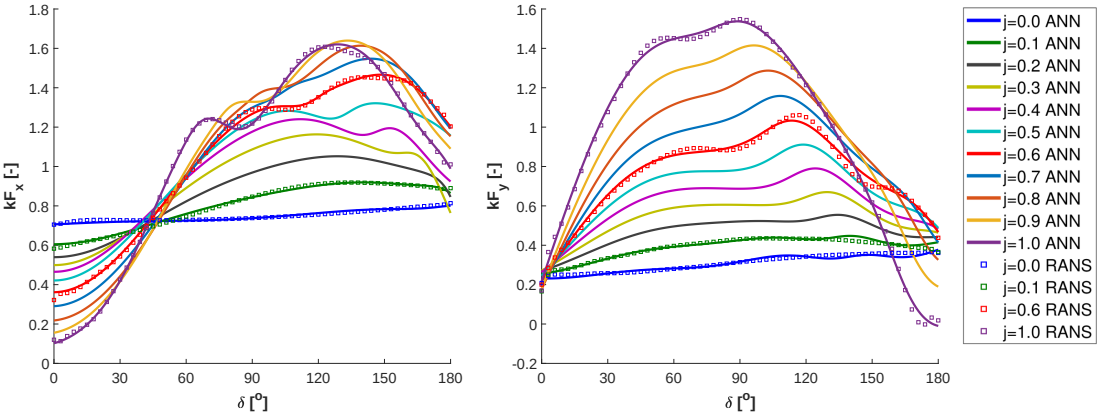

(i) kF_x: $f = 6$ **(j)** kF_y: $f = 6$

Figure D.1: Predicted results and network structures. Solid lines: Trained network predictions. kF_x: 3-12-1. kF_y: 3-9-1.

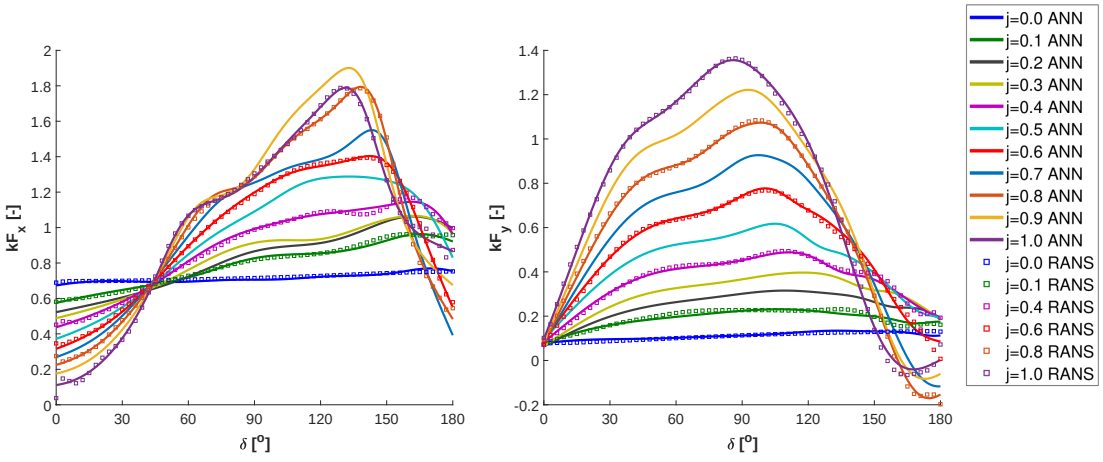

(a) kF_x: $f = 2$ **(b)** kF_y: $f = 2$

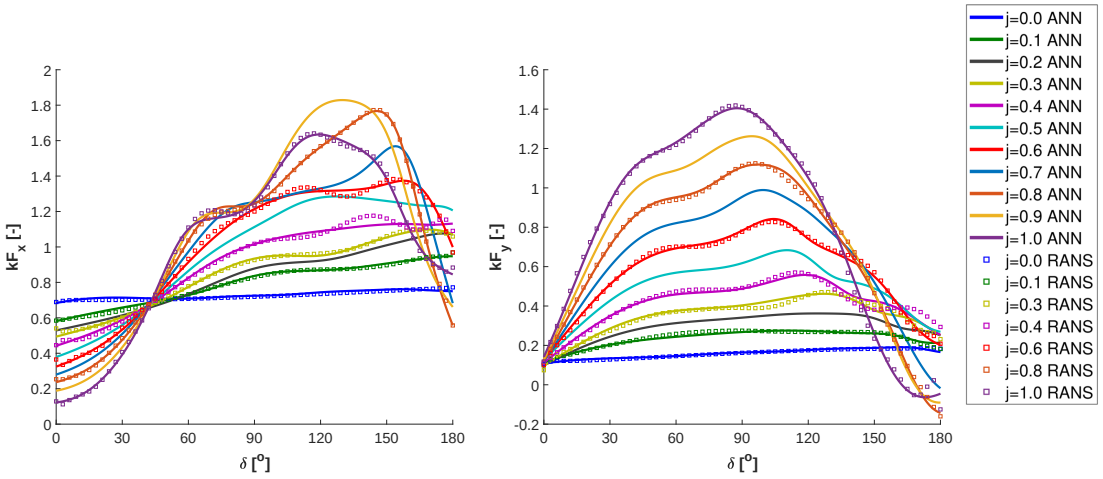

(c) kF_x: $f = 3$ **(d)** kF_y: $f = 3$

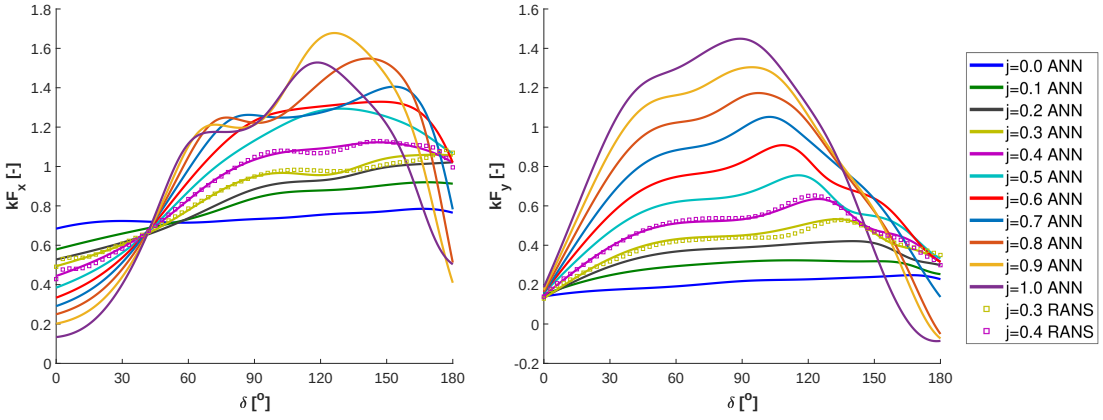

(e) kF_x: $f = 4$ **(f)** kF_y: $f = 4$

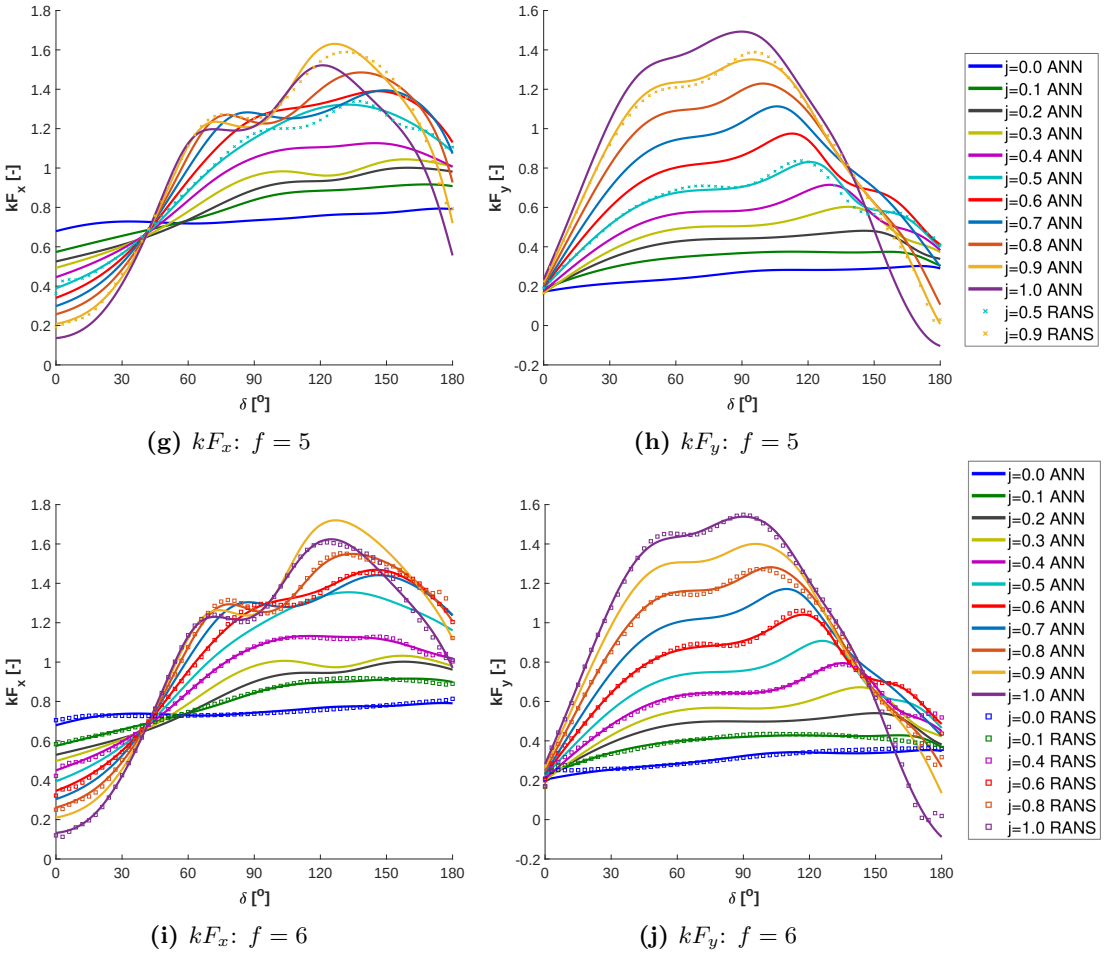

(g) kF_x: $f = 5$ **(h)** kF_y: $f = 5$

(i) kF_x: $f = 6$ **(j)** kF_y: $f = 6$

Figure D.2: Predicted results and network structures. Solid lines: Trained network predictions. kF_x: 3-12-3-1. kF_y: 3-9-3-1.

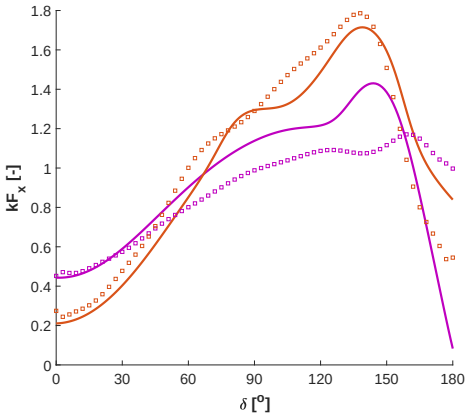

(a) $f = 2$: from original train dataset

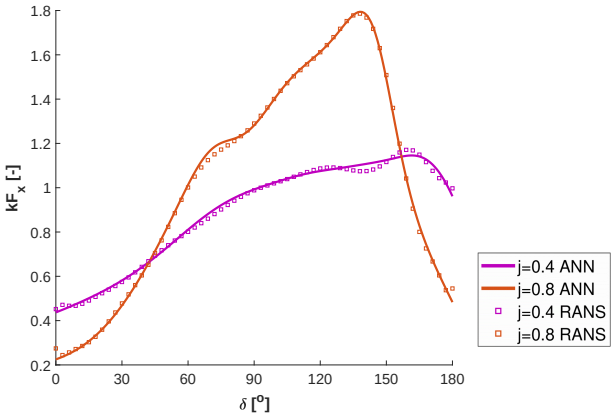

(b) $f = 2$: from extended train dataset

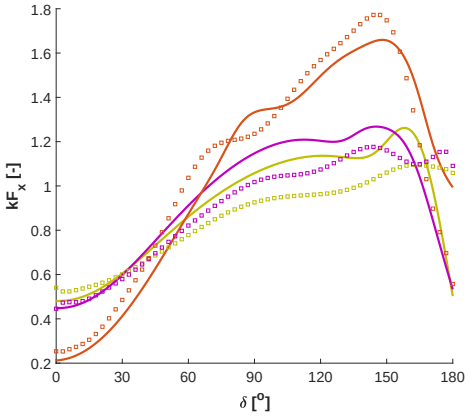

(c) $f = 3$: from original train dataset

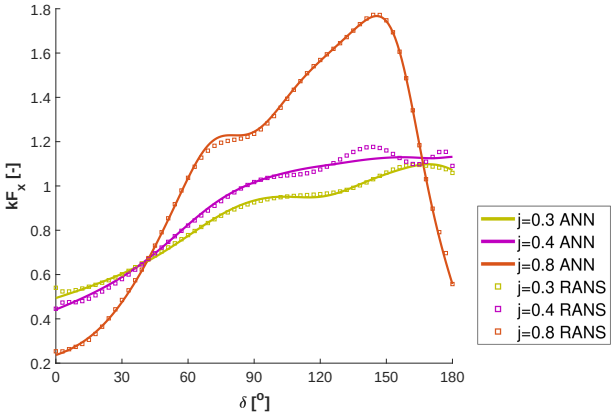

(d) $f = 3$: from extended train dataset

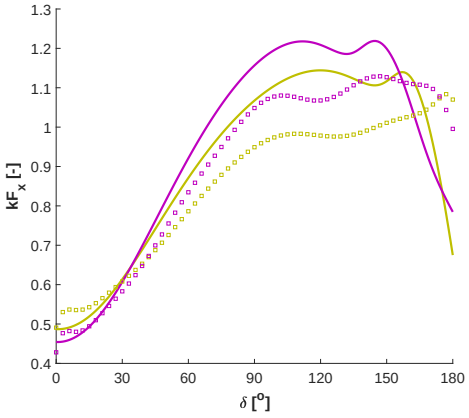

(e) $f = 4$: from original train dataset

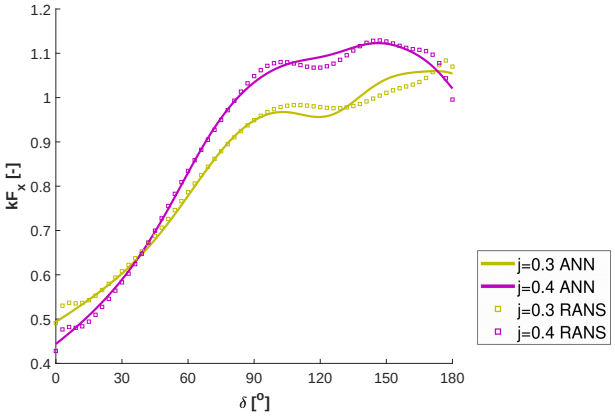

(f) $f = 4$: from extended train dataset

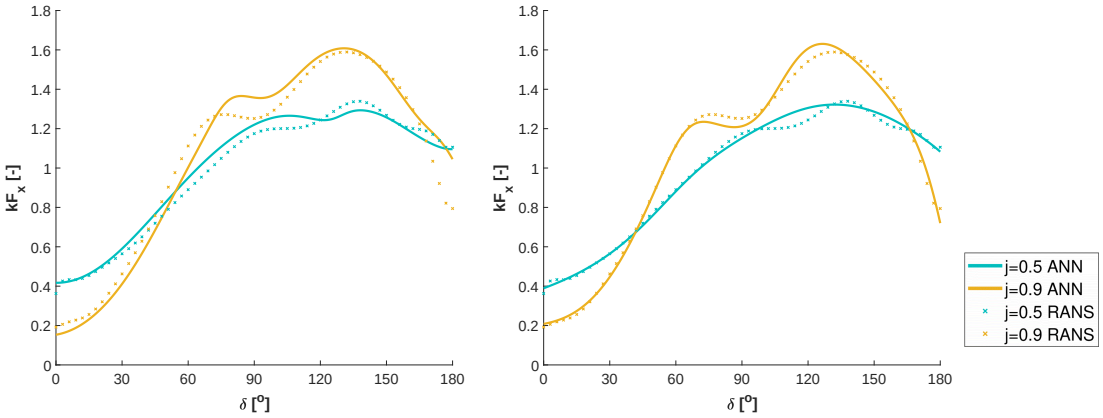

(g) $f = 5$: from original train dataset **(h)** $f = 5$: from extended train dataset

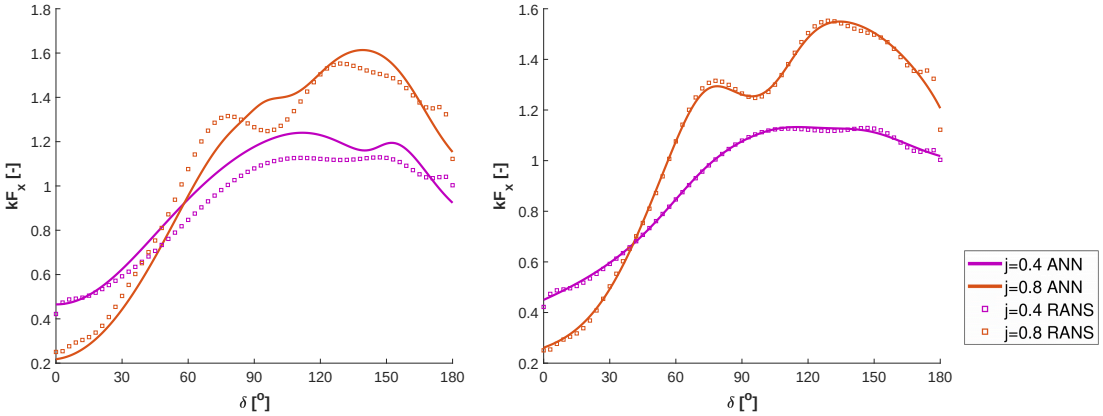

(i) $f = 6$: from original train dataset **(j)** $f = 6$: from extended train dataset

Figure D.3: Comparison of kF_x network interpolation and RANS results: Sparse training data (left), extended data (right).

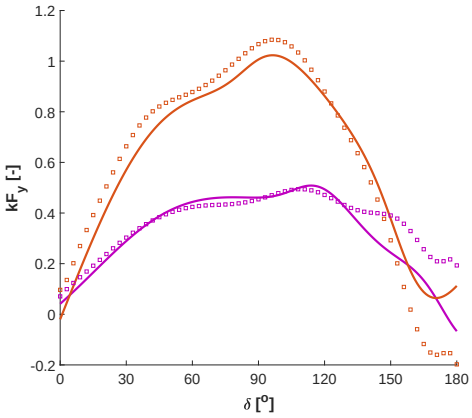

(a) $f = 2$: from original train dataset

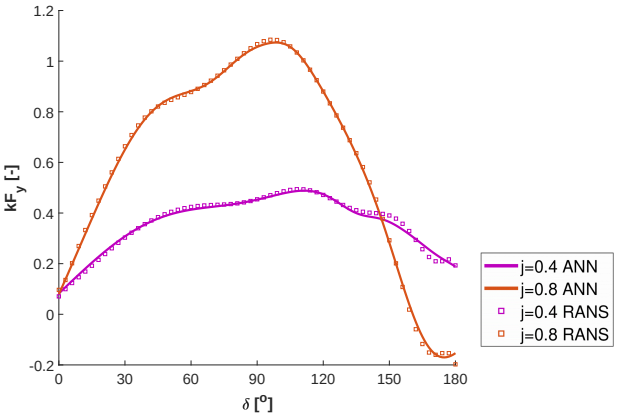

(b) $f = 2$: from extended train dataset

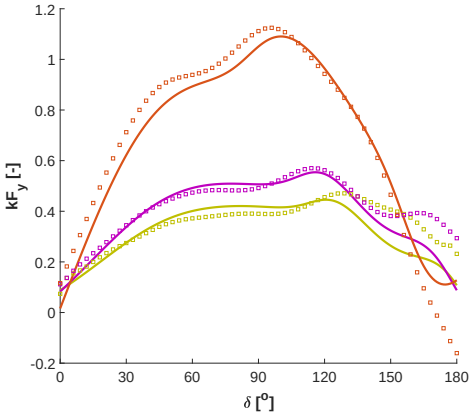

(c) $f = 3$: from original train dataset

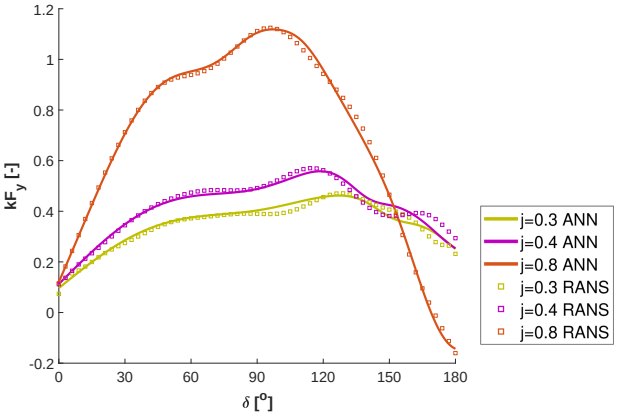

(d) $f = 3$: from extended train dataset

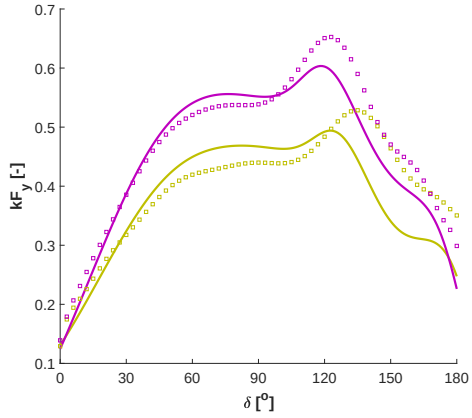

(e) $f = 4$: from original train dataset

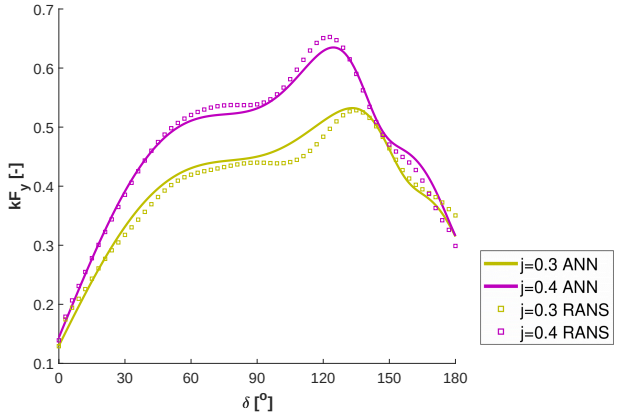

(f) $f = 4$: from extended train dataset

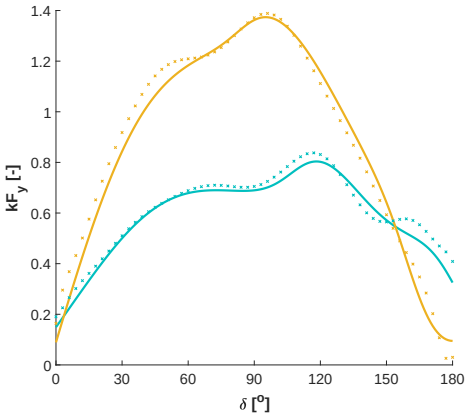

(g) $f = 5$: from original train dataset

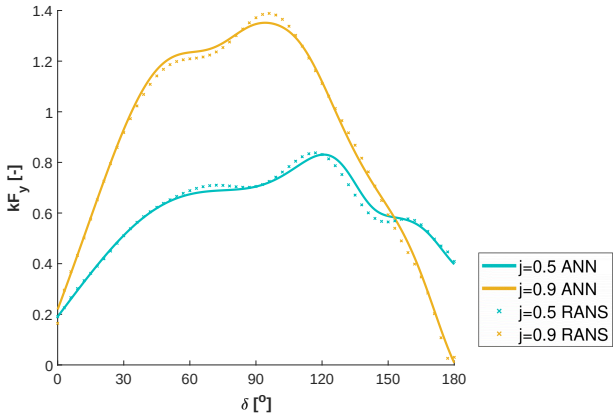

(h) $f = 5$: from extended train dataset

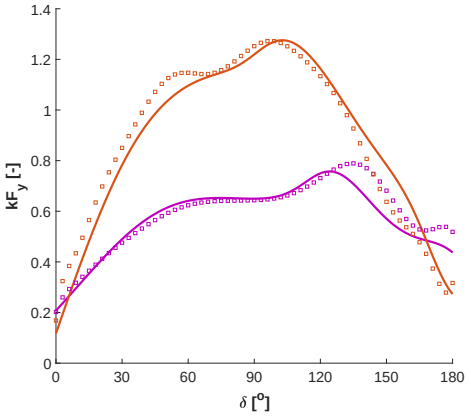

(i) $f = 6$: from original train dataset

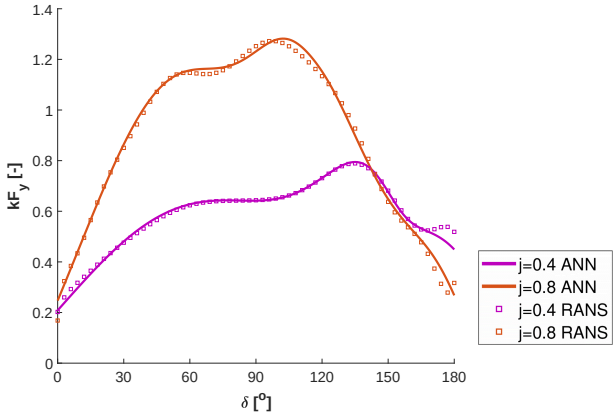

(j) $f = 6$: from extended train dataset

Figure D.4: Comparison of kF_y network interpolation and RANS results: with limited training data (left), extensive training data (right).

E Definition of Dimensionless Hydrodynamic Derivatives

$m' = \frac{\text{mass}}{0.5\rho L^3}$	$I'_{zz} = \frac{I_{zz}}{0.5\rho L^5}$	
u		
$X' = \frac{X}{0.5\rho U^2 L^2}$	$Y' = \frac{Y}{0.5\rho U^2 L^2}$	$N' = \frac{N}{0.5\rho U^2 L^3}$
$X'_u = \frac{X_u}{0.5\rho U^1 L^2}$	$Y'_u = \frac{Y_u}{0.5\rho U^1 L^2}$	$N'_u = \frac{N_u}{0.5\rho U^1 L^3}$
$X'_{uu} = \frac{X_{uu}}{0.5\rho U^0 L^2}$	$Y'_{uu} = \frac{Y_{uu}}{0.5\rho U^0 L^2}$	$N'_{uu} = \frac{N_{uu}}{0.5\rho U^0 L^3}$
$X'_{uuu} = \frac{X_{uuu}}{0.5\rho U^{-1} L^2}$	$Y'_{uuu} = \frac{Y_{uuu}}{0.5\rho U^{-1} L^2}$	$N'_{uuu} = \frac{N_{uuu}}{0.5\rho U^{-1} L^3}$
$X'_{\dot{u}} = \frac{X_{\dot{u}}}{0.5\rho U^0 L^3}$	$Y'_{\dot{u}} = \frac{Y_{\dot{u}}}{0.5\rho U^0 L^3}$	$N'_{\dot{u}} = \frac{N_{\dot{u}}}{0.5\rho U^0 L^4}$
$X'_{\dot{u}u} = \frac{X_{\dot{u}u}}{0.5\rho U^{-1} L^3}$	$Y'_{\dot{u}u} = \frac{Y_{\dot{u}u}}{0.5\rho U^{-1} L^3}$	$N'_{\dot{u}u} = \frac{N_{\dot{u}u}}{0.5\rho U^{-1} L^4}$
$X'_{\dot{u}uu} = \frac{X_{\dot{u}uu}}{0.5\rho U^{-2} L^3}$	$Y'_{\dot{u}uu} = \frac{Y_{\dot{u}uu}}{0.5\rho U^{-2} L^3}$	$N'_{\dot{u}uu} = \frac{N_{\dot{u}uu}}{0.5\rho U^{-2} L^4}$
v		
$X'_v = \frac{X_v}{0.5\rho U^1 L^2}$	$Y'_v = \frac{Y_v}{0.5\rho U^1 L^2}$	$N'_v = \frac{N_v}{0.5\rho U^1 L^3}$
$X'_{vv} = \frac{X_{vv}}{0.5\rho U^0 L^2}$	$Y'_{vv} = \frac{Y_{vv}}{0.5\rho U^0 L^2}$	$N'_{vv} = \frac{N_{vv}}{0.5\rho U^0 L^3}$
$X'_{vvv} = \frac{X_{vvv}}{0.5\rho U^{-1} L^2}$	$Y'_{vvv} = \frac{Y_{vvv}}{0.5\rho U^{-1} L^2}$	$N'_{vvv} = \frac{N_{vvv}}{0.5\rho U^{-1} L^3}$
$X'_{\dot{v}} = \frac{X_{\dot{v}}}{0.5\rho U^0 L^3}$	$Y'_{\dot{v}} = \frac{Y_{\dot{v}}}{0.5\rho U^0 L^3}$	$N'_{\dot{v}} = \frac{N_{\dot{v}}}{0.5\rho U^0 L^4}$
$X'_{\dot{v}v} = \frac{X_{\dot{v}v}}{0.5\rho U^{-1} L^3}$	$Y'_{\dot{v}v} = \frac{Y_{\dot{v}v}}{0.5\rho U^{-1} L^3}$	$N'_{\dot{v}v} = \frac{N_{\dot{v}v}}{0.5\rho U^{-1} L^4}$
$X'_{\dot{v}vv} = \frac{X_{\dot{v}vv}}{0.5\rho U^{-2} L^3}$	$Y'_{\dot{v}vv} = \frac{Y_{\dot{v}vv}}{0.5\rho U^{-2} L^3}$	$N'_{\dot{v}vv} = \frac{N_{\dot{v}vv}}{0.5\rho U^{-2} L^4}$
r		
$X'_r = \frac{X_r}{0.5\rho U^1 L^3}$	$Y'_r = \frac{Y_r}{0.5\rho U^1 L^3}$	$N'_r = \frac{N_r}{0.5\rho U^1 L^4}$
$X'_{rr} = \frac{X_{rr}}{0.5\rho U^0 L^4}$	$Y'_{rr} = \frac{Y_{rr}}{0.5\rho U^0 L^4}$	$N'_{rr} = \frac{N_{rr}}{0.5\rho U^0 L^5}$
$X'_{rrr} = \frac{X_{rrr}}{0.5\rho U^{-1} L^5}$	$Y'_{rrr} = \frac{Y_{rrr}}{0.5\rho U^{-1} L^5}$	$N'_{rrr} = \frac{N_{rrr}}{0.5\rho U^{-1} L^6}$
$X'_{\dot{r}} = \frac{X_{\dot{r}}}{0.5\rho U^0 L^4}$	$Y'_{\dot{r}} = \frac{Y_{\dot{r}}}{0.5\rho U^0 L^4}$	$N'_{\dot{r}} = \frac{N_{\dot{r}}}{0.5\rho U^0 L^5}$
$X'_{\dot{r}r} = \frac{X_{\dot{r}r}}{0.5\rho U^{-1} L^5}$	$Y'_{\dot{r}r} = \frac{Y_{\dot{r}r}}{0.5\rho U^{-1} L^5}$	$N'_{\dot{r}r} = \frac{N_{\dot{r}r}}{0.5\rho U^{-1} L^6}$
$X'_{\dot{r}rr} = \frac{X_{\dot{r}rr}}{0.5\rho U^{-2} L^6}$	$Y'_{\dot{r}rr} = \frac{Y_{\dot{r}rr}}{0.5\rho U^{-2} L^6}$	$N'_{\dot{r}rr} = \frac{N_{\dot{r}rr}}{0.5\rho U^{-2} L^7}$
rv		
$X'_{rv} = \frac{X_{rv}}{0.5\rho U^0 L^3}$	$Y'_{rv} = \frac{Y_{rv}}{0.5\rho U^0 L^3}$	$N'_{rv} = \frac{N_{rv}}{0.5\rho U^0 L^4}$
$X'_{rrv} = \frac{X_{rrv}}{0.5\rho U^{-1} L^4}$	$Y'_{rrv} = \frac{Y_{rrv}}{0.5\rho U^{-1} L^4}$	$N'_{rrv} = \frac{N_{rrv}}{0.5\rho U^{-1} L^5}$
$X'_{vvr} = \frac{X_{vvr}}{0.5\rho U^{-1} L^3}$	$Y'_{vvr} = \frac{Y_{vvr}}{0.5\rho U^{-1} L^3}$	$N'_{vvr} = \frac{N_{vvr}}{0.5\rho U^{-1} L^4}$
rvu		
$X'_{vu} = \frac{X_{vu}}{0.5\rho U^0 L^2}$	$Y'_{vu} = \frac{Y_{vu}}{0.5\rho U^0 L^2}$	$N'_{vu} = \frac{N_{vu}}{0.5\rho U^0 L^3}$
$X'_{vuu} = \frac{X_{vuu}}{0.5\rho U^{-1} L^2}$	$Y'_{vuu} = \frac{Y_{vuu}}{0.5\rho U^{-1} L^2}$	$N'_{vuu} = \frac{N_{vuu}}{0.5\rho U^{-1} L^3}$

$X'_{\dot{v}u} = \frac{X_{\dot{v}u}}{0.5\rho U^{-1}L^3}$	$Y'_{\dot{v}u} = \frac{Y_{\dot{v}u}}{0.5\rho U^{-1}L^3}$	$N'_{\dot{v}u} = \frac{N_{\dot{v}u}}{0.5\rho U^{-1}L^4}$
$X'_{\dot{v}uu} = \frac{X_{\dot{v}uu}}{0.5\rho U^{-2}L^3}$	$Y'_{\dot{v}uu} = \frac{Y_{\dot{v}uu}}{0.5\rho U^{-2}L^3}$	$N'_{\dot{v}uu} = \frac{N_{\dot{v}uu}}{0.5\rho U^{-2}L^4}$
$X'_{ru} = \frac{X_{ru}}{0.5\rho U^{0}L^3}$	$Y'_{ru} = \frac{Y_{ru}}{0.5\rho U^{0}L^3}$	$N'_{ru} = \frac{N_{ru}}{0.5\rho U^{0}L^4}$
$X'_{ruu} = \frac{X_{ruu}}{0.5\rho U^{-1}L^3}$	$Y'_{ruu} = \frac{Y_{ruu}}{0.5\rho U^{-1}L^3}$	$N'_{ruu} = \frac{N_{ruu}}{0.5\rho U^{-1}L^4}$
$X'_{\dot{r}u} = \frac{X_{\dot{r}u}}{0.5\rho U^{-1}L^4}$	$Y'_{\dot{r}u} = \frac{Y_{\dot{r}u}}{0.5\rho U^{-1}L^4}$	$N'_{\dot{r}u} = \frac{N_{\dot{r}u}}{0.5\rho U^{-1}L^5}$
$X'_{\dot{r}uu} = \frac{X_{\dot{r}uu}}{0.5\rho U^{-2}L^4}$	$Y'_{\dot{r}uu} = \frac{Y_{\dot{r}uu}}{0.5\rho U^{-2}L^4}$	$N'_{\dot{r}uu} = \frac{N_{\dot{r}uu}}{0.5\rho U^{-2}L^5}$
$X'_{rvu} = \frac{X_{rvu}}{0.5\rho U^{-1}L^3}$	$Y'_{rvu} = \frac{Y_{rvu}}{0.5\rho U^{-1}L^3}$	$N'_{rvu} = \frac{N_{rvu}}{0.5\rho U^{-1}L^4}$
$X'_{vvu} = \frac{X_{vvu}}{0.5\rho U^{-1}L^2}$	$Y'_{vvu} = \frac{Y_{vvu}}{0.5\rho U^{-1}L^2}$	$N'_{vvu} = \frac{N_{vvu}}{0.5\rho U^{-1}L^3}$
$X'_{\dot{v}vu} = \frac{X_{\dot{v}vu}}{0.5\rho U^{-2}L^3}$	$Y'_{\dot{v}vu} = \frac{Y_{\dot{v}vu}}{0.5\rho U^{-2}L^3}$	$N'_{\dot{v}vu} = \frac{N_{\dot{v}vu}}{0.5\rho U^{-2}L^4}$
$X'_{rru} = \frac{X_{rru}}{0.5\rho U^{-1}L^4}$	$Y'_{rru} = \frac{Y_{rru}}{0.5\rho U^{-1}L^4}$	$N'_{rru} = \frac{N_{rru}}{0.5\rho U^{-1}L^5}$
$X'_{\dot{r}ru} = \frac{X_{\dot{r}ru}}{0.5\rho U^{-2}L^5}$	$Y'_{\dot{r}ru} = \frac{Y_{\dot{r}ru}}{0.5\rho U^{-2}L^5}$	$N'_{\dot{r}ru} = \frac{N_{\dot{r}ru}}{0.5\rho U^{-2}L^6}$

F Some Illustrations from the RANS Simulations

F.1 Force on an Azimuth Thruster at $\delta = 30°$ for $J = 0.6$

Fig. (4.9) illustrates that the unit transverse force F_y is more responsive to changes in azimuth speed f than the unit longitudinal force F_x. For a more thorough investigation, the total unit forces F_x and F_y can be divided into propeller forces $Fp_{x,y}$, duct forces $Fd_{x,y}$, and housing forces $Fh_{x,y}$.

The transverse force for each component during a starboard rotation (positive z-axis) is given in Tab. (F.1). When f is zero, it means that the simulated forces are in a static equilibrium state. On the other hand, when f is equal to 3 rpm, it represents the simulated forces at that azimuth speed. Little variation is observed in the longitudinal forces, while the transverse forces show considerable variation due to the transient effect of the flow on the duct.

Dividing the duct into four different segments allows for a more refined analysis. Although the transverse force on these segments can vary between static and dynamic conditions, the differences in the transverse force are not significant, as shown in Tab. (F.2)

Fig. (F.2) illustrates changes in the velocity field at two different azimuth speeds by extracting the velocity field at $f = 0$ rpm. The highlighted region near the nose of the nozzle shows a clear correlation between the change in velocity and the increase in azimuth speed f. Segments 3 and 4 of the duct experience accelerated flow, while segments 1 and 2 experience decelerated flow. The interaction between azimuth speed and the shape of the duct is responsible for the deviation in transverse force.

Table F.1: A comparison between forces at static and dynamic conditions.

	f = **0 rpm**			f = **3 rpm**		
	Duct	Housing	Propeller	Duct	Housing	Propeller
kF_x	0.188	0.021	0.322	0.192	0.019	0.345
kF_y	0.260	0.105	0.017	0.369	0.124	0.031

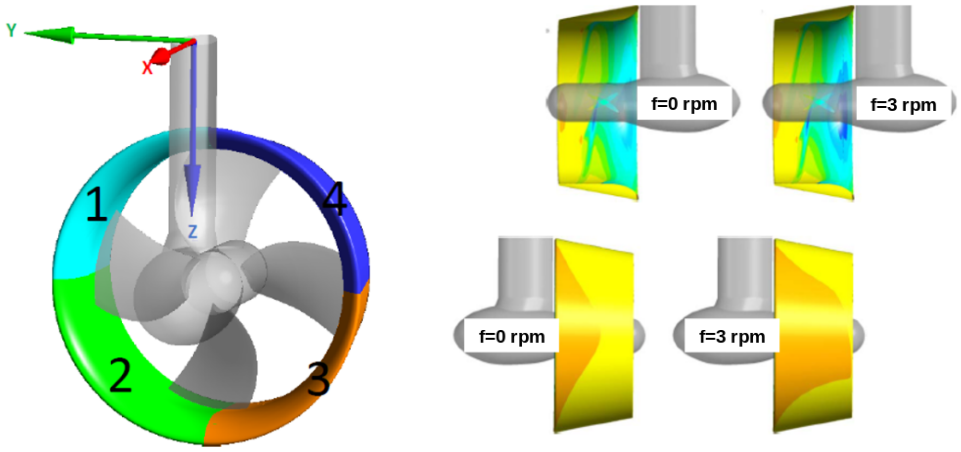

Figure F.1: Illustration of the divided duct (left) and the pressure distribution on segments 3 and 4 (right).

Table F.2: Comparison of kFd_y under static and dynamic conditions.

PART	**1**	**2**	**3**	**4**
$kFd_{\mathbf{y}}$ $\times 10^{-2}$ $(f = 0$ rpm$)$	-3.65	-2.61	17.32	15.38
$kFd_{\mathbf{y}}$ $\times 10^{-2} (f = 3$ rpm$)$	-0.96	0.58	19.86	17.33
DIFF $\times 10^{-2}$	2.68	3.19	2.54	1.95

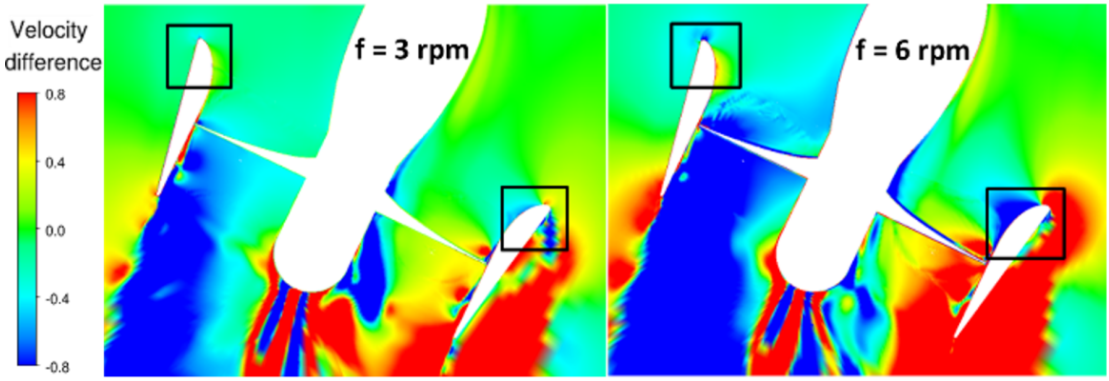

Figure F.2: The velocity field distribution at two azimuth speeds obtained by subtracting the velocity field at $f = 0$ rpm.

F.2 Hull Longitudinal Forces Related to the v and r in the Dynamic Motions

Three possible relationships between the variables X and v in the context of a symmetric hull are shown in Fig. (2.2). In this case, a numerical pure sway test was performed on a bare hull. The test revealed that a displaced flow around the bilge radius results in low pressure at both maximum and minimum sway velocities. This results in the formation of the longitudinal force X', which is approximately symmetric with respect to the velocity v'. Consequently, their relationship can be described by an even function, as shown in Fig. (F.3). The presence of the asymmetric gearbox inside the tunnel, but without a tunnel propeller, could result in an inappropriately asymmetric distribution of forces during the dynamic tests.

Fig. (F.4) shows the correlation between the longitudinal force X' and the yaw rate r'. An odd function is obtained. The asymmetric arrangement of the gearbox located in the tunnel leads to different pressure distributions on the walls during negative and positive yaw rates. Furthermore, as shown in Tab. (F.3), the main cause of this difference is due to the longitudinal force acting on the tunnel wall.

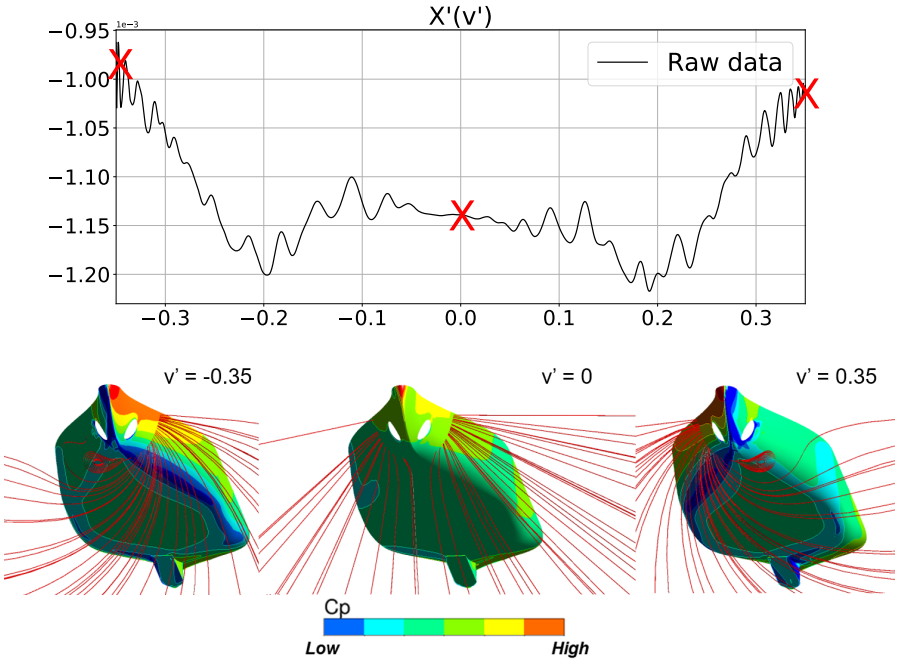

Figure F.3: Relationship between X' and v' (top); an illustration of pressure distribution on the hull in the sway motion test (bottom).

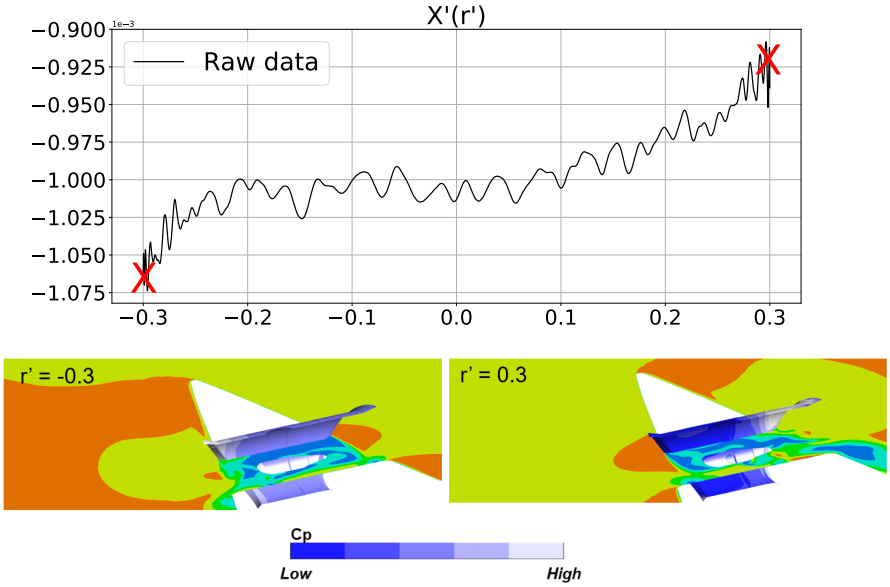

Figure F.4: Relationship between X' and r' (top); an illustration of tunnel wall pressure distribution at negative and positive yaw rates (bottom).

Table F.3: Impact of tunnel wall on X in pure yaw motion.

r' [-]	Hull [kN]	Tunnel wall [kN]	Gearbox [kN]	Total [kN]
-0.3	-8.547	-3.448	-0.034	-12.029
0.3	-8.498	-2.204	-0.038	-10.740
DIFF	0.048	1.244	-0.004	1.289

F.3 Evolution of the Bow Thruster Slipstream during One Period of a Dynamic Test

F.3.1 Sway Motion

The time history of the transverse force, as presented in Section (6.3), shows that the tendency of the transverse force with a working tunnel propeller is comparable to that without a propeller in pure sway motion. The slipstream of the propeller mainly affects the curve progression from position 2 to position 4, see Fig. (F.5). The figure shows that the hull transverse force is the main factor driving changes in the total transverse force. The tunnel propeller forces show minimal change, as noted in Section (4.4). Five sample positions are analyzed at different time points. The transverse force of the hull at these

positions is shown in Fig. (F.6). Fig (F.7) shows the snapshot of the slipstream at the five indicated positions.

At position 1, the sway velocity reaches its maximum value, and the stagnation area near the tunnel inlet on the starboard side generates a negative transverse hull force.

As the ship moves from position 1 to position 2 to its starboard side with decreased sway velocity, the stagnation area switches from the starboard side to the port side, leading to a positive transverse hull force.

As the ship moves from position 2 to position 4, the ship moves with increased sway velocity, the propeller slipstream is pushed to the port side, a higher pressure is observed at position 4.

At position 5, the change in the relative position between the propeller slipstream and the hull creates a low-pressure area on the port side, and at the same time the ship moves to starboard at an increased sway velocity. A negative transverse force is obtained.

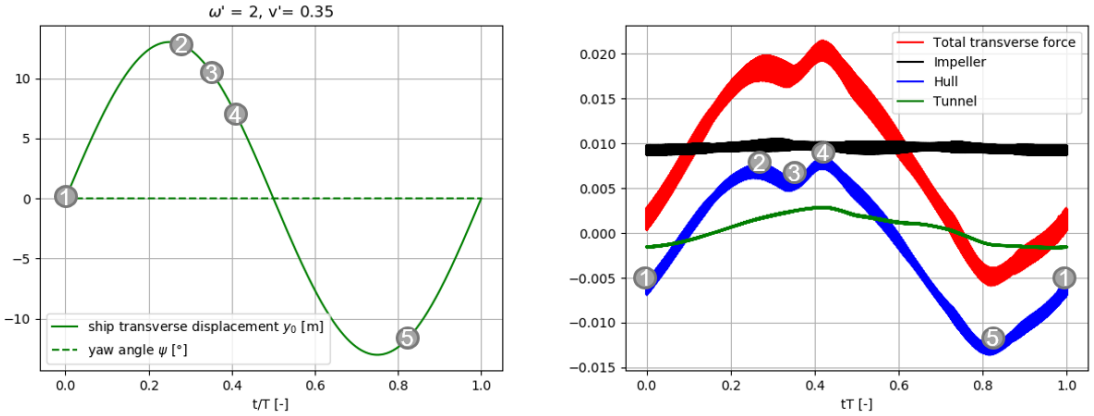

Figure F.5: Transverse force components in the sway motion.

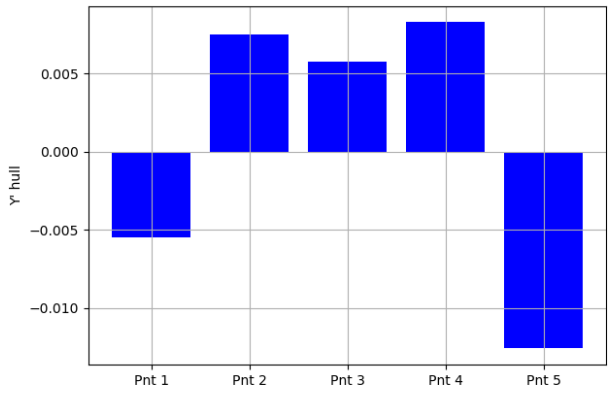

Figure F.6: Hull transverse force at the five time points considered in the sway test.

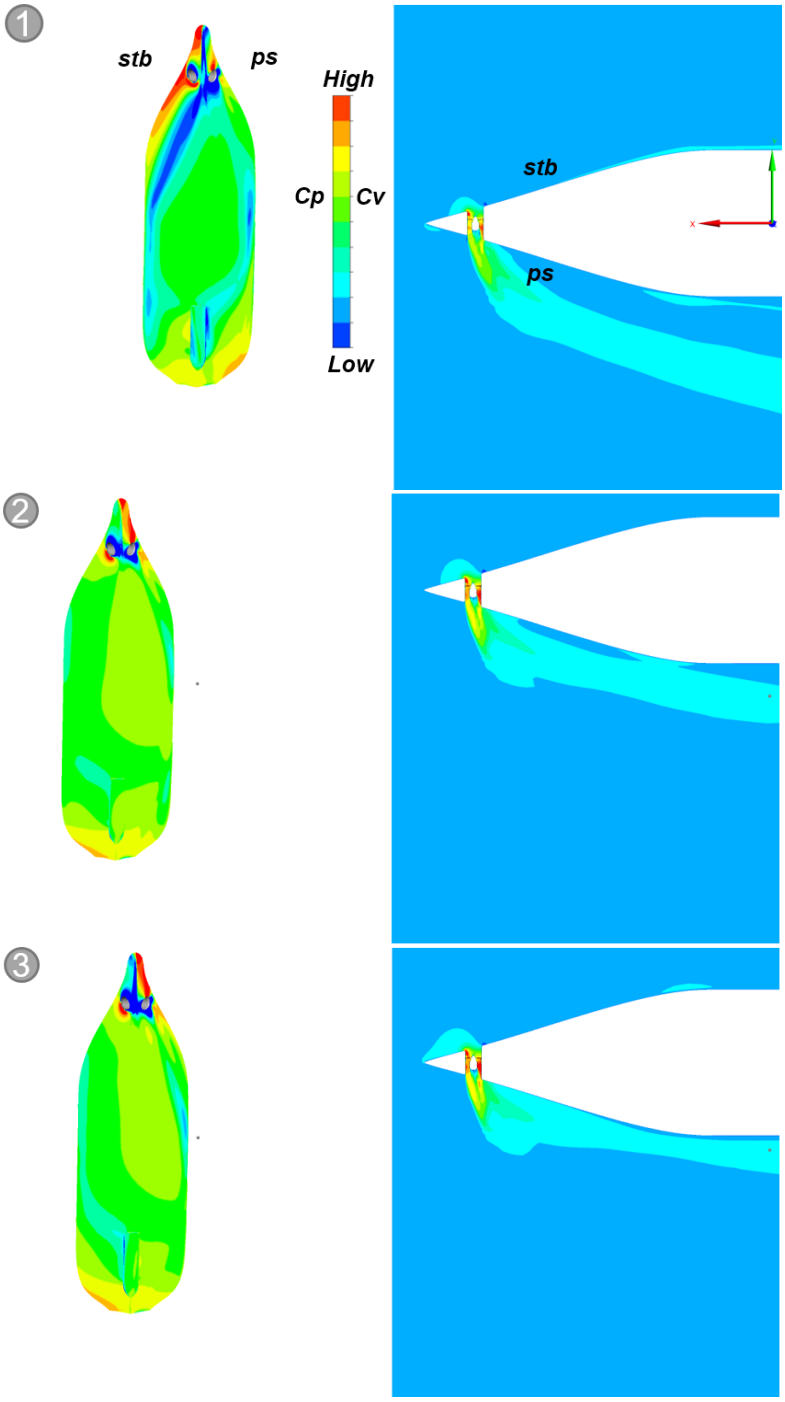

Figure F.7: The evolution of the hull pressure during the sway motion at the five observation points (first part).

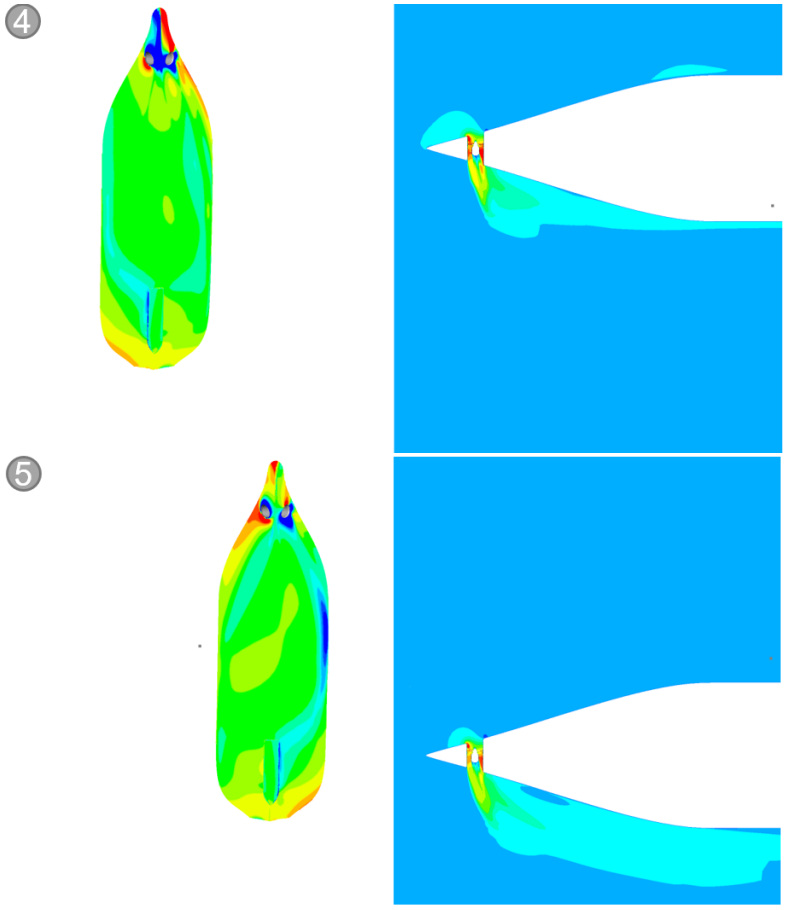

Figure F.7: The evolution of the hull pressure during the sway motion at the five observation points (second part).

F.3.2 Yaw Motion

The evolution of the transverse force of the hull dominates the trend of the total transverse force in both sway and yaw motion. In the yaw motion, this can be seen in Fig. (F.8).

In the pure yaw test without the tunnel propeller, the value of Y' on the hull presented in Fig. (6.7) is not entirely negative. However, Fig. (F.9) shows that the transverse forces acting on the hull become negative when the tunnel propeller is in operation. This suggests that the interaction between the slipstream and the hull is very pronounced.

Fig. (F.10) shows the evolution of the slipstream depending on the ship's motion according to the five snapshots discussed in the following:

1. The ship reaches the minimum y and the zero yaw angle. A slight low-pressure region is observed on the port side of the hull.

2. The ship moves to the starboard side and leaves the slipstream alongside the hull, reducing the attached flow on the hull.

3. The slipstream approaches the hull through the decelerated ship, creating an improved low-pressure area.

4. A slight increase in the Y' hull compared to point 3 is possible for negative yaw (turning the hull away from the slipstream).

5. The position where the slipstream is almost parallel to the shoulder of the hull. The reduction in transverse force is significant.

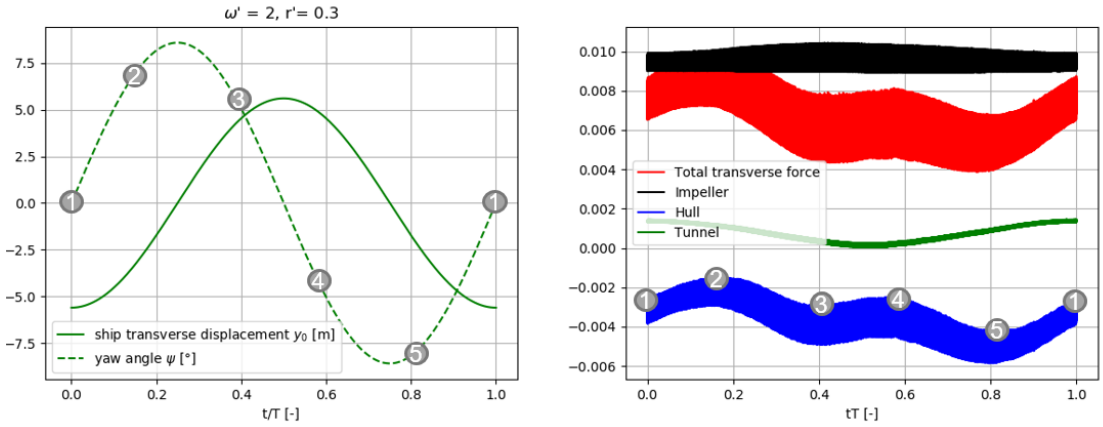

Figure F.8: Transverse force components in the yaw motion.

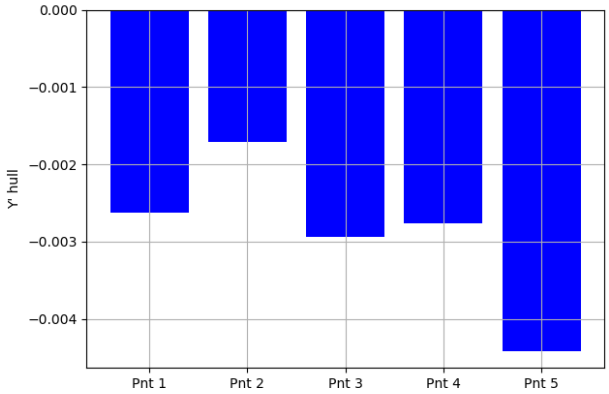

Figure F.9: Hull transverse force at the five time points considered in the yaw test.

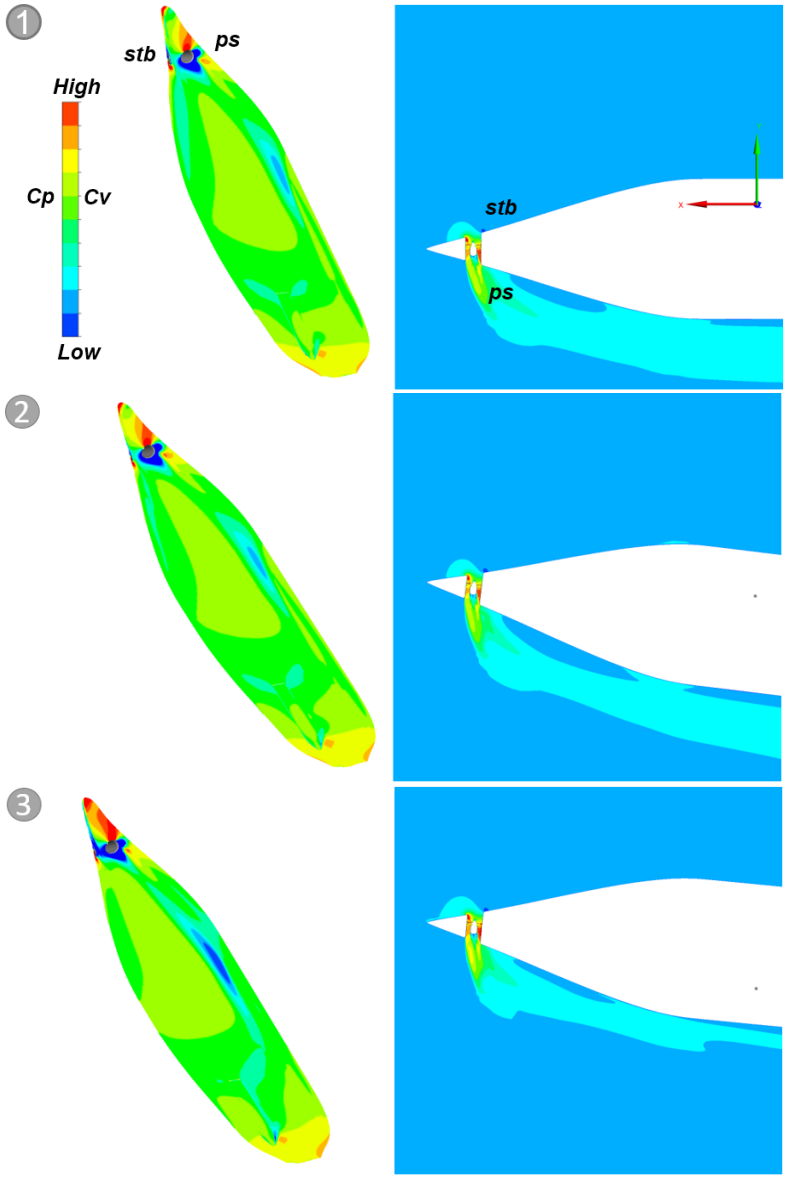

Figure F.10: The evolution of the hull pressure during the yaw motion at the five observation points (first part).

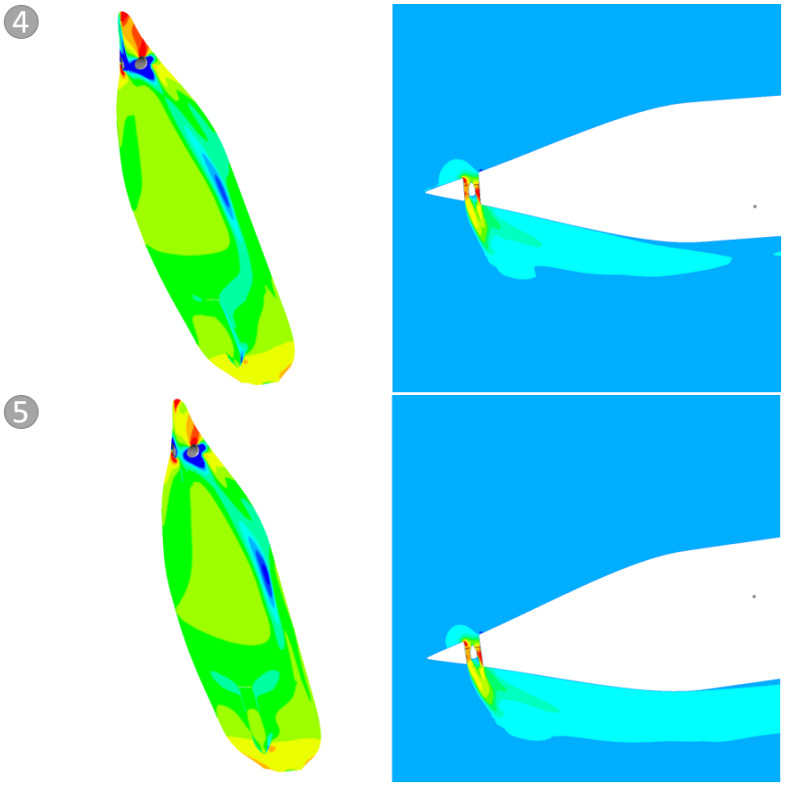

Figure F.10: The evolution of the hull pressure during the yaw motion at the five observation points (second part).